Annual Report 2020

Physik-Department

Lehrstuhl für Funktionelle Materialien

mit dem

Fachgebiet Physik Weicher Materie

Technische Universität München

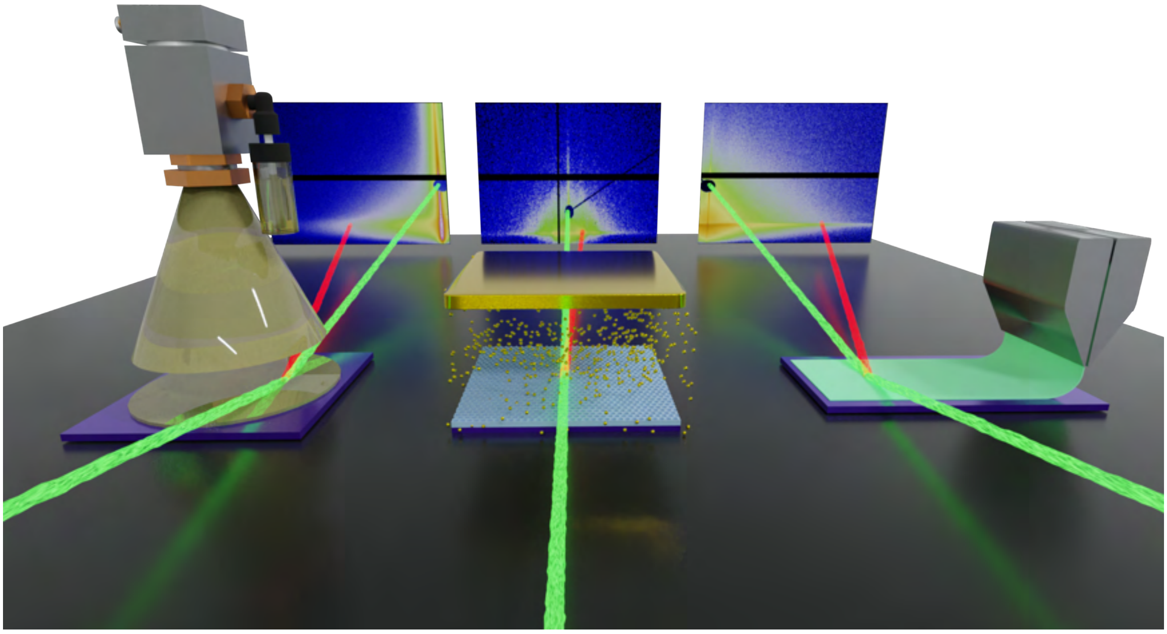

Prof. Dr. Peter Müller-Buschbaum
Chair of Functional Materials
muellerb@ph.tum.de
www.functmat.ph.tum.de
www.polymer.ph.tum.de

Prof. Dr. Christine M. Papadakis
Soft Matter Physics Group
papadakis@tum.de
www.softmatter.ph.tum.de

Physik-Department
Technische Universität München
James-Franck-Straße 1
85748 Garching

Secretaries/Administration:
Marion Waletzki: marion.waletzki@ph.tum.de
Carola Kappauf: carola.kappauf@ph.tum.de

Tel.: +49(0)89 289-12452
Fax: +49(0)89 289-12473

Cover-page picture:

In-situ GISAXS measurement of three different thin film coating processes:
Spray deposition, sputter deposition and slot-die printing

Editor: Dr. Volker Körstgens

Preface

It is a great pleasure to present the annual report for the year 2020 in the name of the staff of the Chair of Functional Materials and the Soft Matter Physics Group. It provides an overview of our teaching, research, and development activities. Our research activities are focused on functional materials and cover a broad range from soft matter physics to developments of methods and instrumentation. We examine the fundamental physics of material properties using mainly scattering methods (neutron, x-ray and light scattering). The general goal of our research is to explain the functional characteristics of soft condensed matter from the knowledge of the molecular dynamics and nanostructure as well as their kinetics.

In 2020, the scientific activities covered the specific areas of polymer solutions and gel, responsive thin films, functional thin films, photovoltaics, polymer-hybrid systems, real-time characterizations and instrumentation and new materials. Like in every place, the Corona pandemic largely influenced the entire life and research activities. From March 18 to April 20, operations of TU Munich were strongly restricted with closed laboratories and all team members working in home-office mode. From April 21 to June 3, we turned into restricted operations with a return of a small number of team members to offices and laboratories. Only in the period June 6 to October 29, a full return of all team members to TU Munich campus was possible, following all the implemented safety rules. After that, again some more restrictions returned.

Despite these challenges, the activities in the fields of polymer films for application in photovoltaics and polymer-hybrid systems were successfully continued. With *"TUM.solar"*, the keylab in the network of in the Bavarian Collaborative Research Project *"Solar Technologies go Hybrid"* (SolTec) headed by Prof. Müller-Buschbaum was running in its nineth year of funding. Research activities covered a broad area of next generation solar cells, such as organic solar cells, dye sensitized solar cells, hybrid solar cells and organometal halide perovskite solar cells. Moreover, thermoelectric materials and energy storage materials with focus on the lithium ion battery technology were actively researched. In addition, we investigated polymers with complex architecture, novel responsive polymers (also under high pressure), self-assembling polymers in solution, multiresponsive and orthogonally switchable polymers as well as polymers for medical applications. Special focus was on the pathways of structural changes upon application of a stimulus.

Due to the Corona pandemic, the in-house experiments available in the laboratories of the chair were supplemented by only a few activities at large-scale facilities, comprising synchrotron radiation and neutron scattering experiments. In particular, the in-house x-ray scattering experiments were operated with full time schedule. Importantly, the general renovation of the laboratories including a reorganizing of the instrument floorplan continued.

In 2020, the Chair of Functional Materials and the Soft Matter Physics group comprised 8 fellows, 53 PhD students, 22 master students, 16 bachelor students, 2 student assistants and 6 administrative and technical staff members. 6 PhD theses were accomplished; moreover, 14 master theses as well as 13 bachelor theses were finished. Different to the years before, we had no possibility to host guests from abroad due to the Corona pandemic.

In general, all members of the chair were very active at virtual conferences and workshops, participating with both, talks and posters. We organized also a limited number of virtual conferences and workshops like the "NINXMACH Workshop" and the "German Neutron Scattering Conference". Unfortunately, the summer school had to be cancelled, as many other events.

Regarding teaching activities of the chair, we offered lectures in *"Advanced Physics for vocational teachers"* (Papadakis). Specialized lectures comprised *"Polymer Physics"* (Müller-Buschbaum), *"Nanostructured Soft Materials"* (Papadakis) and *"Measurement and Sensor Technology"* (Müller-Buschbaum). Prof. Papadakis acted again as a deputy women's representative of the Physics Department. Moreover, Prof. Müller-Buschbaum heads the activities in the *"Network Renewable Energies (NRG)"* in the MSE.

As a service to the community, Prof. Papadakis acted as one of the Editors-in-Chief of *"Colloid and Polymer Science"* and Prof. Müller-Buschbaum served as Associate Editor at *"ACS Applied Materials & Interfaces"*.

This annual report comprises a selection of the different research topics and projects carried out in the individual groups of the chair. It highlights the dedicated as well as successful research activities and collaborations with other groups and large-scale facilities. We wish all chair members a fruitful continuation and a very successful year 2021.

Peter Müller-Buschbaum and Christine M. Papadakis April 2021

Contents

1 Polymer solutions and gels

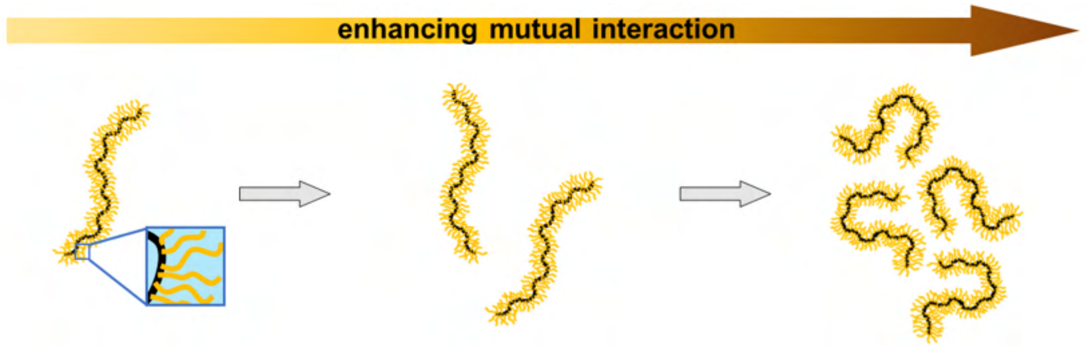

1.1 Rigid-to-soft transition in solutions of molecular bottle brushes

J.-J. Kang, C. Sachse[1], J. Allwang, C.-H. Ko, M. A. Schroer[2], S. Da Vela[2], D. Molodenskiy[2], J. Kohlbrecher[3], R. Jordan[1], C. M. Papadakis

[1] Fakultät Chemie und Lebensmittelchemie, Technische Universität Dresden, Germany
[2] European Molecular Biology Laboratory, c/o DESY, Hamburg, Germany
[3] Laboratory for Neutron Scattering and Imaging, Paul Scherrer Institute, Villigen, Switzerland

Molecular bottle brushes (MBBs) feature a polymeric backbone which is densely grafted with polymeric side chains. In case of a long backbone grafted by relatively short side chains, MBBs resemble a linear polymer with a thick cross section. For solutions, theoretical and simulation studies predict 4 scaling regimes between the chain size R and the concentration c [1]. These encompass the interactions between (i) the backbones, (ii) the persistence segments, (iii) the side chains from neighboring MBBs and (iv) the side chains from the same and from adjacent MBBs. Furthermore, whether a regime appears for the MBB solution is predicted to depend on its architecture. For example, regimes (iii) and (iv) are not observed when the side chains are too short. In the present work, the MBB, P(iPOx)$_{239}$-g-P(nPrOx)$_{14}$, having a long poly(2-isopropenyl-2-oxazoline) (P(iPOx)) backbone and short poly(2-n-propyl-2-oxazoline) (P(nPrOx)) side chains is studied in a good solvent, i.e., ethanol, and the c-dependent conformation is investigated from dilute to semi-dilute condition.

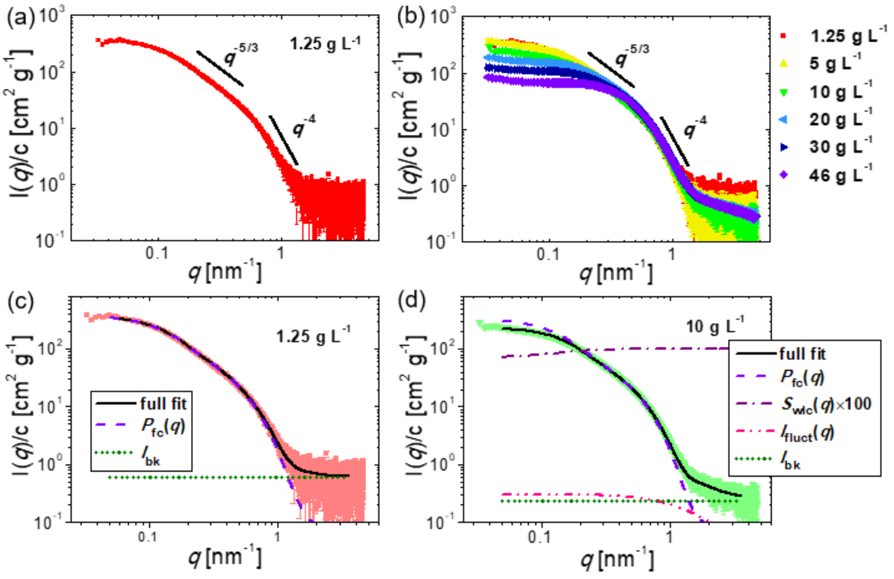

Figure 1.1:
Concentration-normalized SAXS data of the P(iPOx)$_{239}$-g-P(nPrOx)$_{14}$ solution in ethanol at (a) 1.25 and (b) 1.25 – 46 g L^{-1}. Demonstration of the model fitting for low concentrations and high concentrations at the examples of (c) 1.25 and (d) 10 g L^{-1}.

Small-angle X-ray scattering (SAXS) measurements were performed at the Deutsches Elektronen Synchrotron (Hamburg, Germany) at beamline P12. The X-ray energy was 10 keV, and the sample-to-detector distance was 3.0 m, providing a wide range of the momentum tranfers q = 0.03 – 7 nm^{-1}. The concentration-normalized SAXS data are shown in Fig 1.1a,b, which overlap at 1.25 – 5 g L^{-1}. Data at such dilute condition exhibit a plateau at low q and scaling relations of intensity $I \sim q^{-5/3}$ at intermediate and $I \sim q^{-4}$ at high q values (Fig 1.1a). These features suggest that the MBB is a worm-like particle, corresponding to a self-avoiding chain, and the high grafting density of the side chains results in a thick cross section. From 5 to 46 g L^{-1}, the scattering at low q values is steadily suppressed, presumably due to the mutual interactions between the MBBs, while data at high q are unaffected by concentration (Fig 1.1b). For low c (1.25 – 5 g L^{-1}), the SAXS data are modeled by the flexible cylinder form factor $P_{fc}(q)$, as demonstrated in Fig 1.1c. It gives the contour length L, the persistence length l_b and the cross-sectional radius R_c. For 10 – 46 g L^{-1}, $P_{fc}(q)$ is combined with the structure factor of worm-like chains, $S_{wlc}(q)$, with the L and l_b values from $P_{fc}(q)$, as shown in Fig 1.1d. Thus, the interaction between the MBBs depends on their conformation. An additional contribution from the local concentration fluctuations from the side chains, $I_{fluct}(q)$, is included in the fitting model for 10 – 46 g L^{-1}, giving the correlation length ξ.

The analysis results shows that the radius of gyration, R_g, is 11.5 nm between 1.25 and 20 g L^{-1} (Fig 1.2a). Above 20 g L^{-1}, R_g decreases upon increasing c with a scaling of -0.8, implying the effective side chain interactions. Meanwhile, l_b is found to be $\approx$ 10 nm, i.e., much higher than the one of the linear backbone ($l_b \approx$ 1.5 nm), and decreases with increasing c above 10 g L^{-1} until it reaches 3 nm at 46 g L^{-1} (Fig 1.2b), suggesting a drastic decrease of the main chain rigidity. Contrary to R_g and l_b, the structural parameters at small length scales, i.e., R_c and ξ, do not show significant changes upon variation of c (Fig 1.2c,d), meaning that the local structure is unchanged.

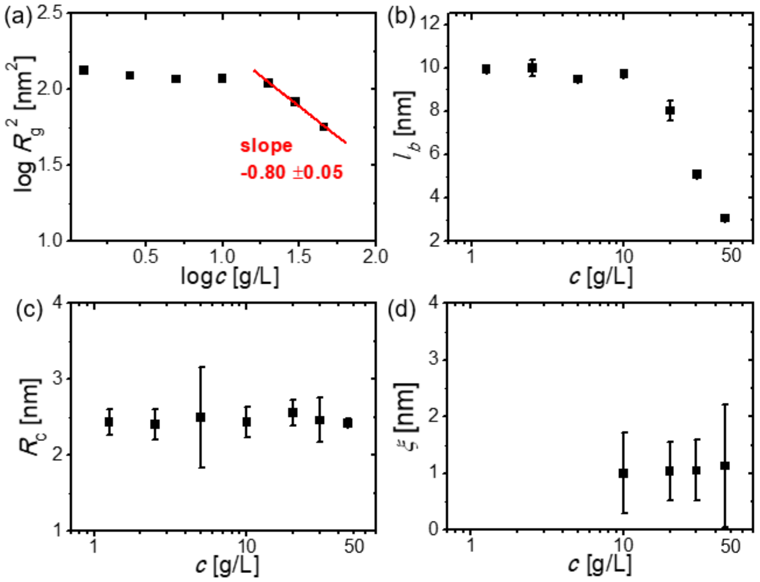

Figure 1.2:
Structural parameters in dependence on concentration. (a) Logarithm of ${R_g}^2$, (b) persistence length l_b, (c) cross sectional radius R_c and (e) correlation length ξ.

To summarize, the conformation of the MBB P(*i*POx)$_{239}$-*g*-P(*n*PrOx)$_{14}$ in the good solvent ethanol depends on concentration: While it assumes a worm-like chain conformation with a rather rigid backbone up to ~15 g L^{-1}, it becomes more flexible at higher concentrations. A direct transition from the isolated state to regime (iv) is observed, which is attributed to the prominent side chain interactions.

This project is funded by Deutsche Forschungsgemeinschaft.

[1] J. Paturej, T. Kreer, *Soft Matter* **13**, 8534-8541 (2017)

1.2 Stimuli-responsive micelles from amphiphilic diblock copolymers

Y. Li, C.-H. Ko, V. Chrysostomou[1], D. Molodenskiy[2], S. Pispas[1], C. M. Papadakis

[1] Theoretical and Physical Chemistry Institute, NHRE, Athens, Greece

[2] DESY, Hamburg, Germany

Stimuli-sensitive micelles based on biocompatible block copolymers poly(2-(dimethylamino) ethyl methacrylate)-*b*-poly(lauryl methacrylate) (PDMAEMA-*b*-PLMA) can change their micellar structures and physical properties in response to external stimuli [1]. We investigate the temperature- and pH-responsive properties of aqueous micellar solutions of PDMAEMA$_{70}$-*b*-PLMA$_{39}$. PDMAEMA is a hydrophilic, weak cationic polyelectrolyte, which is both pH- and temperature-responsive. While it is fully water-soluble at neutral pH, it features lower critical solution temperature (LCST) behavior with transition temperatures of 40-80 °C at pH values above the pK$_a$ of 6.2 [2]. The PLMA block is strongly hydrophobic and lipophilic. The self-assembled micelles formed by these block copolymers can be applied in gene transfer and drug delivery applications. The temperature- and pH-dependent micellar structures of PDMAEMA$_{70}$-*b*-PLMA$_{39}$ depend on concentration. For characterization, dynamic light scattering and synchrotron small-angle x-ray scattering at the BioSAXS beamline (EMBL at DESY, Hamburg) were used.

The polymers were dissolved in tetrahydrofuran, the solvent was evaporated in a rotary evaporator. D$_2$O was used as a solvent to prepare a 3 mg/mL solution, and pH values of 3, 5, and 10 were installed by adding 1 M HCl or NaOH. The pH value was initialled by adding HCl or NaOH. SAXS measurements were carried out at room temperature at the BioSAXS beamline at EMBL, DESY, using a wavelength of 0.124 nm and a sample-detector distance of 3 m. The background from the corresponding buffer was subtracted. Model fitting was carried out using the software SasView.

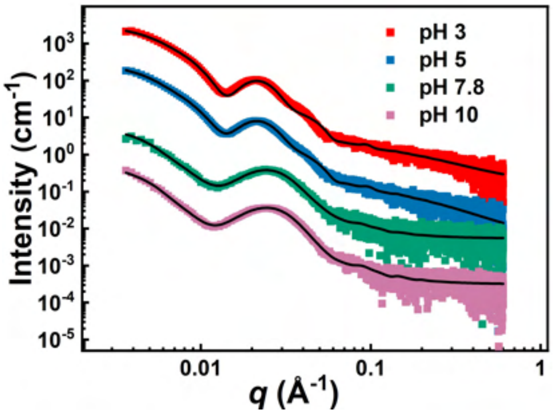

Figure 1.3:
SAXS data of PDMAEMA$_{70}$-*b*-PLMA$_{39}$ solutions at 25 °C and the pH values given in the graph. Symbols represent the data, solid lines the fits.

In fig. 1.3, for all pH values investigated, the shapes of the curves are characteristic of the micellar structures and aggregates. When the pH of the solution is 7.8 or 10, the two curves only include a slope and a broad peak. The slope describes the self-assembled structures of spherical superstructures, consisting of cylindrical micelles. At pH $<$ 7.8, it shows the detailed information of a single micellar size. Especially for the polymer solution with pH 3, the curve shows one shoulder at low q and a peak with a small bridge at the middle q range. We assume the PDMAEMA chains are protonated, so that those aggregates break up into single micelles depending on the repulsive force of stretching chains. The two curves (pH 7.8 and 10) are close, but the typical peak moves to higher q-values as the pH from 7.8 to 10. Comparsed with the neutral solution, the micellar structures are collapsed in the basic polymer solution.

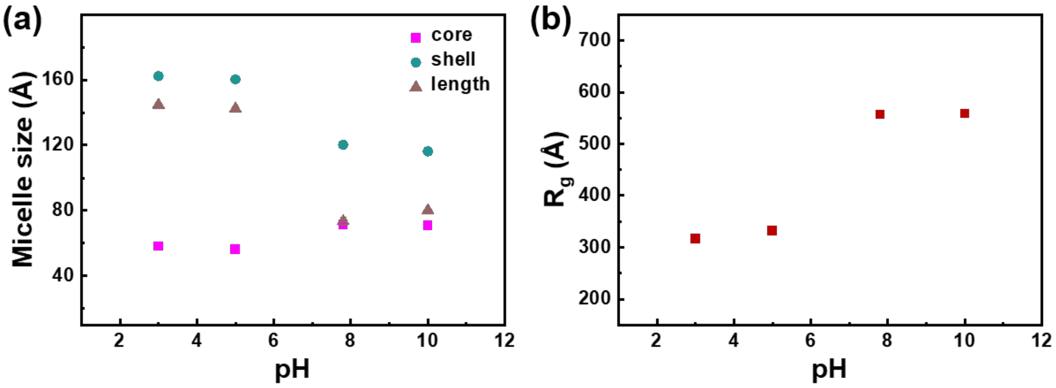

Figure 1.4:
Fitting parameters depend on the pH of PDMAEMA$_{70}$-*b*-PLMA$_{39}$ aqueous solutions. (a) includes core radius, shell thickness, and the length of cylindrical micelles. (b) The radius of gyration of aggregates.

The following model consisting of three terms was used to fit the scattering curves. It includes the Guinier-Porod term to model the forward scattering curves for aggregates, the core-shell cylinder for the micellar shape, and Ornstein-Zernike for the correlation between the chains. Fig. 1.4 (a) shows the micellar sizes: with pH value increasing from 3 to 10, a slightly increasing radius of the cylindrical core but strongly decreasing shell and length of cylindrical micelles. As observed under the completely protonated condition of PDMAEMA blocks, the size of the shell (150 Å) is close to the contour length of the PDMAEMA block (175 Å), but it is larger than the thickness of the shell (80 Å) in a basic solution. From pH 3 to pH 10, the thinner shells and shorter lengths are attributed to the partially deprotonated PDMAEMA chains. In the basic solution, the thickness of the shell is larger than the length of the end-to-end distance of the PDMAEMA chain (20.9 Å). The hydrophilic chains are swollen in basic solutio. The core size of micelles, 60 Å, is larger than the end-to-end distance of PLMA, 15.6 Å. We assume that the cores still contain a small amount of THF. Fig. 1.4 (b) indicates the increasing radius of gyration of the aggregates from pH 3 to 10. Based on the results of Fig. 1.4 (a), in contrast to pH 5, the spherical aggregates contain more cylindrical micelles at pH 7.8 due to the collapse of micellar structures.

We conclude that with pH increasing from 3 to 10, the thickness of shell and length of cylinder decrease due to the collapsed micellar structures consisting of PDMAEMA$_{70}$-*b*-PLMA$_{39}$. At pH 3 and 5, the self-assembled structures prefer to form single and larger micelles due to the strong replusion force between cationic PDMAEMA chains. At pH 7.8 and 10, PDMAEMA chains are deprotonated, and the aggregates are large.

[1] V. Chrysostomou, S. Pispas, *J. Polym. Sci. A: Polym. Chem.* **56**, 598-610 (2018)

[2] F. A. Plamper, M. Ruppel, A. Schmalz, O. Borisov, M. Ballauff, A. H. E. Müller, *Macromolecules* **40**, 8361-8366 (2007)

1.3 Thermal and block length effects on the aqueous nanoscale morphologies of thermoresponsive double hydrophilic block copolymers

A. Vagias[1], A. Papagiannopoulos[2], L. P. Kreuzer, D. Giauzi[2], S. Busch[3], S. Pispas[2], P. Müller-Buschbaum

[1] MLZ, TUM, Garching, Germany
[2] NHRF, Athens, Greece
[3] MLZ, HZG, Garching, Germany

Exploring nanostructural self-assemblies of double hydrophilic block copolymer (DHBC) in water would provide significant efforts from a synthetic approach towards grasping the more complex living cell nanoscaled structure. Double hydrophilic block copolymers (DHBCs) represent a class of stimuli responsive materials [1] where both blocks are hydrophilic and one of them can be sensitive to ionic strength, pH and temperature alterations. In particular, thermoresponsive DHBC (TDHBC) are broadly utilized as so-called "smart" scaffolds for biomedicine, sensor design and as highly successful drug delivery schemes for hydrophobic drug encapsulation [2]. A well-explored thermoresponsive homopolymer case is poly(N-isopropylacrylamide) (PNIPAM) that is characterized by a lower critical solution temperature (LCST) in water close to human body temperature (LCST $\sim$ 32 °C). In cases where PNIPAM and another hydrophilic block are covalently bound, the selective responsivity of solely PNIPAM block to temperature as external stimulus enables diverse self-assembled morphologies of TDHBCs in water. When a hydrophobic block is covalently bound to PNIPAM precipitation could occur [3], however TDHBCs exhibit no precipitation. The LCST can be tuned by covalently binding a block of certain (different) hydrophilicity to PNIPAM and the tunability of the LCST depends on the block length asymmetry. Investigations combining information on the molecular level and on the mesoscopic inner structure of TDHBC self-assemblies, combining knowledge from complementary techniques, such as Fourier transform infrared (FTIR) spectroscopy and small angle neutron scattering (SANS), are lacking.

In this study, we complement FTIR to SANS in order to explore the nanoscale inner morphological characteristics of novel PNIPAM-block-poly(oligo ethylene glycol methyl ether acrylate) (PNIPAM-b-POEGA) self-assemblies [4] and the interplay between solvent and PNIPAM-b-POEGA as TDHBCs at the molecular level. Our aim is to study the effects of PNIPAM chain length and temperature (T) variations below and above the nominal LCST-like transition of PNIPAM on the nanoscale morphology and molecular vibrations from aqueous TDHBC self-assemblies of PNIPAM-b-POEGA with different block lengths for both PNIPAM blocks. By coupling results from SANS to ones from FTIR we realize a correlation between the inter(intra)-molecular interactions at the molecular level and the internal morphology of the self-assemblies, upon variation of block lengths and number of chain end groups. We have prepared heavy water (D_2O) solutions at 1% wt of protonated PNIPAM$_{19}$-b-POEGA$_9$ and PNIPAM$_9$-b-POEGA$_9$ DHBCs, subscripts denoting M_w values in kg/mol. The SANS experiments have been conducted at the SANS-1 instrument (MLZ, Garching, Germany). A wavelength of maximum neutron flux ($\lambda = 4.5$ Å) and three different collimation/sample-detector distances have been used, namely 4m/1.176m, 8m/8m and 20m/20m, in a T-range from 25 °C to 55 °C and also again at T = 25 °C to examine possible presence of thermal hysteresis. After radial averaging of the two dimensional scattering patterns, the macroscopic scattering cross-sections $I(q)$ were obtained.

The fit to the $I(q)$ shown in Fig.1.5 was a sum of three contributions: one describing scattering from single chains, or, from interchain subsections (smallest sizes), another one depicting more well-defined core-shell or fractal core-shell moieties (intermediate sizes) and a last one representing large scale inhomogeneities (largest sizes). The $I(q)$ were fitted over the whole q range probed to assess the nanostructural PNIPAM-b-POEGA morphologies.

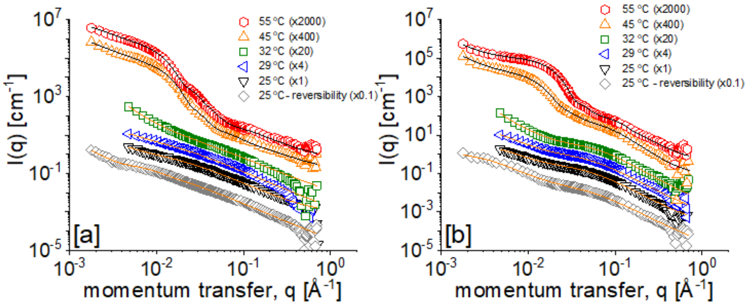

Figure 1.5:
Radially averaged SANS intensities, $I(q)$, at various T values, for 1% wt aqueous [a] PNIPAM$_{19}$-b-POEGA$_9$ and [b] PNIPAM$_9$-b-POEGA$_9$ solutions. Solid orange and black lines denote the fits for each curve. Curves have been multiplied with respect to the experimental $I(q)$ by the displayed factors in the legend, for clarity.

Fig.1.6 depicts T-dependent FTIR results for (a) PNIPAM$_{19}$-b-POEGA$_9$ and (b) PNIPAM$_9$-b-POEGA$_9$ 1% wt D_2O solutions. We identify distinct changes with T for the PNIPAM-b-POEGA molecular vibrations based on the block length asymmetry. With increasing T, SANS results suggest a crossover from less well-defined and more fractal conformation to well-defined morphologies especially at intermediate q values. The absence of a plateau at very low q values suggests presence of large scale clusters and/or mesoglobules at elevated T values. On the other hand, due to its respective wavenumber shift, FTIR proves that the asymmetric stretching vibration is quite sensitive to T alterations.

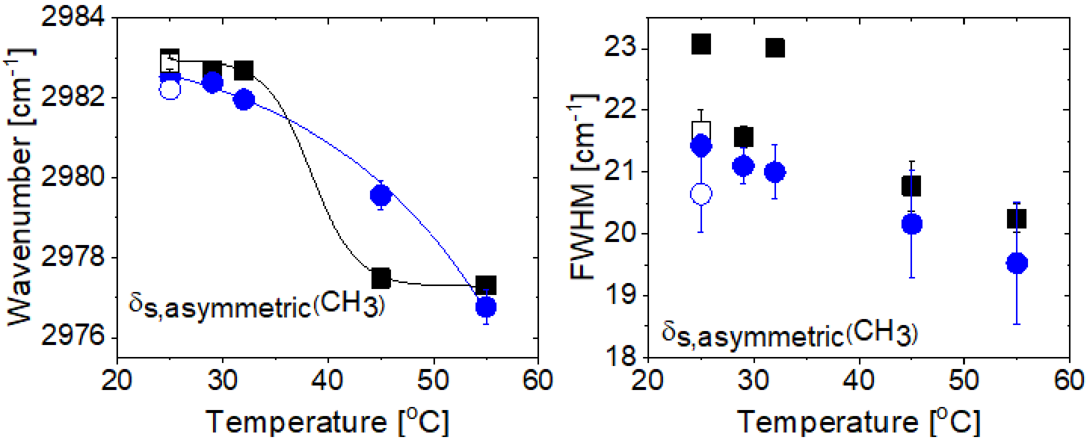

Figure 1.6:
Evolution with respect to T of (left) peak wavenumbers and (right) FWHM, for the asymmetric stretching vibrations of the isopropyl CH_3 side chain for PNIPAM$_{19}$-b-POEGA$_9$ (black squares) and PNIPAM$_9$-b-POEGA$_9$ (blue circles) at 1% wt D_2O solutions. The solid lines are drawn to guide the eye.

In summary, we identified hydrophilic block length effects on the mesoscale self-assembly and on molecular vibrations on double hydrophilic PNIPAM-b-POEGA block copolymers in D_2O. Our results suggest that at these small block M_w values, block length variations exert crucial impact on self-assembly. We speculate that the role of endgroups is also interrelated.

[1] H. Cölfen, *Macromol. Rapid Comm.* **22**, 219 (2001)

[2] A. El Jundi, S. Buwalda, A. Bethry, S. Hunger, J. Coudane, Y. Bakkour, *Biomacromolecules* **21**, 397-404 (2020)

[3] P. Pramanik, S. Ghosh, *J. Polym. Sci. Part A: Polym. Chem.* **53**, 2444 (2015)

[4] D. Giaouzi, S. Pispas, *J. Polym. Sci. Part A: Polym. Chem.* **57**, 1467-1477 (2019)

1.4 Co-nonsolvency effect in solutions of poly(methyl methacrylate)-*b*-poly(*N*-isopropylacrylamide) diblock copolymers in water/methanol mixtures

C.-H. Ko, C. Henschel[1], G. P. Meledam, M. A. Schroer[2], R. Guo, L. Gaetani,
P. Müller-Buschbaum, A. Laschewsky[1,3], C. M. Papadakis

[1] Universität Potsdam, Institut für Chemie, Potsdam-Golm, Germany
[2] European Molecular Biology Laboratory, c/o DESY, Hamburg, Germany
[3] Fraunhofer IAP, Potsdam-Golm, Germany

Amphiphilic block copolymers having a hydrophobic poly(methyl methacrylate) (PMMA) block and a thermo-responsive poly(*N*-isopropylacrylamide) (PNIPAM) block form core-shell micelles in aqueous solution. The micellar shell collapses at the transition temperature of PNIPAM block, and the collapsed micelles form aggregates [1]. The system is not only sensitive to temperature, but also to the solvent composition. Adding methanol as a cosolvent causes the collapse of PNIPAM blocks, thereby decreasing the transition temperature, which is called co-nonsolvency effect.

We aim at exploring the effect of methanol on the morphology of $PMMA_{21}$-*b*-$PNIPAM_{283}$. At this, we use turbidimetry to investigate the influence of the solvent composition on the phase behavior of PMMA-*b*-PNIPAM in a series of D_2O/CD_3OD mixtures to determine the cloud point, differential scanning calorimetry (DSC) to characterize the thermal properties, and synchrotron small-angle X-ray scattering (SAXS) to disclose the structural changes of $PMMA_{21}$-*b*-$PNIPAM_{283}$ in dependence on the solvent composition at 20 °C.

$PMMA_{21}$-*b*-$PNIPAM_{283}$ was synthesized by the reversible addition fragmentation chain transfer (RAFT) method. The polymers were dissolved in mixtures of D_2O/CD_3OD at 10 g L^{-1}. In water-rich solvent mixtures, T_{CP} decreases from 31.2 °C in pure D_2O to 13.6 °C in 70:30 v/v D_2O/CD_3OD. In methanol-rich solvent mixtures, the samples with volume fractions of CD_3OD above 70 % do not feature a cloud point, but are transparent (Fig. 1.7b). SAXS measurements were carried out at the BioSAXS instrument at EMBL, DESY. 20 frames per measurement were collected. The measurement time was 45 ms each frame.

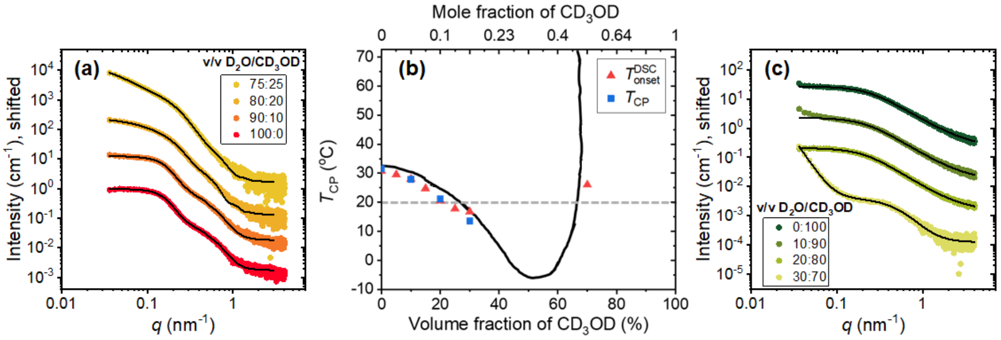

Figure 1.7:
a) SAXS data (symbols) and fitting curves (lines) of 10 g L^{-1} $PMMA_{21}$-*b*-$PNIPAM_{283}$ in water-rich solvent mixtures at 20 °C. b) Phase diagram in dependence on the volume fraction of CD_3OD. The black line depicts the coexistence line found for PNIPAM homopolymers [2]. c) SAXS data and model fits curves in methanol-rich solvent mixtures at 20 °C.

Fig. 1.7a shows the SAXS data of $PMMA_{21}$-*b*-$PNIPAM_{283}$ in water-rich solvent mixtures. For the samples with CD_3OD volume fractions of 0-15 vol%, the scattering curves feature two shoulders. They are modelled by a form factor for spherical core-shell particles, in which the radial SLD profile in the shell decays exponentially. A sticky hard sphere structure factor was chosen to describe the correlations between micelles. For the solutions with CD_3OD volume fractions of 20 and 25 vol%, forward scattering is present (Fig. 1.7a). Besides, at 20 and 25 vol%, the shell is found to be homogeneous, which might be due to the proximity of the cloud point at these compositions (Fig. 1.7b). Therefore, a homogenous shell was used, and the micellar clusters were described as fractal aggregates. At high methanol contents, the SAXS data feature a shoulder at 0.3 nm^{-1} (Fig. 1.7c), indicating the presence of molecularly dissolved chains. These data were fitted using the excluded volume model, giving information on the chain conformation.

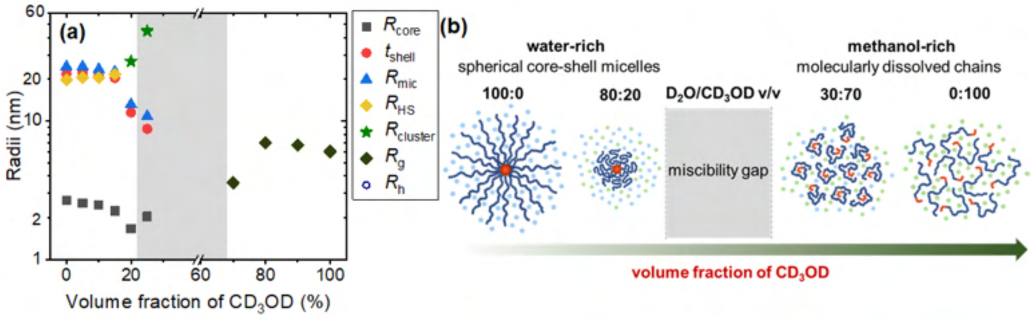

Figure 1.8:
a) Length scales resulting from model fitting. b) Schematic structures of 10 g L^{-1} $PMMA_{21}$-*b*-$PNIPAM_{283}$ in D_2O/CD_3OD mixtures at 20 °C.

The fitting results are shown in Fig. 1.8a. For CD_3OD contents up to 25 vol%, the $PMMA_{21}$-*b*-$PNIPAM_{283}$ diblock copolymers self-assemble into spherical core-shell micelles. Upon increasing CD_3OD volume fraction, the micellar core radius and the aggregation number of micelles decrease slightly, which is due to the presence of CD_3OD that weakens the intermolecular interactions between PMMA blocks in the micellar core. Besides, the micellar shell thickness decreases slightly up to 15 vol% of CD_3OD and is much lower at 20 vol%, which is ascribed to a reduced solvent quality for PNIPAM blocks, caused by the co-nonsolvency effect, that makes them shrink. Furthermore, the clusters formed by the collapsed micelles appear at 20 vol% of CD_3OD, which is presumably due to the enhanced attractive interactions between micelles, starting at 15 vol%. For 70 vol% of CD_3OD, the radius of gyration of the polymers, R_g, determined by SAXS is only 3.6 nm, indicating that the diblock copolymers are molecularly dissolved. For CD_3OD above 70 vol%, R_g is 7 nm and decreases again slightly up to 100 vol% of CD_3OD, which may be attributed to the overall enhancement solubility of the PMMA blocks by CD_3OD.
In summary, the solvent-induced structural changes of $PMMA_{21}$-*b*-$PNIPAM_{283}$ in D_2O/CD_3OD mixtures at 20 °C are schematically depicted in Fig. 1.8b. The diblock copolymers form spherical core-shell micelles for CD_3OD up to 25 vol%. The internal morphology of the micelles is altered by the solvent composition in two ways: CD_3OD enhances the solubility of PMMA in the micellar core, while it has a co-nonsolvency effect on the PNIPAM micellar shell. On the other hand, as the CD_3OD content is 70 vol% or above, the diblock copolymers are molecularly dissolved. With increasing CD_3OD volume fraction, the polymers become more swollen.

The project is funded by Deutsche Forschungsgemeinschaft (DFG).

[1] C.-H. Ko, C. Henschel, G. P. Meledam, M. A. Schroer, P. Müller-Buschbaum, A. Laschewsky, C. M. Papadakis, *Macromolecules* **54**, 384-397 (2021)

[2] H. G. Schild, M. Muthukumar, D. A. Tirrell, *Macromolecules* **24**, 948-952 (1991)

1.5 Pressure-dependence of the co-nonsolvency effect in aqueous PNIPAM solutions

B.-J. Niebuur, C.-H. Ko, X. Zhang, K.-L. Claude, L. Chiappisi[1,2], A. Schulte[3],
C. M. Papadakis

[1] ILL, Grenoble, France
[2] TU Berlin, Germany
[3] University of Central Florida, Orlando, U.S.A.

The origin of co-nonsolvency and its breakdown upon application of pressure are under vivid discussion. The present work focuses on the influence of a cosolvent on the structural properties of semidilute aqueous poly(*N*-isopropylacrylamide) (PNIPAM) solutions in dependence on pressure. In pure water, this thermo-responsive polymer features a lower critical solution temperature (LCST) behavior. In mixed solvents, e.g. in water/methanol, the cloud point T_{cp} is suppressed, and a miscibility gap appears. This feature is termed the co-nonsolvency effect. We investigate a semidilute PNIPAM solution in a water/methanol mixture using small-angle neutron scattering (SANS) at temperatures up to the cloud point at pressures covering a broad range [1]. The scaling behavior of the susceptibility and the correlation length of the concentration fluctuations is established, and the pressure dependence of the effective Flory-Huggins interaction parameter between the PNIPAM segments and the solvent mixture is calculated.
The pressure-dependent cloud points of PNIPAM with a molar mass $M_n = 36$ kg/mol and a concentration of 3 wt% in an 80:20 v/v mixture of fully deuterated methanol (CD_3OD) and heavy water (D_2O) were determined using turbidimetry. SANS measurements were conducted at the instrument D11 at the Institut Laue-Langevin (ILL), Grenoble, France. A wavelength of the incident neutron beam of $\lambda = 6.0$ Å and sample-detector distances of 3.0, 10.0 and 39.0 m were chosen. The sample was mounted in a temperature-controlled CuBe pressure cell with an optical path length of 2 mm. The Ornstein-Zernike function was used to model scattering from concentration fluctuations at small length scales and to determine their correlation length ξ, which corresponds to the average distance between overlap points.
Figure 1.9a shows the cloud points T_{cp} in dependence on pressure. At elevated pressures, the presence of a cosolvent significantly increases the one-phase region. Figure 1.9b displays scattering curves of the PNIPAM solution in D_2O/CD_3OD in dependence on temperature up to T_{cp} at 265 MPa. Scattering from local concentration fluctuations gives rise to the shoulder at momentum transfers $q \approx 0.1 - 1$ nm^{-1}. In addition, weak forward scattering at $q < 0.05$ nm^{-1} is present, pointing to large-scale inhomogeneities.

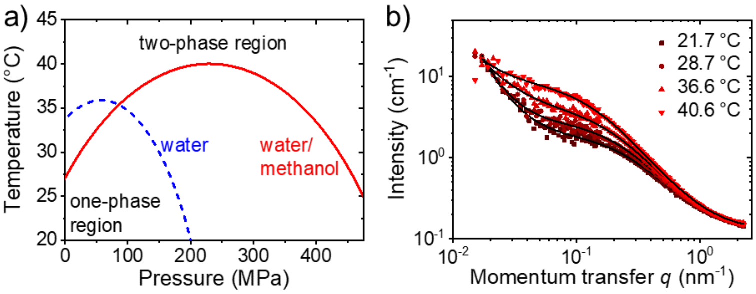

Figure 1.9:
(a) Coexistence lines $T_{cp}(p)$ of the PNIPAM solution in pure D_2O (dashed blue line) and in 80:20 v/v D_2O/CD_3OD (full red line). (b) Representative SANS data at 265 MPa below T_{cp} (symbols). Lines are model fits.

The values of ξ, resulting from the fits of the Ornstein-Zernike function are given in Figure 1.10a. In the one-phase state, ξ increases with temperature at all pressures and diverges near $T_{cp}(p)$. Thus, with increasing temperature, the chains shrink, which increases the distance between overlap points between the chains. Its critical temperature dependence allows determining the effective Flory-Huggins interaction parameter, χ_{eff}, which describes the interaction strength between the polymer segments and the solvent mixture. At all pressures, χ_{eff} is ca. 0.45-0.47 at the lowest measured temperatures and increases with temperature (Figure 1.10b). Thus, at all pressures, the solvent mixture changes from being a good solvent far below $T_{cp}(p)$ to being a theta solvent for PNIPAM near the cloud point.

Both local entropic and enthalpic effects contribute to χ_{eff}. In the commonly used expression $\chi_{\text{eff}} = \chi_\sigma + \chi_h/T$, these contributions are described by the parameters χ_σ and χ_h, respectively. Fits of this expression to the data (Figure 1.10b) allows us to examine the pressure dependence of both contributions individually (Figure 1.10c and d). χ_σ may originate from the hydrophobic effect, which favors demixing. The decrease of this parameter with increasing pressure indicates that the hydrophobic effect is weakened at high pressures. This may be due to the release of methanol from the PNIPAM chains at high pressures [2], which leads to an enrichment of the solvent phase with methanol. This weakens the hydrophobic effect and stabilizes the one-phase region. The observed increase in χ_h with pressure suggests that the tendency to mix on enthalpic grounds becomes weaker, which may be due to a lower number of hydrogen bonds between the polymers chains and water at high pressure. The resulting reduction in overall chain solvation may therefore lead to weaker enthalpic polymer–solvent interactions, which is consistent with the contraction of the chain conformation in the one-phase state at high pressures (Figure 1.10e).

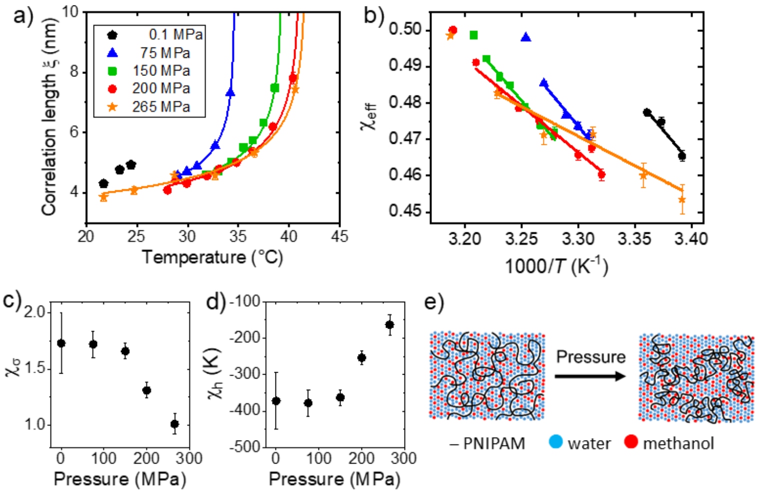

Figure 1.10:
(a) Correlation length of concentration fluctuations, ξ, in dependence on temperature in the one-phase state at the pressures given in the graph. The lines are fits of power laws. (b) Effective polymer-solvent interaction parameter χ_{eff} in dependence on inverse temperature. Same symbols as in (a). The lines are fits. (c, d) Entropic and enthalpic components of the polymer-solvent interaction parameter, χ_σ and χ_h, in dependence on pressure. (e) Change of chain conformation upon application of pressure.

To conclude, high-pressure SANS measurements in the one-phase state of PNIPAM in water/methanol reveal the pressure dependent chain conformation. Analysis of the effective Flory-Huggins interaction parameter indicates that the enthalpic polymer-solvent interactions are weakened at high pressure, which may be related to the contracted chain conformation. These changes in interactions may be related to the largely expanded solubility region in the temperature-pressure phase diagram in the water/methanol mixture compared to pure water.

The project is funded by Deutsche Forschungsgemeinschaft.

[1] B.-J. Niebuur, C.-H. Ko, X. Zhang, K.-L. Claude, L. Chiappisi, A. Schulte, C. M. Papadakis, *Macromolecules* **53**, 3946-3955 (2020)

[2] A. Pica, G. Graziano, *Biophys. Chem.* **231**, 34-28 (2017)

1.6 Water dynamics in an aqueous solution of perdeuterated poly(*N*-isopropylacrylamide) across the demixing transition

B. Yazdanshenas, B.-J. Niebuur, D. Schanzenbach[1], A. Laschewsky[1,2], M. Zamponi[3], D. Noferini[3], M. Wolf[3], W. Lohstroh[3], A. Schulte[4], C. M. Papadakis

[1] Universität Potsdam, Potsdam-Golm, Germany
[2] Fraunhofer IAP, Potsdam-Golm, Germany
[3] MLZ, TUM, Garching, Germany
[4] University of Central Florida, Orlando, U.S.A.

Hydration water is a key factor for the functionality of responsive polymers in aqueous solution. A general feature of the hydration water is that its motion is spatially and/or temporally hindered with respect to bulk water. The water dynamics in aqueous solutions of the thermoresponsive polymer poly(N-isopropylacrylamide) (PNIPAM) was studied using quasi-elastic neutron scattering (QENS, [1,2]). It was found that the population of the hydration shell splits into two contributions at the phase transition temperature. However, the energy range used as well as the scattering signals from the polymer chains did not allow to resolve the dynamics of hydration water unambiguously.

In the present study, we aim to obtain a more comprehensive picture of the hydration water dynamics in this system by using a deuterated polymer as well as carrying out QENS over a wide frequency range. Deuteration of PNIPAM suppresses the incoherent scattering from the polymer chain, while high-resolution backscattering QENS provides information on the phase behaviour of the low frequency dynamics, that can be combined with the faster dynamics of bulk water.

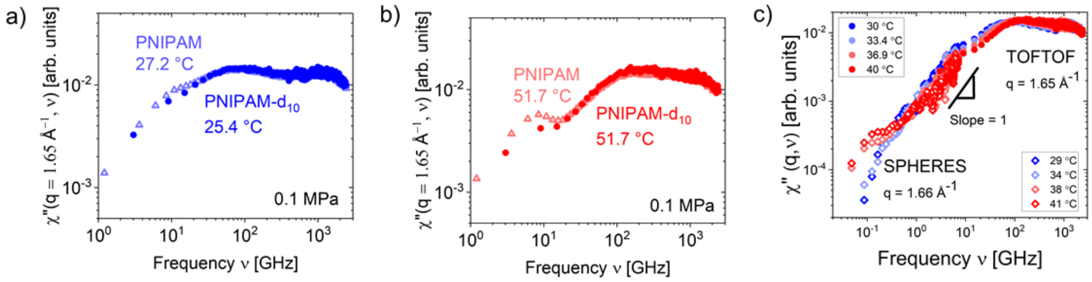

Figure 1.11:
(a) Dynamic structure factors from SPHERES at a momentum transfer $q = 0.60$ Å^{-1} of the resolution (gray open circles) and the sample below (blue open squares) and above (red open triangles) the cloud point. The full lines are fits of a sum of two Lorentzian functions. (b, c) Widths of the narrow (b) and the broad Lorentzian (c). The q range, where coherent scattering by the polymer is strong, is shaded gray.

Perdeuterated PNIPAM-d$_{10}$ with a molar mass $M_n = 8350$ g/mol was dissolved in H_2O at a concentration of ca. 25 wt%. High-resolution QENS measurements were conducted at the backscattering instrument SPHERES at MLZ, Garching, Germany. A wavelength of the incident neutron beam of 6.27 Å with a resolution of ca. 0.32 μeV (HWHM) were used. The sample was mounted in the slit of an annular aluminum cell. A heating scan around the cloud point ($T_{CP} = 33.9 \pm 0.1$ °C) was performed with measuring times of 8 h per temperature. A sample measurement at 3 K was used as an approximation for the resolution function, and the empty cell scattering was subtracted from all data. A QENS measurement at the time-of-flight spectrometer TOFTOF at MLZ was carried out to characterize the faster dynamics of hydration and bulk water. A neutron wavelength of 6 Å and a resolution of ca. 0.025 meV (HWHM) were selected. The sample was mounted in an aluminum pressure cell. A heating scan around the cloud point was performed with a measuring time of 1 h. The spectra were normalized to the incoming neutron flux and a vanadium standard measurement, and the empty cell scattering was subtracted.

Fig. 1.11 (a) depicts representative dynamic structure factors $S(q{=}0.60\ \text{Å}^{-1}, \Delta E)$ from SPHERES at temperatures below and above the cloud point together with the resolution function. Two Lorentzian functions were fitted to the data in the range $|\Delta E|{<}0.6\ \mu$eV and $q{<}1\ \text{Å}^{-1}$, where the signal to noise ratio was best. The q-dependence of the resulting widths is shown in Fig. 1.11 (b, c). Above the cloud point, the narrow Lorentzian having a width of ca. 2 μeV for all q values, is rather strong. It is attributed to strongly bound water (H-bonded to the amide group). The broad Lorentzian has a width of 15 - 40 μeV, independent of temperature and q, suggesting that a faster type of hydration water is present, possibly hydrating the hydrophobic groups.

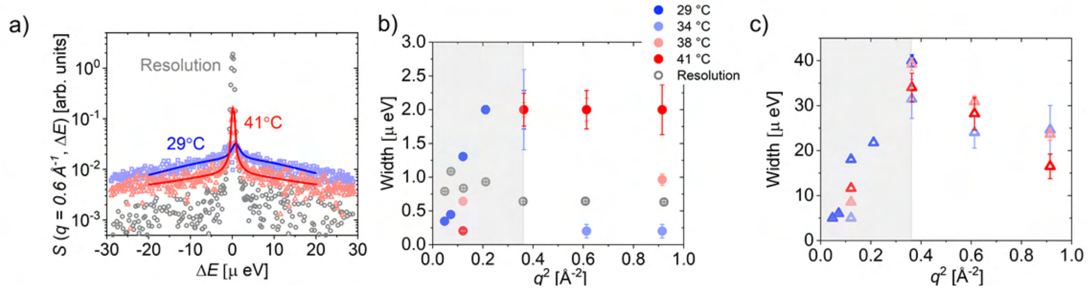

Figure 1.12:
Dynamic susceptibility $\chi''(q = 1.65\text{Å}^{-1}, \nu)$ of the aqueous solution of PNIPAM-d$_{10}$ (closed circles) in comparison with the one of non-deuterated PNIPAM (open triangles, [2]) below (a) and above (b) the cloud point. (c) Dynamic susceptibility of the aqueous solution of PNIPAM-d$_{10}$ in dependence on temperature from SPHERES (open diamonds) and TOFTOF (closed circles).

Fig. 1.12 (a, b) shows the dynamic susceptibility from TOFTOF on the non-deuterated PNIPAM [2] and the perdeuterated one, for a temperature below and above the cloud point, respectively. In both cases, the curves are nearly equal for PNIPAM-d$_{10}$ and PNIPAM above 20 GHz, where the dynamics of bulk water is observed. Moreover, they show similar dynamic behaviour, i.e. a decrease of the contribution from hydration water (ca. 20 GHz) when heating above the cloud point. However, as expected, the PNIPAM-d$_{10}$ spectra feature lower intensity than the ones from PNIPAM at frequencies below $\sim$ 20 GHz, corresponding to the slow dynamics due to hydration water and the polymer chains. Thus, the contribution from the polymer is indeed suppressed. Combining the susceptibility spectra from both instruments in Fig. 1.12 (c) gives a more comprehensive image on the relaxation processes in the system. In the frequency range of 1-10 GHz, the spectra from two experiments nicely overlap, as expected. Moreover, below the cloud point, a slope of 1 is detected, confirming the previously observed shape of the contribution of the hydration water in a PNIPAM solution [2]. In addition, the peak appearing above the cloud point at ca. 0.2 GHz indicates the presence of the strongly bound water.

To summarize, a combined analysis over a wide range of frequencies on a perdeuterated PNIPAM-d$_{10}$ has been undertaken to study the hydration water dynamics in this system. These findings point to new opportunities for studies of more complex systems using QENS.

This work was funded by Deutsche Forschungsgemeinschaft.

[1] M. Philipp, K. Kyriakos, L. Silvi, W. Lohstroh, W. Petry, J. K. Krüger, C. M. Papadakis, P. Müller-Buschbaum, *J. Phys. Chem. B* **118**, 4253-4260 (2014)

[2] B.-J. Niebuur, W. Lohstroh, M.-S. Appavou, A. Schulte, and C. M. Papadakis, *Macromolecules* **52**, 1942-1954 (2019)

2 Responsive thin films

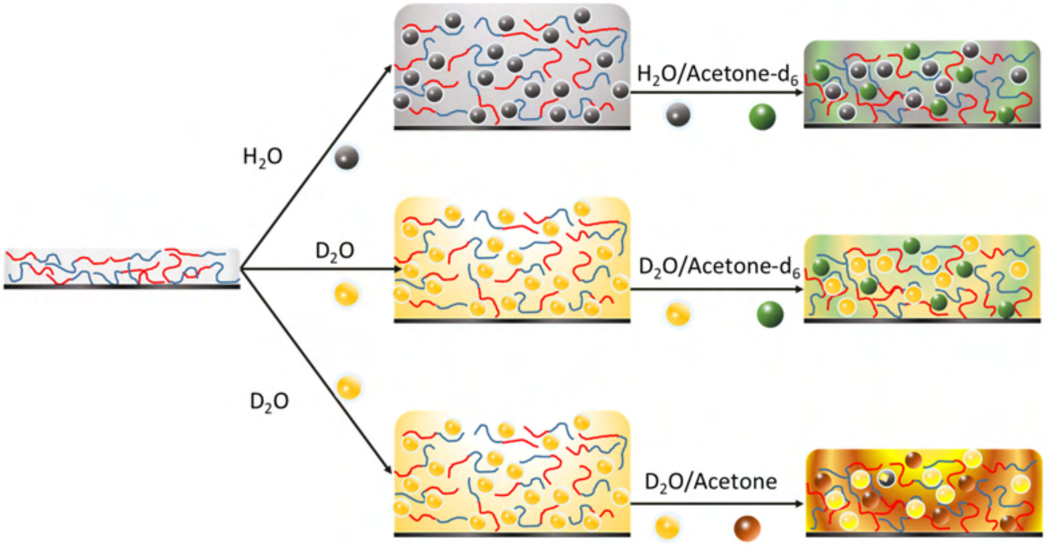

2.1 Studying the structure-sensitivity relationship of PS-*b*-PNIPAM thin films for use in soft robotics

G. Budryte, C. Geiger, P. Müller-Buschbaum

Polymeric actuators, subject of the emerging research field of soft robotics,[1] require precise controllability of mechanical movement: it should be to a fixed degree, reversible and repeatable. Similar to biological systems, that often serve as design inspriation, actuation is triggered by environmental stimuli, such as temperature or humidity changes.

Poly(*N*-isopropylacrylamide) (PNIPAM) is a famous example of a highly responsive material. In solution, PNIPAM undergoes a reversible coil-to-globule transition upon temperature increase above the lower critical solution temperature (LCST). Analogously, PNIPAM-based hydrogels and hydrated thin films contract and reswell, as the volume phase transition temperature (VPTT) is crossed. Pressure, pH, osmolytes and co-solvents are known to strongly influence the LCST/VPPT. The resulting multi-responsiveness makes PNIPAM-based systems ideal candidates for soft actuators, based on the PNIPAM degree of swelling, which can be operated by any combination of the aforementioned stimuli.

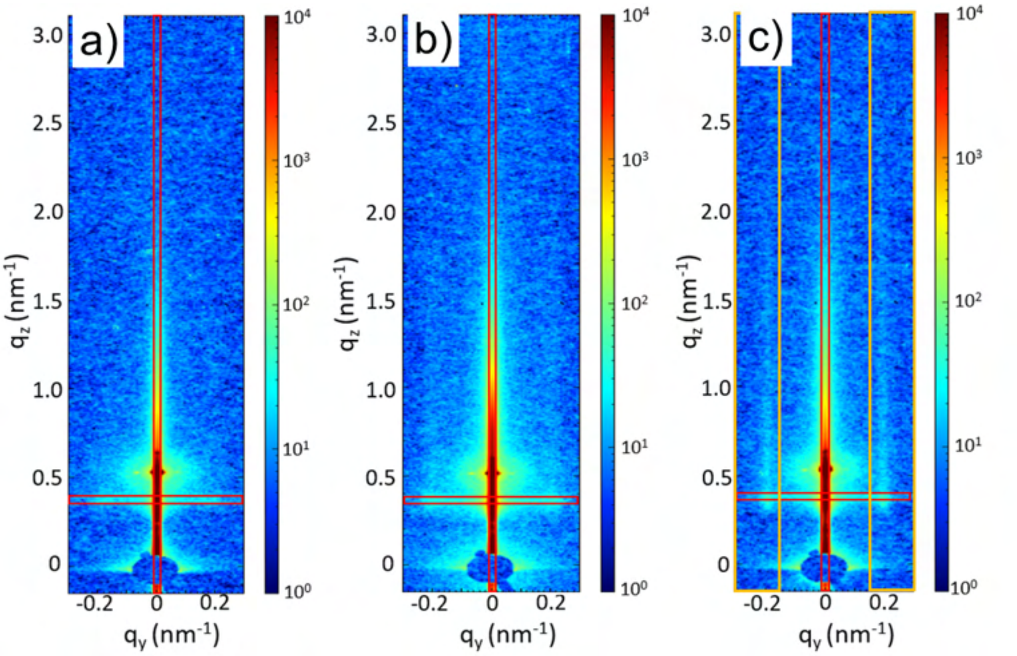

Figure 2.1:
Insets of 2D GISAXS data of PS-*b*-PNIPAM thin films after different post-treatments: a) as-prepared reference, b) thermally annealed, and c) solvent-vapor annealed samples (mapped on the logarithmic intensity scale). All data indicate long-range structural order by the presence of Bragg peaks at $q_y \approx \pm 0.2\,\mathrm{nm}^{-1}$, that are streaked out into the z-direction for the thermally annealed and solvent-vapor annealed samples. Red and yellow rectangles indicate where vertical, horizontal and off-specular vertical line-cuts were performed for structural evaluation.

We fabricated thin films from the diblock copolymer poly(styrene)-*block*-poly(*N*-isopropylacrylamide) (PS-*b*-PNIPAM) with different degrees of microphase separation. We then investigated the influence of the film morphology on the film response to relative humidity, temperature and co-nonsolvency stimuli.

In the case of the used material (PS(11500)-*b*-PNIPAM(24000)), the ideal morphology, according to the theoretical diblock copolymer phase diagram, is hexagonally packed cylinders of PS in a PNIPAM matrix. To realize films with different degrees of microphase separation, we prepared thermally annealed (T above T_g of both blocks), solvent-vapor annealed (according to the experimental protocol established by Xia and co-workers [2]) and untreated reference samples. After the film quality was checked by optical microscopy and X-ray reflectometry, the microphase separation was probed with atomic force microscopy (AFM) and grazing-incidence small-angle X-ray scattering (GISAXS) at our in-house instrument.

Insets of the summed-up GISAXS detector patterns for the as-prepared reference, thermally annealed and solvent-vapor annealed samples are shown in Fig. 2.1. Analysis of the lateral order was performed by modeling the scattered intensity along the horizontal cuts with scattering contributions from three cylindrical domains (radii and center-to-center distances of ordered PS-cylinders, disordered PS-cylinders and perturbed hexagonal clusters of PS-cylinders inside PNIPAM matrix). In comparison to the as-prepared sample, the single cylinders within the thermally annealed sample had a smaller radius and first-neighbor distance, indicating a higher overall polymer density. The solvent-vapor annealed sample featured the sharpest Bragg peak along q_y, and indeed exhibited the largest domain size of hexagonally ordered clusters of cylinders, indicating the highest long-range order.

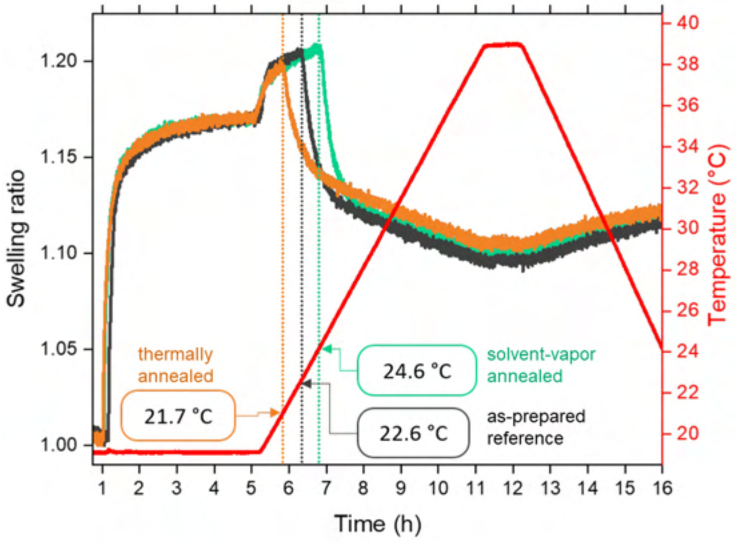

Figure 2.2: Thin film swelling ratio with changing environment (drying 1 h in N_2, swelling 4 h in H_2O vapor, heating, and cooling (5 h each)). The VPTT, taken at the onset of rapid film contraction during heating, is marked by dashed vertical lines for the as-prepared (grey), thermally annealed (orange) and solvent-vapor annealed (green) films.

The thin film responsive behavior was examined by sampling the film thickness *in-situ*, using our environmental chamber [3] with spectral reflectance. We found the films' morphological characteristics, as described earlier, had a clear influence on the swelling ratio, as depicted in Fig. 2.2. Compared to the as-prepared reference, the closer packing of smaller cylinders in the thermally annealed sample, indicating an overall increased polymer density, caused a shift of the VPTT to lower temperatures. In contrast, while a similar single cylinder radius and domain distances were found within the solvent-vapor annealed sample, the increased long-range order and preferential vertical orientation of cylinders caused a shift of the VPTT towards higher temperatures.

[1] N. Park, J. Kim, *Adv. Intell. Sys.* **2**, 1900135 (2020)

[2] S. Xia, L. Song, V. Körstgens, M. Opel, M. Schwartzkopf, S. V. Roth, P. Müller-Buschbaum, *Nanoscale* **10**, 11930-11941 (2018)

[3] T. Widmann, L. P. Kreuzer, G. Mangiapia, M. Haese, H. Frielinghaus, P. Müller-Buschbaum, *Rev. Sci. Instrum.* **91**, 113903 (2020)

2.2 Responsive behavior of PMMA-*b*-PNIPMAM films probed with ToF-NR

C. Geiger, G. Mangiapia[1], J.-F. Moulin[1], C. Henschel[2,3], A. Laschewsky[2,3], C. M. Papadakis, P. Müller-Buschbaum

[1] GEMS at MLZ, Garching, Germany
[2] Universität Potsdam, Potsdam-Golm, Germany
[3] Fraunhofer IAP, Potsdam-Golm, Germany

Poly(*N*-isopropylmethacrylamide) (PNIPMAM) is a structural analogue to the well-known thermo-responsive amphiphilic polymer, poly(*N*-isopropylacrylamide) (PNIPAM), differing by an additional methyl residue located on the polymer backbone. In aqueous solution, both analogues undergo an abrupt coil-to-globule transition upon heating past the lower critical solution temperature ($LCST_{PNIPAM} \approx 32\,°\mathrm{C}$, $LCST_{PNIPMAM} \approx 44\,°\mathrm{C}$), that is followed by a further aggregation into mesoglobules. While the sensitivity and structural properties of PNIPAM solutions, gels and thin films are fairly well-understood,[1] a large part of the corresponding studies of PNIPMAM-based systems is missing.

The Chair of Functional Materials and Soft Matter Physics Group have therefore recently increased the research activity focussed on understanding PNIPMAM's structural behavior in solutions,[2] as well as the thermo-responsive [3] and co-nonsolvency-induced behavior in thin films. In the following, our latest thin film study will be described, for which we employed the diblock copolymer, poly(methyl methacrylate)-*block*-poly(*N*-isopropylmethacrylamide) (PMMA-*b*-PNIPMAM). An overview of the experiment is presented in Fig. 2.3.

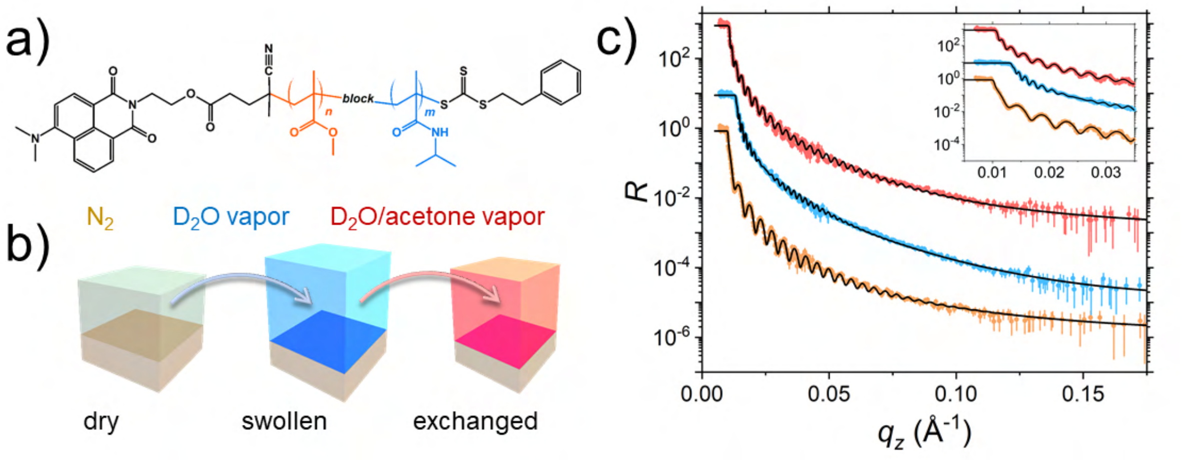

Figure 2.3:
a) Chemical structure of the studied diblock copolymer PMMA$_n$-*b*-PNIPMAM$_m$. The number average degrees of polymerization DP$_n$, determined by UV-vis spectroscopy, are $n = 23$ for the PMMA (red) and $m = 325$ for the PNIPMAM block (blue). b) Experimental sequence (drying in N_2, swelling in D_2O vapor, exchange to D_2O/acetone vapor). c) Static ToF-NR data (vertically shifted for visual clarity) for the dry (orange), D_2O swollen (blue), and D_2O/acetone exchanged (red) film equilibrium states, with fits of the reflectivity (black solid lines).

We found the addition of the PMMA block not only promotes the formation of especially smooth thin films (spin-coated onto Si wafers, followed by thermal annealing), but also provides mechanical stability at the exposure to saturated vapors, which *e.g.* is beneficial for non-horizontal sample orientations or multiple swelling and contraction cycles.

To examine their responsive properties, the swelling and contraction of PMMA-*b*-PNIPMAM thin films ($d \approx 150\,\mathrm{nm}$) was followed *in-situ* by simultaneous spectral reflectance (SR) and time-of-flight neutron reflectometry (ToF-NR). The ToF-NR data were collected at the REFSANS horizontal reflectometer operated by the German Engineering Materials Science Center (GEMS) at the Heinz Maier-Leibnitz Zentrum (MLZ). After drying the films in a N_2 flow, swelling was induced by D_2O vapor, after which a rapid film contraction was observed upon switching to mixed D_2O/acetone vapor. The scattering length density (SLD) profiles of the thin films in the dry, swollen and exchanged equilibrium states (extracted from static ToF-NR data), as well as selected SLD profiles of the films during D_2O swelling and D_2O/acetone exchange (extracted from kinetic ToF-NR data) are shown in Fig. 2.4.

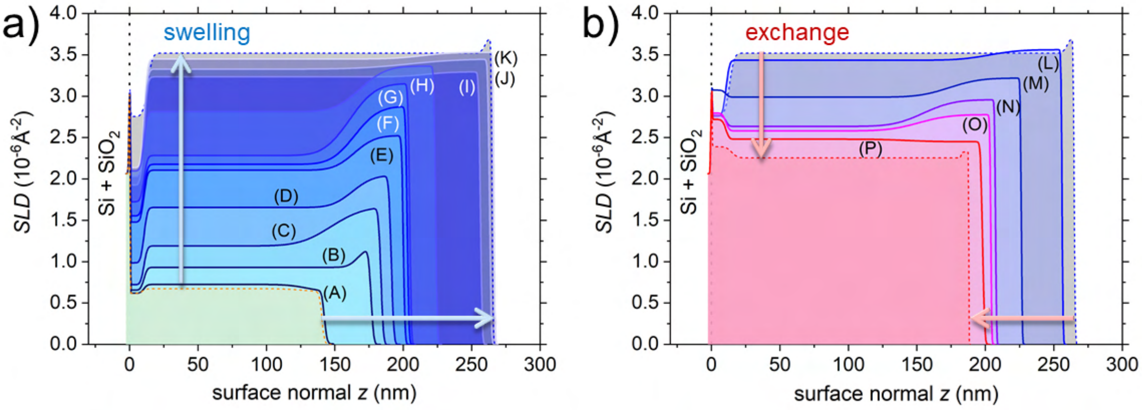

Figure 2.4:
Representative SLD profiles of a thin PMMA-*b*-PNIPMAM film during a) swelling in D_2O vapor and b) exchange to mixed D_2O/acetone vapor. Arrows indicate the general developments of film thickness (x-axis) and SLD (y-axis). Profiles extracted from static data (dry, swollen and exchanged equilibrium states) are marked with dashed lines (orange, grey, and red), intermediate profiles extracted from kinetic ToF-NR data with solid lines (A to K and L to P, respectively).

We found that the swelling in D_2O vapor happens in a two-step process, which was observed in both ToF-NR and SR measurements. An initial slow swelling phase is followed by a faster swelling phase, which is led by the formation of a strong gradient in water content along the films' vertical. Notably, the film contraction in mixed D_2O/acetone vapor is happening on a much faster timescale than the swelling in D_2O vapor, which we attribute to the co-nonsolvency effect known for acrylamides.

We address the responsive behavior of PMMA-*b*-PNIPMAM thin films seen during the faster swelling phase and the rapid contraction to the build-up and depletion of the hydration shell through cooperative hydration around the PNIPMAM hydrophobic moieties. This accelerating effect, unique to the PNIPMAM chemical structure, could be exploited to improve the response time of acrylamide-based sensors, actuators and switches.

[1] A. Halperin, M. Kröger, F. Winnik, *Angew. Chem., Int. Ed.* **54**, 15342-15367 (2015)

[2] C.-H. Ko, K.-L. Claude, B.-J. Niebuur, F. A. Jung, J.-J. Kang, D. Schanzenbach, H. Frielinghaus, L. C. Barnsley, B. Wu., V. Pipich, A. Schulte, P. Müller-Buschbaum, A. Laschewsky, C. M. Papadakis, *Macromolecules* **53**, 6816-6827 (2020)

[3] S. Nieuwenhuis, Q. Zhong, E. Metwalli, L. Bießmann, M. Philipp, A. Miasnikova, A. Laschewsky, C. M. Papadakis, R. Cubitt, J. Wang, P. Müller-Buschbaum, *Langmuir* **35**, 7691-7702 (2019)

2.3 Cyclic swelling and drying of doubly thermoresponsive poly(sulfobetaine)-based diblock copolymer thin films

L. P. Kreuzer, T. Widmann, G. Mangiapia[1], V. Hildebrand[2], A. Laschewsky[2],
C. M. Papadakis, P. Müller-Buschbaum

[1] GEMS at MLZ, Garching, Germany
[2] University of Potsdam, Potsdam-Golm, Germany

The use of polymer thin films, e.g. as sensors, artificial muscles, or functional surface coatings, inevitably is accompanied by an exposure of the film with its surrounding, which in most cases is simply air. Water molecules in the air can penetrate the polymer thin film, which typically results in a swelling and plasticization process and the thin film becomes thicker and softer. This can be used for example to move objects or close gaps.

By using stimuli-responsive polymers and a suited external stimulus, such as temperature, pressure, or light, the absorption and release of water molecules from the surrounding can be controlled. In the presented project we focus on thermo-responsive polymers that show either an upper or lower critical solution temperature (UCST or LCST), i.e. a miscibility gap above this critical upper or lower temperature. The combination of appropriate UCST- and LCST-type homopolymers, creates doubly thermo-responsive diblock copolymers (DBCs), which show an unique solution behavior. It was seen recently, that UCST-type poly(sulfobetaine)s (PSB) and LCST-type poly(N-isopropylmethacrylamide)s (PNIPMAM) form core-shell particles, that upon heating invert their micellar structure. Dependent on the relative position of the UCST and LCST, this inversion is realized via a fully hydrophobic (UCST $<$ LCST) or a fully hydrophilic regime (UCST $>$ LCST). [1] A schematic presentation can be seen in Figure 2.5a Since, in particular the UCST of the PSB block strongly shifts with changing polymer concentration, an extrapolation of its behavior in aqueous solution to thin film geometry is impossible.

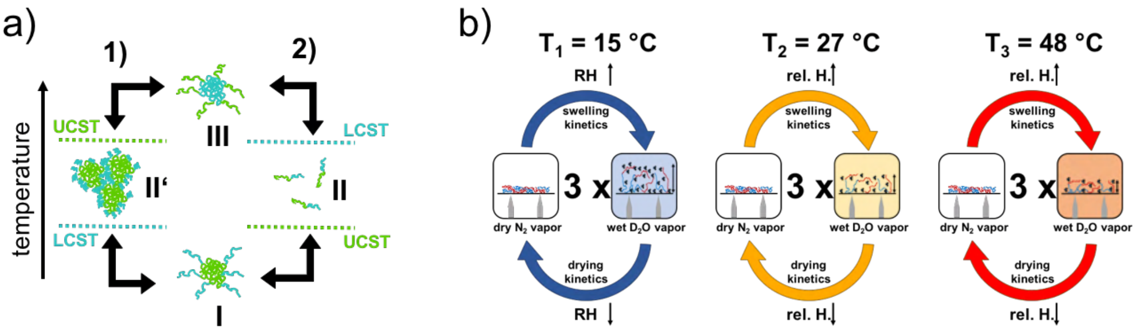

Figure 2.5:
a) Micellar inversion of a doubly thermo-responsive PSB-*b*-PNIPMAM in aqueous solution via 1) a fully hydrophobic and 2) a fully hydrophilic regime. Graphic was adapted from [1].
b). Schematic overview of the three performed experiments: Three full swelling and drying cycles are followed with ToF-NR and FTIR in-situ at 15 °C(blue), 27 °C (orange) and 48 °C (red). The graphic is adapted from [3].

This study investigates in-situ the cyclic swelling and drying of a doubly thermo-responsive DBC, that consists of a PSB (UCST at 31 °C) and a PNIPMAM block (LCST of 38 °C). [2,3] While a fundamental understanding of the water absorption and release mechanism into and out of the thin film is of great scientific interest, a reproducible and reliable swelling and contraction process is of equally high importance, in particular with respect to future applications.

The spin-coated thin films on a silicon substrate are placed in a custom-made sample environment, that assures good control over key parameters, such as the relative humidity (RH) and the temperature. [4] In three individual experiments, the thin films undergo three full swelling and drying cycles at a temperature of 15 °C, 27 °C, and 48 °C. Figure 2.5b shows the schematic principle of the applied measurement protocol. The swelling and drying kinetics of the thin films at the respective temperatures are followed in-situ on a mesoscopic level with time-of-flight neutron reflectometry (ToF-NR) and on a molecular level with Fourier-transform infrared spectroscopy (FTIR). Thus, information about water content and film thickness and about polymer-water interactions and chain conformation (FTIR) are obtained.

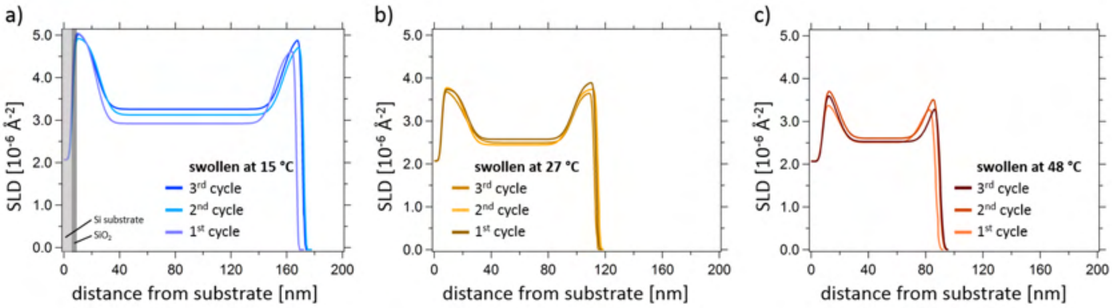

Figure 2.6:
ToF-NR measurements: The SLD profile of the swollen thin films at a) 15 °C, b) 27 °C, and c) 48 °C. The graphic is adapted from [3].

It was found that the first swelling and drying cycle differ from the subsequent second and third cycle, which is attributed to the spin-coating process, that yields a non-equilibrated film structure. During the first swelling process, the thin film is allowed to equilibrate due to a higher polymer chain mobility, which is the consequence of an increased water content. Apart from that, a reliable and reproducible thin film behavior upon swelling and drying was observed. With higher temperatures, the amount of absorbed water decreases, while simultaneously the needed time until an equilibrated swollen and dried thin film state is reached, shortens. This hints towards, strongly shifted UCST and LCST of the PSB and PNIPMAM block, respectively. In addition, water-enrichment layers were found at both interfaces of the thin film. This can be seen in SLD profiles, shown in Figure 2.6, which illustrate the vertical thin film composition. FTIR reveals deuteration processes that lead to the generation of a third water species, HDO, besides the absorbed D_2O and the small amount of initially present H_2O. Furthermore, it was found that while the overall hydration behavior of the thin film changes with temperature due to a changing hydrophobicity of the DBC, the hydration around certain characteristic groups such as the SO_3^- and amide group remains constant.

In summary, the reproducible swelling and drying processes seem promising for future application, whereas the observed complex mechanisms stress the need of a fundamental understanding of such doubly thermo-responsive polymers.

[1] N. Vishnevetskaya, V. Hildebrand, N. M. Nizardo, C.-H. Ko, Z. Di, A. Radulescu, L. C. Barnsley, P. Müller-Buschbaum, A. Laschewsky, C. M. Papadakis, *Langmuir* **35**, 9660-9676 (2019)

[2] N. Vishnevetskaya, V. Hildebrand, B.-J. Niebuur, I. Grillo, S. K. Filippov, A. Laschewsky, P. Müller-Buschbaum, C. M. Papadakis, *Macromolecules* **50**, 3985-3999 (2017)

[3] L. P. Kreuzer, T. Widmann, N. Aldosari, L. Bießmann, G. Mangiapia, V. Hildebrand, A. Laschewsky, C. M. Papadakis, P. Müller-Buschbaum, *Macromolecules* **53**, 9108-9121 (2020)

[4] T. Widmann, L. P. Kreuzer, G. Mangiapia, M. Haese, H. Frielinghaus, P. Müller-Buschbaum, *Rev. Sci. Instrum.* **91**, 113903 (2020)

2.4 Investigation of co-nonsolvency phase transition of poly(sulfobetaine)-based diblock copolymer thin films

P. Wang, R. Cubitt[1], A. Laschewsky[2], C. M. Papadakis, P. Müller-Buschbaum,

[1] ILL, Grenoble, France
[2] Universität Potsdam, Potsdam-Golm, Germany

Co-nonsolvency attracts great interest of the scientific community mainly due to its close relation to lots of fundamental processes, such as stabilization, crystallization or formulation [1]. As is known, the polymer transition behavior and the critical solution temperature closely depends on the local environment of polymer chains, and, for example, can be significantly modulated by the addition of salts and osmolytes [2]. The phenomenon of co-nonsolvency is another special case. Co-nonsolvency occurs if a mixture of two good solvents causes the collapse or demixing of polymers into a polymer-rich and a polymer-poor phase within a certain compositional range of these two solvents [1]. Many thermosensitive polymers show co-nonsolvency properties. One of the best characterized examples is the nonionic thermo-responsive polymer, poly(N-isopropylmethacrylamide) (PNIPMAM) [3]. However, a co-nonsolvency response of its diblock copolymer (DBC), containing zwitterionic poly(sulfobetaine)s, poly(4-((3-methacrylamidopropyl)dimethyllammonio)butane-1-sulfonate)) (PSBP), which exhibits an lower upper critical solution temperature and shows a strong swelling behavior in aqueous media, is newly studied. Since the mechanism of co-nonsolvency has not been adequately clarified yet, [3] the investigation of the co-nonsolvency transition, both in theoretical and experimental studies, is necessary to utilize its wide potential for application.

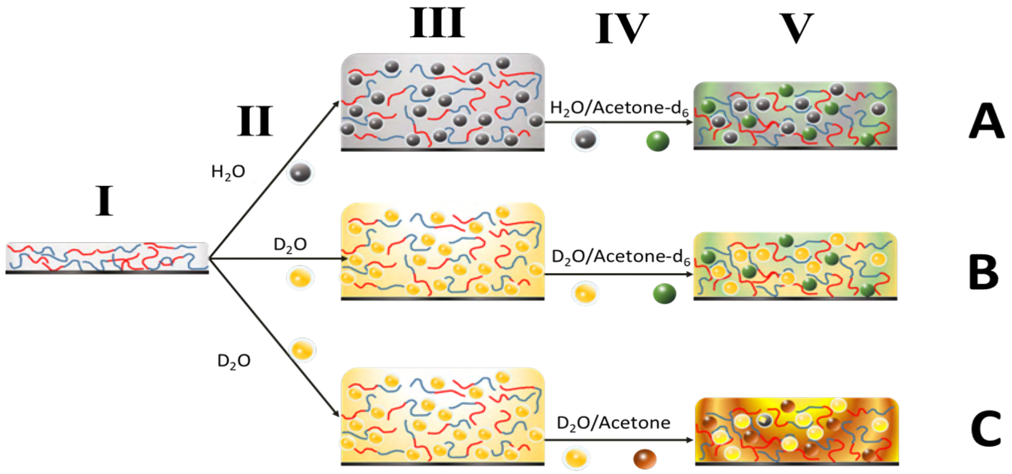

Figure 2.7:
Scheme of three performed experimental protocols. Each protocol consists of three static stages: drying state(I), swollen state(III) and collapsed state(V), and two kinetic stages: swelling(II) and co-solvent switch(IV).

In the present study, we focus on the co-nonsolvency behavior of PSBP-*b*-PNIPMAM thin films in a series of (partially) deuterated water/acetone binary mixtures. The chemical structure of the studied DBC shows a very similar length of the zwitterionic and nonionic block). Fig. 2.7 shows the detailed experimental design of the three performed *in-situ* ToF-NR protocols at the Insitute Laue-Langevin (ILL). Throughout all measurements the temperature is kept constant at 18 °C), which is below both transition temperatures, $CP_{PNIPMAM}$ and CP_{PSBP}, of the investigated DBC. Every experiment was divide into five stages (I-V): N_2 drying static, water swelling kinetic, water swollen static, co-solvent switch kinetic and co-solvent switch static. In experiment A, H_2O swelling is followed by a deuterated acetone switch, while in experiment B, D_2O swelling is followed by an acetone switch. For experiment C, D_2O swelling is followed by a deuterated acetone switch. All of the solvents mentioned here are introduced into the sample environment system via a 100 % saturated stream for water and a 90/10 % saturated stream for water/co-solvent mixtures.

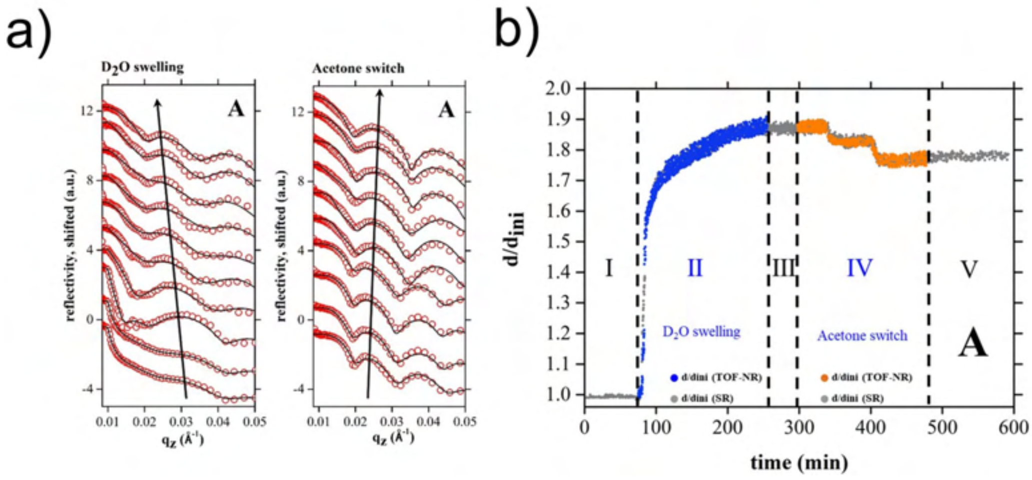

Figure 2.8:
a) Representative kinetic TOF-NR curves with corresponding three-layer model fits of protocol A. b) Swelling ratio over time of protocol A. d/d_{ini}(TOF-NR) yielded from kinetic TOF-NR measurements and d/d_{ini}(SR) obtained from SR data.

Here we present the kinetic ToF-NR data of protocol A, shown in Fig. 2.8 a), which is evaluated using the Motofit plugin for the IGOR PRO software with the best fits of a three-layer model. The changing spacing of Kiessig fringes along q_z is indicated by the two black arrows, and becomes smaller over time once the swelling process is triggered, which indicates that the thickness of the thin film is increasing during D_2O swelling (II). This changing trend is reversed after the cosolvent is introduced. Since the information of film thickness over time can be yielded from corresponding neutron data, the thickness changes in all five processes are presented in Fig. 2.8 b). Compared to stage II, the co-nonsolvency behavior in stage V attracted our interest more, due to an obvious two step collapse.

In this work, the PSBP-*b*-PNIPMAM thin films show a pronounced sensitive switching behavior (an almost 100 % thickness increase during water swelling and a 35 % decrease after the cosolvent switch is realized), which would make a promising benefit to many potential applications, such as designing smart polymers for thermal sensors and modeling precipitation of size controlled nanoparticles, [4] especially in drug release applications [2].

[1] M. J. A. Hore, B. Hammouda, Y. Li, R. Gehrke, H. Cheng, *Macromolecules* **19**, 7894-7901 (2013)

[2] N. S. Vishnevetskaya, V. Hildebrand, M. A. Dyakonova, B. J. Niebuur, K. Kyriakos, K. N. Raftopoulos, Z. Di, A. Laschewsky, P. Müller-Buschbaum, C. M. Papadakis, *Macromolecules* **7**, 2604-2614 (2018)

[3] D. Mukherji, C. M. Marques, K. Kremer, *Nat. Commun.* **5**, 4882-4888 (2014)

[4] Q. Zhong, E. Metwalli, G. Kaune , M. Rawolle, A. M. Bivigou-Koumba, A. Laschewsky, C. M. Papadakis, R. Cubitt, P. Müller-Buschbaum, *Macromolecules* **8**, 5241-5249 (2012)

2.5 Influence of salt concentration on the thermoresponsive behavior of thin polymer films

J. Reitenbach, V. Hildebrandt[1], A. Laschewsky[1], P. Müller-Buschbaum

[1] Universität Potsdam, Potsdam-Golm, Germany

The ability of ions to influence protein stability, enzyme activity, macromolecule crystallization, as well as protein and polymer folding is well known. This phenomenon is strongly influenced by the type of the salt in the aqueous solution and follows a trend called the Hofmeister series, which is generally more pronounced for anions than for cations. The typical order of the anion series is: $CO_3^{2-} > SO_4^{2-} > S_2O_3^{2-} > H_2PO_4^- > F^- > Cl^- > Br^- \approx NO_3^- > I^- > ClO_4^- > SCN^-$. The species to the left of Cl^- are referred to as kosmotropes and those to the right are called chaotropes. These terms were originally used to describe the ability of an ion to modify the hydrogen bonding network of water. The kosmotropes are strongly hydrated in water and believed to be *water structure makers*, which have stabilizing and salting-out effects on macromolecules and proteins. In contrast, the chaotropes are weakly hydrated and are referred to as *water structure breakers*, which are able to destabilize folded proteins and lead to a salting-in effect. Recent work casts doubt on the idea that water network making and breaking by salts is the origin of the Hofmeister series.[1] A hypothesis was proposed, that direct ion-macromolecule interactions are the major cause of this phenomenon. It was found that the transition temperature of thermoresponsive polymers in aqueous solutions, such as for poly(*N*-isopropyl acrylamide) (PNIPAM), can be greatly influenced by the addition of salts. The impact on the lower critical solution temperature (LCST) of PNIPAM is not only dependent on the type of ion, which is added, but also on the concentration of the salt. Depending on the nature of the salt, different interactions between the ion and PNIPAM were discussed. First, the ions are able to polarize a hydrogen bonded water molecule at the amide group. Second, ions can raise the surface tension of the polymer-water interface. Third, the ions can bind directly to the amide moiety.[2] An interesting alternative to PNIPAM would be the investigation of the also thermoresponsive poly(*N*-isopropyl methacrylamide) (PNIPMAM), which differs only by an additional methyl group in the polymer backbone. The structures of PNIPAM and PNIPMAM are shown in figure 2.9.

Figure 2.9: Chemical structures of PNIPAM (left) and PNIPMAM (right).

The additional methyl group results in an enhanced steric hindrance and in an increase of the hydrophobicity of the polymer backbone. Based on this effects it is assumed, that the LCST of PNIPMAM is impacted differently by the addition of salts. The additional steric hindrance could cause that the amide group to be less accessible for the ions and the increased hydrophobicity could enhance the surface tension between the water and the polymer. Therefor, a stronger decrease of the LCST of PNIPMAM by the addition of chaotrope ions is assumed than for the LCST of PNIPAM in aqueous solution.

To further elucidate this phenomenon we investigate thin films of PNIPMAM with different concentrations of NaBr within a water atmosphere. The advantage of thin films compared to polymers in solution or in bulk is that a certain mechanical stability is given with only a little loss in responsiveness of the system. However, the complexity of the system is further increased for thin films due to the interactions at the interfaces.

To investigate the film thickness evolution and the reversibility of the swelling in an aqueous atmosphere, spectral reflectance (SR) measurements were performed with a temperature gradient. The underlying experimental design included an initial drying step of the thin films in N_2 atmosphere, a swelling step by injection of pure D_2O into the measurement chamber and a heating-cooling cycle where the temperature was increased from 15 °C to 55 °C (above the LCST) and then again cooled down to 15 °C. The resulting plot of the measured relative thickness and the temperature gradient (red) over time for the PNIPMAM films without NaBr (black) and with 0.01 M NaBr (blue) is shown in figure 2.10.

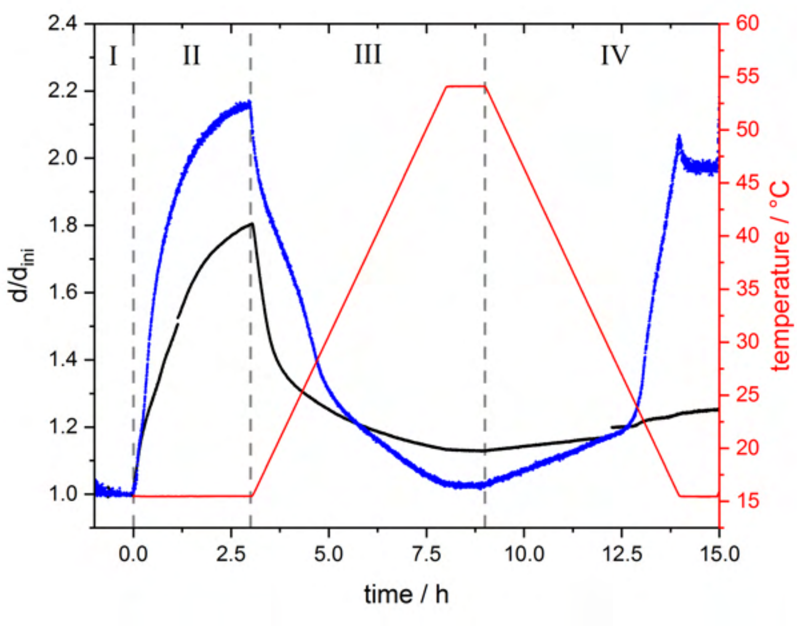

Figure 2.10:
SR measurements of PNIPMAM thin films without NaBr (black) and with 0.01 M NaBr (blue). (I) drying step; (II) swelling with D_2O; (III) heating from 15 °C to 55 °C; (IV) cooling down from 55 °C to 15 °C.

It can be seen that the PNIPMAM film containing 0.01 M has a more pronounced swelling and collapse behavior than the PNIPMAM film without the addition of salt. Additionally, the PNIPMAM film with 0.01 M NaBr shows stronger reswelling in the cooling step (IV). This can be attributed to the higher polarity of the system. A weak hydration shell is formed around the ions which can be easily dehydrated and rehydrated upon temperature change.

In the future, we want to systematically investigate the dependence of the swelling on the ion concentration and further elucidate the phenomenon with FTIR measurements to gain insights into inner morphology changes, functional group participation and diffusion rates.

[1] Y. Zhang, S. Furyk, L. B. Sagle, Y. Cho, D. E. Bergbreiter, P. S. Cremer, *J. Phys. Chem.*, **111**, 8916-8924 (2007)

[2] Y. Zhang, S. Furyk, D. S. Berbreiter, P. S. Cremer, *J. Am. Chem.*, **127**, 14505-14510, (2005)

2.6 Charge-dependent microphase separation in thin films from a multiresponsive pentablock quaterpolymer

F. A. Jung, D. Posselt[1], D.-M. Smilgies[2], P. A. Panteli[3], C. Tsitsilianis[4],
C. S. Patrickios[3], C. M. Papadakis

[1] IMFUFA, Department of Science and Environment, Roskilde University, Roskilde, Denmark
[2] Cornell High Energy Synchrotron Source (CHESS), Cornell University, Ithaca, United States
[3] Department of Chemistry, University of Cyprus, Nicosia, Cyprus
[4] Department of Chemical Engineering, University of Patras, Patras, Greece

The ability of block copolymers to self-assemble into a plethora of morphologies is attractive for many applications. By now, the phase behavior of diblock copolymers is well known and can be predicted with high accuracy, but they are limited to few morphologies. To achieve a higher diversity of morphologies and better control of the self-assembly, multiblock copolymers [1] and block copolymers with charged segments [2] are attractive candidates. However, the understanding of these systems is still at an early stage.

In this work, the self-assembly behavior of the pentablock quaterpolymer P(nBuMA$_8$-*co*-TEGMA$_8$)-*b*-PDMAEMA$_{50}$-*b*-PEG$_{46}$-*b*-PDMAEMA$_{50}$-*b*-P(nBuMA$_8$-*co*-TEGMA$_8$) in thin films is investigated at low and high degrees of ionization α of the PDMAEMA (poly(2-dimethylamino)ethyl methacrylate) blocks using grazing-incidence small-angle X-ray scattering (GISAXS). The endblocks are statistical copolymers of the thermoresponsive TEGMA (triethylene glycol methyl ether methacrylate) and the hydrophobic nBuMA (n-butyl methacrylate). The central PEG (poly(ethylene glycol)) block is permanently hydrophilic. The films were prepared by spin-coating from 3 wt % solutions in D_2O resulting in homogeneous films with thicknesses of 50-60 nm. The values of α were controlled by adjusting the pD values of the solutions to 8.5 ($\alpha \approx 0.17$; weakly charged PDMAEMA) and 2.3 ($\alpha \approx 1.00$; fully charged PDMAEMA) using small amounts of HCl.

GISAXS experiments were performed at beamline D1 at CHESS. The data were modeled by fitting of simulated scattering patterns using BornAgain [3] and self-written Python codes according to the procedure described in ref [4]. At this, scattering from surface roughness and background contributions from the sample holder were explicitly taken into account. Experimental ($q_y > 0$) and simulated ($q_y < 0$) 2D GISAXS patterns of films at pD 8.5 and pD 2.3 are show in Figure 2.11a and b, respectively. While at pD 8.5, only weak diffuse scattering is present without any significant features in the horizontal line cuts (Figure 2.11c), at pD 2.3, two scattering peaks at $q_y \approx 0.2$ nm^{-1} and $q_y \approx 0.4$ nm^{-1} indicate the presence of a nanostructure in the film (Figure 2.11d).

The film at pD 8.5 was successfully modeled without a nanostructure (homogeneous film); thus, it is disordered (Figure 2.11e). This is due to a low segregation strength of the uncharged blocks, which enables mixing. At pD 2.3, the pattern is modeled by two types of correlated spheres; larger spheres having radii of $\sim$9.6 nm and distances of $\sim$26.1 nm and smaller spheres with radii of $\sim$5.2 nm and distances of $\sim$15.3 nm. These values allow us to propose the following nanostructure of the film prepared at pD 2.3: The smaller spheres are formed by PEG and the larger spheres by P(nBuMA-*co*-TEGMA) which are embedded in a matrix of PDMAEMA (Figure 2.11f). The assignment is based on the ratio of sphere volumes (6.3), which is comparable to the ratio of block volumes (5.7).

The enhancement of the segregation strength by increasing α, which may promote microphase separation, was predicted for diblock copolymers [2] and is demonstrated here for the case of a pentablock quaterpolymer. We attribute the enhancement of segregation strength to a selective charge solubilization of the Cl^- counterions within the charged PDMAEMA matrix.

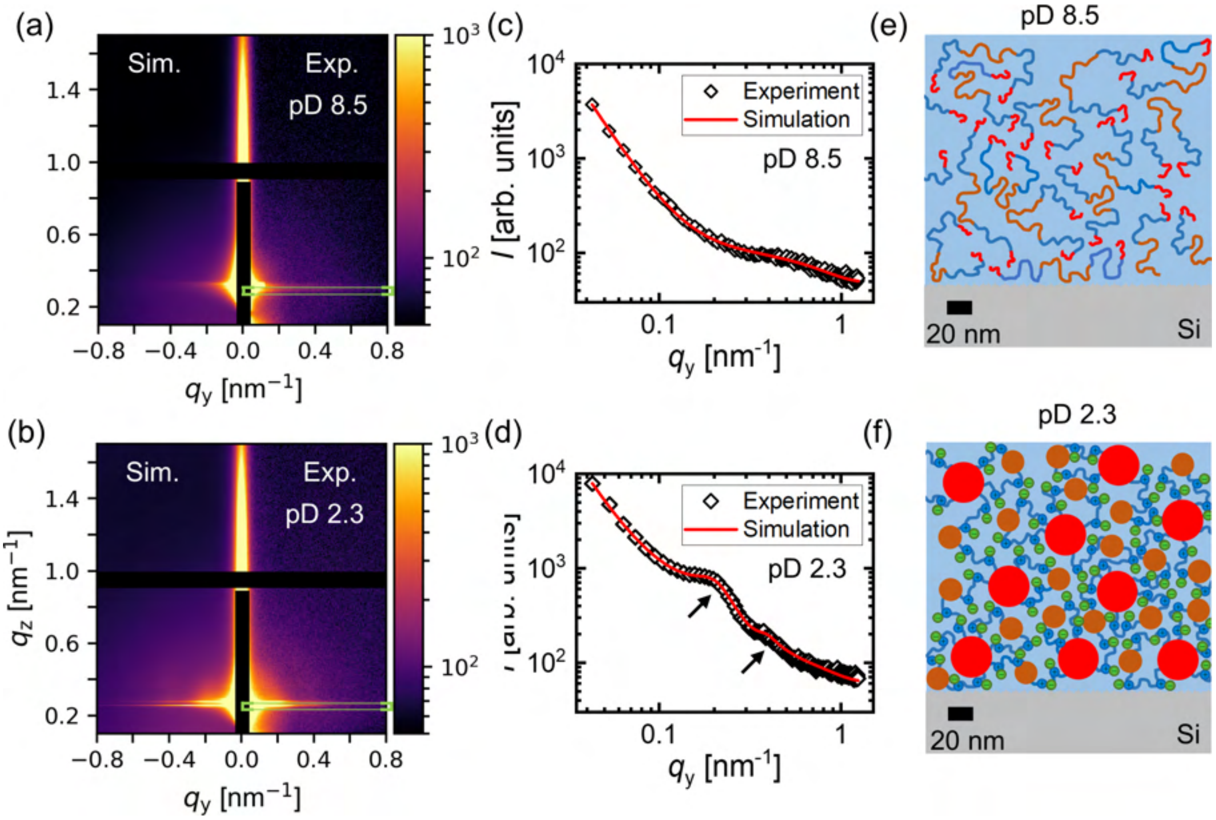

Figure 2.11:
(a,b) Experimental ($q_y > 0$) and simulated ($q_y > 0$) 2D GISAXS patterns of as-prepared thin films of the pentablock quaterpolymer at (a) pD 8.5 and (b) pD 2.3 measured at incident angles of 0.17° and 0.14°, respectively. The color bar gives the logarithmic intensities. (c,d) Horizontal line cuts in the Yoneda regions (green boxes in (a,b)) of experiment (open symbols) and simulation (solid red line). Arrows indicate scattering peaks. (e,f) Schematic view of the morphologies of as-prepared thin films from the pentablock quaterpolymer for (e) pD 8.5 and (f) pD 2.3. Colors represent P(*n*BuMA-*co*-TEGMA) (red), PDMAEMA (blue) and PEG (brown). Adapted with permission from ref [4].

In conclusion, it is shown that the combination of multiblock copolymers with charged segments is a powerful tool for creating nanostructures via self-assembly. Multiblock copolymers give access to complex morphologies (in the present case: two types of phase-separated domains) while the charged segments allow to alter the segregation strength of blocks and tune the phase behavior. Furthermore, we show that the use of blocks based on weak polyelectrolytes and a variation of the pH value during film preparation is an efficient way to control α.

The project is funded by Deutsche Forschungsgemeinschaft (DFG) (Pa771/19-1).

[1] F. S. Bates, M. A. Hillmeyer, T. P. Lodge, C. M. Bates, K. T. Delaney, G. H. Fredrickson, *Science* **336**, 434-440 (2012)

[2] C. E. Sing, J. W. Zwanikken, M. Olvera de la Cruz, *Nat. Mater.* **13**, 694-698 (2014)

[3] G. Pospelov, W. Van Herck, J. Burle, J. M. Carmona Loaiza, C. Durniak, J. M. Fisher, M. Ganeva, D. Yurov, J. Wuttke, *J. Appl. Cryst.* **53**, 262-276 (2020)

[4] F. A. Jung, D. Posselt, D.-M. Smilgies, P. A. Panteli, C. Tsitsilianis, C. S. Patrickios, C. M. Papadakis, *Macromolecules* **53**, 6255-6266 (2020)

3 Functional thin films

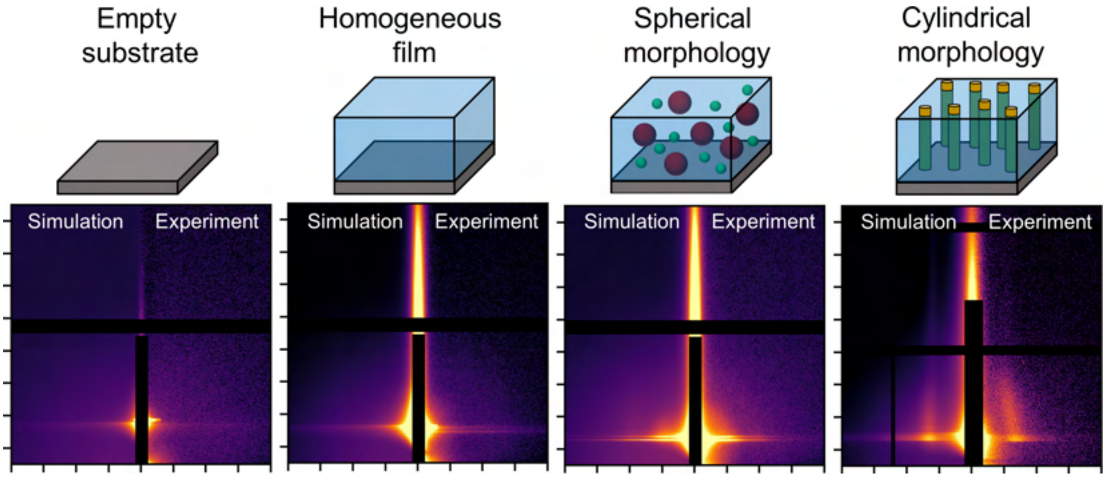

3.1 Colloidal quantum dot ink towards printable near-infrared photodetector

W. Chen, H. Tang[1], H. Liu[1], K. Wang[1], P. Müller-Buschbaum

[1] Southern University of Science and Technology, Shenzhen, China

Lead sulfide (PbS) quantum dots are attractive in many optoelectronic applications including light-emitting diodes,[1] solar cells (SCs)[2, 3], and photodetectors (PDs)[4] in the near-infrared (NIR) range. To realize an efficient charge carrier transmission in the QDs solid for SCs or PDs, QDs are treated by a ligand exchange process, in which the organic ligands, such as oleic acid (OA), are replaced by short-chain ligand or halides ions, and thus the neighboring QDs exhibit a small inter-dot distance. The conventional treatment of PbS QDs is described as a solid-state ligand exchange treatment, in which OA capped QDs are treated by short-chain ligand precursor after the deposition. A rinsing process is performed afterward to complete a single treatment step. To make sure a homogeneous thin-film morphology and a certain thickness of the final QD solid, the treatment step is repeated several times, which is known as a layer by layer (LBL) process, as seen in Fig.3.1.[5] Though the LBL process is an efficient method towards obtaining strongly coupled QD solid and the related devices exhibit promising device performance, the compliance of the LBL process hinders low-cost and up-scaling fabrications of the QD based devices.

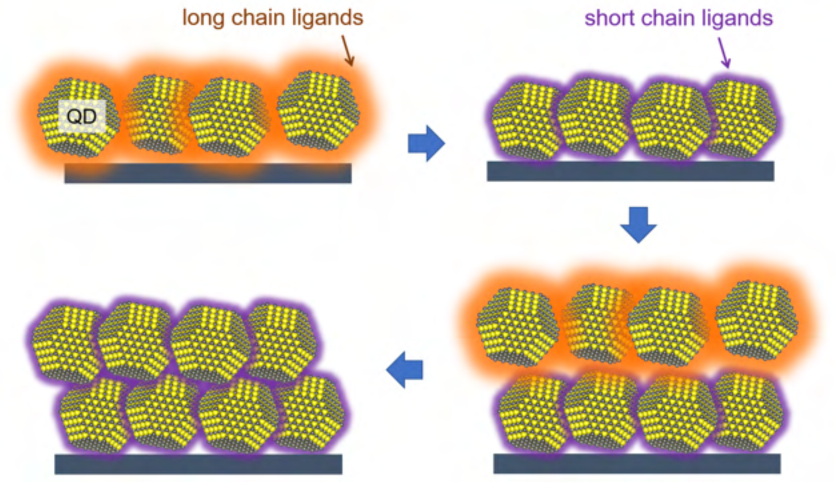

Figure 3.1: Schematic of solid-state ligand exchange treatment and LBL process.

The QD ink technique, known as the solution-phased ligand exchanged QDs, emerged recently and it has been well used in many SC devices with promising device performance. The QD ink is mainly fabricated by a phase-separation process in which OA capped QDs in octane automatically transfer to lead halide capped QDs in dimethylformamide (DMF), as illustrated in Fig.3.2.[6] After purification and precipitation, the ink component are redispersed in a metal-coordinate solvent, such as butylamine, and the solution can be directly used as printable ink. The QD ink technique is supposed to be a good method towards printing QD solid thin-films. However, QDs with photon response in NIR spectral range suffer bad dispersity after conventional ink fabrication process. This is because PbS QDs with a narrow bandgap normally exhibit a large QD size (diameter) and a consequently large proportion of the area of (100) facets on the QD surface.[7] While the (100) facet normally has smaller surface energy than that of the (111) facet leading to a bad coating of lead halides on the facets, and thus a bad dispersity of large-sized QDs in the ink solution. Previous work has tried to use sodium ions (sodium acetate, NaAc) to passivate all facets of the QDs, however, the carboxylate component is potentially introduced to the final ink and it might hinder the device performance.

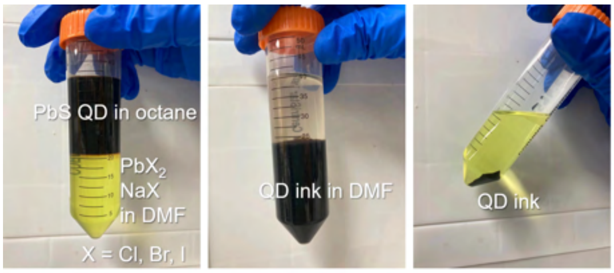

Figure 3.2:
Picture flow of solution-phase ligand exchange process and as obtained ink component after centrifugation.

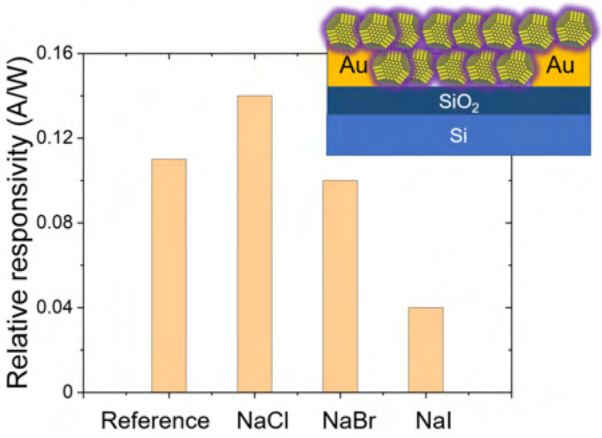

Figure 3.3:
Schematic of the laterally structured photodetector (right-up) and responsivity performance of the PDs

In our work, we employ different fully inorganic sodium salts, such as sodium chloride (NaCl), sodium bromide (NaBr), and sodium iodide (NaI) to modify the QD ink fabrications. In the initial part of the project, we have fabricated corresponding QD solids based on the inks and the deposition is implemented via conventional spin-coating instead of printing in early study. The inner structures of the final QD solids are investigated by grazing-incidence small-angle X-ray scattering (GISAXS). Moreover, transient absorption spectroscopy (TAS) is used to compare the energetic disorder of the QD solids. Laterally structured photodetectors are also made and we found NaCl modified device exhibits the best device performance with the highest relative responsivity as seen in Fig.3.3. Larger-sized QDs with photon response wavelength up to 1550 nm will be employed for ink fabrication and corresponding device fabrication via printing deposition afterward.

[1] L. Gao, L. N. Quan, F. P. García de Arquer, Y. Zhao, R. Munir, A. Proppe, R. Quintero-Bermudez, C. Zou, Z. Yang, M. I. Saidaminov, O. Voznyy, S. Kinge, Z. Lu, S. O. Kelley, A. Amassian, J. Tang, E. H. Sargent, *Nat. Photonics*, **14**, 227-233 (2020)

[2] Y. Xia, W. Chen, P. Zhang, S. Liu, K. Wang, X. Yang, H. Tang, L. Lian, J. He, X. Liu, G. Liang, M. Tan, L. Gao, H. Liu, H. Song, D. Zhang, J. Gao, K. Wang, X. Lan, X. Zhang, P. Müller-Buschbaum, J. Tang, J. Zhang, *Adv. Funct. Mater.*, **30**, 2000594 (2020)

[3] M. Liu, F. Che, B. Sun, O. Voznyy, A. Proppe, R. Munir, M. Wei, R. Quintero-Bermudez, L. Hu, S. Hoogland, A. Mandelis, A. Amassian, S. O. Kelley, F. P. García de Arquer, E. H. Sargent, *ACS Energy Lett.*, **4**, 1225-1230 (2019)

[4] W. Chen, H. Tang, Y. Chen, J. E. Heger, N. Li, L. P. Kreuzer, Y. Xie, D. Li, C. Anthony, Z. Pikramenou, K. W. Ng, X. W. Sun, K. Wang, P. Müller-Buschbaum, *Nano Energy*, 2020, 105254 (2020)

[5] C. H. Chuang, P. R. Brown, V. Bulovic and M. G. Bawendi, *Nat. Mater.*, **13**, 796-801 (2014)

[6] M. Liu, O. Voznyy, R. Sabatini, F. P. Garcia de Arquer, R. Munir, A. H. Balawi, X. Lan, F. Fan, G. Walters, A. R. Kirmani, S. Hoogland, F. Laquai, A. Amassian, E. H. Sargent, *Nat. Mater.*, **16**, 258-263 (2017)

[7] H. Beygi, S. A. Sajjadi, A. Babakhani, J. F. Young, F. C. J. M. van Veggel, *Appl. Surf. Sci.* **457**, (2018)

3.2 Monitoring the formation of a transparent electrode during IZO sputter deposition in situ with grazing incidence X-ray scattering

J. E. Heger, S. V. Roth[1,2], P. Müller-Buschbaum

[1] DESY, Hamburg, Germany
[2] KTH, Stockholm, Sweden

Transparent conductive oxides (TCOs) play an important role in optoelectronic devices, such as organic light-emitting diodes (OLEDs) and hybrid solar cells. Used as transparent electrodes light can pass and thus TCOs provide charge carriers for the generation of light in OLEDs or collect from absorbed light harvested charge carriers in hybrid solar cells . Metal doped indium oxides like indium zinc oxide (IZO) are state of the art materials with a low sheet resistance. For an economical use of the material, however, large scale and minimum consumption deposition techniques, such as sputter deposition, need to be applied. To understand the formation of TCOs made from IZO and their percolation threshold, in situ investigations during sputter deposition are highly conclusive.

In this project, we investigate IZO formation on a pristine transparent glass substrate and a hybrid solar cell stack, which is made of a biotemplated TiO_2:P3HT active layer and covered by a MoO_3 blocking layer, with in situ grazing incidence small-angle X-ray scattering (GISAXS). This measurement technique is a powerful tool to understand the formation and the growth process from atomic to bulk scale with high temporal resolution [1]. The experiments are carried out in a vacuum chamber, which is filled with an Argon atmosphere. The sample substrates are placed below an IZO target. By applying radio frequency alternating voltage, the Argon plasma gets ignited and starts to kick out atomic IZO from the target, which subsequently deposits on the sample substrates. Simultaneously monitoring this process by GISAXS through X-ray transparent windows yields the desired information about different morphological growth phases. In addition, in situ UV/VIS reveals the formation of optoelectronic states.

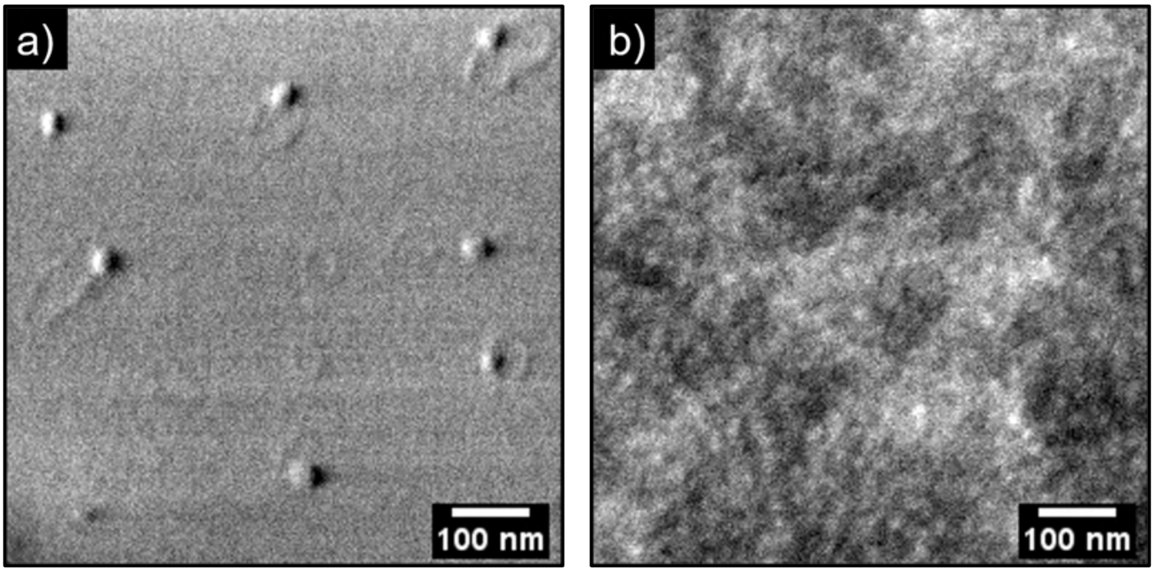

Figure 3.4:
SEM images after IZO sputter deposition. a) Glass substrate showing large IZO islands forming and suggesting Vollmer-Weber growth. b) Hybrid stack substrate uniformly covered by IZO suggesting Stranski-Krastanov growth.

The in situ measurements are complemented with static grazing incidence ultra small-angle X-ray scattering (GIUSAXS), X-ray reflectometry (XRR), and real-space microscopy techniques such as optical and scanning electron microscopy (OM and SEM), to characterize the formed IZO layer after relaxation of the growth kinetics and compare the sample substrates before and after deposition, respectively. GIUSAXS shifts the accessible length scale to larger structure sizes with hundreds of nanometers in diameter. XRR measurements extract vertical morphology information of the samples, e.g. embedded layers, film thickness, and surface roughness. OM and SEM complement the surface-related information by real-space imaging.

A first qualitative interpretation of the results shows, that IZO growths not only differently on pristine glass compared to the hybrid solar cell stack substrate, but also different than other electrode materials, such as gold on functional polymer films [2], [3]. SEM images of the glass substrate after deposition show large, separated IZO islands (Figure 3.4a), whereas the hybrid stack is covered by densely packed IZO particles (Figure 3.4b). These findings are also reflected by 1D GISAXS intensity profiles. The peak position in Figure 3.5a shifts to lower angles α_f, indicating the formation of a low density layer consisting of the separated IZO islands. This suggests that IZO avoids the formation of interfacial areas on the glass substrate. In contrast, Figure 3.5b shows a rising peak that is in good agreement with the characteristic peak position of indium zinc oxide. This suggests the formation of a more uniform and densely packed IZO layer. A shift of the intensity oscillations to lower angles α_f and a slight decrease in their width indicates the growth of IZO clusters in height and of the overall layer thickness, respectively. A possible reason for the uniform deposition is defects on the MoO_3 surface, which are introduced by evaporation on the rough active layer and acting as nucleation centers. This different behavior between the two substrates suggests Vollmer-Weber type growth of IZO clusters on glass and a Stranski-Krastanov type on the hybrid stack.

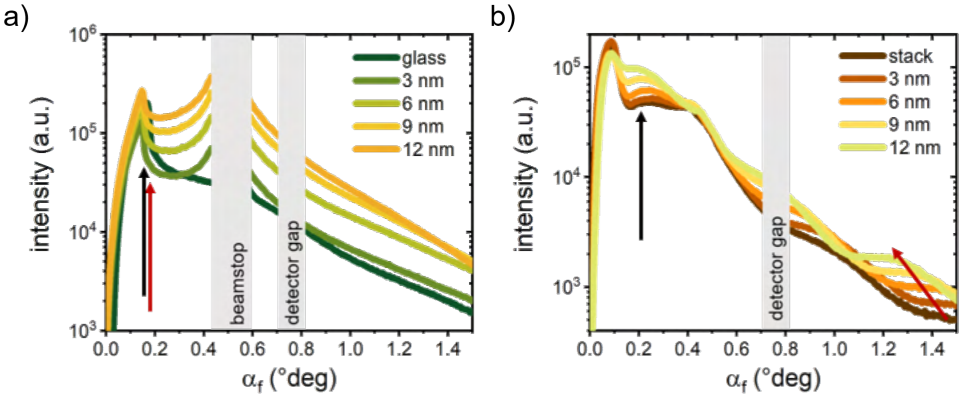

Figure 3.5:
1D GISAXS intensity profile cuts along the z-axis of the detector yielding height and density information of IZO growth on the a) glass and b) hybrid stack substrate. The color scale shows the theoretically sputtered thickness. Black and red arrows indicate structural changes during deposition as described in the text.

[1] M. Schwartzkopf, S.-J. Wöhnert, V. Waclawek, N. Carstens, A. Rothkirch, M. Gensch, J. Drewes, S. J. Schaper, V. Körstgens, P. Müller-Buschbaum, F. Faupel, S. V. Roth, *Nanoscale Horiz.*, **6**, 132-138 (2021)

[2] F. C. Löhrer, V. Körstgens, G. Semino, M. Schwartzkopf, A. Hinz, O. Polonskyi, T. Strunskus, F. Faupel, S. V. Roth, P. Müller-Buschbaum, *ACS Appl. Mater. Interfaces* **12**, 1132-1141 (2020)

[3] L. Song, M. A. Niedermeier, V. Körstgens, F. C. Löhrer, Y. Chen, S. V. Roth, P. Müller-Buschbaum, *ACS Appl. Nano Mater.* **3**, 5987-5994 (2020)

3.3 Thermoelectric PEDOT:PSS thin films via DMSO treatment

S. Tu, T. Tian, A. L. Oechsle, P. Müller-Buschbaum

The recently discovered high-performing inorganic thermoelectric (TE) materials based on chalcogenides such as Ge-Te, Pb-Te and Sn-Se based alloys, have been reported to show remarkale ZT values of >2 at room temperature. However, several major obstacles of these inorganic TE materials greatly hinders their practical use in commercial applications, including scarcity of raw materials, high cost of fabrication processes, difficulty in scale-up, intrinsically high k, brittleness in addition to environmental concerns due to possible toxicity of heavy-metal elements [1]. Organic semiconductors have attracted intense attention because of their potential application in mechanically flexible, lightweight, and inexpensive electronic devices. Among various organic semiconductors, poly(3,4-ethylenedioxythiophene): poly(styrenesulfonate) (PEDOT:PSS), a commercially water dispersion in which insulating PSS polymer serves as both dispersant and counterion for conducting polymer PEDOT, has therefore been regarded as a promising candidate due to its intrinsically high electrical conductivity, low thermal conductivity, and high mechanical flexibility in thermoelectric generators [2]. The energy conversion efficiency of a TE material is typically evaluated by a dimensionless figure of merit ZT and defined as ZT= $S^2\sigma T/k$, where S is the Seebeck coefficient, σ is the electrical conductivity, T is the absolute temperature, k is the thermal conductivity, and $S^2\sigma$ is defined as the power factor (PF). However, it is generally considered that it is difficult to obtain a high ZT value of TE materials, due to the fact that the parameters S, σ, and k are interdependence as a function of carrier concentration and hard to be optimized simultaneously. To date, there are two facile strategies to significantly enhance ZT values of PEDOT:PSS films. One is secondarily doping organic solvents. Another effective way to enhance the TE performance of conducting polymers is to implement organic solvents or ionic liquids post-treatment. Herein, we adopt a combination of 5% DMSO addition and subsequent DMSO post-treatment to engineer TE performance of PEDOT:PSS thin film.

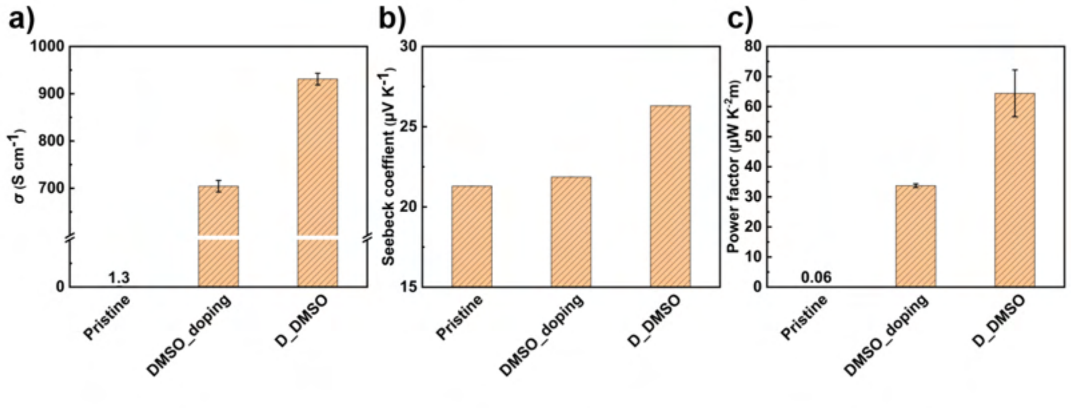

Figure 3.6:
Thermoelectric properties of PEDOT: PSS thin films: a) electrical conductivity, b) Seebeck coefficient, and c) power factor.

Fig. 3.6 shows the TE performance of PEDOT:PSS thin films. From the reference PF value of pristine PEDOT: PSS film of approximately 0.06 $Wm^{-1}K^{-1}$ due to its poor σ of 1.3 S/cm, a significant increase of σ is observed after DMSO addition, yielding a value of 704 S/cm. Interestingly, the S for DMSO-doping PEDOT:PSS film almost remains unchanged, leading to a PF value of 33.7 $WK^{-2}m^{-1}$. In the case of DMSO-doped PEDOT:PSS film via DMSO post-treatment, we find a simultaneous increase of σ and S, up to 931 S/cm and 26. 3μV/K respectively. This can be attributed to conformation alteration from the benzoid structure favoring a coil formation and quinoid structure favoring a linear or expanded coil structure. It has been documented that linear or expanded coil conformations contribute to high charge -carrier mobility, and interchain interactions among conductive PEDOT chains also increase [3]. Thus, a maximum PF of 64.4 $\mathrm{WK^{-2}m^{-1}}$ can be achieved. The improvement of PF renders a dual DMSO treatment approach feasible regarding enhancement of TE properties. It can be concluded that the enhancement of PF originates from following two aspects: 1) DMSO can induce charge screening effect by weakening the ionic interaction between PEDOT and PSS chains, resulting in phase separation; 2) increase in both S and σ suggests the improvement of the charge mobility because of a decrease in tunneling distance between conducting molecules overpowers the decrease in carrier concentration.

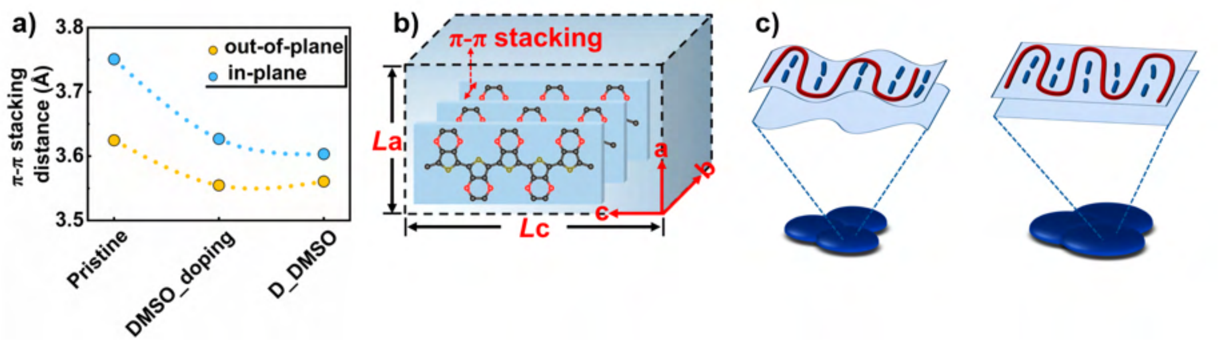

Figure 3.7:
a) π-π stacking distance, b) crystalline domain in PEDOT: PSS films, c) schematic diagrams showing the structural change of the PEDOT: PSS films.

It is generally acknowledged that a decrease of π-π stacking distance of PEDOT chains siganls an increase in level of molecular packing and thus an enhancement in the local crystallinity[3]. Based on our calculations shown in 3.7a), we observe that the π-π stacking distance decreases via DMSO treatment, indicating that the π-π interchain coupling of conductive host moleculars (3.7b)) in PEDOT:PSS film can be improved after DMSO treatment. It is because the local ordering and the interchain distance of PEDOT chains exponentially affect the π-electronic overlap, which in turn offers a pathway for π-π interchain chage transfer over an individual polymer [4]. We propose a morphological model of PEDOT:PSS films before and after DMSO treatment as shown in Fig. 3.7c). After DMSO treatment, the oblate ellipsoidal-shaped PEDOT nanocrystals increase and the layers composed of alternating PEDOT and PSS polymer chains become more planar, accounting for improvement of σ. Thus, it is expected that a combination of solvent addtion and post-treatment will contribute to a promising manipulation for optimizing TE properties of PEDOT:PSS films.

[1] Y. Wang, L. Yang, X. L. Shi, L. D. Chen, M. S. Dargusch, J. Zou, Z. G. Chen, *Adv. Mater.* **31**, 1807916 (2019)

[2] S. D. Xu, M. Hong, X. L. Shi, Y. Wang, L. Ge, B. Yang, L. Z. Wang, M. S. Dargusch, J. Zou, Z. G. Chen, *Chem. Mater.* **31**, 5238-5244 (2019)

[3] N. Kim, B. Lee, D. Choi, G. Kim, H. Kim, J. Kim, J. Lee, Y. Kahng, K. Lee, *Phys. Rev. Lett.* **109**, 106405 (2012)

[4] H. Martens, H. Brom, *Phys. Rev. B* **64**, 201102 (2001)

3.4 Fabrication on plasmonic nanostructures in optoelectronic devices

T. Guan, P. Müller-Buschbaum

Plasmonic metal-dielectric composites have fascinated a great interest in various fields, owning to surface plasmon resonance (SPR) induced by incident radiation.[1] Nobel metal structures serve as a guide and manipulate via visible light to the localized electrical area. The plasmon induced electric excite could be changing photoenergy localization and the lifetime of excited states materials. Certain location of metal nanostructure combined with semiconductor materials is a key factor to successful utilization of SPR in oscillating collectively of induced electron clouds. Thus, nanostructure geometry has a virtual influence on SPR performance and its applications. Recently, many types of plasmonic nanoparticles (NPs), including the precise shapes, sizes, and spacings of nanospheres (NSs), nanorods (NRs), nanostars, nanocubes, etc., have been incorporated in optoelectronic devices to improve their efficiency.[2] It has been proved that the employ of plasmonic nanostructures is commonly presented as a means to additionally boost the light absorption in the broad wavelength range as well as promoted charge transportation and collection of the devices.[3] The introduction of plasmonic metal nanostructures into optoelectronic devices is assumed to be the most promising technique to increase the performance of the devices without changing the device size. However, the systematical fundamental study and effect of SPR in plasmonic enhanced optoelectronics still need to be explored. Therefore, optimizing metal nanostructure and identifying suitable fabrication processes to achieve high efficiency optoelectronic devices are crucially important.

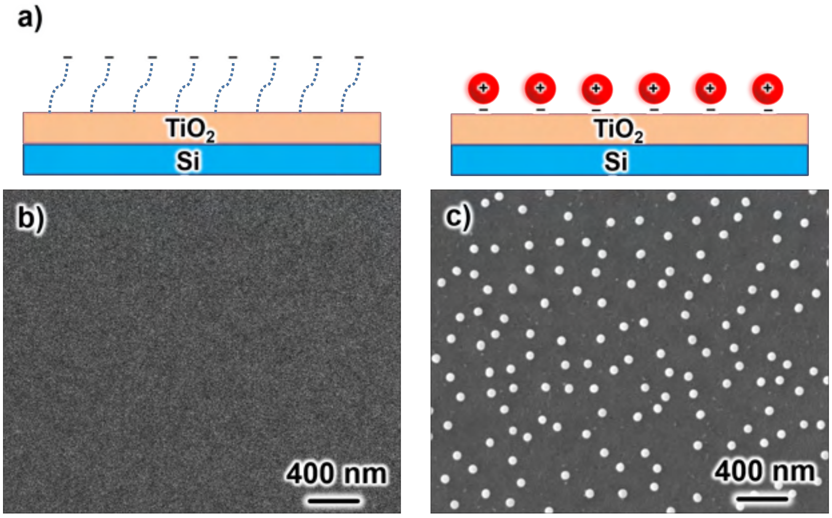

Figure 3.8:
Schematic diagram of Au NSs assembled on the top of the TiO_2 film. SEM images of b) pristine TiO_2 film and c) Au NPs assembled on TiO_2 film.

To well explore the plasmonic effect for the enhancement of optoelectronic activities of metal-interface and plasmonic behavior, an in-depth study is required. At this point, we used the self-assembly technique with tunable plasmonic effects to excogitate the precise modulation of metallic nanostructures. The self-assembly methods of charge inversion and the relevant assembly of Au NSs are shown in Fig. 3.8 a. First, we surface modified the ITO/TiO_2 substrate with negative charges and then assembled Au NSs which were prepared through a seed-mediated growth procedure.[4] Fig. 3.8 b shows the pristine TiO_2 substrate and c assembled with Au NSs substrate, we can see the Au NSs are well as dispersion on the top of flat TiO_2 film. And both of these two substrates will be used to fabricate the $CH_3NH_3PbI_3$ perovskite film to investigate the influence of $CH_3NH_3PbI_3$ film with the introduction of Au NSs. As is shown in Fig. 3.9 a, we used spin coating methods to directly deposition the $CH_3NH_3PbI_3$ film on these two substrates. Fig. 3.9 b, d, and c, e, shows the SEM images and cross-section images of $CH_3NH_3PbI_3$ film without and with Au NSs, respectively. From Fig. 3.9 b and c, the perovskite films show almost the same grain size on the two types of substrates which means the incorporation of Au NSs has rarely influenced the crystal quality of $CH_3NH_3PbI_3$ film. Besides, the grazing incidence wide angle X-ray scattering (GIWAXS) techniques have proven a valuable addition as they are able to probe the inner film morphology.[5] To further study the properties of plasmonic structures in perovskite film, GIWAXS will be used to investigate the mechanism of plasmonic structure application. We expect that these fabrication methods plasmonic nanostructured can also be utilized in a wide range of optoelectronic devices.

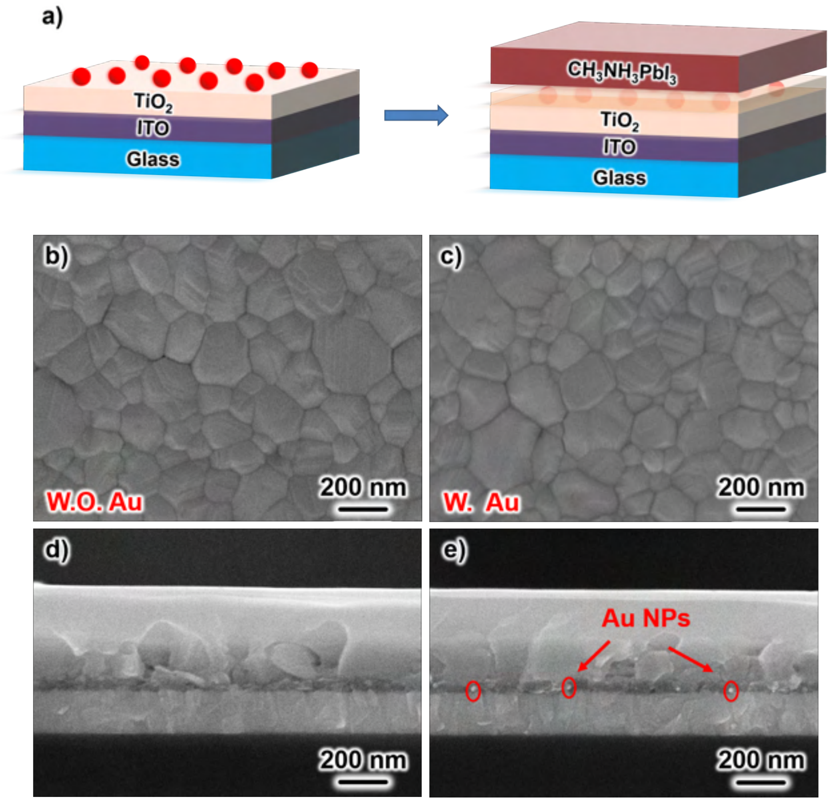

Figure 3.9:
Schematic diagram of perovskite film spin coated on the TiO_2/Au substrate. SEM images of b) $CH_3NH_3PbI_3$ film on bare TiO_2 film without (W.O.) Au NPs and c) with (W.) Au NPs.

[1] Z. Liang, J. Sun, Y. Jiang, L. Jiang, X. Chen, *Plasmonics* **9**, 859–866 (2014)

[2] A. Zada, P. Muhammad, W. Ahmad, Z. Hussain, S. Ali, M. Khan, Q. Khan, M. Maqbool, *Adv. Funct. Mater.* **30**, 1906744 (2020)

[3] N. Kholmicheva, P. Moroz, H. Eckard, G. Jensen, M. Zamkov, *ACS Energy Lett.* **2**, 154-160 (2017)

[4] Q. Ruan, L. Shao, Y. Shu, J. Wang, H. Wu, *Adv. Optical Mater.* **2**, 65–73 (2014)

[5] J. Schlipf, P. Müller-Buschbaum, *Adv. Energy Mater.* **7**, 1700131 (2017)

3.5 Hybrid energy harvester based on triboelectric nanogenerator and solar cell

T. Xiao, W. Chen, W. Cao, S. Wöhnert[1], S. V. Roth[1,2], C. Zhang[3], P. Müller-Buschbaum

[1] DESY, Hamburg, Germany
[2] KTH, Stockholm, Sweden
[3] BINN, Beijing, China

Developing clean energy lies the heart of the sustainable development of human society.[1] Triboelectric nanogenerator (TENG) originating from Maxwell's displacement current is a new type of energy harvester for harnessing ambient mechanical energy based on the coupling of triboelectrification and electrostatic induction effect.[2] Compared with other counterparts, such as electromagnetic generator, owing to the light-weight, low-cost, and easily fabricated, TENG has become one of the most promising candidates in replacement of conventional fossil fuels and attracted worldwide attention in the past years. Since TENG has been first proposed in 2012, many kinds of TENGs have been fabricated for converting various energies into electricity.[3] However, to further increase the energy harvesting efficiency and broaden application fields, integrating the TENG with other kinds of energy harvesters in one device is a possible way to meet these needs.

In the present work, in order to suit for potential applications in soft robotics and smart home systems, a TENG based hybrid energy harvester is designed and fabricated on the flexible polyethylene terephthalate (PET) substrate. This hybrid device consists of a single-electrode mode TENG component and a PbS quantum dots (QDs) based solar cell component, which can harness both mechanical and solar energy from ambient environment to directly generate electricity through different working mechanisms. The structure of as-fabricated hybrid energy harvester is schematically shown in Fig. 3.10a, which is with the common configuration of ITO-PET/ZnO/PbS QDs/Au as the solar cell under the bottom and covered by the fluorinated ethylene propylene (FEP) film on the top as the dielectric material for TENG. Here, gold serves as both the bottom electrode for TENG and the anode for solar cell. And Fig. 3.10b presents a photograph of the hybrid device at bending state, showing its good flexibility.

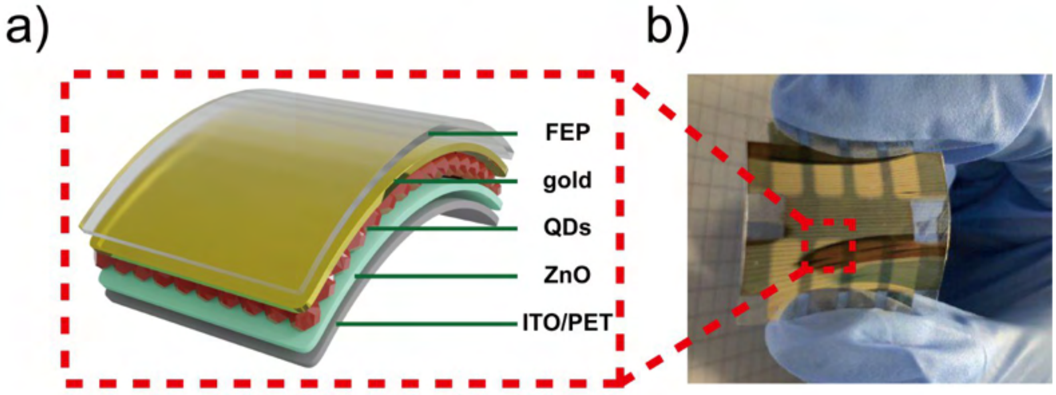

Figure 3.10:
a) The schematic illustration of as-fabricated hybrid energy harvester. b) The photograph of the hybrid device at bending state.

For the output performance of the hybrid device, we begin with the solar cell component. It can be observed from Fig. 3.11a that the power conversion efficiency (PCE) of the solar cell component from the champion sample achieves 4.9% with a short-circuit current of 22.8 mA/cm^2, an

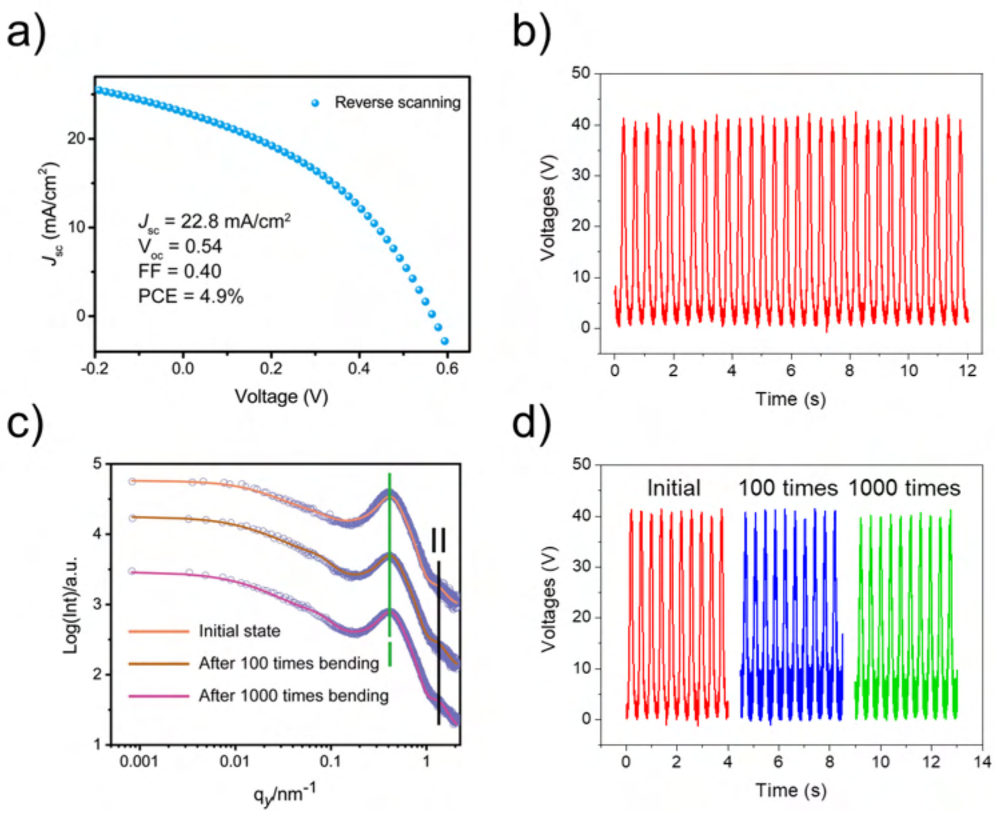

Figure 3.11:
a) The output performance of solar cell component. b) The average output voltages of TENG component. c) The GISAXS horizontal line cuts and fitted curves at different states. d) The average output voltages of TENG component at different states.

open-circuit voltage of 0.54 V and a fill factor of 40%. Meanwhile, as shown in Fig. 3.11b, 41.0 V of average output voltages are obtained by TENG component

under pressing. Moreover, in order to investigate the bending stability of the hybrid device, grazing incidence small-angle X-ray scattering (GISAXS) is used to characterize the morphology changes of the mesoscale structure.[4] Fig. 3.11c shows the GISAXS horizontal cutting data and fitted curves of the solar cell component at different states. Here, because of the similar critical angle of ZnO and PbS, the peak I is originated from the inter-dot distance between neighboring ZnO nanoparticles (NPs) in the function layer. Besides, the peak II is originated from the inter-dot distance between neighboring PbS QDs in the film. According to the modelling results, the inter-dot distances of ZnO NPs and QDs remain nearly stable at (3.8 ± 0.6 nm and 1.5 ± 0.3 nm) respectively after bending, exhibiting the high stability in structure level. From Fig. 3.11d, we can also find that there is only a 2.2% decrease (from 41.0 V to 40.1 V) on average output voltages of the TENG component after 1000 times bending, demonstrating the high bending stability of the whole hybrid device.

[1] B. O'regan, M. Grätzel, *Nature* **353**, 737 (1991)

[2] Z. L. Wang, *Mater. Today* **20**, 74 (2017)

[3] L. Zheng, Z. Lin, G. Cheng, W. Wu, X. Wen, S. Lee, Z. L. Wang, *Nano Energy* **9**, 291-300 (2014)

[4] P. Müller-Buschbaum, *Adv. Mater.* **46**, 7692-7709 (2014)

4 Photovoltaics

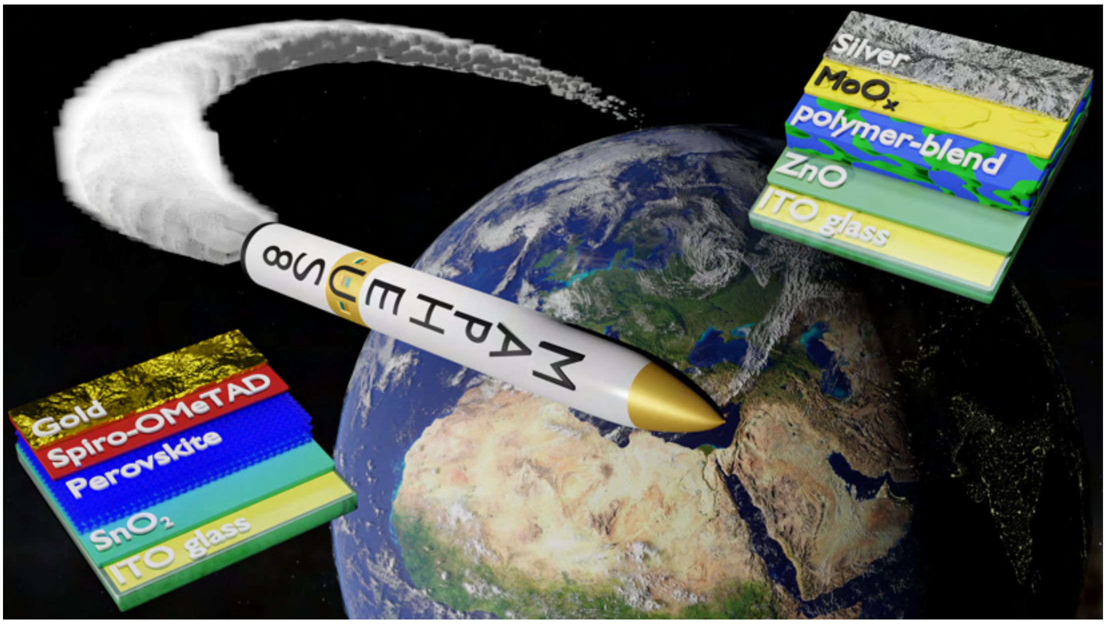

4.1 Morphological investigation of non-fullerene bulk heterojunction blends for application in photovoltaics

S. Grott, A. Kotobi, M. Schwartzkopf[1], S. V. Roth[1,2], P. Müller-Buschbaum

[1] DESY, Hamburg, Germany
[2] KTH, Stockholm, Sweden

Photoactive polymers have attracted high attention over the recent years due to various different applications in the field of organic light emitting diodes (OLED) or organic photovoltaics. Thereby, the usage of polymer thin films as the photoactive material for energy conversion has a variety of potential advantages. Those polymers can be synthesized from low-cost and abundant precursor materials. Therefore, they enable the possibility to manufacture thin, light-weight and flexible films with tunable color. Since those polymers can be processed from solution, upscalable and low-cost processing techniques like roll-to-roll printint or spray coating can be applied. Based on these advantages, OPV and OLED devices could be implemented into a variety of applications, thereby combining functionality with design in fields like clothing, architecture or mobility. Since these devices represent a promising alternative to conventional solar cells, we focus on the investigation of OPV and thereby on the influence different solvents have on the morphological differences caused by the usage of different solvents. These changes in morphology influence the final device performance and thus are of crucial interest.

Understanding the influence of solvents on the final morphology of the polymer thin film plays a crucial role to identify potential ways to enhance the performance of these OPV devices. Investigations on the homogeneity and the inner morphology of the formed bulk heterojunction of major importance to correlate the processing pathways and the final device performance. Since such photoactive bulk heterojunction layers consist of two different components, an acceptor polymer and a donor molecule, the inner structure is of high interest. In the recent years new donor material have emerged and step by step replacing the commonly used fullerene based donor molecules, due to their tunability in absorption properties and hence improve to efficiency of OPV devices.[1-2] In this case we study the influence of three different solvents on the morphology of such bulk heterojunction blends to investigate ways to enhance the final device performance. To get a first insight, the spin coated films are investigated via optical microscopy.

Figure 4.1:
Microscope images of spin-coated active layers out of a) chlorobenzene, b) dichlorobenzene and c) chloroform .

In Fig. 4.1 microscopy images of the films are shown. Thereby Fig. 4.1 a) shows the film obtained from a bulk heterojunction blend solution out of chlorobenzene, b) out of dichlorobenzene and c) chloroform, respectively. Thereby it can be observed that the homogeneity of the thin films is influenced by varying the solvent and that the film made out of chlorobenzene exhibits the highest homogeneity.

To get deeper insight into the homogeneity and the inner morphology of these bulk heterojunction thin film grazing incidence small angle X-ray scattering (GISAXS) experiments are performed. [2] This technique is a powerful tool to investigate thin films in a non destructive manor with high statistics. The acquired data sets were analyzed using the data reduction software DPDAK. Hereby, the 2D raw data were cut at the specific regions of interest, such as the horizontal line cuts presented in Fig. 4.2.This gives information about the lateral film morphology.

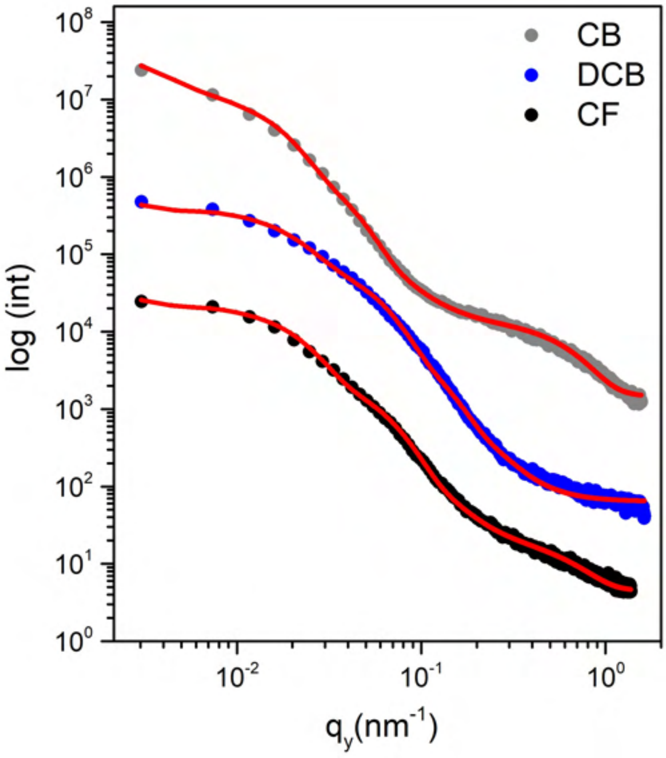

Figure 4.2: GISAXS horizontal line cuts of the 2D data for the three different solvents.

In Fig. 4.2 the horizontal line cuts of the respective bulk heterojunction thin films are shown as well as the corresponding modeling of the data. The obtained GISAXS line cuts for the respective solvents differ strongly and indicate changes in the inner morphology of the bulk heterojunction thin films, which is in accordance with the observations in the optical microscopy experiment. The modelling of the obtained cuts enables insight into structure sizes and structure distances. Comparing the obtained structure sizes with structure sizes in the range of the exciton diffusion length, might give first hints towards the most suited solvent for this fullerene free bulk heterojunction blend. To gain deeper understanding of the correlation between the inner morphology of this non fullerene bulk heterojunction blend and the final device performance, further investigation on the opto-electronic properties are performed. The morphological findings presented mark a key step towards further optimization of organic photovoltaics and help to increase the power conversion efficiency of organic solar cells.

[1] W. Zhao, D. Qian, S. Zhang, S. Li, O. Inganäs, F. Gao, J. Hou, *Adv. Mater.* **28**, 4734-4739 (2016).

[2] S. H. Park, A. Roy, S. Beaupre, S. Chao, N. Coates, J. S. Moon, D. Moses, M. Leclerc, K. Lee, A. J. Heeger, *Nat. Photon.* **3**, 297-302 (2009).

[3] P. Müller-Buschbaum, *Anal. Bioanal. Chem.* **376**, 3-10 (2003).

4.2 It is dangerous to dope perovskite solar cells

R. Guo, P. Müller-Buschbaum

Perovskite materials have been a promising technology for the application of photovoltaic, photo-detector and transistor and light-emitted diode [1]. Such materials attract much interest in the recent ten years due to their low-fabrication cost, excellent optoelectronic properties and a variety of fabrication methods [2]. Among most of the applications, the power conversion efficiency (PCE) of perovskite solar cells have achieved 25.4 % because of diligent work by researchers in this field. However, there is still a distance towards the Shockley–Queisser limit (31.3 %) regarding PCE. Thus, we need to understand what is losing in the real device. Besides, it is also critical to tackling these losses for reaching the Shockley–Queisser limit.

Nowadays, V_{OC} deficits of only 60 mV concerning the radiative V_{OC} limit have been reported in the literature, which is very close to the theoretical limits [3]. The J_{SC} of solar cells is also close to theoretical limitation. Hence, the main limitation of PCE for perovskite solar cells is the fill factor (FF). The FF of solar cells can be referred to three properties: 1) the charge extraction of electron-hole pairs; 2) the series resistance; 3) the ideal factor defined by non-radiative recombination. To further improve the FF of solar cells, we should work on these three directions. For properties 1) and 2), it is hard to improve due to current technical limitations for other hole or electron transporting layers, and top and back electrodes for the device. Thus, it is the most practical strategy to enhance the PCE of perovskite solar cells by lowing the ideal factor defined by non-radiative recombination. The non-radiative recombination centers are usually considered, locating at the surface or in the bulk of perovskite materials. Hence, surface and bulk passivation could be useful strategies to enhance the FF of perovskite solar cells.

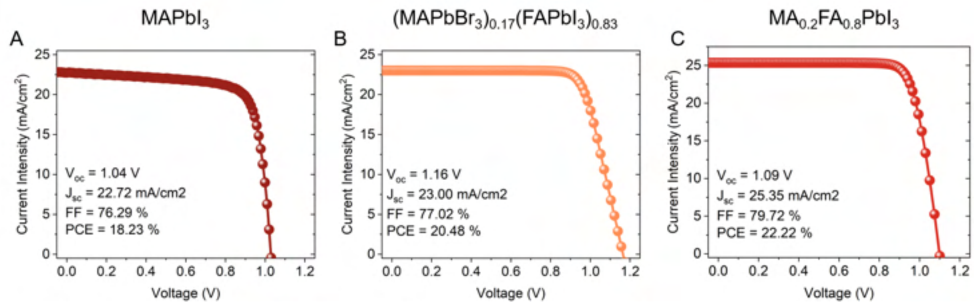

Figure 4.3:
Champion power conversion efficiency with different components of A) $\mathrm{MAPbI_3}$, B) $\mathrm{(MAPbBr_3)_{0.17}(FAPbI_3)_{0.83}}$ and (C) $\mathrm{MA_{0.2}FA_{0.8}PbI_3}$

Jiang et al. proposed a useful and reproducible surface passivation strategy by the use of an organic halide salt phenethylammonium iodide (PEAI) [4-5]. But there are less reproducible bulk passivation strategies. Fig.4.3 shows PCE of perovskite solar cells in our E13 group for $\mathrm{MAPbI_3}$, $\mathrm{(MAPbBr_3)_{0.17}(FAPbI_3)_{0.83}}$ and $\mathrm{MA_{0.2}FA_{0.8}PbI_3}$ respectively. To test similar organic halide salt like phenethylammonium iodide, we dope different concentrations of p-f-PEAI into the bulk of $\mathrm{(MAPbBr_3)_{0.17}(FAPbI_3)_{0.83}}$ perovskite solar cells. However, we found that the improvement of FF of perovskite solar cells is not significant as shown in Fig.4.4. The PCE of p-f-PEAI doped perovskite solar cells decreases dramatically with the increasing concentration of p-f-PEAI.

The aim of our experiment is to minimize the bulk defect because the functional group (amine) in p-f-PEAI can suppress the formation of lead-related non-radivative recombination centers, and iodine can decrease the halides-related non-radivative recombination centers. However,

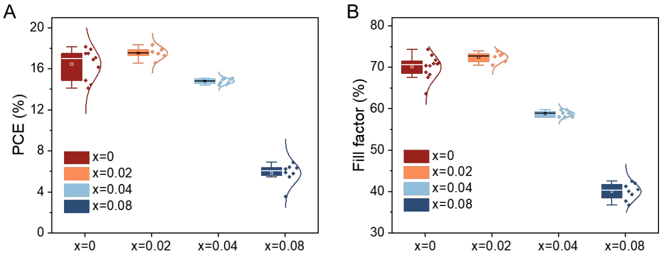

Figure 4.4: Statical parameters for perovskite solar cells A) PCE and B) FF.

the 2D perovskite phases formed due to the addition of p-f-PEAI have more significant effects on the PCE of perovskite solar cells rather than defects passivation (Fig.4.5 A). This is due to the insulating nature of 2D perovskite phases, which is super harmful for charge separation, although the addition of p-f-PEAI induces the formation a new texture at the Bragg peak (100) of perovskite (Fig.4.5 B).

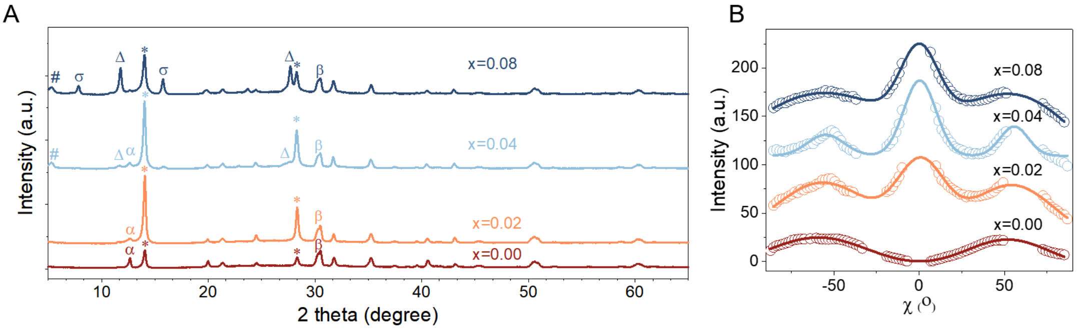

Figure 4.5:
(A) XRD data of the perovskite films with different p-f-PEAI concentrations. Characteristic Bragg peaks of the $(p\text{-}f\text{-}PEAI)_2Pb(I_{0.85}Br_{0.15})_4$ (number sign), intermediate phases (sigma and delta), PbI_2 (alpha), 3D perovskite (star) and ITO (beta) are highlighted. (B)Tube cuts of the (001) perovskite Bragg peak from the 2D GIWAXS data (symbols) and corresponding fits with Gaussian functions (solid line) for different p-f-PEAI concentrations x.

To conclude, doping materials in the perovskite bulk to suppress defects may not a good strategy, although the same material already shows a successful application for the surface passivation even with trace doping.

[1] S. A. Veldhuis, P. Boix, N. Yantara, and M, Li, T, Sum, N , Mathews, S. Mhaisalkar, *Adv. Mater.* **32**, 6804–6834 (2016)

[2] H. S. Jung, and N. G. Park, *Small* **11**, 10-25 (2015)

[3] Z. Liu, L Krückemeier, B. Krogmeier, B. Klingebiel, J. Marquez, S. Levcenko, S. Öz, S. Mathur, U. Rau, T .Unold, *ACS Energy Lett.* **4**, 110-117 (2018)

[4] Q. Jiang, Y. Zhang, X. Zhang, X. Yang, Y. Chen, Z. Chu, Q. Fei, X. Li, Z. Yin, J. You, *Nat. Photonics* **13**, 460-466 (2019)

[5] G. Kim, H. Min, S. K. Lee, S. M. Yoon, S .Seok, *Science* **32**, 108–112 (2020)

4.3 Internal nanoscale architecture of non-fullerene bulk heterojunction active layers in organic solar cells

X. Jiang, H. Kim, S. V. Roth[1,2], P. Müller-Buschbaum

[1] DESY, Hamburg, Germany
[2] KTH, Stockholm, Sweden

The internal nanoscale structure as well as the crystallity of the active layer have a great importance to the performance of OSCs. Both could be easily tuned by several approaches, such as introducing additives, third components and post-treatments. Among these methods, introducing additives is a pervasive and effective way. Since solvent additives enable polymers to have a higher degree of molecular order, which is beneficial for the device performance.[1] In this work,we investigate the influence of the amount of the solvent additive DIO to tailor the nanoscale morphology of the active layer.

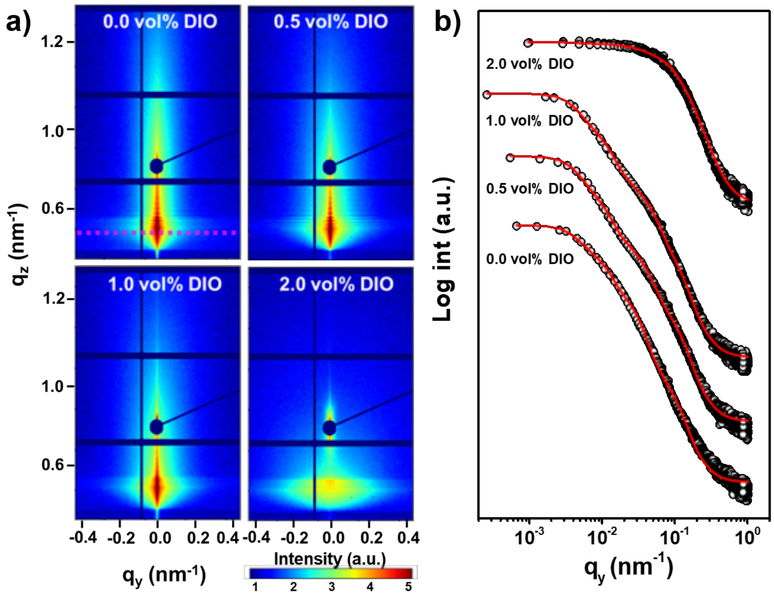

Figure 4.6:
a) 2D GISAXS data of the active layers with addition of different DIO volumes as indicated. The red dotted line represents the Yoneda peak position of PBDB-T-2F. b) Horizontal line cuts of 2D GISAXS data (black symbols) for PBDB-T-2F: IT-M thin films prepared with addition of different DIO volumes. The red lines are the model fits. All curves are shifted along the y-axis for clarity of the presentation.

The inner nanoscale morphology of PBDB-T-2F: IT-M thin films with different amounts of DIO addition is investigated with GISAXS measurements in Fig. 4.6. Without DIO, the 2D intensity shows a narrow intensity distribution along the scattering plane, while the intensity becomes broader and extends toward higher q_y values with increasing the DIO concentration. Moreover, fringes in intensity are seen along the q_z direction, which is caused by the X-ray waveguide effect, suggesting a conformal roughness between the substrate and the active layer surfaces.[2] Notably, the ripple structure becomes most pronounced when 0.5 vol% DIO is added, while it smears out gradually as the DIO concentration increases. To model the lateral polymer structures in the active layer, three cylindrical objects with different radii and inter-distances are used in the framework of the distorted wave Born approximation assuming the effective interface approximation. All PBDB-T-2F domain radii decrease with increasing the concentration of DIO. In more detail, in the film without DIO additive, the average large, medium, and small-sized domain radii are (122 ± 5) nm, (46 ± 2) nm, and (13 ± 1) nm, respectively. Adding 0.5 vol% DIO, they decrease to (113 ± 4) nm, (29 ± 2) nm, and (11 ± 1) nm, for 1.0 vol% DIO to (103 ± 4) nm, (28 ± 2) nm, and (11 ± 1) nm and for 2.0 vol% DIO to (13 ± 3) nm, (9 ± 1) nm, and (5 ± 1) nm. When donor and acceptor are well blended, smaller distances between neighboring donor domains appear to be beneficial for the OSCs to facilitate the inner charge carrier transport. Thus, from a morphology perspective, the addition of 0.5 vol% DIO will cause the best suited inner

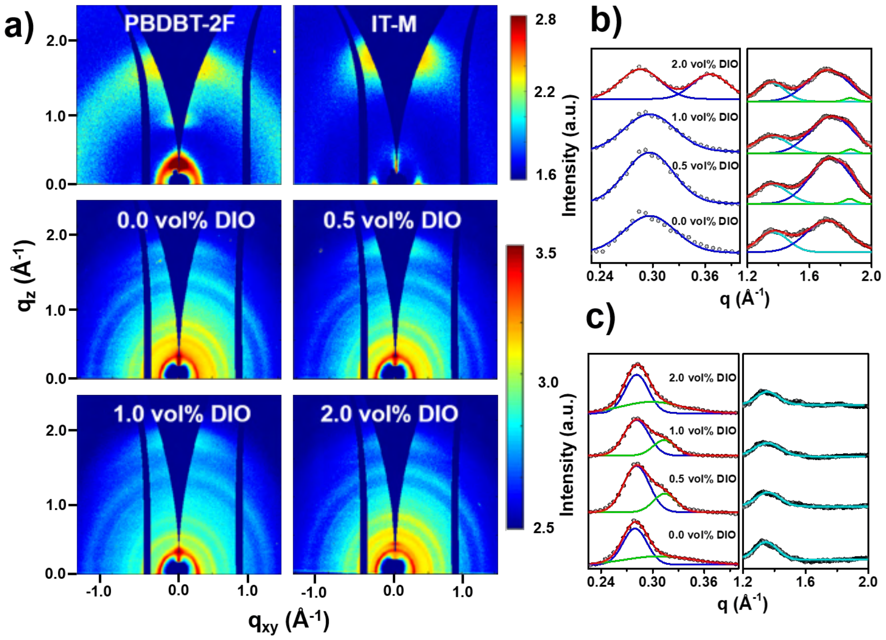

Figure 4.7:
a) 2D GIWAXS data of PBDB-T-2F and IT-M films as well as PBDB-T-2F:IT-M active layers with different volume of DIO addition.Cake cuts of 2D GIWAXS data in b) out-of-plane and c) in-plane direction for PBDB-T-2F:IT-M active layers prepared with addition of different DIO volumes. Model fits are shown with solid lines. Blue lines represent oriented PBDB-T-2F crystals, green lines represent isotropous PBDB-T-2F crystals and red lines represent oriented IT-M crystals. All curves shifted along the y-axis for clarity of the presentation.

film morphology on the nanoscale by balancing domain distance and sizes to match exciton diffusion lengths.

The information about the crystalline part of the thin films is determined with GIWAXS in Fig. 4.7. The neat PBDB-T-2F film shows both face-on and edge-on orientation of the polymer crystallites. In contrast, the neat IT-M film shows a typical face-on orientation to the substrate. To give more insights into the effect of DIO on the crystallinity of the individual components from the active layers, Bragg peaks in the cake cuts from the 2D GIWAXS data are analyzed with a Gaussian model. IT-M chains tend to transform into a pronounced face-on structure when the active layer is processed with DIO. The lamellar stacking crystal size of IT-M strongly increases from (63 ± 1) Å (0.0 vol%) to (141 ± 1) Å (0.5, 1.0 vol%) and decreases again to (71 ± 1) Å (2.0 vol%). The corresponding lamellar stacking distances remain largely unchanged as (20.3±0.1) Å (0.0, 0.5 and 1.0 vol%) even at 2.0 vol% DIO (20.9 ± 0.1 Å).The edge-on crystal structure of PBDBT-2F remains constant with the lamellar stacking distance of (20.9 ± 0.1) Å and a crystal size of around (81 ± 1) Å for a DIO amount below 2.0 vol%. At 2.0 vol% in this direction the crystal size increases to (113 ± 1) Å and two different lamellar stacking distances appear ((21.7 ± 0.1) and (17.0 ± 0.1) Å). The face-on oriented PBDB-T-2F crystals have a size of (188 ± 1) Å in the lamellar stacking direction for all DIO amounts despite of the thin film processed with 0.5 vol% DIO ((141 ± 1) Å). The lamellar stacking distance of face-on PBDB-T-2F crystals remains constant ((22.4 ± 0.1) Å) for all probed DIO amounts.

[1] W. Wang, L. Song, D. Magerl, D. Moseguí González, V. Körstgens, M. Philipp, J. F. Moulin, S. V. Roth, P. Müller-Buschbaum, *Adv. Funct. Mater.* **7**, 1602000 (2017)

[2] P. Müller-Buschbaum, M. Stamm, *Macromolecules* **31**, 3686–3692 (1998)

4.4 Influence of printing temperature on the efficiency of organic solar cells

L. Huber, K. S. Wienhold, S. V. Roth[1,2], P. Müller-Buschbaum

[1] DESY, Hamburg, Germany
[2] KTH, Stockholm, Sweden

The demand for clean and sustainable energy has risen drastically in the last decades. Solar power is potentially an important part of the solution to supply the world with clean energy. In recent years organic solar cells have been proven to be advantageous in many ways. They are light-weight, semitransparent , non-toxic and have been proven to have high efficiencies [1]. In order to supply the world with clean energy at reasonable prices, mass production of organic solar cells needs to be enhanced. This can be achieved by decreasing the amount of individual production steps and exploring technologies with high scale-up potential. By printing the active layer of the organic solar cell, faster production cycles can be achieved and therefore both cost and product output can be increased. The effect printing has, on the performance of the solar cell and the molecular structure of the polymer, also needs to be investigated.

PBDB-T-SF:IT-4F solar cell devices use the high efficiency polymer donor material PBDB-T-SF and the acceptor material IT-4F. Fluorine is also introduced to increase chemical stability and obtain higher absorption coefficients. Crystallinity and charge transport can also be increased by the introduction of fluorine [1-3].

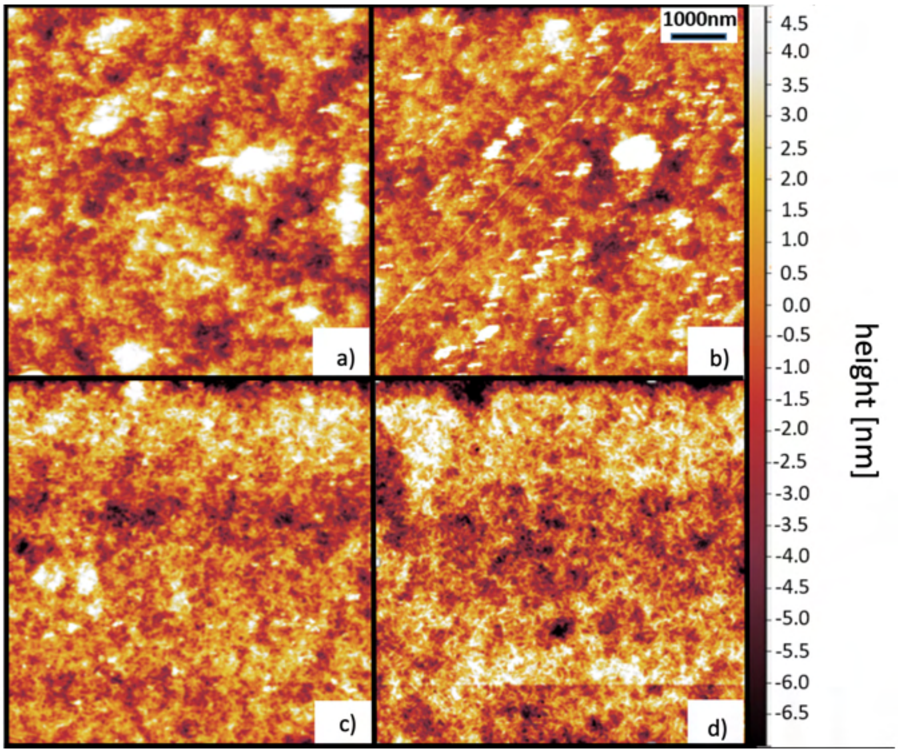

Figure 4.8: AFM images for four different printing temperatures. a) 20 °C, b) 40 °C, c) 60 °C, d) 80 °C

In the AFM images (Figure 4.8) a trend in structure size and surface roughness can be seen. The more the active layer is heated during printing, the faster is the evaporation of solvent. This faster drying process seems to lead to smaller structure sizes and a higher surface roughness.

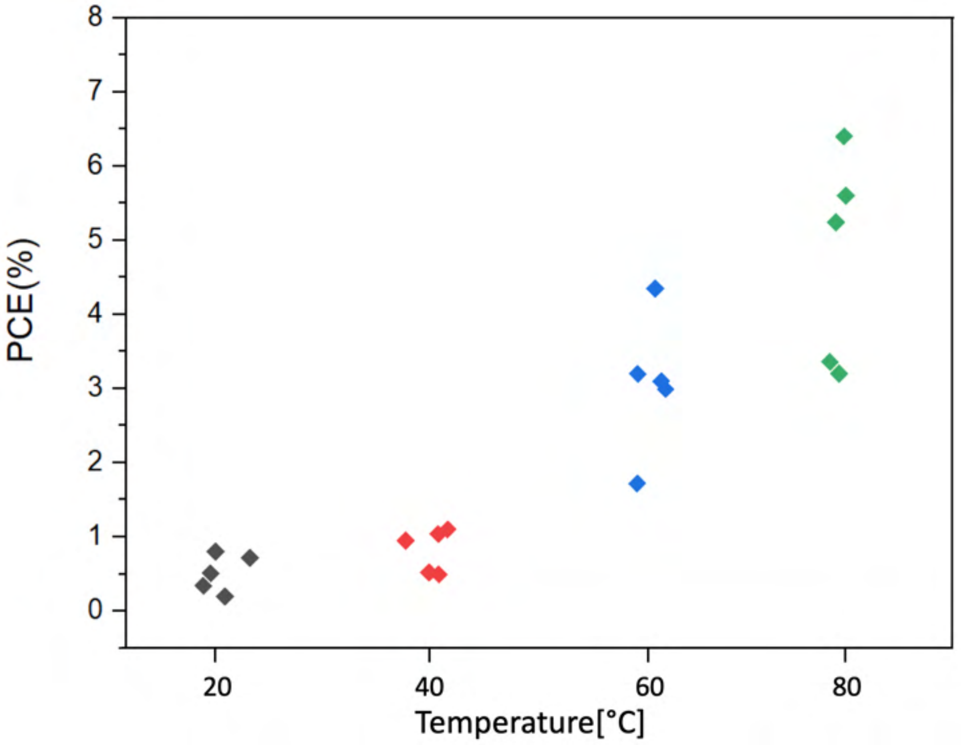

Figure 4.9: Power conversion efficiencies for organic solar cells printed at different temperatures.

The power conversion efficiencies for the printed organic solar cells can be seen in (Figure 4.9). Heated printing seems to positively influence the PCE for the investigated materials. This improvement can be attributed to the decreased structure roughness and smaller structure sizes seen in the AFM images (Figure 4.8). A reduction of very large structures is beneficial to the OSC device, as it reduces recombinations in these structures and therefore increases the electrical power extracted from the device. Decreasing average structure sizes increase the interface area between donor and acceptor. Therefore charge transfer is facilitated [4]. A bigger distance between structures decreases the Coulomb forces and therefore can lower recombination probabilities [5]. To support the morphological data, SEM and GISAXS were measured (not shown here) and the trend of decreasing average structure sizes was reaffirmed.

[1] W. Zhao, S. Li, H. Yao, S. Zhang, Y. Zhang, B. Yang, J. Hou, *J. Am. Chem. Soc.* **139**, 7148-7151 (2017)

[2] S. H. Park, A. Roy, S. Beaupre, S. Chao, N. Coates, J. S. Moon, D. Moses, M. Leclerc, K. Lee, A. J. Heeger, *Nat. Photon* **3**, 297-302 (2009)

[3] R. Xue, J. Zhang, Y. Li, *Small* **14**, 1801793 (2018)

[4] C. M. Proctor, M. Kuik, T.-Q. Nguyen, *Prog. Polym. Sci.* **38**, 1941-1960 (2013)

[5] T. M. Clarke, J. R. Durrant, *Chem. Rev.* **110**, 6736-6767 (2010)

4.5 A further step to space – perovskite and organic solar cells on a rocket flight

L. K. Reb, M. Böhmer[1], C. Dreißigacker[2], R. Gernhäuser[1], A. Meyer[2], P. Müller-Buschbaum

[1] TU Zentrales Technologielabor, Garching, Germany
[2] DLR Materialphysik, Köln, Germany

The emerging technologies of perovskite and organic solar cells experienced unprecedented development progress within the last years, catching up with the power conversion efficiency of conventional silicon solar cells. On the other hand side, they are typically deposited from solution at ambient temperatures with mass-production compatible manufacturing techniques. Here, low temperature processing makes a fundamental difference and enables the processing of perovskite and organic solar cells onto thin and flexible polymer foils. This feature opens up new possibilities for their utilization, where rigid and heavy silicon solar cells are inconvenient. The combination of high efficiency and light weight yields solar cells with an extremely high power-per-weight or so-called specific power, which can reach values that is magnitudes above the specific power of the best conventional solar cells.

Thus, weight limitations of solar panels for space applications can be easily overcome and it could be possible to save a large fraction of the space solar panel weight or to produce multiple times the electric power with the same weight. Moreover, the superior light-harvesting behavior in diffuse and faint light conditions known from terrestrial testing of perovskite and organic solar cells could extend the working distances of solar-powered spacecrafts to regions in the outer solar system.

However, in space the solar cells need to withstand exotic and extreme conditions, such as vacuum, very low and high temperatures, the hard solar irradiation with strong UV-light and cosmic particle radiation. For a long time there has been little information about the stability of the new materials in these environmental conditions. A pioneering project in 2014 lead by our chair could demonstrate notable stability of organic solar cells during operation in vacuum and simulated AM0 sun-light (as present above Earth's atmosphere) as seen from their performance parameters and supported by morphological investigations [1].

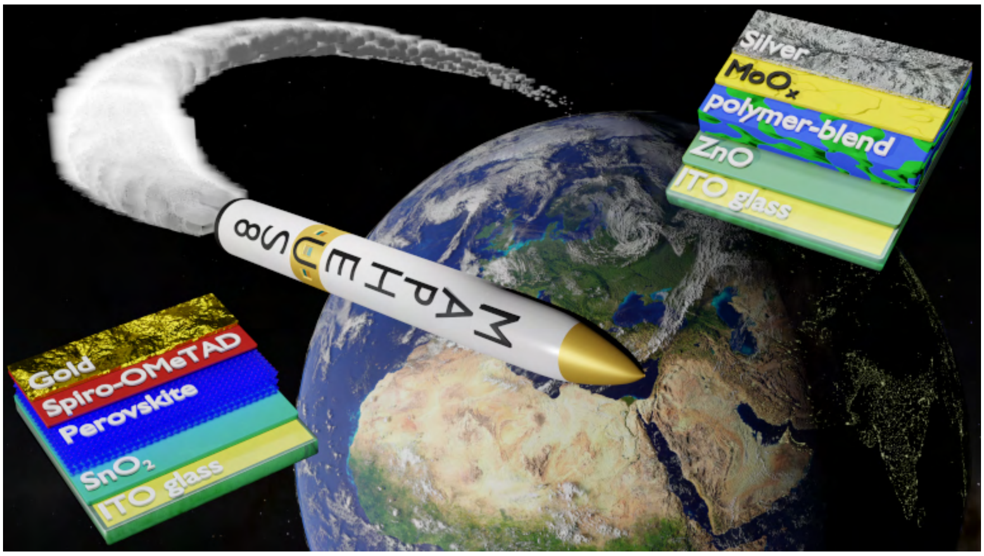

Figure 4.10: Schematic overview of the solar cell flight experiment. The sub-orbital rocket reached about 240 km altitude, carrying 128 perovskite and organic solar cells.

In this collaborative project with the Deutsche Zentrum für Luft- und Raumfahrt (DLR), we had the unprecedented opportunity to send our perovskite and organic solar cells into space, aboard a sub-orbital sounding rocket flight with scientific payload (see 4.10 for a schematic overview). During around six minutes of µ-gravity above Earth's atmosphere in altitudes of more than 100 km, the experiment collected several current-voltage measurement cycles for all solar cells.

This is the very first time to investigate these solar cell types in orbital altitudes as common for satellites in low-Earth orbits. After re-entry and parachute landing, the entire scientific payload including our experiment could be recovered, together with the solar cells and the measured data.

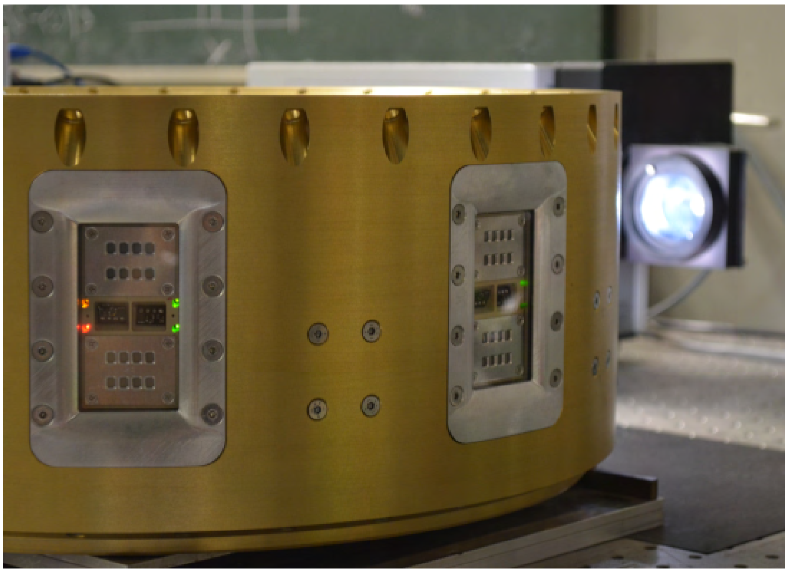

Figure 4.11:
Photograph during tests of the entire experiment unit in our labs before the maiden flight. The lamp in the background simulates sun light shining onto the outside of the experiment ring from one side. Behind each of the experiment windows, a perovskite and an organic solar module are positioned for the flight, each consisting of eight independent solar cells. The blinking LEDs show nominal operation of the data acquisition systems and indicate the active measurement process.

The data analysis shows that the experiment proceeded nominally and collected current-voltage measurements of the solar cells over the full measurement time. In addition, the collected data shows functionality and significant power generation of all four solar cell types, consisting of two perovskite solar cells in different architecture (SnO_2 planar and TiO_2 mesoporous n-i-p) and two organic solar cells with different absorber bulk heterojunctions (PBDB-T:ITIC and PTB7-Th:$PC_{71}BM$ in inverted architecture).

A detailed investigation of the performance of the solar cells during flight can be found in our recently published work [2]. In brief, we could obtain current-voltage measurements for all solar cell types during strong solar irradiation, which revealed strong power generation for all of them, reaching similar performance levels in extraterrestrial space conditions as in the pre-flight laboratory tests. This highlights that it is possible to bring these fascinating technologies to space together with their high efficiencies. Furthermore, in a short moment during µ-gravity time we could show that perovskite and organic solar cells are capable of producing power by just harvesting diffuse light sunlight reflected from Earth's surface. These results are particularly interesting for applications in low-light intensities as present in the outer solar system or deep-space exploration, since this proves their above-mentioned ability to produce electricity by shining only faint light onto them for extraterrestrial conditions. This work adds evidence that the emerging technologies of perovskite and organic solar cells should be considered very promising candidates for future energy production, in Earth orbit and beyond.

[1] S. Guo, C. Brandt, T. Andreev, E. Metwalli, W. Wang, J. Perlich, P. Müller-Buschbaum, *ACS Appl. Mater. Interfaces* **6**, 17902-17910 (2014)

[2] L. K. Reb, M. Böhmer, B. Predeschly, S. Grott, C. L. Weindl, G. I. Ivandekic, R. Guo, C. Dreißigacker, R. Gernhäuser, A. Meyer, P. Müller-Buschbaum, *Joule* **4**, 1880-1892 (2020)

4.6 Structural and morphological investigations of slot-die coated perovskite layers for photovoltaics

O. A. Shindelov, M. A. Scheel, S. V. Roth[1,2] and P. Müller-Buschbaum

[1] DESY, Hamburg, Germany
[2] KTH, Stockholm, Sweden

The field of perovskite solar cells was developing rapidly and reached efficiency value of 25.5%. [1] However, despite the rapid evolution, there are still some problems to face. One of the crucial points is establishing a qualitative, reproductive, and scalable manufacturing process. There are many candidates for filling this role in the future: spray coating, dip coating, roll-to-roll technology, and slot-die coating, etc. [2]

In the course of this work, the standard layered structure for perovskite solar cells was used. Homemade meniscus guided slot-die coater was used to produce the desired layers. First, the hole transporting layer (HTL) was deposited using the same slot-die coater on top of the glass substrate with pre-deposited indium tin oxide (ITO) layer. Materials used for HTL are tin oxide (SnO_2) or PEDOT:PSS. In the further stage, the deposition of methylammonium lead iodide (MAPI) perovskite layer was performed. The resulted layer was achieved in two steps: 1) deposition of lead iodide (PbI_2) solution in DMF with additives, 2) deposition of methylammonium iodide (MAI) in 2-propanol for the conversion of the PbI_2 layer into MAPI. This two-step method was shown to be advantageous in comparison to the one-step deposition method due to its higher versatility and modifiability. [3] The main goal of this work was to try out some additives in the solution at the step of PbI_2 layer deposition and resulted in how do they influence the resulting film morphology and structure. The main studying methods were X-ray diffraction (XRD), grazing-incidence wide-angle X-ray scattering (GIWAXS), and scanning electron microscopy (SEM).

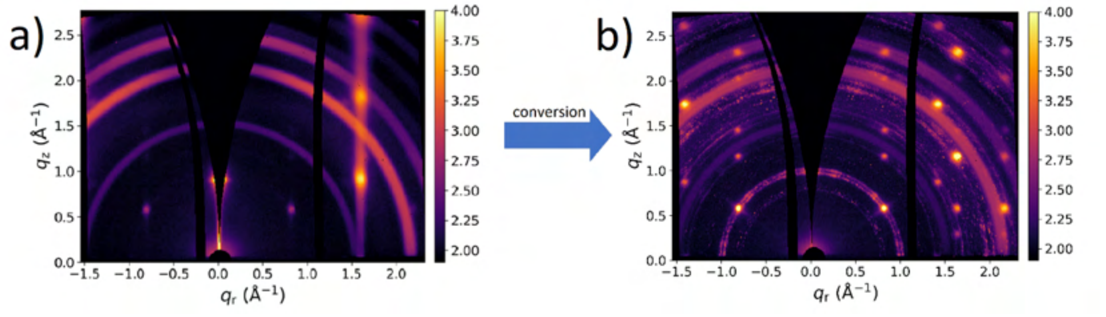

Figure 4.12:
GIWAXS patterns of a) lead iodide layer printed at 82 °C, b) perovskite layer after the conversion process.

All printing conditions stayed the same except for the printing temperature which was varied from 50 °C to 90°C. Comparing to our basic PbI_2 sample line with 5% of DMSO, the resulting PbI_2 structure has shown more oriented behavior from GIWAXS pattern analysis. This analysis is mainly performed using azimuthal cuts over small q range in GIWAXS. The PbI_2 films itself was found to be highly oriented with the main orientation of (001) plane being parallel to the substrate in Fig. 4.12 a). Resulting from additives, incorporated MAPI crystals in the PbI_2 layer were observed to have 3 preferential orientations: face-up, corner-up and edge-up, which is in agreement with previous studies. [4]

Converted MAI-seeded MAPI with GIWAXS presented in Fig.4.12 b) films were observed to have four preferential MAPI orientations, sometimes with residual PbI_2 with the same face-up

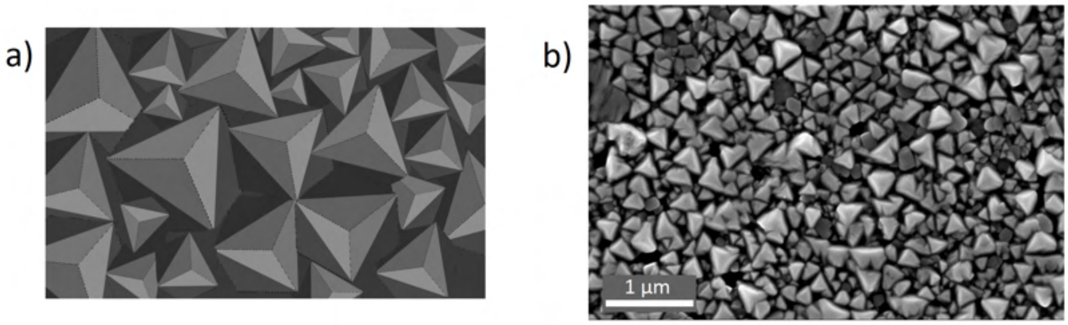

Figure 4.13:
a) Theoretical representation of the SEM view of corner-up crystal stacking deduced from GIWAXS analysis, b) SEM picture of the MAPI sample baked from the PbI_2 film printed at 82 °C. It could be observed, that crystals are highly corner-up oriented and are in agreement with the theoretical picture.

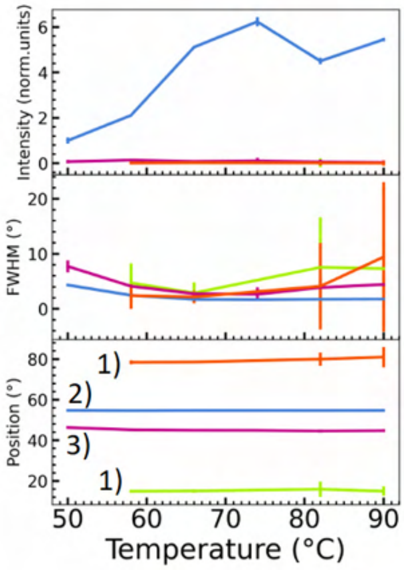

Figure 4.14:
Parameters of fitting GIWAXS tube cuts of MAPI films at the (002)/(110) reflex. Different colors stay for different Bragg spots observed in $MAPbI_3$ (002)/(110) tube cut. Numbers stated correspond to the observed $MAPbI_3$ orientations. The orange and green peak trends are produced by the same orientation.

stacking orientation as in the unconverted films.Comparing to the control sample, the additive seems to increase the amount of oriented crystals. The printing temperature rise causes narrowing of all observed orientations and shifting from preferring of the face-up orientation to the corner-up orientation. The sample itself is homogeneous and contains no pinholes. The amount of reacted PbI_2 is high since the sample is highly crystalline. Received SEM images support the data about corner-up oriented MAPI being dominating orientation type extracted from XRD and GIWAXS(Fig.4.13). The analysis of perovskite crystal growth is crucial for achieving high-efficiency solar cells. The addition of MAI seeds and regulation of temperature allows to tune the orientation of resulting MAPI film (Fig.4.14).

[1] M. Green, E. Dunlop, J. Hohl-Ebinger, M. Yoshita, N. Kopidakis, X. Hao, *Prog. Photovolt. Res. Appl.* **29**, 3– 15 (2021)

[2] Y. Rong, Y. Ming, W. Ji, D. Li, A. Mei, Y. Hu, H. Han, *J. Phys. Chem. Lett.* **9**, 2707-2713 (2018)

[3] M. Petrus, J. Schlipf, C. Li, T. P. Gujar, N. Giesbrecht, P. Müller-Buschbaum, M. Thelakkat, T. Bein, S. Huettner, P. Docampo, *Adv. Energy Mater.* **7**, 1700264 (2017).

[4] L. Oesinghaus, S. Schlipf, N. Giesbrecht, L. Song, Y. Hu, T. Bein, P. Docampo, P. Müller-Buschbaum, *Adv. Mater. Interfaces.* **3**, 1600403 (2016).

4.7 Dynamics in polymer-fullerene blends for photovoltaic applications

D. M. Schwaiger, W. Lohstroh[1], P. Müller-Buschbaum

[1] MLZ, TUM, Garching, Germany

In organic photovoltaics, donor - acceptor bulk heterojunctions are often used as active materials due to their superior performance compared to e.g. planar layered devices.[1] After the absorption of a photon and the creation of an exciton, this intermixed structure provides an interface for the dissipation of the exciton that must be reached within its lifetime. Subsequently, the separated charge carriers can be extracted at the respective electrodes. A well established model system is the combination of PTB7 as donor and PCBM as acceptor material. There are lots of studies on structure and morphology in this system, but yet none dealing with the molecular dynamics, which have been proven to also have major influence on electronic properties and thus device performance.[2] In our experiment, we determined molecular dynamics in PTB7:PCBM bulk heterojunction films. Beyond different mixing ratios between the conjugated donor polymer PTB7 and the fullerene acceptor material PCBM, two performance enhancing measures were also studies with focus on their influence on molecular dynamics. These two methods are a methanol posttreatment of the film to remove residual solvent[3] and the addition of 1,8-diiodooctane (DIO) to the solution, which leads to a more favorable microstructure of the polymer-fullerene blend.[4]

For the present experiments, we prepared eight films (ca.10 μm) of the respective sample material by dropcasting from a chlorobenzene solution on aluminum foils and stacked them in order to ensure sufficient scattering intensity in the neutron measurements. These measurements were performed at the cold neutron time of flight spectrometer TOFTOF at MLZ (Garching). This instrument measures the energy transfer between neutrons and the sample by measuring the time, they need from the sample position to the detector. This energy transfer is attributed to motions of hydrogen atoms within the sample. In the analysis, we can draw conclusions about type and intensity of these motions on a molecular level.

To evaluate the effect of blending on polymer dynamics, we produced four samples: pure PTB7, pure PCBM, a 1:1 and a 1:1.5 (wt.) PTB7:PCBM-blend. The methanol and DIO treatments were applied to the 1:1.5 sample. Since we could not observe any motions within the energy window of the instrument for the PCBM sample, data from this sample was not analyzed further.

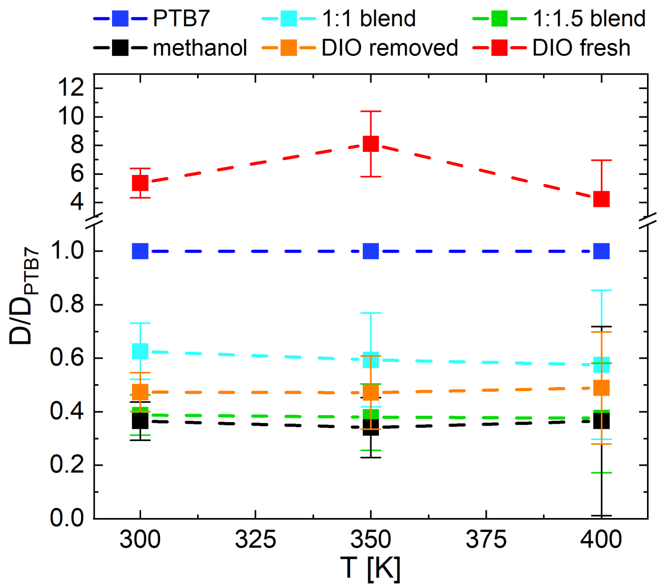

Figure 4.15:
Relative diffusion coefficients of all measured samples. Values are normalized to the diffusion coefficient of the pure PTB7 sample at the respective temperature

Figure 4.15 shows the calculated diffusion coefficients for all six samples. For better clarity, all values are normalized by the diffusion coefficient of the pure PTB7 sample (blue) at the respective temperature. It is obvious that the addition of PCBM significantly decreases the diffusion coefficient of the blend, compared to pure PTB7. A 1:1 ratio (cyan) ranges around values of 60 %, whereas values for the 1:1.5 blend (green) already dropped to 45 to 50 %. There is no significant difference in the diffusion coefficients of the methanol (black) and the 1:1.5 (green) sample evident, which implies that the performance enhancing effect of the methanol treatment is solely caused by structural aspects and not by dynamical. For the addition of DIO, a different picture appears: While the aged sample (orange) that has completely dried at 400 K in vacuum yields only slightly increased values compared to 1:1.5 (green), the fresh DIO sample (red), which was dried with the usual protocol, as used for all other samples, shows extremely high values, increased by a factor of more than 10.

Since it is unusual to get that large discrepancies for two samples, which were expected to behave essetially identical, we also studied the development of a fresh sample at a temperature of 400 K in vacuum conditions. Figure 4.16 shows the development of the diffusion coefficient from a very fresh towards an aged sample over the course of 12 hours.

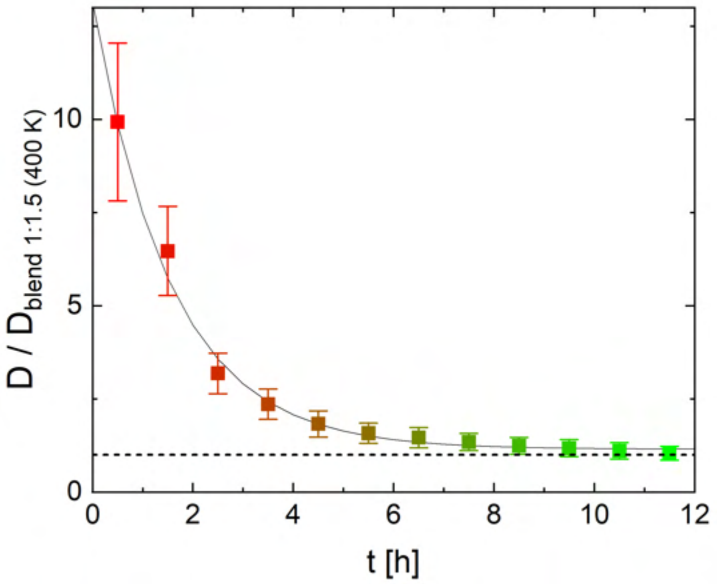

Figure 4.16:
Evolution of the calculated diffusion coefficient of a fresh DIO sample over 12 hours. Values are normalized by the diffusion coefficient of PTB7 at 400 K (dashed line). Each data point represents a one hour measurement and thus a mean value. The solid black line corresponds to a fitted simple exponential decay-function.

It is obvious from Figure 4.16 that the diffusion coefficient of the DIO sample decays exponentially over time and converges towards the value for the simple 1:1.5 blend. After an analysis of scattering data, we came to the awareness that a considerable fraction of the scattering is caused by residual DIO in the film and not only by the film itself. It is not surprising that DIO has a much larger mobility than polymer side chains. A comparison of the decay functions of DIO content and diffusion coefficient shows, that the DIO content decreases faster, which leads to the conclusion that the presence of DIO in the film induces a higher mobility in the PTB7:PCBM bulk heterojunction structure. Even after the very mobile DIO left the film completely, the film is still subject to reorientations and thus the dynamics of polymer sidechains is increased.

[1] G. Dennler, M. C. Scharber, C. J. Brabec, *Adv. Mater.***21**, 1323 - 1338 (2009)

[2] J. Obrzut, K. A. Page, *Phys. Rev. B* **80**, 195211 (2009)

[3] S. Guo, B. Cao, W. Wang, J.-F. Moulin, P. Müller-Buschbaum, *ACS Appl. Interfaces* **7**, 4641 - 4649 (2015)

[4] S. Guo, E. Herzig, A. Naumann, G. Tainter, J. Perlich, P. Müller-Buschbaum, *J. Phys. Chem. B* **118**, 344 - 350 (2014)

4.8 Impact of different solvents on the morphology and optical absorption of slot-die coated polymer based organic solar cells

D. M. Steger, K. S. Wienhold, S. V. Roth[1,2] and P. Müller-Buschbaum

[1] DESY, Hamburg, Germany
[2] KTH, Stockholm, Sweden

Climate change and increasing need for clean energy is one of the main topics of todays society. Therefore efficient and diverse ways of harvesting renewable energy sources such as the sun are needed and are key objectives of many research projects. In contrast to the well developed silicon based devices, organic solar cells based on polymer - non-fullerene acceptor blends still are yet to be fully understood. Especially the impact of multiple processing parameters of the active material thin films on the morphology are one of the key factors to aim for high efficiency and, especially important for large scale production, reproducibility of organic solar cells.
In this work the impact on different solvents on the active layer morphology of organic solar cells, based on the polymer donor PBDB-T-SF and the non-fullerene acceptor IT-4F, which have shown efficiencies over 13 %[1], are being investigated. Chlorobenzene, chloroform, o-dichlorobenzene and toluene are the four solvents the active materials are dissolved in. Contrasting to most other studies, the active layers investigated during this work are produced via slot-die coating, whereas most other projects are using spin coating techniques.

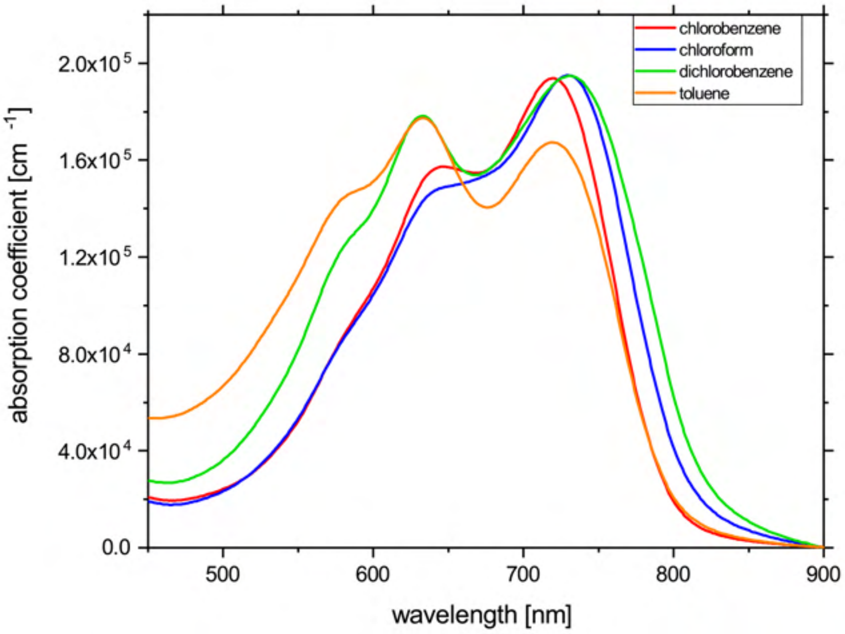

Figure 4.17: UV/VIS-spectroscopy data for printed thin films of PBDB-T-SF:IT-4F on glass substrates.

UV-VIS spectroscopy measurements of corresponding thin films for all four solvents are shown in Figure 4.17. Considering the polymer-related peaks of the absorption spectra at around 625 nm, differences in the peak heights between the solvents can be observed, which relates to differences in crystallinity: higher overall crystallinity has been shown to result in an increased absorption in other materials[2]. Therefore the dichlorobenzene sample seems to exhibit the highest crystallinity, followed by chlorobenzene and chloroform. For toluene a different ration of polymer and acceptor materials has to be assumed, according to a, in comparison, much lower acceptor peak height. To further investigate and affirm the correlation with the crystallinity, grazing-incidence wide-angle x-ray scattering measurements have been performed (P03 beamline, DESY), as they can resolve length scales in the sub nanometer regime and therefore give information about the crystallinity. From the GIWAXS patterns shown in Figure 4.18, one can observe a significantly higher crystallinity of the o-dichlorobenzene processed thin film, consolidating the assumption made from the UV/VIS-data. This also leads to higher-order peaks visible in the pattern. Furthermore the GIWAXS measurements allow for identification of the predominant crystal orientations present. A strongly pronounced (010) peak along the q_z-axis hereby indicates a higher amount of face-on orientation, whereas a strongly pronounced (100) peak along the q_z-axis suggests a predominant edge-on orientation. As the o-DCB processed sample shows a significantly stronger (010)-peak one can assume a more face-on oriented crystal structure, which is beneficial for solar cell applications, as it favours charge transport[3]. Oh the other hand toluene shows the by far strongest signal of the (100) peak related to edge on orientation, which is related to large polymer particles shown by optical microscopy, which originate from low solubility of PBDB-T-SF in toluene. Furthermore, when looking at the chloroform processed film, one can observer a much more homogeneous distribution of the signal over all angles. This indicates a much more isotropic crystallite distribution, which occurs due to the high vapor pressure and therefore fast evaporation of the solvent, as it leaves less time for the crystallites to orientate in a certain way. In contrast dichlorobenzene has a very low vapor pressure and therefore takes much longer to evaporate. In correlation with the fact that the dichlorobenzene processed shows the by far highest share of face-on oriented crystallites of all the samples, this can hint to face-on orientated crystallites mainly forming in late stages of the drying process. Yet the influence of other properties of the solvents has to be considered.

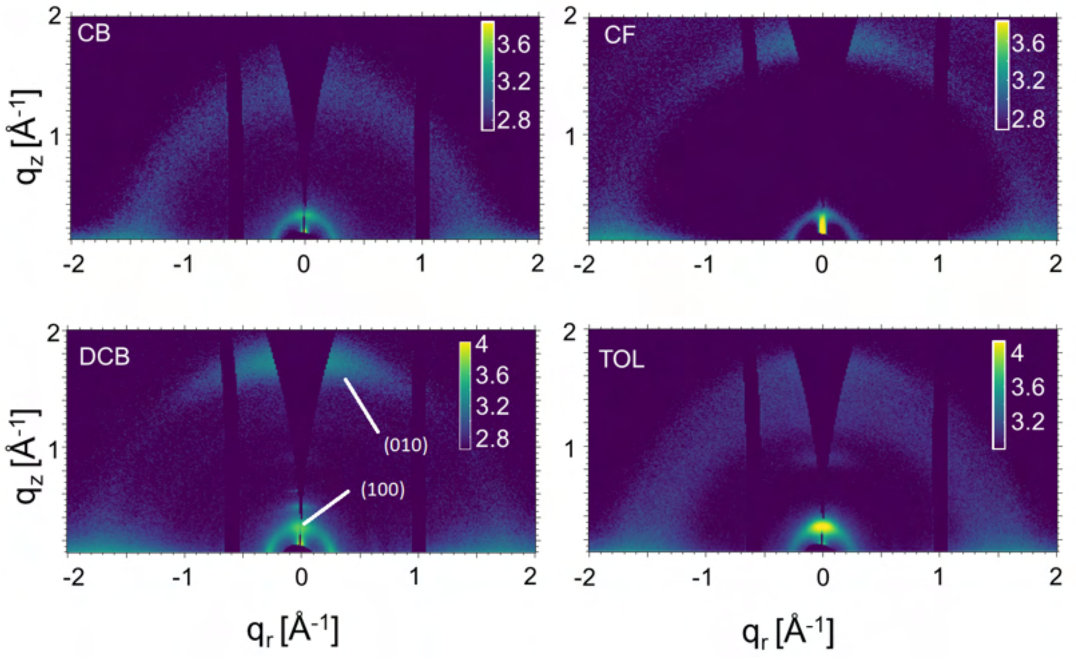

Figure 4.18: 2D-GIWAXS patterns of thin films printed from four different solvents.

[1] W. Zhao, S. Li, H. Yao, S. Zhang, Y. Zhang, B. Yang, J. Hou, *J. Am. Chem. Soc.* **139**, 7148 (2017)

[2] U. Zhokhavets, T. Erb, G. Gobsch, M. Al-Ibrahim, O. Ambacher, *Chem. Phys. Lett.* **418**, 347 (2006)

[3] R. Noriega, J. Rivnay, K. Vandewal, et al. *Nat. Mater.* **12**, 1038 (2013)

4.9 The effect of the CsBr-doping on the crystal orientation and optoelectronic properties of perovskite film

Y. Zou, P. Müller-Buschbaum

Metal halide perovskite-based solar cells have attracted broad attention and been regarded as excellent candidates as photo-electronic conversion materials due to their superior photoelectric properties including tunable bandgap, low exciton binding energy, and excellent ambipolar carrier transport property. In recent years, perovskite solar cells (PSCs) have gained remarkable achievements in the field of solar energy conversion and exhibited huge development prospective. However, PSCs also faced huge challenges by further improving their power conversion efficiencies (PCEs) and long-term operation stability. Perovskite film is polycrystalline, which contains higher trap-state density in its bulk and surface compared with the monocrystalline counterparts. This is attributed to the rapid crystallization undergo by the perovskite solution during the film formation. During this progress, various defects can generate unavoidably. These defects can cause the non-radiative recombination of a large number of photo-generate carriers. As a result, the final devices could suffer from the current-voltage (J-V) hysteresis and poor performance.

Various strategies have been applied to passivate defects and boost the device optoelectronic properties of PSCs. For instance, it was reported that applying CsBr/methanol to modify the surface of the active layer can passivate the bulk and surface defects simultaneously. The non-radiative recombination of charge carriers and the migration of charged defects are both suppressed effectively, resulting in a high PCE and improved long-term operational stability.[1]

Herein, we propose a simple method to improve the performance of PSCs. Different from the previous study, we introduce a small amount of CsBr into MAPbI3 perovskite precursor solution for mixed perovskite substrate through component engineering. The structures of bare and doped perovskite crystals are shown in Fig.4.19

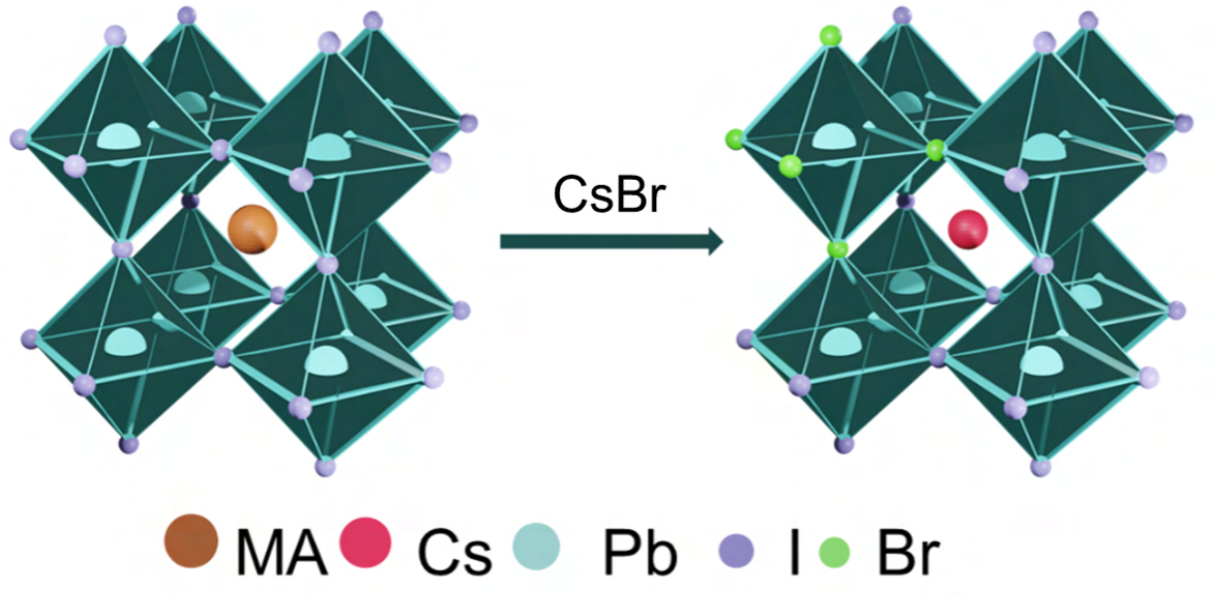

Figure 4.19:
The schematic diagram of the evolution of active layer components after doping CsBr in the perovskite crystal.

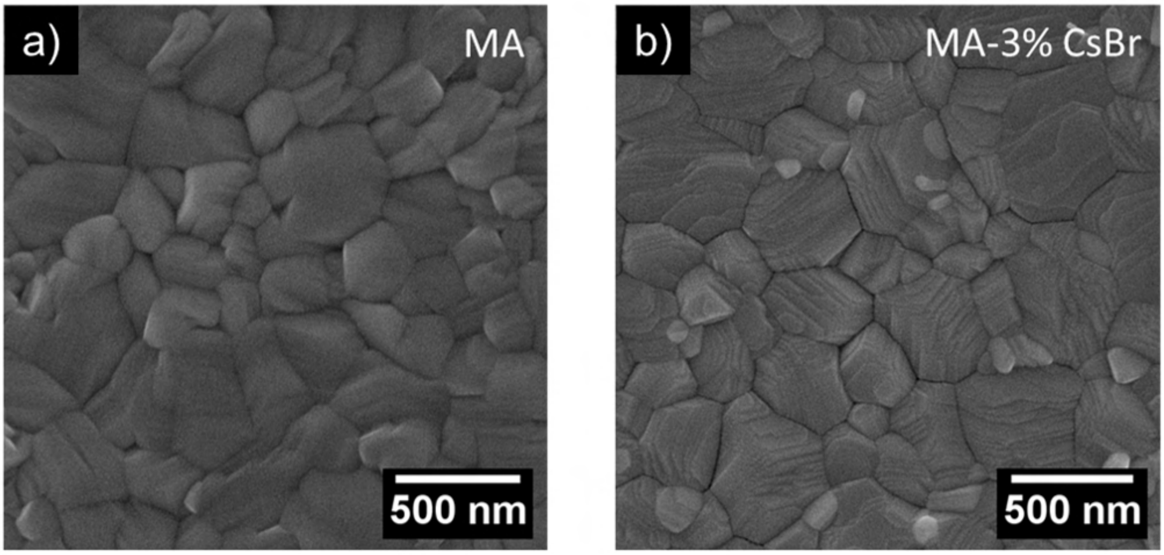

Figure 4.20: The SEM images of bare and CsBr doped perovskite films.

Additionally, the scanning electronic microscopy (SEM) was employed to study the effect of CsBr-doping on the morphology of perovskite film, as shown in Fig.4.20. The obvious differences between these two perovskite films can be observed in the SEM images. Compared to the bare film, the doped film exhibits more compact and has a larger crystal size of grains. Generally, the larger grains have fewer grain boundaries which usually act as the recombination centers of free charge carriers. Therefore, we can expect that CsBr-doping is beneficial to reduce the trap-state density and further improve the PCE of the final PSC device. Moreover, some textures can be found clearly in the CsBr-doping film. This indicates that such perovskite film is relatively stable. In conclusion, this component engineering strategy indicates that the CsBr-doping can effectively improve the quality of the perovskite film, leading to the enhanced performance of the final device.

[1] K. Liu, L. Xie, P. Song, K. Lin, L. Shen, Y. Liang, J. Lu, W. Feng, X. Guan, C. Yan, C. Tian, *Sol. RRL* **4**, 2000224 (2020)

[2] C. Fei, L. Guo, B. Li, *Nano Energy* **27**, 17-26 (2016)

5 Polymer-hybrid systems

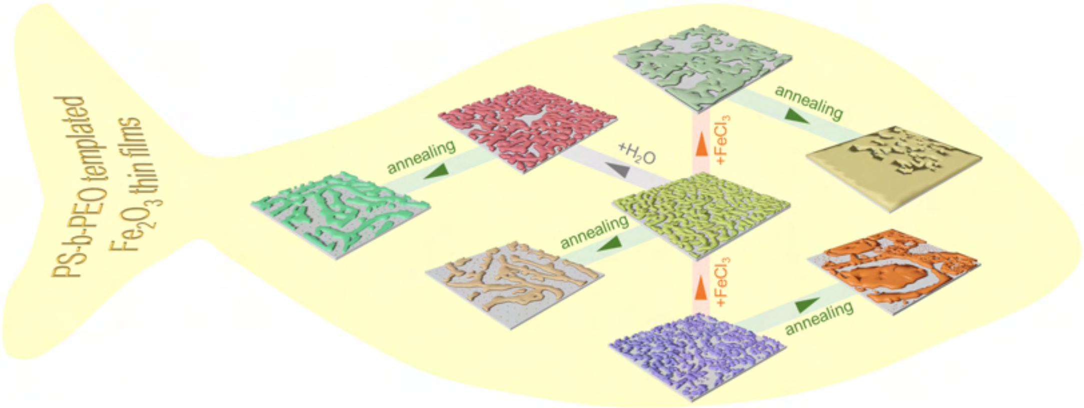

5.1 Synthesis of mesoporous silica thin films by amphiphilic block copolymer

I. Pivarnikova, P. Müller-Buschbaum

Silicon has been considered one of the most promising materials for lithium-ion battery anodes, especially, thanks to its low cost, non-toxicity and high theoretical gravimetric capacity (4200 mAh/g) [1]. However, Si suffers from high volume expansion during the lithiation and delithiation process, which leads to the degradation, poor cyclic stability and capacity loss of the Li-ion batteries and causes safety issues. Therefore, there is a high demand for designing structurally stable, mechanically flexible structures that can accommodate the volume changes and buffer mechanical stress. One of the strategies is the synthesis of porous Si-based materials that can exhibit the above-mentioned properties.

In particular, this work is focused on the synthesis of nanostructured porous Si and SiO_x thin films using wet chemical methods. Wet chemical synthesis of functional nanostructured thin films such as SnO_2, GeO_x have also previously been reported [2,3]. These thin films can be used, due to their wide applicability, as photovoltaic cells, gas sensors, membranes, optical devices and lithium-ion battery anodes.

The synthesis of highly ordered hybrid materials with porous structure involves the formation of inorganic-organic composites by a self-assembly mechanism, where the organic phase serves as a template for the inorganic structure. By adjusting the synthesis conditions (choice of the template/surfactant or the concentration of the reaction compounds (e.g. precursor, catalyst), deposition technique etc.), different structures (lamellar, 2D hexagonal, 3D hexagonal, cubic) and pore sizes (macropores, mesopores) can be obtained. The use of block copolymers as the structuring agents is one of the most promising choices, thanks to their high degree of order, low cost and low toxicity. Thin films are usually prepared by liquid deposition methods such as spin coating, dip coating or drop-casting. These techniques enable gradual evaporation-induced self-assembly (EISA) process. Solvent evaporation induces the micelle formation, assembly with inorganic precursor and polycondensation of the silica network.

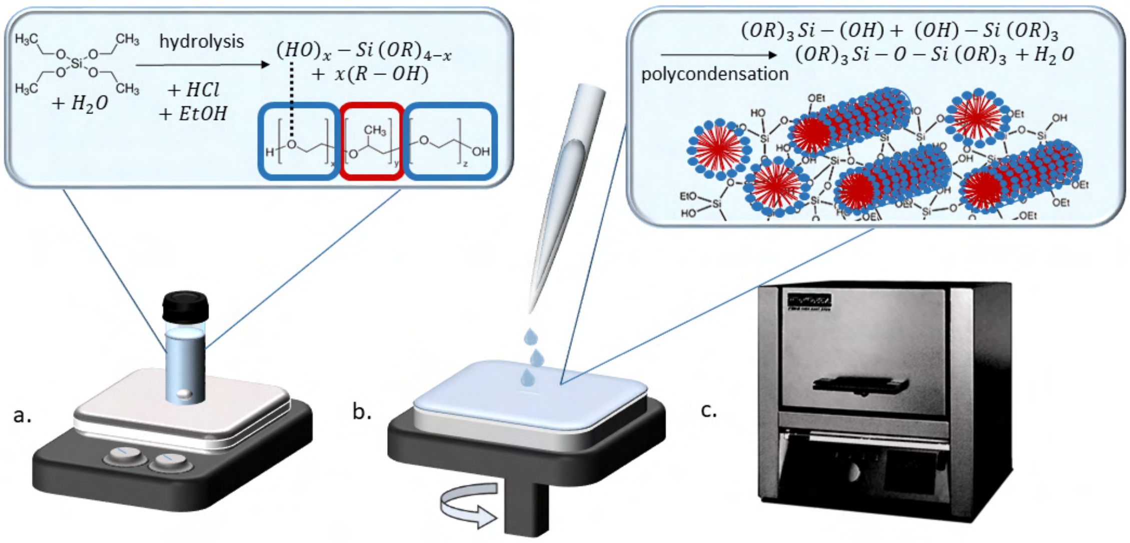

Figure 5.1:
Schematic view of the preparation process of silica thin films: a) solution preparation, b) spin coating, c) heat treatment – polymer template removal. Detailed views show the mechanism of the sol-gel reaction and film formation mechanism.

The objective of this work is the copolymer assisted sol-gel synthesis of mesoporous silica structures [4,5]. Initial solutions are prepared using tetraethoxysilane (TEOS) as the silica precursor and the poly(ethylene glycol)-block-poly(propylene glycol)-block-poly(ethylene glycol (PEG-b-PPG-b-PEG) non-ionic block copolymer as a template, in the presence of ethanol, H_2O and under acidic conditions (HCl). The sols can be spin spin-coated on the cleaned thin copper, glass or silicon wafers in order to study different properties of thin films. Template removal is done by the thermal treatment (calcination) at 400 °C for 4 hours with the heating rate 1 °C/min. Afterwards, the porous structured transparent thin film is obtained. The schematic representation of the preparation process is shown in Fig. 5.1. The scanning electron microscopy (SEM) pictures of the thin film coated onto Cu substrate are shown in Fig. 5.2.

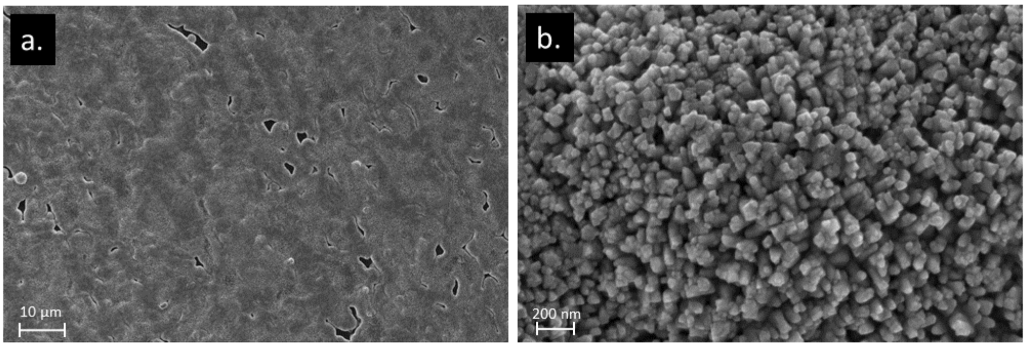

Figure 5.2:
Scanning electron microscopy images of silica thin film spin coated onto Cu substrate a) surface morphology view (low-magnification) and b) detailed surface morphology view (high-magnification).

The mechanism of this process has previously been described as follows [6]: Firstly, the metal alkoxide (in this case TEOS) is hydrolyzed in the solution. During hydrolysis, the residual silanol groups of the ceramic precursor interact through hydrogen bonding with hydroxyl groups (hydrophilic part) of the polymer. After the deposition onto a substrate, when solvent evaporation occurs, block copolymers where in this case, PEG is the hydrophilic and PPG the hydrophobic part, form several self-assembled structures (spherical or cylindrical micelles etc.). Parallel to that, polycondensation reaction of the silica network is occurring until the full rigid silica network is formed.

In the future, the work will focus on the optimization of the preparation process in order to reach desired film properties and microstructure suitable for Li-ion battery anode application. The usage of new solvent, precursor and deposition methods will be introduced.

[1] X. X. Zuo, J. Zhu, P. Müller-Buschbaum, Y. J. Cheng, *Nano Energy* **31**, 113-143 (2017)

[2] S. Yin, T. Tian, K. S. Wienhold, C. L. Weindl, R. Guo, M. Schwartzkopf, S. V. Roth, P. Müller-Buschbaum, *Adv Mater Interfaces* **7** (18), 2001002 (2020)

[3] N. Hohn, X. Wang, M. A. Giebel, S. Yin, D. Müller, A. E. Hetzenecker, L. Bießmann, L. P. Kreuzer, G. E. Möhl, H. Yu, J. G. C. Veinot, T. F. Fässler, Y. J Cheng, P. Müller-Buschbaum, *Acs Appl Mater Inter* **12** (41), 47002-47009 (2020)

[4] H. Zou, S. Wu, J. Shen, *Chem. Rev.* **108** (9), 3893-3957 (2008)

[5] S. P. Naik, S. Yamakita, M. Ogura, T. Okubo, *Microporous and Mesoporous Materials* **75** (1-2), 51-59 (2004)

[6] D. Grosso, A. R. Balkenende, P. A. Albouy, A. Ayral, H. Amenitsch, F. Babonneau, *Chem. Mater.* **13** (5), 1848-1856 (2001)

5.2 The morphology of printed and spray deposited hybrid active layers investigated with TOF-GISANS

V. Körstgens, L. Diaz Piola, C. Geiger, J. Heger, L. Kreuzer, T. Widmann, M. Nuber[1], K. Stallhofer[1], H. Iglev[1], R. Kienberger[1], G. Mangiapia[2], P. Müller-Buschbaum

[1] LS Laser- und Röntgenphysik, TUM, Garching, Germany
[2] GEMS at MLZ, Garching, Germany

In the broad field of emerging alternative photovoltaics we follow the concept of water-processed hybrid solar cells. The use of harmful or toxic materials is avoided in the production of devices. The fabrication process is also very efficient in terms of energy demand and costs. These solar cells consist, on the one hand, of a water-soluble polythiophene which acts as a donor in the active layer. On the other hand TiO_2-nanoparticles are used, which serves as an electron acceptor in the cell. Thus advantages of both organic and inorganic materials are combined. The organic material provides high absorption and flexibility, while the inorganic part provides good conductivity and stability [1]. From the processing perspective, continuous ongoing research is devoted to combine roll-to-roll (R2R) compatible deposition techniques for solution-processed photovoltaics, which allows for fast fabrication of thin films that can be produced at large scales and at a low cost. Therefore, here two different R2R-compatible deposition methods are used: spray and slot die coating [2, 3]. To study the morphology of the active layers produced over large sample areas, Time-of-Flight Grazing Incidence Small Angle Neutron Scattering (TOFGISANS) is used at the Refsans instrument of MLZ, Garching. The scattering technique allows to obtain statistically relevant information on surfaces and buried structures of thin films. The Time-of-Flight mode, additional to the well-established GISANS technique, allows to obtain scattering patterns at different wavelength bands in one single experiment. Several studies have demonstrated this technique to be a powerful tool to study nanostructured systems for energy applications [2, 4].

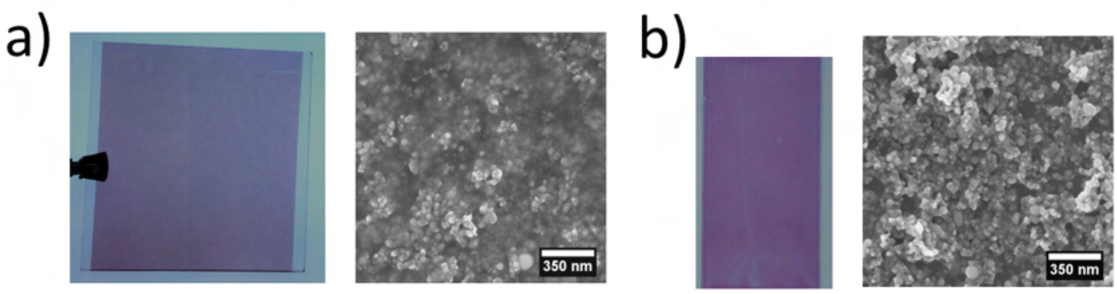

Figure 5.3:
Active layers for hybrid solar cells of laser-ablated titania dispersed in a polymer matrix. Photographs for films of a few square centimeter and corresponding SEM images for a) spray deposited and b) slot-die printed samples, respectively.

With both depostition techniques, spray deposition and slot-die printing, homogeneous layers can be obtained in the size of several square centimeter as given in Fig. 5.3. The corresponding SEM images reveal the distribution of TiO_2-nanoparticles at the surface of the fims. In order to obtain information about the film structure in the direction perpendicular to the substrate, in-plane cuts at $q_y = 0$ are performed for selected wavelengths, shown in Fig. 5.4. Between the sample horizon and the specular peak, the Yoneda peak shifting towards the specular peak for increasing wavelength appears, and it is highlighted in a blue region. From these wavelengths

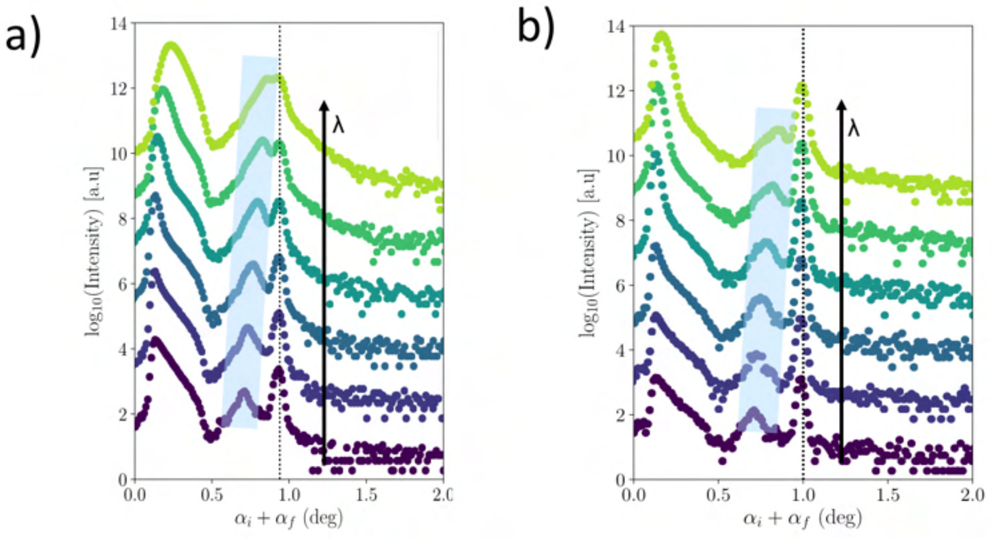

Figure 5.4:
Vertical cuts around q_y = 0 for selected wavelengths λ for (a) sprayed sample and (b) slot-die-coated sample.

the critical angle and consequently the scattering length density (SLD) of the material can be extracted. The Yoneda peaks for the two different samples are clearly
seen, making the determination of the material SLD straightforwardly possible from the data. To obtain its value Gaussian fits are performed around the Yoneda region (blue shaded in Fig. 5.4). Once the Yoneda peaks are determined consistently, the SLD of the material for the two deposition techniques can be obtained by plotting the critical angle against the wavelength of each TOFGISANS channel. This allows to compare the obtained SLD of the mixed material with the SLD coming from the polymer P3P6T and titania nanoparticles separately and therefore the mixing ratio can be determined. The experimentally determined SLD yields a volume ratio for the sprayed sample, which is in very good agreement with the initially as-prepared volume ratio. On the other hand, for the slot-die coated sample the experimental value differs significantly from the as-prepared solution value. This difference implies less content of titania nanoparticles within the polymer matrix. To obtain information about lateral structures inside the probed film, horizontal line cuts in q_y direction are performed. Two spherical form factors as scattering objects are used to fit the data, and their center-to-center distances are assumed to be distributed on a 1D paracrystal lattice. The sizes of the scattering objects with radii of (16 ± 1) nm and (54 ± 5) nm and their nearest neighbor distances (40 ± 6) nm and (220 ± 32) nm are obtained for the sprayed sample. Whereas for the slot-die coated sample the radii are (15 ± 2) nm and (52 ± 6) nm with the corresponding distances of (56 ± 9) nm and (350 ± 44) nm. The structural sizes obtained for the bulk films are in agreement with the surface morphology observed with SEM.

[1] V. Körstgens, S. Pröller, T. Buchmann, D. Mosegui Gonzalez, L. Song, Y. Yao, W. Wang, J. Werhahn, G. Santoro, S. V. Roth, H. Iglev, R. Kienberger, P. Müller-Buschbaum, *Nanoscale* **7**, 2900-2904 (2015)

[2] K. Wang, N. Hohn, L. Kreuzer, T. Widmann, M. Haese, J.-F. Moulin, P. Müller-Buschbaum, *ACS Appl. Mater. Interfaces* **11**, 10998-11005 (2019)

[3] K. S. Wienhold, V. Körstgens, S. Grott, X. Jiang, M. Schwartzkopf, S. V. Roth, P. Müller-Buschbaum, *ACS Appl. Mater. Interfaces* **11**, 42313-42321 (2019)

[4] R. S. Märkl, N. Hohn, E. Hupf, L. Bießmann, V. Körstgens, L. P. Kreuzer, G. Mangiapia, M. Pomm, A. Kriele, E. Rivard, P. Müller-Buschbaum, *IUCrJ* **7**, 268-27 (2020)

5.3 Morphology tunability of mesoporous ZnO thin films with slot-die coating technique

T. Tian, S. Yin, M. Schwartzkopf[1], S. V. Roth[1,2], P. Müller-Buschbaum

[1] DESY, Hamburg, Germany
[2] KTH, Stockholm, Sweden

ZnO has attracted tremendous attention for technological applications due to the ease of achieving a rich variety of different nanostructures with desired optical and electrical properties.[1] Regarding the fabrication ZnO nanostructures, existing synthesis routes mainly focus on chemical vapor deposition, hydrothermal synthesis, electrodeposition, sputter deposition, atomic layer deposition and so forth. Among the different synthesis routes, block copolymer assisted sol-gel technique has been corroborated to be a powerful tool for obtaining nanoscale ZnO materials with varied morphologies.[2] Considering the solution-processable nature, this method is perfectly suited to be integrated into industrial fabrication process and thus holds great promise for achieving large-scale production.[3] In this work, slot-die printing technique is introduced for the ZnO thin film deposition and the effect of the precursor content on both the surface and inner morphologies is investigated in more detail.

After removing the organic polymer template by subjecting composite films to a high temperature sintering process, varied ZnO morphologies have been obtained. As Fig. 5.5a) shown, morphological change caused by precursor content is clearly observable: with a weight ratio of the PS-b-PEO to ZAD of 3:3, the final mesoporous ZnO film shows a sponge-like feature with a highly interconnected network, which is especially promising for providing a good electron passway for multiple applications. With ZAD content increasing, the as-obtained inorganic ZnO films tend to be less mesoporous. When the weight ratio of the PS-b-PEO to ZAD reaches 3:12, the obtained ZnO film shows an almost poreless structure, which appears similar to the compact ZnO film prepared from pure ZAD ingredient. Fig. 5.5b) shows the corresponding inner morphologies probed by GISAXS, all samples show a semicircular scattering feature, however, distinct scattering pattens, especially the enhanced scattering signal along the q_y direction can be observed, indicating the pronounced structure difference existing within the entire film thickness. For obtaining the quantitative information, horizontal cuts along the corresponding material-specific Yoneda peak position are performed. Fig. 5.5c) plots the measured GISAXS data together with the fitting curves. Two characteristic structure and form factors are used for fitting the former two samples while three for latter two.

All the extracted structure parameters are summerized in Fig. 5.5d) and Fig. 5.5e), the small-sized and middle-sized structures show a decreasing trend for both domain size and center-to-center distance with an increasing ZAD to PS-b-PEO ratio, until the appearance of large-sized structure when the template-to-precursor ratio reaches to 3:12. Among that, the small structures originates from the small ZnO nanoparticles produced from the hydrolysis and condensation of the ZAD, the middle-sized structures are from the ZnO framework templated from PS-b-PEO, while the largest structures represent the crack caused by the mechanical stress in the high-temperature sintering process due to excessive ZAD content. These fitting results are in good accordance with the morphology observation in SEM images. Putting all these information together, it can be concluded that there is a trade-off between self-organizing inorganic particles and a self-assembling polymer matrix. With excess precursor in the solution for deposition, the limited self-assembled polymer scaffold cannot accommodate all ZnO nanoparticles, thus yeilding the formation of ZnO aggregate.

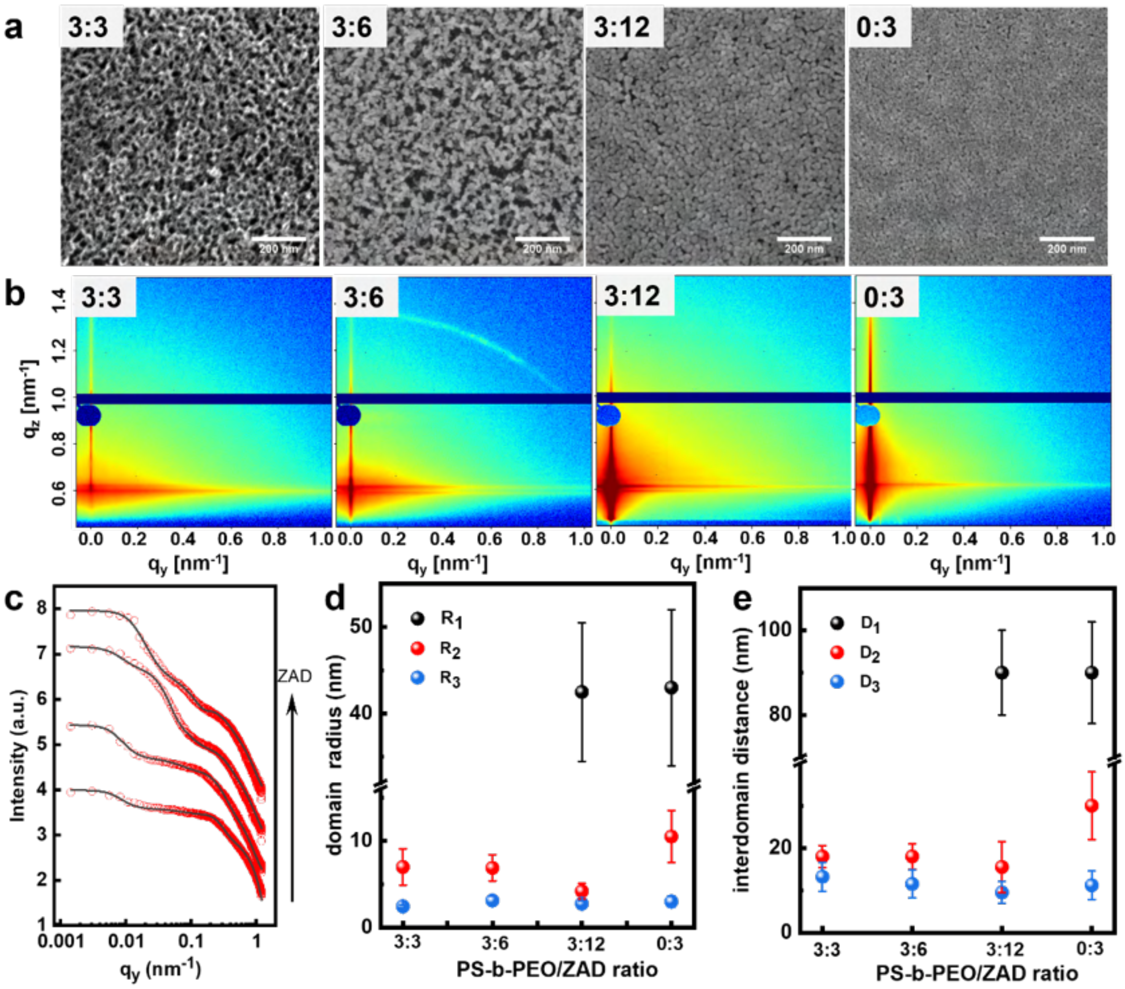

Figure 5.5:
a) SEM micrographs and b) 2D GISAXS patterns of printed mesoporous ZnO films with the varied precursor content after calcination of the PS-b-PEO template at 400°C in air. The upper left insets show the corresponding weight ratio between polymer template-to-precursor (ωPS-b-PEO: ωZAD). c) Horizontal line cuts of the 2D GISAXS data with the arrow pointing out the increasing ZAD content from bottom to top. The black lines denote the fits to the meassured data (open symbols). All curves are shifted along the intensity axis for clarify of the presentation. The extracted structure-related parameters: d) the domain size and e) the interdomain distance as a function of increasing ZAD content.

Although the final inorganic ZnO architectures are conceptually defined by the self-assembly of the polymer, the content of the precursor part should also be carefully controlled to achieve an elaborate replication of the elaborate microphase-separated nanostructure.

[1] L. Schmidt-Mende, J. Macmanus-Driscoll, *Mater. Today* **10**, 40-48 (2007)

[2] K. Sarkar, M. Rawolle, E. M. Herzig, W. J. Wang, A. Buffet, S. V. Roth, P. Müller-Buschbaum, *ChemSusChem* **10**, 664-671 (2009)

[3] F. C. Krebs, *Sol. Energ. Mat. Sol. Cells* **93**, 394-412 (2009)

5.4 Oxygen plasma effects during gold sputtering on polyzwitterionic thin films

A. Vagias[1], S. J. Schaper, J. E. Heger, Y. Zou, S. Yin, C. Geiger, M. Gensch, M. Schwartzkopf[2], A. Laschewsky[3,4], S. V. Roth[2,5], P. Müller-Buschbaum

[1] MLZ, TUM, Garching, Germany

[2] DESY, Hamburg, Germany

[3] Universität Potsdam, Potsdam-Golm, Germany

[4] Fraunhofer IAP, Potsdam-Golm, Germany

[5] KTH, Stockholm, Sweden

Polyzwitterionic films exhibit strong potential as antifouling agents, on account of their strong hydrophilicity [1]. Additionally, sulfobetaine-based polyzwitterions have recently been used as highly promising interlayers in organic solar cells between a gold cathode and the active layer [2]. The presence of permanent charges in their macromolecular structure exhibits a permanent dipole. This dipole allows to reduce the work function of the overlaying electrode, thus facilitating charge transport between active layer and cathode. High power conversion efficiency (PCE) values close to 9% have been reported in solar cells with polysulfobetaine interlayers [2]. Meanwhile, solar cells performance can be dampened by prolonged exposure to sunlight [3]. Post-treatment with oxygen plasma was shown to increase the solar cell fill factor and avoid degradation side-effects. However, the lateral and vertical morphology of polysulfobetaine-metal hybrid functional layers with and without plasma etching remains unexplored.

Metal sputtering under vacuum is an industrially relevant process that allows stringent morphological control in the fabrication of hybrid metal-polymer nanocomposites [4]. Oxygen plasma can affect morphological features, such as metal cluster size, cluster distance and surface coverage, thus could potentially impair their forthcoming application as interlayers. It is intriguing to investigate how the presence (or not) of charges as well as sulphur-containing functional groups will affect metal cluster growth kinetics and metal cluster morphology.

We spin-coated polysulfobetaine methacrylate (SPE) homopolymer thin films with M_w= 272 kg/mol from trifluoroethanol (TFE) solutions at $c_{polymer}$ = 25 mg/mL onto silicon wafers at 1500 rpm for 15 min, followed by 15 min annealing under TFE vapor. Using an irradiation energy of 11.9 keV with an incident angle $\alpha_i = 0.5°$, we performed in-situ microfocus μGISAXS experiments during sputtering from a gold target at P03/MiNaXS beamline (PETRA III, DESY), inside a radiofrequency sputter chamber (DESY, Hamburg) at a sample-detector distance = 2.633 m. We obtained horizontal intensity $I(q_y)$ cuts, at the q_z Yoneda reflection position for the SPE polymer, to assess in-plane correlations of gold clusters, e.g. center-to-center spacing of nearest neighbor clusters. Moreover, we fitted the vertical $I(q_z)$ cuts (at q_y = 0 nm^{-1}) and inspected the evolution of the modulation fringe spacing over time. The actual metal layer thickness during sputtering could be assessed, reaching finally a $\sim$15 nm thick gold layer.

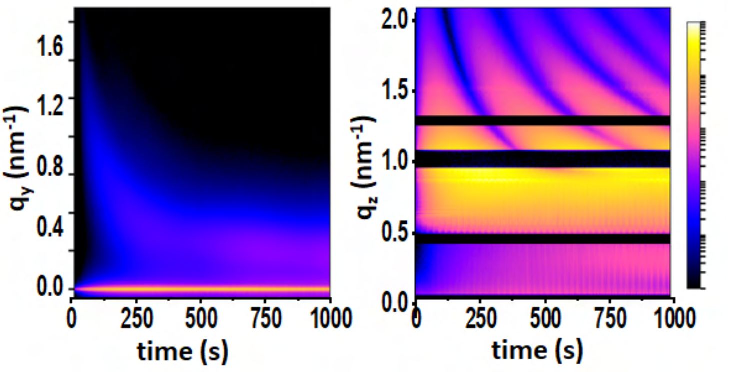

Figure 5.6: Two-dimensional (2D) color maps from (left) horizontal (q_y, nm^{-1}) and (right) vertical (q_z, nm^{-1}) intensity cuts vs. time, in s, on thin ($\sim$ 60 nm) SPE$_{272k}$ polymer films. The color bar denotes the intensity scale range spanning from 10^0 to 1×10^5.

Fig.5.6 depicts 2D color maps of $I(q_y)$ and $I(q_z)$ cuts vs. time which follow the evolution of gold clusters along and across the film's plane on thin ($\sim$ 60 nm) SPE homopolymer films.
We also calculated the effective final thickness, δ_{final}, being equal to the product of (constant) sputter rate with sputter time. The maximum peak positions obtained from modelling the experimental cuts with monodisperse structure factors represent the center-to-center distances d_y^* between nearest neighboring clusters. These values exhibit distinct differences depending on the plasma treatment, over a broad δ range. Modelling of gold cluster growth on classical polymers such as polystyrene was successfully described by a hexagonal arrangement of hemispherical gold clusters [4]. Assuming this model works in our SPE homopolymer films as well, we calculated the evolution vs. δ of the cluster radius $R_{cluster}$ and the ratio $2R_{cluster}/d^*_{y,cluster}$. The results are drawn in Fig.5.7.

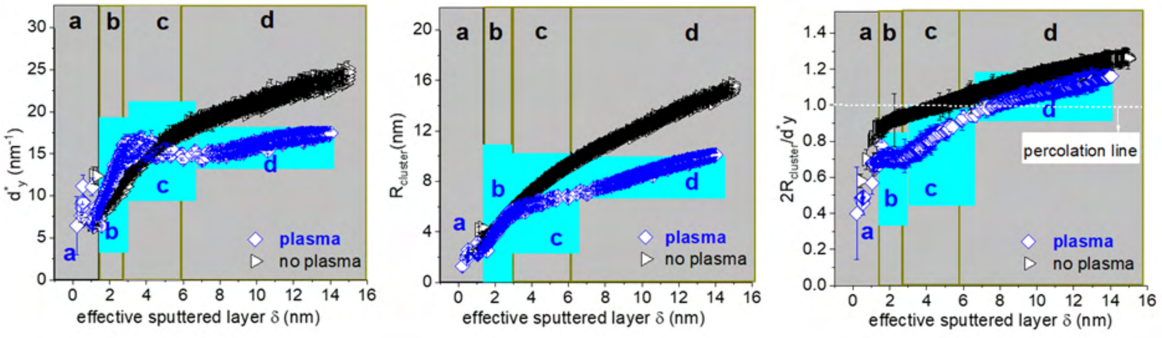

Figure 5.7:
Dependence on effective sputtered gold thickness δ of $d^*_{y,cluster}$ (left), $R_{cluster}$ (middle) and 2 $\times R_{cluster}$/ $d^*_{y,cluster}$ (right) on thin ($\sim$ 60 nm) SPE_{272k} homopolymer films. Tentative growth zones (a)-(d) per color-matching dataset are separated by vertical lines.

The difference growth phases represent [4] adsorption of gold adatoms from the metal target and nuclei formation (regime a), fusion of nuclei into clusters and diffusion-limited cluster growth (regime b); adsorption-limited growth (regime c); percolation (regime d). Only in the first phase (a), differences in cluster growth are hard to be distinguished. With increasing δ values, the growth trends do not superimpose anymore. The results vs. δ in the different zones show strong oxygen plasma effects on the developed gold cluster morphologies on top of the SPE_{272k} sample surface. Between (1 nm $< \delta <$ 3 nm), gold nuclei diffuse along the film surface and coalesce into larger clusters with different trends.
The diverse trends also propagate in the adsorption controlled zone (c) as well as after the systems reach percolation in zone (d). In conformity to earlier studies on gold cluster growth onto polystyrene, the gold percolation threshold is achieved for either examined film at $\sim$ 6 nm [4], providing support towards generality of the percolation threshold for gold growth on polymeric thin films. In summary, we identified distinct gold cluster growth kinetics upon oxygen plasma treatment of thin polyzwitterionic homopolymer films. Our results suggest interplay between polyzwitterion macromolecular structure and surface free energy.

[1] A. Laschewsky, A. Rosenhahn, *Langmuir* **35**, 1056-1071 (2019)

[2] Z. A. Page, Y. Liu, V. V. Duzhko, P. Thomas, T. Emrick, T. P. Russell, T. Emrick, *Science* **346**, 441-444 (2014)

[3] W. Xu, R. Xia, T. Ye, L. Zhao,Z. Kan, Y. Mei, C. Yan, X. W. Zhang, W. Y. Lai, P. E. Keivanidis, W. Huang, *Adv. Sci.* **3**, 1500245 (2016)

[4] M. Schwartzkopf, A. Hinz, O. Polonskyi, T. Strunskus, F. C. Löhrer, V. Körstgens, P. Müller-Buschbaum, F. Faupel, S. V. Roth, *ACS Appl. Mater. Interfaces* **9**, 5629-5637 (2017)

5.5 Silicon-Germanium nano-structure synthesis guided by amphiphilic diblock copolymer templating

C.L. Weindl, C. Fajman[1], T.F. Fässler[1], P. Müller-Buschbaum

[1] Chemie Department, TUM, Garching, Germany

Latest research has revealed promising results for Silicon (Si) and Germanium (Ge) as anode materials for lithium-ion batteries (LIBs). [1] Owing to their high energy capacity these two group XIV semiconductors are considered as auspicious alternatives to graphite anodes in LIBs. Si in particular is a potential anode material due to environmentally friendly production, resource abundance and low cost and its outstanding high theoretical capacity 4200 mAh/g (roughly ten times larger than graphite). [1] Although Ge is relatively expensive and less abundant, it is very interesting as anode material due to higher conductivity and thus improved Li+ diffusivity. [2] As a consequence SiGe-alloys as anode coatings for LIBs move more into focus.

There are several different approaches to template inorganic semiconductor thin-films such as lithography, molecular beam epitaxy or chemical vapor deposition. However, these technologies have the significant disadvantages that the processes are comparatively expensive and time-consuming. Our concept is to synthesize porous SiGe thin-films chemically via an amphiphilic diblock copolymer template as already well investigated with TiO_2. [3] For this sol-gel approach, the blockcopolymer polystyrene-b-polyethylene oxide (PS-b-PEO) is used with as a structure agent. Owing to the nature of amphiphilic diblocks a structure control can be achieved by using certain ratios of a bad and a good solvent, as ethylenediamine (en) and toluene respectively (see Figure 5.8). With a solubility parameter close to PEO and PS, toluene dissolves both blocks quite well, whereas en being hardly able to dissolve any of the two blocks properly.

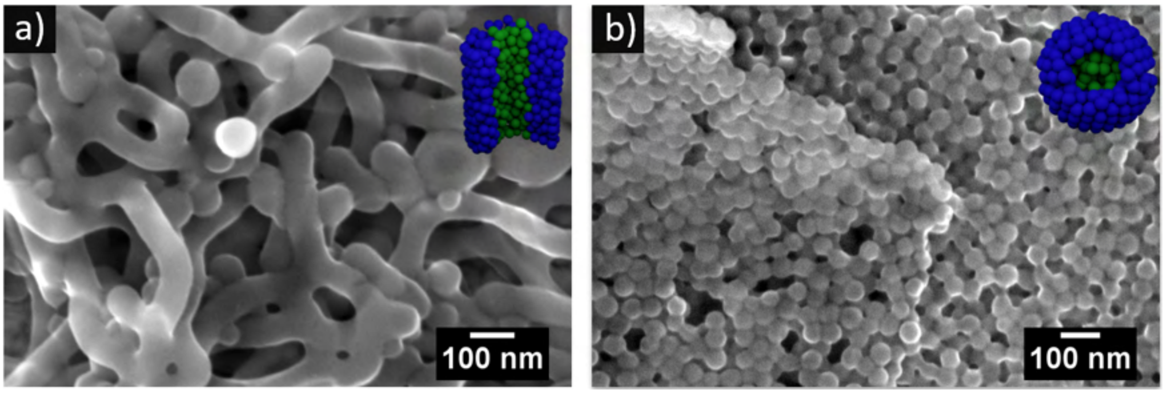

Figure 5.8:
Scanning electron microscopy (SEM) images of PS-b-PEO thin films with a worm-like (a)) and a spherical microphase separation (b)) with corresponding sketches of the inner structures with PS (green) and the PEO (blue).

For decreased toluene content in the toluene/en mixture a worm-like structure can be observed (see Figure 5.8 a)). By increasing the toluene content, the polymer gets more dissolved and forms micellar structures. Both setups have different specifications such as pore size, surface-to-volume ratio or backfilling-ability.

Contrary to former projects, where only Ge was templated with diblock copolymers, a Si and Ge Zintl phases is used in this study. [4] These clusters are polyanionic cages formed in intermetallic compounds between alkali or alkaline earth metals and p-block (semimetals). [5] In this study the non-oxide source of the two semiconductors is the precursor $K_{12}Si_{17-x}Ge_x$.

Here the toluene/en/polymer mixture is blended with the Zintl-phase dissolved in en solution. With this concept different SiGe ratios can be achieved by varying the content of Si in the synthesised precursor itself. The master-solution is then spin cast on pre-cleaned silicon substrates and then calcined at 600 °C. By varying the toluene/en ratio different morphologies are achieved (see Figure 5.9 a) and b)).

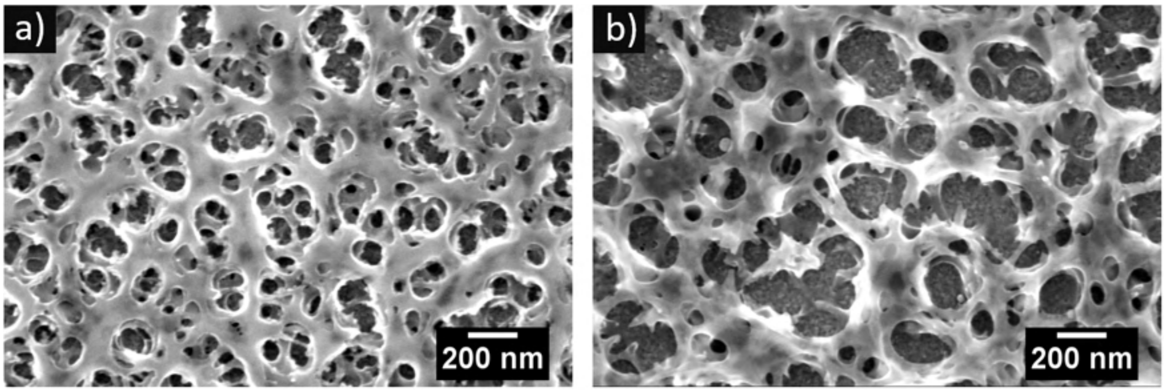

Figure 5.9: SEM images of SiGe thin-films with increasing toluene content from a) to b).

In Figure 5.9 different ratios of toluene/en are used for the thin-film synthesis. Higher amounts of toluene result in larger pore sizes and increased reduced wall thickness (see Figure 5.9b)). This tendency seems to be opposite to the pure polymer films in Figure 5.8. However, the calcination process plays the decisive role here and has to be further analyzed. At this point in time, we are not yet able to make any statements about the dynamics in the thin-film during the calcination process, which will have a major effect on the resulting structures. Latest experiments also revealed oxygen residues in the thin-film, which will have a huge impact on the optoelectronic properties. Additional treatments such as surface passivation and functionalization thus become unavoidable. In order to analyze the surface and inner structures with even higher resolution, reciprocal space analysis methods as grazing-incidence X-Ray scattering are required. [6] With this setup both surface and inner morphology can be resolved from Å to several hundreds of nm non-destructively by using a wide-angle or a small-angle mode. As a result, this well established method allows access to crystal data such as orientation and lattice parameters as well as pore size and shape of the internal structures.

[1] X. Zuo, Y. Wen, Y. Qiu, Y. Cheng, S. Yin, Q. Ji, Z. You, J. Zhu, P. Müller-Buschbaum, L. Ma, P. G. Bruce, Y. Xia, *ACS Appl. Mater. Interfaces* **39**, 43785–43797 (2020)

[2] Y. Yang, S. Liu, X. Bian, J. Feng, Y. An, C. Yuan, *ACS nano* **3**, 2900–2908, (2018)

[3] N. Hohn, S. J. Schlosser, L. Bießmann, S. Grott; S. Xia, K. Wang, M. Schwartzkopf, S. V. Roth., P. Müller-Buschbaum, *Nanoscale* **11**, 5325-5334 (2018)

[4] N. Hohn, A. E. Hetzenecker, M. A. Giebel, S. Geier, L. Bießmann, V. Körstgens, N. Saxena, J. Schlipf, W. Ohm, P. S. Deimel, F. Allegretti, J. V. Barth, S. V. Roth, T. F. Fässler, P. Müller-Buschbaum, *Macromolecules* **4**, 2048–2055 (2019)

[5] M. M. Bentlohner, M. Waibel, P. Zeller, K. Sarkar, P. Müller-Buschbaum, D. Fattakhova-Rohlfing, T. F. Fässler, *Angew. Chem.* **7**, 2487–2491 (2016)

[6] P. Müller-Buschbaum, *A Basic Introduction to Grazing Incidence Small-Angle X-Ray Scattering* in M. Gomez, A. Nogales, M. Garcia-Gutierrez, T. Ezzquerra, *Applications of Synchrotron Light to Scattering and Diffraction in Materials and Life Sciences*, *Springer*, **vol 776.**, (2009)

5.6 Morphology control of PS-b-P$_4$VP templated monolayer mesoporous Fe$_2$O$_3$ thin films

S. Yin, W. Cao, M. Schwartzkopf[1], S. V. Roth[1,2], P. Müller-Buschbaum

[1] DESY, Hamburg, Germany

[2] KTH, Stockholm, Sweden

Mesoporous Fe$_2$O$_3$ thin films with large area homogeneity demonstrate tremendous application potential in the photovoltaic industry, lithium-ion batteries, gas sensors.[1-2] In the present work, the synthesis of morphology-controlled Fe$_2$O$_3$ thin films is realized with the polystyrene-block-poly(4-vinyl pyridine) (PS-b-P$_4$VP) diblock copolymer assisted sol-gel chemistry. The effect of the solvent category and polymer-to-FeCl$_3$ ratio on the film morphology are systematically investigated during the sol-gel synthesis process. Spin coating is used for the thin film deposition and a calcination process in the air condition is used for removing the PS-b-P$_4$VP polymer template.

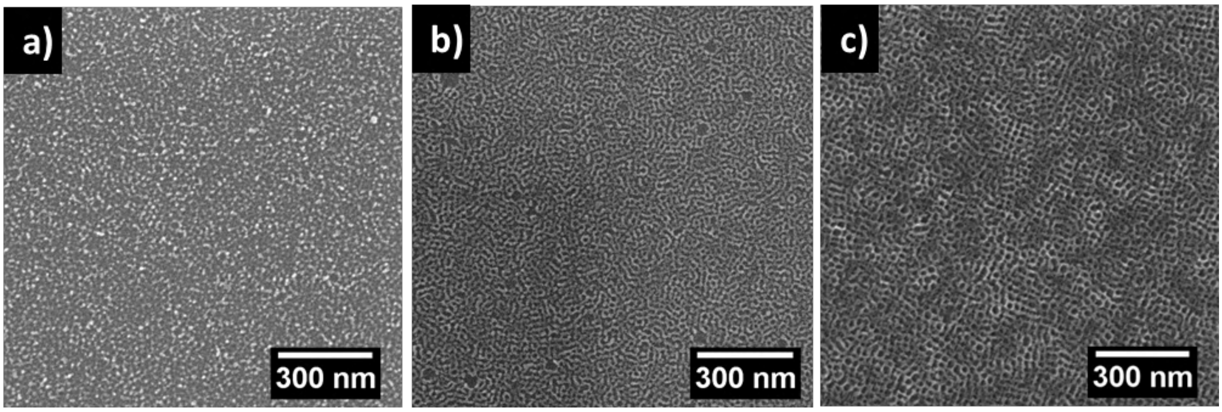

Figure 5.10:
SEM images of the Fe$_2$O$_3$ thin films prepared by DMF solvent. The corresponding PS-b-P$_4$VP to FeCl$_3$ ratios in Fig.5.10a, b and c are 1:2, 1:1 and 2:1, respectively.

Fig.5.10 shows the SEM images of the Fe$_2$O$_3$ thin films prepared with DMF solvent. The corresponding PS-b-P$_4$VP to FeCl$_3$ ratios used for the thin film preparation are 1:2, 1:1, and 2:1 from Fig.5.10 a to Fig.5.10 c, respectively. We can observe that the thin film prepared with PS-b-P$_4$VP to FeCl$_3$ ratio of 1:2 is mainly composed of small nanoclusters (Fig.5.10a). When increasing the PS-b-P$_4$VP to FeCl$_3$ ratio to 1:1, a nanopattern consist of spherical pore structures is formed.
The pore structures formed within the thin film are directly associated with the template effect of the micellar structures in the solution. Due to the preferential affinity of the DMF solvent to the P$_4$VP chains, spherical micelles consisting of PS cores and P$_4$VP/Fe^{3+} coronas are prone to be formed no matter in DMF solution or the final dry film. The structural transition from the nanoclusters to the patterned nanostructures can be related to the micellization of the PS-b-P$_4$VP template at the critical concentration, which is proportional to the concentration of the block copolymer. However, the formed micellar structures are liable to fusion at the early stage of the micellization due to the highly swollen condition of the core-forming chains by the solvent. This might account for the existence of the secondary large pore structures in Fig.5.10b. By further increasing the PS-b-P$_4$VP to FeCl$_3$ ratio to 2:1, a more uniform distribution of the pore structures and a slight increase of the pore size are observed within the thin film (Fig.5.10c). The influence of copolymer concentration on the micellar morphology can be ascribed to the increased number of polymer chains in an aggregate.[3]

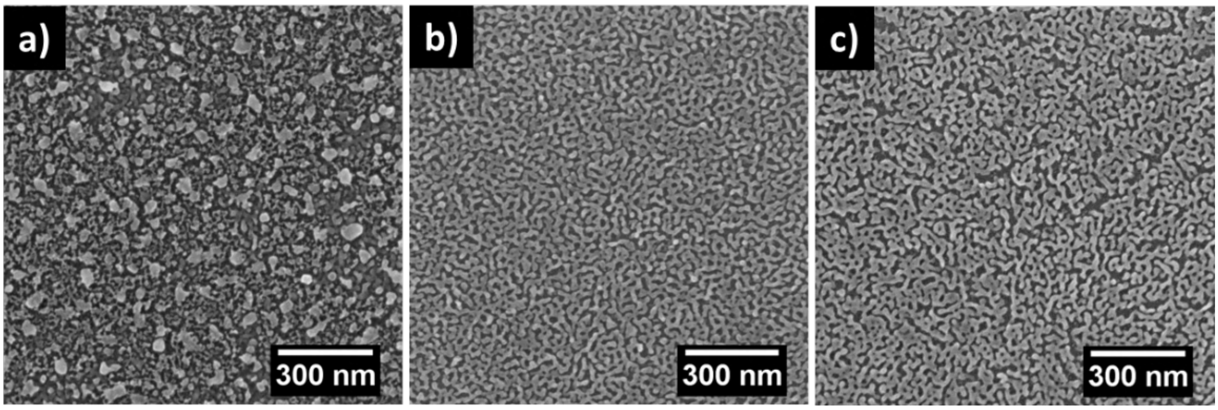

Figure 5.11:
SEM images of the Fe_2O_3 thin films prepared by 1,4-dioxane solvent. The corresponding PS-b-P_4VP to $FeCl_3$ ratios in Fig.5.11a, b and c are 1:2, 1:1 and 2:1, respectively.

Fig.5.11 refer to the SEM images of the Fe_2O_3 thin films prepared with 1,4-dioxane solvent. Compared to the DMF counterpart, completely different morphologies are observed in the 1,4-dioxane system. When the PS-b-P_4VP to $FeCl_3$ ratio is 1:2, discrete nanoclusters accompanied with large aggregates are observed. By increasing the PS-b-P_4VP to $FeCl_3$ ratio to 1:1 and 2:1, uniformly distributed wormlike structures with enhanced ordering are acquired. In addition, the inter-domain distance of the wormlike structure decreases by increasing the PS-b-P_4VP to $FeCl_3$ ratio from 1:1 to 2:1, which is against the trend shown in the DMF solvent system. The decreased inter-domain distance induced by the increase of the PS-b-P_4VP to $FeCl_3$ ratio can be assigned to the unique shape of the micellar structure. It is observed that the thin films prepared with PS-b-P_4VP to $FeCl_3$ ratio of 1:1 and 2:1 are mainly composed of interconnected wormlike structures (Fig.5.11a), which is prone to deform into more elongated form for accommodating more polymer chains and maintaining low surface energy in the monolayer geometry.

The drastic morphology variation of the thin films with respect to the solvent category can be attributed to the preferential affinity of the solvent to the polymer blocks. DMF is a selective solvent to the P_4VP block whereas 1,4-dioxane exhibit very weak selectivity to the PS and P_4VP blocks. The strong selectivity of the DMF solvent significantly inhibits the stretching of the PS blocks and thus promotes the formation of spherical PS micelles. In contrast, the weak selectivity of the 1,4-dioxane solvent to the PS and P_4VP blocks leads to the enhanced stretching of the PS blocks. Thus the fusion probability of the $FeCl_3$ species increases and symmetrical wormlike micelle geometry is prone to be formed. Accordingly, large aggregates in Fig.5.11a and the wormlike structures in Fig.5.11b and Fig.5.11c are observed.

[1] K. Fan, J. Guo, L. Cha, Q. Chen, J. Ma, *J. Alloys Compd.* **698**, 336-340 (2017)

[2] Y. Jiang, D. Zhang, Y. Li, T. Yuan, N. Bahlawane, C. Liang, W. Sun, Y. Lu, M. Yan, *Nano energy* **4**, 23-30 (2014)

[3] Y. Mai, A. Eisenberg, *Chem. Soc. Rev.* **291-292**, 5969-5985 (2012)

6 Real-time characterizations

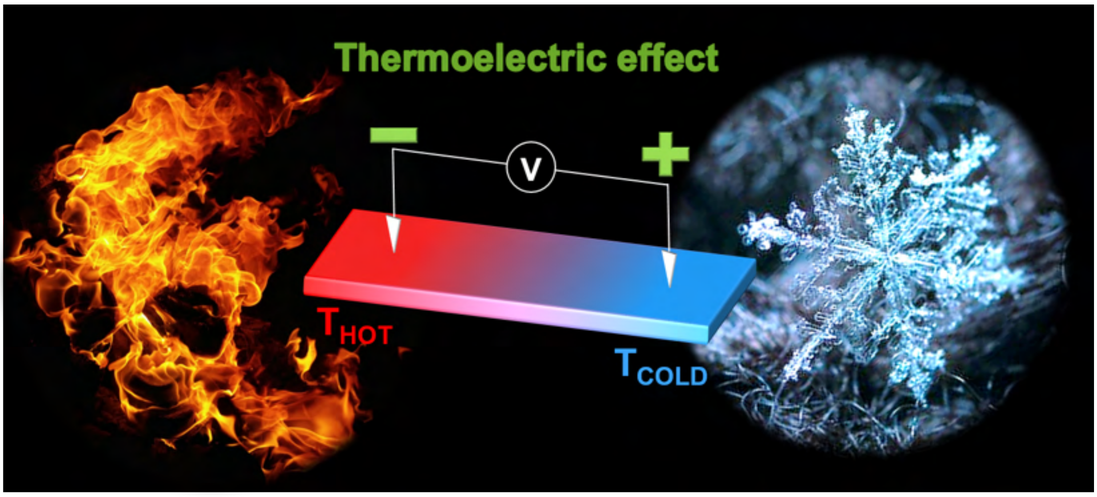

6.1 *In situ* study of morphology development during printing of magnetic hybrid polymer films

W. Cao, S. Yin, M. Bitsch[1], M. Plank[2], M. Gallei[1], M. Schwartzkopf[3], S. V. Roth[3,4],
P. Müller-Buschbaum

[1] UDS, Saarbrücken, Germany
[2] TUD, Darmstadt, Germany
[3] DESY, Hamburg, Germany
[4] KTH, Stockholm, Sweden

Magnetic hybrid polymer films have gained increasing interest for a host of applications that include information storage and magnetic sensors [1]. Because the hybrid films possess the combined characteristic performance of polymers and magnetic nanoparticles (NPs). In some areas, a spatial alignment of magnetic NPs is essentially required. Diblock copolymers (DBCs) have been proven to be suitable templates for the alignment of magnetic NPs, due to their ability to form various periodic structures such as spheres, cylinders, and lamellae resulting from microphase separation [2]. So far, various approaches, such as solution casting, spin coating, and printing have been applied for the fabrication of magnetic hybrid films. Among the above-mentioned methods, printing has attracted great attention because of its compatibility with large-scale fabrication processes [3]. However, most studies have only focused on the final printed magnetic hybrid films [3]. To achieve a desired morphology, it is significant to study the kinetic processes during the printing process systematically.

In the present work, printing is applied to fabricate magnetic hybrid films from solution precursors containing ultra-high molecular weight (UHMW) DBC polystyrene-block-poly(methyl methacrylate) (PS-b-PMMA) and magnetic FePt NPs. Kinetic processes during the solvent evaporation are investigated by in situ grazing incidence small-angle X-ray scattering (GISAXS) measurements, which are performed at the P03 beamline in DESY, Hamburg.

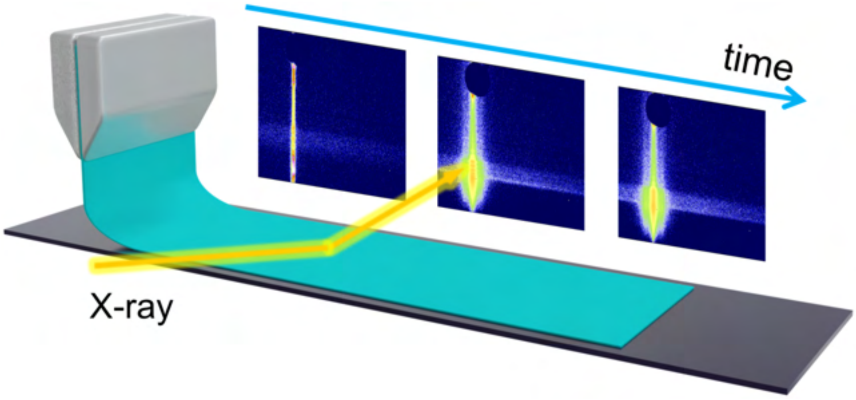

Figure 6.1:
Schematic of the experimental set up used for real-time and in situ GISAXS measurements with simultaneous printing.

Fig. 6.1 shows the in situ experimental set up used for simultaneous printing and GISAXS measurements. The employed protocol for the in situ GISAXS measurements was composed of 0.1 s exposure and 2 s waiting time in alternating sequence. To obtain information on the measured samples over a large area and to also avoid beam damage, the sample stage was kept sweeping along the sample surface y-direction, which was vertical to the X-ray beam direction. After 30 cycles, beam damage test was performed.

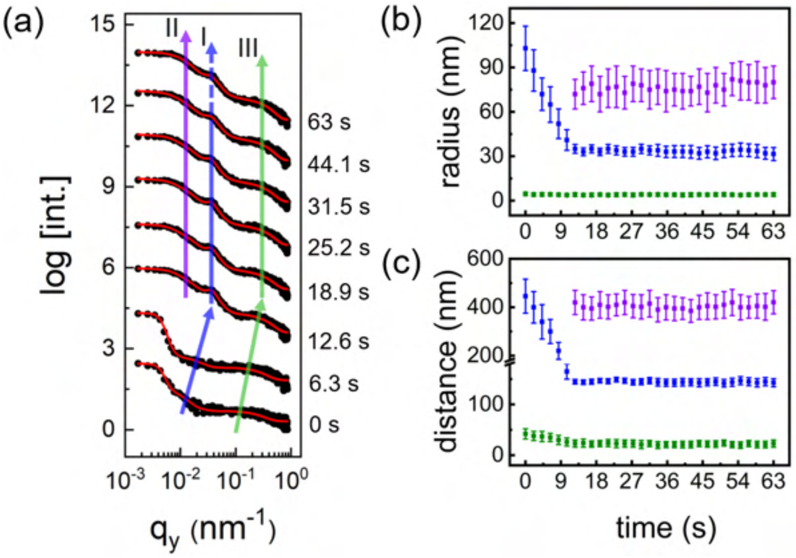

Figure 6.2:
(a) Selected horizontal line cuts (black dots) from the 2D GISAXS data of magnetic hybrid film with increasing time. The red lines show the fits. Curves are shifted along the intensity axis for clarity of the presentation. Structure I (blue arrow), II (purple arrow) and III (green arrow) are structure factors of PMMA cylinders, PMMA elongated structure and magnetic NPs, respectively. (b) Radius and (c) distance of the PMMA cylinders, PMMA elongated structure and magnetic NPs extracted from the fits.

To quantify the structure evolution during printing, horizontal line cuts of 2D GISAXS data are performed at the material characteristic Yoneda peak position. Fig. 6.2a shows the selected horizontal line cuts and corresponding fits. The selected horizontal line cuts are modeled based on the distorted-wave Born approximation, which relates to the effective interface approximation. In Fig. 6.2a, three main features are observed. They are structure factors of PMMA cylinders (all PMMA cylinders along the radius direction), PMMA elongated structure (lying-down PMMA cylinders along the length direction) and magnetic FePt NPs and are marked with I, II and III, respectively. As the time increases, the shift of structure I to higher q_y values is observed due to the solvent evaporation. The solvent evaporation results in a rapid shrinkage of the domain size and distance during the time from 0 s to 12.6 s. The corresponding average radius and center-to-center distance of the PMMA cylinders, extracted from structure I, decrease from around 102 nm to 33 nm (Fig. 6.2b) and from around 425 nm to 150 nm (Fig. 6.2c), respectively. Finally, a film with a relatively ordered PMMA structure is obtained at t $\geq$ 12.6 s. However, the relatively ordered nanostructure was observed to be metastable as the structure I becomes slightly weaker after 31.5 s. This behavior may be due to the reorganization of the polymer chains caused by the residual solvent inside the film. In contrast, no obvious changes in the value and error bar can be observed for structure II (PMMA elongated structure) during the printing process. The corresponding average radius and center-to-center distance of the PMMA elongated structure remain stable at around 70 nm and 415 nm, respectively.

In addition, a broad scattering feature (III) appears at higher q_y values, which represents the structure factor of the FePt NPs. It shifts slightly to a higher q_y value and stays constant at t $\geq$ 12.6 s. The corresponding average NP radius keeps constant at around 4.2 nm, while the average center-to-center distance decreases from 41 nm to 15 nm as the time increases from 0 s to 12.6 s. The decrease of center-to-center distance is mainly a result of the solvent evaporation which is similar to the discussion in structure I (PMMA cylinders). Hereafter, the structure is arrested because of lacking mobility in later stages.

[1] Y. Zang , F. Zhang , D. Huang , C. Di, D. Zhu, *Adv. Mater.* **27**, 7979-7985 (2015)

[2] S. Xia, L. Song, N. Hohn, K. Wang, S. Grott, M. Opel, M. Schwartzkopf, S. V. Roth, P. Müller-Buschbaum, *Adv. Funct. Mater.* **29**, 1808427 (2019)

[3] S. Xia, L. Song, V. Körstgens, M. Opel, M. Schwartzkopf, S. V. Roth, P. Müller-Buschbaum, *Nanoscale* **10**, 11930 (2018)

6.2 *In situ* GISAXS investigation of iron sputter deposition on hybrid diblock copolymer films containing magnetic nanoparticles

C. R. Everett, M. Plank[1], M. Gallei[2], M. Schwartzkopf[3], S. V. Roth[3,4], P. Müller-Buschbaum

[1] TUD, Darmstadt, Germany
[2] UdS, Saarbrücken, Germany
[3] DESY, Hamburg, Germany
[4] KTH, Stockholm, Sweden

Hybrid thin films composed of diblock copolymers (DBCs) and magnetic nanoparticles (NPs) are interesting candidates for applications as magnetic sensors and in magnetic data storage devices [1]. DBCs form various periodic nanostructures such as spheres, cylinders, and lamellae and are thus suitable templates for magnetic NPs. By modifiying the surface of the NPs, it is possible to precisely control the arrangement of the NPs in the periodic nanostructures of the DBC film. For use in magnetic data storage devices, which rely on materials that retain their magnetization after the removal of an external magnetic field, these hybrid films require magnetic NPs that exhibit ferromagnetic or ferrimagnetic behavior. Iron oxide NPs with a diameter larger than 20 nm display ferrimagnetism. However, incorporation of such large NPs into conventional films is challenging as the low molecular weight of the DBCs leads to domain sizes that are too small for the NPs. The NPs are thus expelled from film due to the polymer elastic penalty. This effect can be overcome by utillizing ultra high molecular weight (UHMW) DBCs, which can have domain size greater than 150 nm [2]. Previous work has demostrated the ferrimagnetic properties of Fe_3O_4 NPs in UHMW DBC films [3]. In order to improve device performance, exchange anisotropy as a result of interface coupling can be utilized [4]. This effect, observed first in systems with antiferromagnetic and ferromagnetic interfaces, has been reported in a wide range of magnetic systems, including at ferrimagnetic and ferromagnetic interfaces [5]. In this work, films containing large iron oxide NPs ($D = 30.0 \pm 2.5$ nm) are sputtered with iron and the iron layer growth is monitored *in situ* with grazing incidence small angle X-ray scattering (GISAXS).

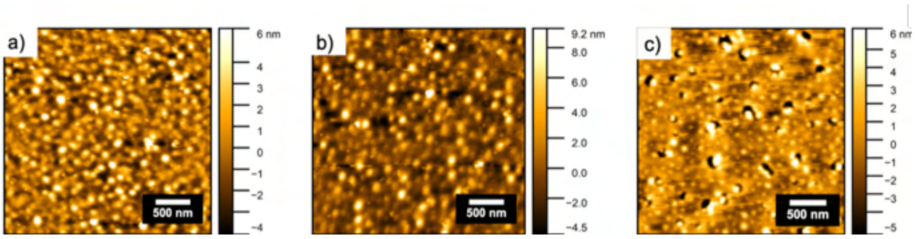

Figure 6.3:
AFM images of hybrid films with a constant iron oxide NP concentration of 5 wt% annealed with solvent vapor for (a) 3 h, (b) 9 h, and (c) 15 h. The dark matrix is PS whereas the bright domains and bright dots are PMMA and iron oxide NPs, respectively.

Thin films were fabricated from solution precursors composed of UHMW polystyrene-*block*-poly(methyl methacrylate) (PS-*b*-PMMA) and magnetite NPs (Fe_3O_4, 5 wt%) by spin coating and a subsequent solvent vapor annealing (SVA) step (3 h, 9 h, 15 h). Atomic force microscopy (AFM) images of the fabricated films can be seen in Fig. 6.3. With increasing annealing time, the film morphology becomes more ordered as can be observed by the increasing uniformity of the cylinder-forming PMMA domains. For SVA times of 3 h and 9 h, the oleic acid coated iron oxide NPs are located selectively inside the PS matrix. However, as seen in Fig. 6.3c, at a SVA time of

15 h, the iron oxide NPs appear as aggregates on the surface of the film. Thus, if the annealing time is too long, the NPs are expelled from the PS matrix and the precise arrangement of the NPs is no longer controllable.

An overview of the growth process is illustrated in Fig.6.4. Various selected two-dimensional (2D) GISAXS patterns show the evolution of scattering features throughout the sputter deposition process of Fe on top of a hybrid film containing 5 wt% iron oxide NPs and with a 9 h SVA process. In total, 20 nm of Fe were sputtered onto the film. At the beginning of the sputter process, a broad side peak along q_y at high q_y values can be seen. This can be attributed to the growth of Fe nanostructures with poor lateral order on top of the film. As sputtering continues, this peak shifts towards smaller q_y values. Such shifts are related to coalescence effects which lead to an increase in the average center-to-center distance between the Fe clusters. In addition, peaks along q_z appear during sputtering and these peaks shift to lower q_z values as sputtering continues. This observation is correlated to the vertical growth of the thin film. A complete analysis of the *in situ* GISAXS data can give insights in the Fe cluster morphologies throughout the sputter deposition and provide details about the growth mechanism of Fe nanostructures on polymer substrates.

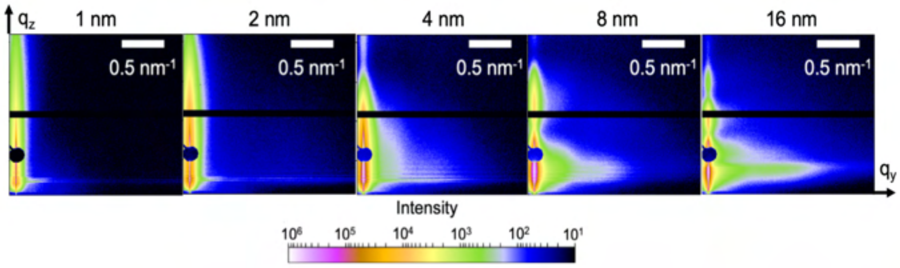

Figure 6.4:
Selected 2D GISAXS patterns of the *in situ* sputter growth of Fe on top of a hybrid film containing 5 wt% iron oxide NPs and with a SVA time of 9 h. The spectral beam stop, used to prevent oversaturation of the detector, is seen as the dark circle. Intermodular detector gaps are indicated by the black horizontal stripes.

In summary, the formation of a Fe layer by sputtering on a UHMW PS-*b*-PMMA hybrid film containing iron oxide nanoparticles appears to be a complex process consisting of various stages of growth from clustering metal atoms. Understanding the formation of Fe nanostructures on polymer substrates is important as it will impact future device performance. Further data analysis of the *in situ* GISAXS data will be combined with magnetic measurements utilizing a superconducting quantum interference device.

[1] Y. Yao, E. Metwalli, B. Su, V. Körstgens, D. M. González, A. Miasnikova, A. Laschewsky, M. Opel, G. Santoro, S. V. Roth, P. Müller-Buschbaum, *ACS Appl. Mater. Interfaces* **7**, 13080-13091 (2015)

[2] J. K. D. Mapas, T. Thomay, A. N. Cartwright, J. Ilavsky, J. Rzayev, *Macromolecules* **49**, 3733-3738 (2016)

[3] W. Cao, S. Xia, X. Jiang, M. Appold, M. Opel, M. Plank, R. Schaffrina, L. P. Kreuzer, S. Yin, M. Gallei, M. Schwartzkopf, S. V. Roth, P. Müller-Buschbaum, *ACS Appl. Mater. Interfaces* **12**, 7557-7564 (2020)

[4] J. Nogués, I. K. Schuller, *J. Magn. Magn. Mater.* **192**, 203-232 (1999)

[5] M.-H. Phan, J. Alonso, H. Khurshid, P. Lampen-Kelley, S. Chandra, K. S. Repa, Z. Nemati, R. Das, Ó. Iglesias, H. Srikanth, *J. Nanomater.* **6**, 221 (2016)

6.3 *In situ* GISAXS investigation of aluminium sputter deposition on conjugated diblock copolymer thin films

M. Gensch[1], P. Müller-Buschbaum, S. V. Roth[1,2]

[1] DESY, Hamburg, Germany
[2] KTH, Stockholm, Sweden

Nanostructured polymer-metal-composite films demonstrate great perspectives for optoelectronic applications, e.g. as sensors [1] or organic photovoltaics (OPV) [2]. The performance of these organic thin film devices is strongly depending on their nanomorpohology. A diblock copolymer thin film with a conjugated block can be a route to create these nanostructures in a controlled way to improve the efficiency compared to bulk heterojunctions. The amorphous domains of these diblock copolymer can be removed and replaced by an acceptor material [3]. The morphology growth of an electrode on such organic photovoltaic device needs better understanding in order to fabricate highly efficient devices [4]. Common techniques to prepare these nanocomposites of metal/polymer films are spin coating for thin polymer thin films in the nanometer range and subsequent sputter deposition to create a thin metal film. Thin nanostructured metal films can be controlled precisely by the sputter deposition process. During sputter deposition the interface morphology of the growing films was investigated by grazing incidence small angle X-ray scattering (GISAXS) to obtain information about the lateral and vertical arrangement of the metal clusters on the polymer template. The thin films were deposited by solution casting with a concentration of 5 mg/mL for the diblock copolymer thin film on acid cleaned silicon substrates. The *in situ* GISAXS experiments were performed at the beamline P03 in Hamburg DESY [5]. A custom made DC sputter deposition chamber was used with an aluminium target. The measurements were performed at an incident angle of α_i= 0.4° and the X-Ray energy wavelength of 0.985 Å. The sample to detector distance was SDD = 2462 mm. The detector was a Pilatus 300k with a pixel size of 172x172 μm^2. At the Yoneda peak, which is characteristic for every material, horizontal line cuts (Yoneda cut) were made to analyse the lateral formation of the aluminium clusters on the polymer domains.

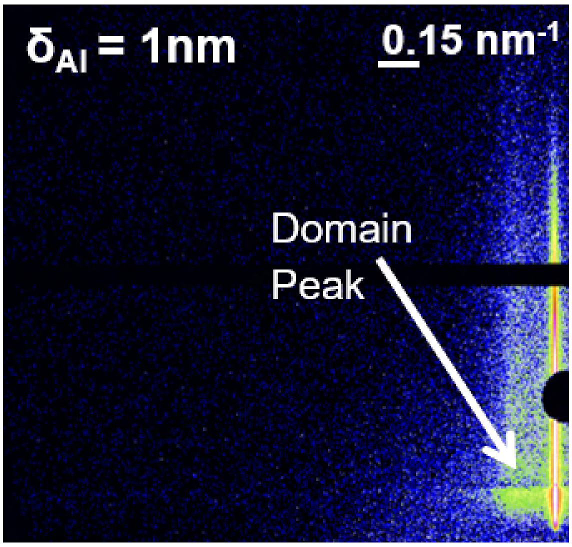

Figure 6.5:
The GISAXS pattern of the PMMA-b-P3HT copolymer thin film with δ_{Al} = 1 nm clearly shows a selectively metal decorated domain peak for the thin films indicated by a white arrow.

Fig. 6.5 shows the GISAXS pattern of PMMA-b-P3HT. From the results of the GISAXS measurements one obtains the size of the domain period of the copolymer template of around L = (42 ± 4) nm for the 20 nm thin diblock copolymer layer. The domain peak is shown in Fig. 6.5 by a white arrow. The cluster peak is not yet seen for δ_{Al} = 1 nm, which could be attributed to much lower electron density contrast from the aluminium compared to silver. The cluster peak is starting to appear around δ_{Al} = 2 nm as seen in Fig.6.6a (green dashed arrow). The average distance of the aluminium clusters is increasing indicated by the evolution of the cluster peak from high to low reciprocal space values. The domains are seen as lateral strips in the contour plot of the Yoneda cuts in fig. 6.6a (red dashed arrow). The selective decoration of the aluminium clusters on one of the polymer blocks can be followed by the increasing intensity of the polymer domain peak in Fig. 6.6a. The intensity increasement is a result of the electron contrast enhancement on the preferred polymer domain block.

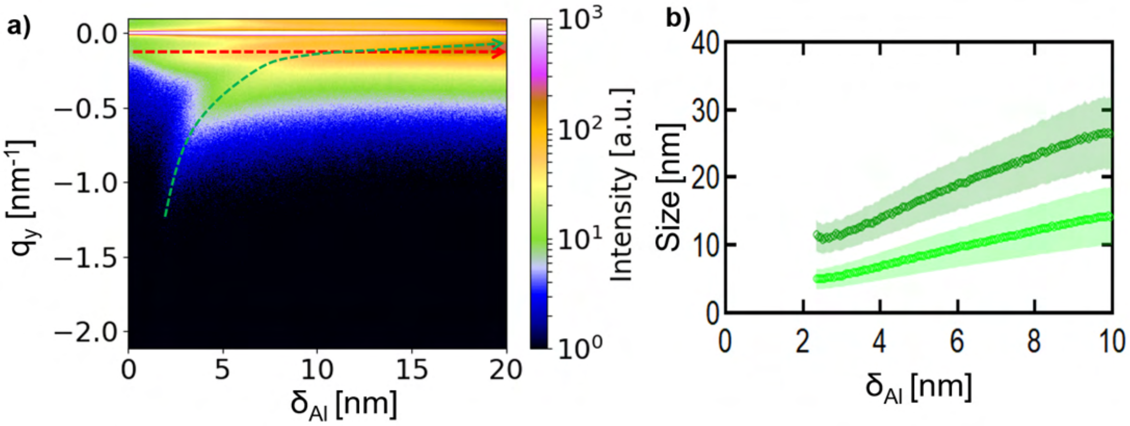

Figure 6.6:
a) Contour plot of Yoneda cuts from the *in situ* GISAXS data during sputter deposition on PMMA-b-P3HT as a function of effective Al thickness. The domain peak is shown by a red dashed arrow. The cluster peak is indicated by a green dashed arrow. b) Evolution of the average interparticle distance (dark green) and radii (light green) on the PMMA-b-P3HT diblock copolymer template with increasing Al thickness.

From the horizontal line cuts of the GISAXS measurements, the average mean distance and the radii from the clusters were extracted by the geometrical model from Schwartzkopf et al. [6] see fig. 6.6b. The lateral aluminium cluster formation follows a linear growth behavior, which is a different growth behavior compared to the silver cluster formation on these diblock copolymer thin film.

[1] F. Faupel, V. Zaporojtchenko, T. Strunskus, M. Elbahri, *Adv. Eng. Mater.* **12**, 1117–1190 (2010)

[2] G. Kaune, M. A. Ruderer, E. Metwalli, W. Wang, S. Couet, K. Schlage, R. Röhlsberger, S. V. Roth, P. Müller-Buschbaum, *ACS Appl. Mater. Interfaces* **1**, 353–360 (2009)

[3] I. Botiz, S.B. Darling, *Macromolecules* **42**, 8211–8217 (2009)

[4] F. C. Löhrer, V. Körstgens, G. Semino, M. Schwartzkopf, A. Hinz, O. Polonskyi, T. Strunskus, F. Faupel, S. V. Roth, P. Müller-Buschbaum, *ACS Appl. Mater. Interfaces* **12**, 1132–1141 (2020)

[5] A. Buffet, A. Rothkirch, R. Döhrmann, V. Körstgens, M. M. A. Kashem, J. Perlich, G. Herzog, M. Schwartzkopf, R. Gehrke, P. Müller-Buschbaum, S. V. Roth, *Journal of Synchrotron Radiation* **19**, 647–653 (2012)

[6] M. Schwartzkopf, G. Santoro, C. J. Brett, A. Rothkirch, O. Polonskyi, A. Hinz, E. Metwalli, Y. Yao, T. Strunskus, F. Faupel, P. Müller-Buschbaum, S. V. Roth, *ACS Appl. Mater. Interfaces* **7**, 13547–13556 (2015)

6.4 Solvent vapor annealing of a diblock copolymer thin film with solvent mixtures: Importance of pathway for the morphological changes

F. A. Jung, A. V. Berezkin, T. B. Tejsner[1], D. Posselt[1], D.-M. Smilgies[2], C. M. Papadakis

[1] IMFUFA, Department of Science and Environment, Roskilde University, Roskilde, Denmark

[2] Cornell High Energy Synchrotron Source (CHESS), Cornell University, Ithaca, United States

Block copolymers (BCP) self-assemble, which makes them attractive for many applications requiring ordered nanostructures on length scales of 10-100 nm. However, the rapid solvent removal during solution-based preparation methods, such as spin-coating, prevents long-range order, since the BCPs become kinetically trapped. To overcome this, solvent vapor annealing (SVA) is often used to allow restructuring to occur [1]. Another advantage is the ability to alter the morphologies of BCP thin films by selective swelling of one domain [2]. Solvent mixtures of non-selective and selective solvents have emerged as a powerful way to combine both effects. An open question is, however, the choice of the SVA protocol.

In this work, we follow the morphological changes in thin films of polystyrene-*b*-poly(dimethyl siloxane) (PS-*b*-PDMS) during four SVA protocols in mixed solvent vapors using in-situ grazing-incidence small-angle X-ray scattering (GISAXS). The minority block is PDMS ($f_{\mathrm{PDMS}} = 0.36$), which, after spin-coating, forms randomly oriented cylinders (RAND) in a glassy PS matrix ($T_{\mathrm{g,PS}} \approx 100\,^\circ$ C). As solvents, toluene, which is a non-selective solvent, and *n*-heptane, which is selective for PDMS, are used [3]. The four protocols are: (i) Swelling in a 3:7 *n*-heptane:toluene ratio for 3000 s followed by drying for 1500 s at constant solvent ratio, (ii) swelling in pure toluene for 3000 s and subsequent stepwise exchange of toluene with *n*-heptane until a ratio of 3:7, followed by rapid drying, (iii) swelling in pure toluene for 3000 s, subsequent complete exchange with *n*-heptane over a period of 2700 s, installation of a 3:7 ratio for 1200 s followed by rapid drying, (iv) swelling in *n*-heptane for 3000 s and subsequent complete exchange with toluene.

The in situ GISAXS experiments are performed at beamline D1 at CHESS using a custom made sample chamber equipped with a spectral reflectometer for complementary film thickness measurements [2]. From the 2D GISAXS patterns, we extract the morphology as well as the solvent distribution inside the films, which allows us to calculate the solvent swollen effective volume fraction of the solvent-swollen PDMS f_{eff} and the polymer volume fraction ϕ_{p} and to construct a diagram of states for each protocol (Figure 6.7a-d).

During protocol (i), the trajectory is almost vertical and no morphological transition is observed, even though enough toluene has entered the film to cross the glass transition of PS at $\phi_{\mathrm{p}} \approx 0.8$ (Figure 6.7a). Thus, the solvent ratio 3:7 allows swelling at constant composition.

During protocol (ii), the trajectory is inclined to the left, i.e., the PS matrix is swollen slightly more than the PDMS cylinders (Figure 6.7b). At $\phi_{\mathrm{p}} \approx 0.5$, a transition towards hexagonally oriented lying cylinders (HEX) is found, which is evidenced by a distinct set of scattering peaks in the 2D GISAXS patterns. Upon drying, the morphology changes back to RAND.

The initial swelling in toluene in protocol (iii) is the same as in protocol (ii) (Figure 6.7c). During the exchange with *n*-heptane, the trajectory shifts towards a more symmetric compositions. At $f_{\mathrm{eff}} \approx 0.4$, a morphology transition is initiated, presumably to the lamellar state. However, at higher *n*-heptane contents, PS becomes glassy, and the morphology is kinetically trapped in the transitional state (TRANS). Installing subsequently a 3:7 *n*-heptane:toluene ratio mobilizes the PS matrix again, but also promotes the RAND morphology, which is the reason why the lamellae state cannot fully develop during this protocol.

During protocol (iv), the trajectory is inclined to the right, since PDMS is selectively swollen (Figure 6.7d). At $f_{\mathrm{eff}} \approx 0.4$, a morphological transition towards lamellae is initiated, similar to protocol (iii), but, since PS remains glassy, the transition is slow and trapped in the TRANS

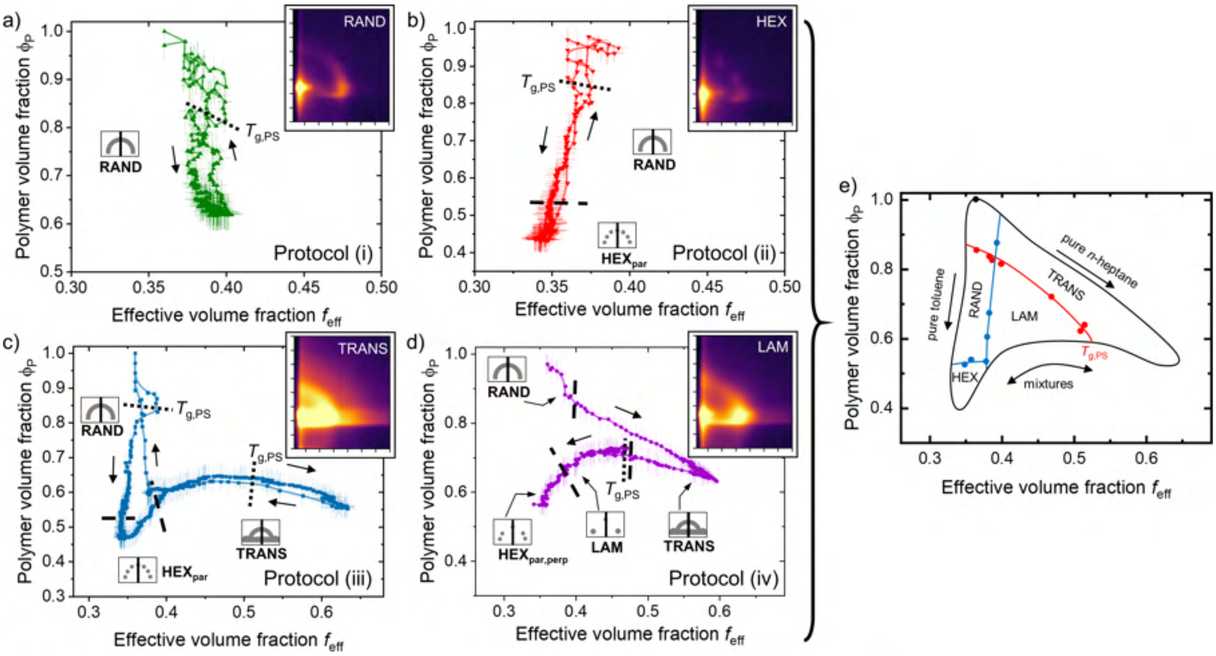

Figure 6.7:
(a-d) Trajectories of the system during SVA for protocols (i-iv). Dotted lines indicate the glass transition of PS, in the solvent mixture. Dashed lines indicate morphological transitions. Insets show representative 2D GISAXS patterns of the RAND, HEX, TRANS and LAM states (see text). (e) Emerging diagram of states of PS-*b*-PDMS thin films swollen in toluene/*n*-heptane solvent vapor mixtures. Blue circles indicate observed morphology transitions and red circles the glass transition of the PS matrix. Adapted from [4].

state. Only during the addition of toluene to the solvent vapor mixture does the PS matrix swell sufficiently to allow rearrangements, and at this point, the lamellae (LAM) fully form. At higher toluene contents, the HEX state forms, including both lying and standing cylinders.

The emerging diagram of states with the observed morphological transitions and glass transitions of the four protocols is shown in Figure 6.7e. At high toluene contents, either the RAND ($\phi_p > 0.5$) or the HEX ($\phi_p < 0.5$) states form. At high *n*-heptane contents, the LAM state should form, but a large TRANS state exists, at which the PS matrix is glassy and immobile. The formation of the LAM state is pathway-dependent: It forms more easily when entered from the TRANS state (protocol (iv)) compared to the HEX state (protocol (iii)). The orientation of the cylinders in the HEX state is affected by the pathway as well: When entered from the RAND state (protocols (ii and iii)), the cylinders are lying, whereas they are both lying and standing when entered from the LAM state (protocol (iv)).

The project is funded by Deutsche Forschungsgemeinschaft (DFG) (Pa771/10-2).

[1] D. Posselt, J. Zhang, D.-M. Smilgies, A. V. Berezkin, I. I. Potemkin, C. M. Papadakis, *Prog. Polym. Sci* **66**, 80-115 (2017)

[2] A. V. Berezkin, F. Jung, D. Posselt, D.-M. Smilgies, C. M. Papadakis, *Adv. Funct. Mater.* **28**, 1706226:1-15 (2018)

[3] K. W. Gotrik, A. F. Hannon, J. G. Son, B. Keller, A. Alexander-Katz, C. A. Ross, *ACS Nano* **6**, 8052-8059 (2012)

[4] F. A. Jung, A. V. Berezkin, T. B. Tejsner, D. Posselt, D.-M. Smilgies, C. M. Papadakis, *Macromol. Rapid Commun.* **41**, 2000150:1-12 (2020)

6.5 *In operando* GISAXS study of degradation in titania-based solid-state dye-sensitized solar cells

N. Li, R. Guo, S. Bernstorff[1], P. Müller-Buschbaum

[1] ELETTRA, Trieste, Italy

Dye-sensitized solar cells (DSSCs) have attracted large attention as potential alternative to conventional silicon photovoltaic devices due to its low cost, mechanical flexibility, easy production and high efficiency reaching 12.3%.[1] As a crucial element in DSSCs, sensitizers play a significant role on the efficiency and stability of the devices. Normally, high efficiency DSSCs have function groups such as a carboxy ligand (-COOH) through which the dye can firmly anchor on the titania film surface. Particularly, D205, as an organic dye, possess prominent advantages, such as low cost, environmentally friendly and ease of synthesis, although this dye provides lower efficiencies as compared to the most efficient ruthenium complex based sensitizers like N719.[2]

Until now, 7.2% power conversion efficiency was reported for titania-D205 sensitizer solar cells using an ionic-liquid electrolyte.[3] However, the liquid electrolyte hole transporters face leaking and electrode-corrosion issues and thus hinder their market expansion. Thus, solid-state hole-transport materials (HTMs) have been exploited to replace the liquid electrolyte. Spiro-OMeTAD has prevailed as the dominant HTM for the high-efficiency perovskite solar cells and solid-state DSSCs (ssDSSCs) due to its many merits such as relatively simple recipe for solution-processable deposition procedures and proper energy levels.

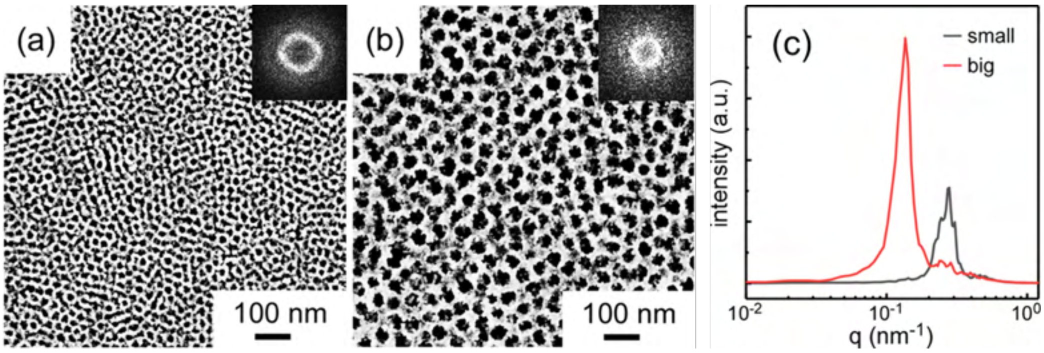

Figure 6.8:
SEM images of the mesoporous TiO_2 films after calcination: (a) small-pore and (b) big-pore samples. (c) PSD functions of small-pore and big-pore samples.

The present work focuses on the stability of titania-D205 based ssDSSCs with a HTM spiro-OMeTAD. Thus, titania/D205/sprio-OMeTAD ssDSSCs can be understood as a well-established model system using a carboxylic anchoring group. Since the anchoring group of the dye helps to form a monomolecular layer, which ensures high chances of electron injection from the dye molecules to titania films. Detachment of the adsorbed dye on the surface of titania films may occur and thus degrade the charge transfer in the titania/dye interface. Therefore, we track the morphology evolution via synchrotron-based in-operando grazing-incidence X-ray scattering (GISAXS). Simultaneously, the development of the photovoltaic characteristics is probed. In this study, the correlation between the morphology evolution and ssDSSC device performance is revealed. Furthermore, we compare two types of mesoporous titania films with different pore sizes since the pore size of titania films influences not only the efficiency, but also the stability of ssDSSCs.

We obtain two ordered mesoporous titania films with different pore sizes via a sol-gel approach, in which the polystyrene-block-polyethylene oxide (PS-b-PEO) plays a role as a structure-directing template. Fig. 6.8 shows the surface scanning electron microscopy (SEM) images of the mesoporous titania films after calcination. Both films show an interconnected titania network with ordered structures which benefit for charge carrier transport, but the pore sizes differ. These two samples with small and big mesopore arrays are denoted as small-pore and big-pore, respectively. The small-pore film displays ordered titania arrays with a titania wall of about 9 nm and uniform mesopores of around 15 nm in diameter (Fig. 6.8a). In contrast, the big-pore film has a thicker titania framework of around 12 nm and a pore size of around 37 nm (Fig. 6.8b). To evaluate structural order, two-dimensional fast Fourier transform (2D-FFT) patterns are extracted from the SEM images. With a comparison of these two films, a second-order ring only appears in 2D-FFT pattern for the small-pore sample, indicating a higher ordered structure existing in this type. The related power spectral density (PSD) functions demonstrate different q values. The corresponding center-to-center distances are around 23.3 nm and 47.1 nm for the small-pore and big-pore samples, respectively.

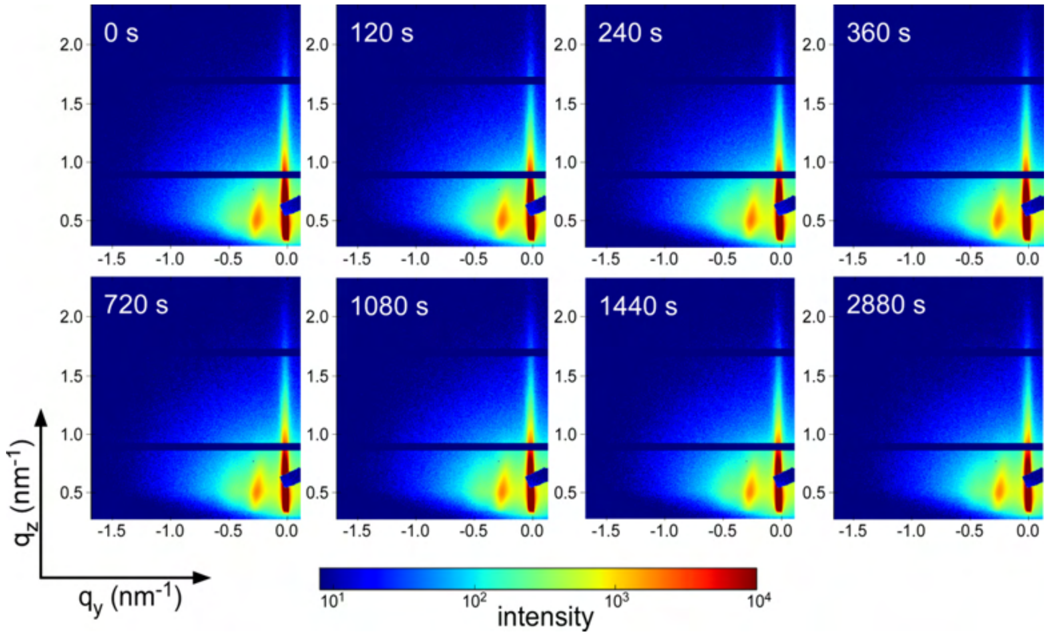

Figure 6.9: 2D GISAXS data of the small-pore ssDSSCs after different illumination.

To reveal the morphology evolution of the active layer under illumination of the solar cells, GISAXS measurements are performed in the Austrian SAXS beamline of the ELETTRA synchrotron source. The strong Bragg rods in Fig. 6.9 imply highly ordered lateral structures inside the film, which is in good agreement with the above SEM image (as shown in Fig. 6.8a).

[1] A. Yella, H.-W. Lee, H. N. Tsao, C. Yi, A. K. Chandiran, M. K. Nazeeruddin, E. W.-G. Diau, C.-Y. Yeh, S. M. Zakeeruddin, M. Grätzel, *Science* **334**, 629-633 (2011)

[2] H. Wang, M. Liu, M. Zhang, P. Wang, H. Miura, Y. Cheng, J. Bell, *Phys. Chem. Chem. Phys.* **13**, 17359-17366 (2011)

[3] D. Kuang, S. Uchida, R. Humphry-Baker, S. M. Zakeeruddin, M. Grätzel, *Angew. Chemie* **120**, 1949-1953 (2008)

6.6 *In situ* GISAXS observation of sputter-deposited gold nanostructure on mesoporous titanium dioxide template

S. Liang, W. Chen, S. Yin, S. J. Schaper, J. Drewes[1], N. Carstens[1], T. Strunskus[1], F. Faupel[1], M. Gensch[2], M. Schwartzkopf[2], S. V. Roth[2,3], P. Müller-Buschbaum

[1] CAU, Kiel, Germany
[2] DESY, Hamburg, Germany
[3] KTH, Stockholm, Sweden

Gold/titanium dioxide (Au/TiO_2) nanohybrid materials have attracted significant attention due to the outstanding optical, photocatalytic and photovoltaic performance.[1] Compared to chemical synthesis and lithography, sputter deposition is a facile and scalable method to produce metallic thin films and nanoparticles on substrates in precise controllability. Using nanostructured templates, ordered metal nanostructures were achieved through the sputter deposition approach.[2] Herein, we propose a strategy to fabricate nanostructured Au/TiO_2 hybrid thin films by sputter-depositing Au on mesoporous TiO_2 template. In order to investigate the kinetics of the sputter-deposited Au growth on the TiO_2 template, *in situ* grazing-incidence small-angle X-ray scattering (GISAXS) during sputter deposition was measured.

The mesoporous TiO_2 template was prepared by a typical sol-gel synthesis approach.[3] The stock solution was firstly prepared by dissolving the diblock copolymer polystyrene-block-poly(ethylene oxide) (PS-b-PEO) into 1,4-dioxane, followed by adding titanium tetraisopropoxide (TTIP) as titania precursor and 37% concentrated hydrochloric acid (HCl) as poor solvent. Then, the TiO_2 thin film was obtained by spin-coating the stock solutions on glass substrate, followed by a calcination process at 500 °C for 2 h in air. The illustrated morphology and corresponding SEM image of as-obtained mesoporous TiO_2 template are shown as Fig.6.10a and Fig.6.10b, respectively. The sputter-deposition process and *in situ* GISAXS measurement is illustrated in Fig.6.10c. The scattered signal was collected by a detector with a sample to detector distance (SDD) of (2462 ± 2) mm. In this work, the Au sputter depositions on the TiO_2 templates were performed for 150 s, and the *in situ* GISAXS measurements collected 20 2D GISAXS patterns every second to obtain a time-resolution of 0.05 s.

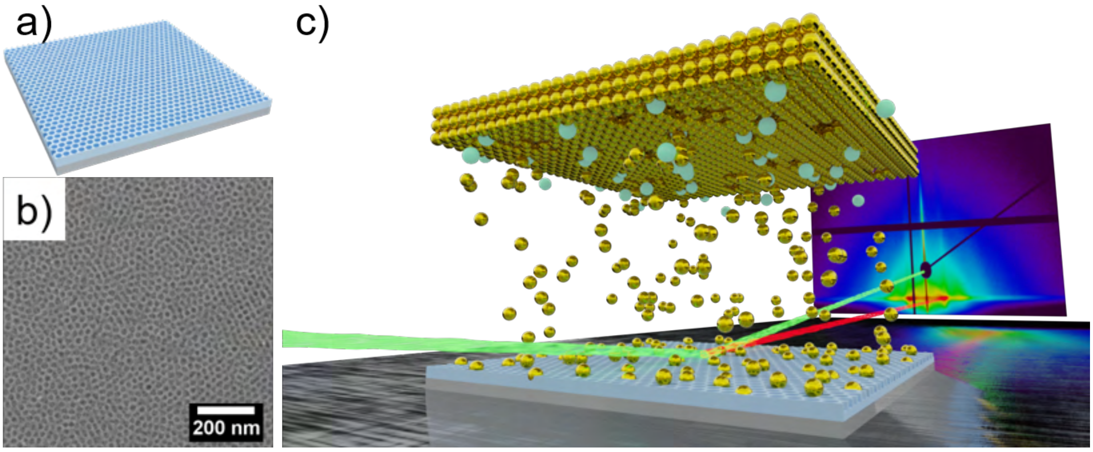

Figure 6.10:
a) Schematic diagram and b) SEM image of the mesoporous TiO_2 template. c) Illustration of Au sputter deposition on the mesoporous TiO_2 template probed with the in situ GISAXS measurements.

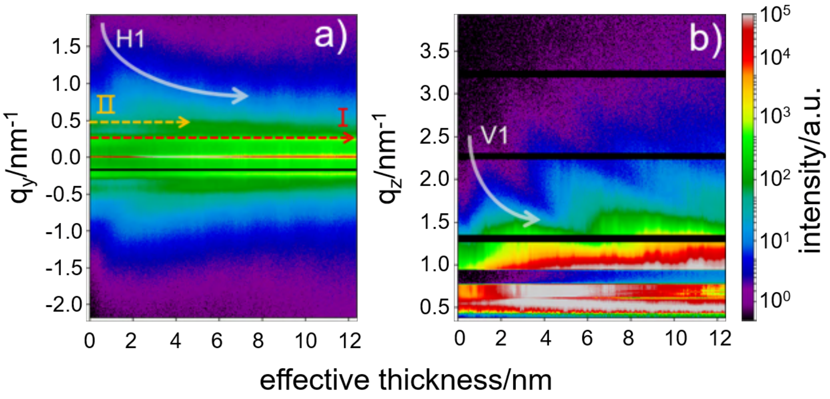

Figure 6.11:
a) Horizontal and b) vertical line cut evolution as a function of effective film thickness on the mesoporous TiO_2 template.

Au deposition kinetics on the mesoporous TiO_2 templates is quantitatively analyzed, based on selected line cuts and related modeling. The horizontal line cuts are taken along an integrated q_z region (q_z = 0.59 nm^{-1} $< q_z <$ 0.63 nm^{-1}, above the critical angle of TiO_2), while the vertical line cuts are taken at q_y = 0 nm^{-1} (q_y = 0.018 nm^{-1}), as displayed in Fig. 6.11a and Fig. 6.11b, respectively. At the beginning of the sputter deposition, the pseudo-Bragg peak (peak I) and a well-visible second-order peak (peak II) originate from the well-ordered porous structure of the TiO_2 film. When the effective Au layer thickness reaches about 0.8 nm, a broad side-peak (H1) emerges at q_y = 1.8 nm^{-1}, corresponding to the scattering from small-size Au clusters. These small-sized Au clusters have small distances and are formed after random walk and nucleation. With further deposition, the peak H1 shifts toward smaller q_y values, which indicates a gradually increased inter-structure distance of the Au clusters due to the diffusion-mediated coalescence of the clusters and adsorption-mediated cluster growth. When the effective Au layer thickness increases to about 8 nm, peak H1 reaches the q_y value (q_y = 0.23 nm^{-1}) where the peak I is located. This infers that the further expansion of the Au clusters is influenced by the substrate morphology, namely the pore-structure of the TiO_2 layer, thereby acting as the template effect. With further Au deposition, peak H1 tends to be stable at q_y = 0.23 nm^{-1}, which suggests that the Au morphology templated by the TiO_2 nanostructure dominates the scattering in the observed length scale regime. Notably, larger structures form due to the further merging of Au clusters, which contribute to an increase of the scattering in the small q_y region. Thus, the rod reflection peak (q_y = 0 nm^{-1}) intensity is becoming stronger with increasing the sputter-deposited Au thickness, which is also an indication for the formation of large compact Au regions. In addition, peak I intensity increases gradually with increasing the Au sputter deposition. Thus, the template-induced Au cluster growth exhibits its dominance in the scattering during sputter deposition. However, peak II intensity decreases gradually, indicating the gradual disappearance of the ordered structure due to the interconnection of large Au clusters at the late stage of sputter deposition. In Fig. 6.11b, the peak V1 represents the first maximum of the intensity modulation in qz direction in the vertical line-cut evolution, indicating the effective thickness increase of the Au layer. With the onset of Au deposition, several peaks, which are similar to the peak V1, appear at higher q_z values and shift towards lower q_z values during sputter deposition. These intensity features are caused by correlated roughness and similar to Kiessig fringes are related to the interference of X-ray beams diffusely reflected at the Au-air and Au-TiO_2 interfaces.

[1] H. Wang, T. You, W. Shi, J. Li, L. Guo, *J. Phys. Chem. C* **116**, 6490 (2013)

[2] W. Chen, S. Liang, F. C. Löhrer, S. J. Schaper, N. Li, W. Cao, L. P. Kreuzer, H. Liu, H. Tang, V. Körstgens, M. Schwartzkopf, K. Wang, X. W. Sun, S. V. Roth, P. Müller-Buschbaum, *ACS Appl. Mater. Interfaces* **12**, 46942 (2020)

[3] S. Yin, L. Song, S. Xia, Y. Cheng, N. Hohn, W. Chen, K. Wang, W. Cao, S. Hou, P. Müller-Buschbaum, *Small Methods* **4**, 1900689 (2020)

6.7 *In situ* investigation of the thermal stability of thermoelectric thin films based on EMIM DCA post-treated PEDOT:PSS

A. L. Oechsle, S. Bernstorff[1], P. Müller-Buschbaum

[1] Elettra, Trieste, Italy

Close to two-third of the global electricity is nowadays still produced by powering engines with heat created from burning fossil fuel, like oil, coal or gas[1]. Though, these heat engines typically operate at around *30 %* to *40 %* efficiency, leading to a tremendous loss of energy in form of waste heat. However, not only in thermal power plants, but also in other fields of electricity/power production, industrial procedures or in daily life processes a huge amount of produced heat dissipates unused into the environment. As depicted in Fig. 6.12 (left) in total we lose around *66 %* of primary energy as waste heat[2]. In this respect, it is very clear that there is a compelling demand for sustainable waste-heat recovery techniques like thermoelectric devices, which enable the direct conversion of low-grade waste heat into electrical power. The basic underlying principle is the Seebeck effect, imaged in Fig. 6.12 (right).

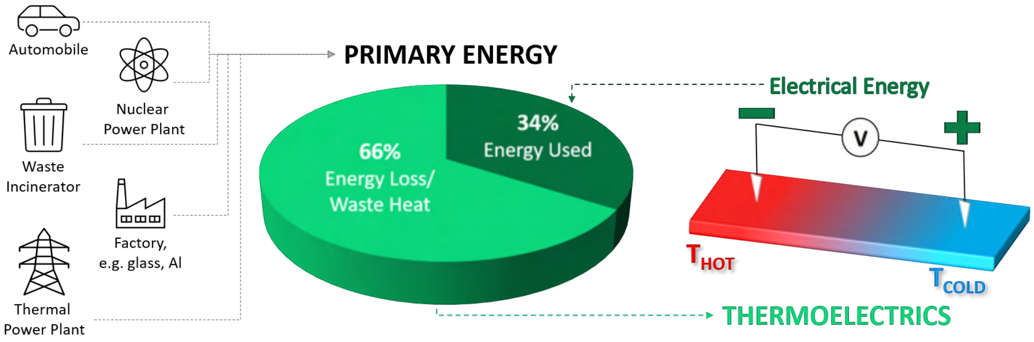

Figure 6.12:
Schematic overview of the basic principle that allows thermoelectric devices to recycle some of the large waste heat amounts arising from different industries and processes.

Our research work is focusing on polymer based organic thermoelectric materials as they provide promising properties, like low or non toxicity, and the possibility of a low-cost, large-scale solution-based processability, which also facilitate the fabrication of lightweight and flexible thin-film devices. Furthermore, these organic materials typically show low thermal conductivities, thus are good at maintaining a temperature gradient and therefore hold the potential to be used in low temperature applications[3]. More precisely, we use the organic semi-conducting polymer blend PEDOT:PSS (*poly(3,4-ethylene dioxythiophene):poly(styrene sulfonate)*) as thermoelectric material. In the past our group has shown that a post-treatment of PEDOT:PSS thin films with ionic liquids like EMIM DCA (*1-ethyl-3-methylimidazolium dicyanamide*) leads to an improvement of its thermoelectric properties, namely a simultaneous increase in its electrical conductivity (σ) and its Seebeck coefficient (S)[4]. In this work we investigate the influence of temperature on the properties of EMIM DCA treated PEDOT:PSS thin films to get an idea about the stability of these organic thermoelectric films under operation. Therefore, we prepare PEDOT:PSS thin films on cleaned glass substrates and post-treat them with 0.05 M EMIM DCA. Then we place these films on a temperature controlled heatable copper plate and contact the films electrically to measure their electrical conductivity in-situ. The setup, built within a chamber to allow for a nitrogen inert gas atmosphere, is then installed in the SAXS beamline at the ELETTRA synchrotron in Trieste, which can be seen in Fig. 6.13a). Now the EMIM DCA treated PEDOT:PSS thin films are heated for 5 h to 50 °C and 100 °C, respectively, while in-situ measuring the electrical conductivity and investigating the morphological changes via grazing-incidence small-angle X-ray scattering (GISAXS).

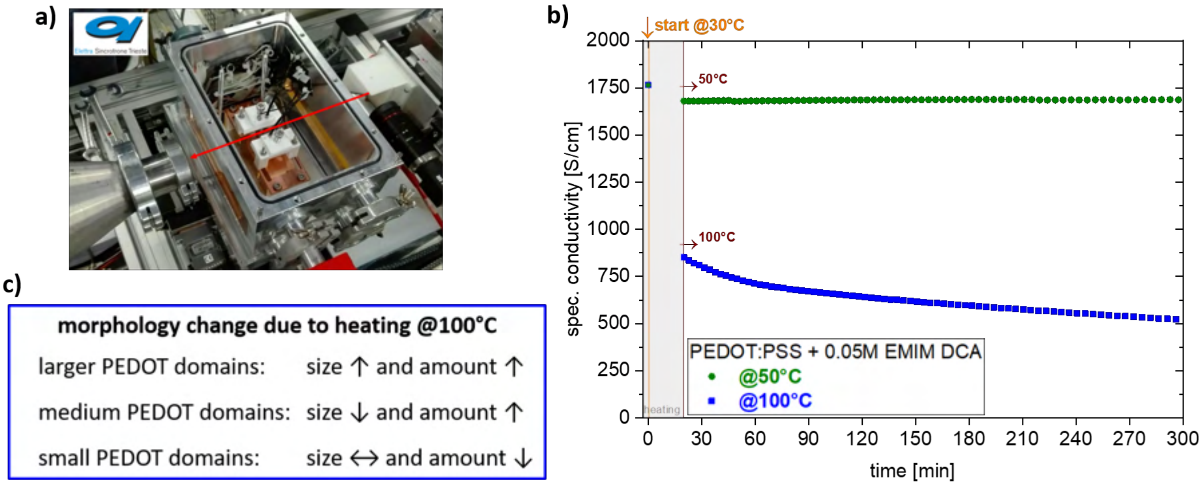

Figure 6.13:
a) Photo of the measurement setup installed in the SAXS beamline at ELETTRA. b) Specific conductivity of 0.05 M EMIM DCA treated PEDOT:PSS thin films, over the time of heating to 50 °C (green) and 100 °C (blue), respectively. c) Summary of the observed morphological changes within PEDOT:PSS during the heating process at 100 °C investigated with GISAXS.

The developments of the film conductivities for the respective applied temperatures can be observed in Fig. 6.13b). Already during the first 20 min of heating up, we observe a conductivity drop for the 100 °C-sample from 1765 $\frac{S}{cm}$ to 850 $\frac{S}{cm}$, while the 50 °C-sample just drops by 85 $\frac{S}{cm}$. Furthermore, after thermal equilibrium is reached, the 100 °C-sample shows a continuous decrease in its conductivity compared to the mainly stable 50 °C-sample, which indicates that film degradation processes occur. The in-situ GISAXS measurements allowed us to investigate the inner morphology of the treated PEDOT:PSS thin films during heating. From evaluating and modelling GISAXS data, we get information about the amount and size of conductive PEDOT-rich domains embedded in the non-conductive PSS matrix. In this case we are able to model und distinguish three different PEDOT domain sizes (large 45 nm, medium 10 nm & small 2 nm). While the domain morphology seems to be mostly stable for the 50 °C-sample, we observe the following changes for the PEDOT:PSS thin film heated to 100 °C (summarized in Fig. 6.13c)): The large PEDOT domains become larger and increase in number, the medium domains decrease a bit in size but increase in number, while the small domains seem to be stable in size but their amount decreases. In conclusion, these results imply a coarsening of the PEDOT domains due to heating at 100 °C, which we suggest impairs the inter-domain conductivity and therefore cause the measured decrease in the film conductivity.

[1] bp, *Statistical Review of World Energy* **69th edition**, 1-68 (2020)

[2] Fitriani, R. Ovik, B. D. Long, M. C. Barma, M. Riaz, M. F. M. Sabri, S. M. Said, R. Saidur, *Renew. Sustain. Energy Rev.* **64**, 635-659 (2016)

[3] Zhang, Y. Sun, W. Xu, D. Zhu, *Adv. Mater.* **26**, 6829-6851 (2014)

[4] N. Saxena, B. Pretzl, X. Lamprecht, L. Bießmann, D. Yang, N. Li, C. Bilko, S. Bernstorff, P. Müller-Buschbaum, *ACS Appl. Mater. Interfaces* **11**, 8060-8071 (2019)

6.8 *In situ* GIWAXS analysis of 2-step printed perovskite formation

M. A. Scheel, L. K. Reb, M. Schwartzkopf[1], S. V. Roth[1,2], P. Müller-Buschbaum

[1] DESY, Hamburg, Germany
[2] KTH, Stockholm, Sweden

Understanding the morphology-function relationship in perovskite absorber materials is an important step on the road to commercial perovskite products such as LED or PV applications. Transforming well established lab-scale methods to industry-compatible processes, e.g. roll-to-roll deposition, is often not straight-forward and requires detailed understanding about the processes involved during thin-film formation. In particular, slot-die coating is a promising deposition method for high-throughput production of large-scale PV modules with minimal waste accumulation. Additionally, it supports the potential to use ultrathin flexible plastic foils, which is beneficial for highly specialized applications and efficient resource usage. In PV devices the absorber material is of key interest, and thus structure and morphology control during thin-film formation is essential in achieving highly homogeneous and thus high-performing absorber layers.

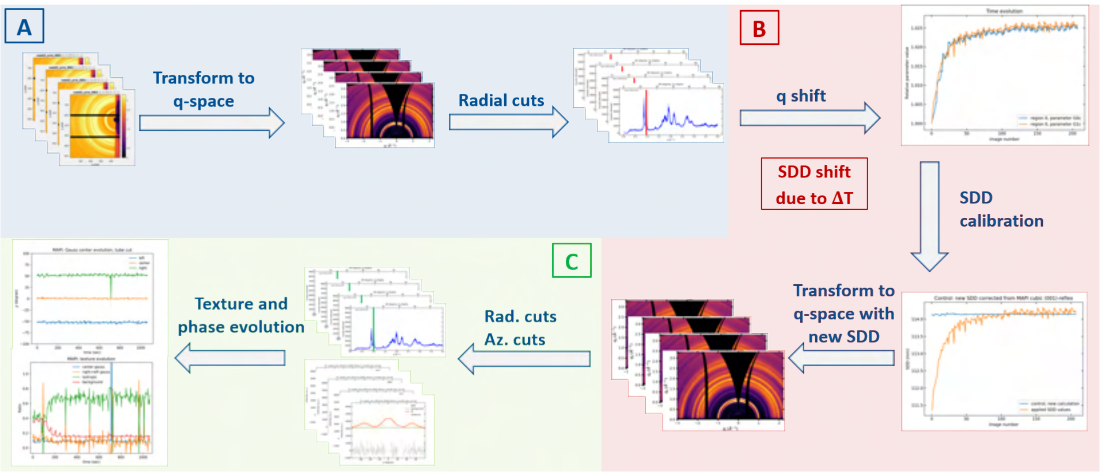

Figure 6.14:
In situ batch analysis workflow developed for large count data frames. A) 2D detector images are transformed to q-space (reshaping) in order to extract sample detector distances accurately from pseudo-XRD patterns with the help of an internal calibrant. B) Raw 2D images are SDD corrected and reshaped again. C) Radial and azimuthal cuts are performed on each frame to extract phase and morphology evolution over time.

Grazing-incidence X-ray scattering measurements are well suited to probe the influence of deposition parameters, e.g., temperature, ambient moisture and precursor composition by probing stochastically relevant large sample areas in situ.[1] We apply the technique of grazing-incidence wide-angle X-ray scattering (GIWAXS) to the conversion process of slot-die coated lead-precursor and slot-die coated methyl ammonium iodide precursor to the desired tetragonal perovskite phase. GIWAXS is a powerful non-destructive technique to investigate the crystal structure and texture of thin-films. Using synchrotron radiation, the process can easily be time-resolved (frame rate around 1 Hz). This results in a comparable large data set which makes it impractical to analyze ”by hand”. Thus, in a first step a batch flow analysis workflow was established. The process is depicted in Fig. 6.14 and includes the transformation of the raw 2D detector images to q-space (reshaping), the frame-by-frame sample-detector-distance (SDD) correction and the subsequent radial and azimuthal cuts for texture and phase evolution analysis. All is done automatically by self-written software and the program GIXSGUI.[2] By azimuthal integration a pseudo-XRD pattern can be created that gives information about the phases present in the thin-film. Modeling the Bragg reflexes of the pseudo-XRD pattern gives the opportunity to follow the phase evolution over the time of annealing. Fig. 6.15 a shows the amplitude evolution of the respective phase components. When reaching a temperature of about 100 °C the conversion process starts and leads to the strong increase in perovskite signal amplitude. At the same time the precursor-solvent phase drastically decreases in signal strength,suggesting a conversion of the precursor into perovskite. Herein, the precursor-complex phase plays a critical role and determines morphology of the final film, as known from previous findings.[3,4]

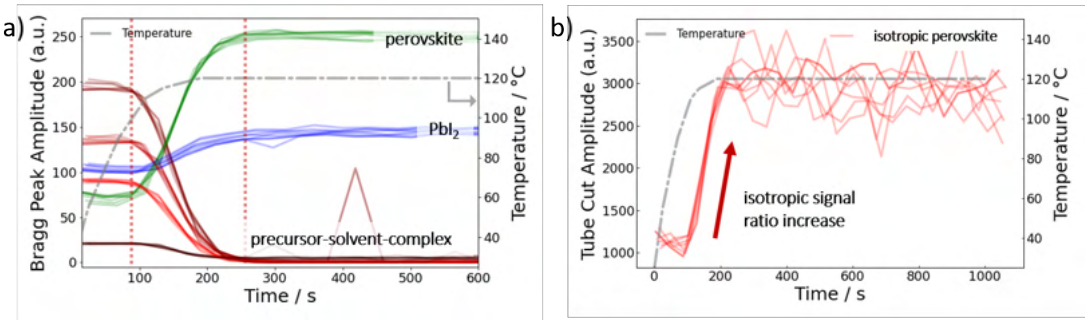

Figure 6.15:
a) Time evolution of the respective Bragg signal intensities as extracted from the peak amplitudes of pseudo-XRD data. Perovskite intensity is increasing roughly threefold, while all Bragg reflexes corresponding to the precursor-solvent phase diminish over time until reaching zero intensity. Each line of one color represents a different position measured on the sample with a spacing of roughly 1 mm in order to obtain a representative signal.

From azimuthal cuts the orientation of the forming perovskite can be analyzed. Fig. 6.15 b shows that newly formed perovskite is of isotropic crystal orientation. At the same time face-on and corner-on oriented perovskite do not show significantly increased signal strength. This might be due to the slow release of lead from the precursor-solvent phase and subsequent randomly oriented nucleation. Isotropic perovskite formation is favored which can be beneficial for PV application and shows how solvent-containing precursor complexes can influence the final thin-film morphology. It suggests that solvent engineering in combination with a carefully designed temperature and deposition process can be used to tune morphological features.[5] Our findings also make it possible to correlate pre-annealing morphology of lead-containing species with the resulting perovskite film morphology, thus giving insights into crystal growth mechanisms. This motivates us to investigate the slot-die coating process in detail and to obtain a deeper scientific understanding of the involved processes of perovskite formation which in turn will help us to improve slot-die coated film morphology for improved solar cells.

[1] L. Oesinghaus, J. Schlipf, N. Giesbrecht, L. Song, Y. Hu, T. Bein, P. Docampo, P. Müller-Buschbaum, *Adv. Mater. Interfaces* **2**, 1313-1330 (2016)

[2] Z. Jiang, *J. Appl. Crystallogr.* **48, 3**, 917-926 (2015)

[3] J. Li, R. Munir, Y. Fen, T. Niu, Y. Liu, Y. Zhong, Z. Yang, Y. Tian, B. Liu, J. Sun, D.-M. Smilgies, S. Thoroddsen, A. Amassian, K. Zhao, S. Liu, *Joule* **2**, 1313-1330 (2018)

[4] T. Song, Z. Yuan, F. Babbe, D. P. Nenon, E. Aydin, S. De Wolf, C. M. Sutter-Fella, *ACS Appl. Energy Mater.* **3**, 2386-2393 (2020)

[5] M. T. Sirtl, M. Armer, L. K. Reb, R. Hooijer, P. Dörflinger, M. A. Scheel, K. Tvingstedt, P. Rieder, N. Glück, P. Pandit, S. V. Roth, P. Müller-Buschbaum, V. Dyakonov, T. Bein, *ACS Appl. Energy Mater.* **3, 12**, 11597–11609 (2020)

6.9 Following *in operando* the degradation of printed organic solar cells

K. S. Wienhold, W. Chen, S. Yin, R. Guo, M. Schwartzkopf[1], S. V. Roth[1,2], P. Müller-Buschbaum

[1] DESY, Hamburg, Germany
[2] KTH, Stockholm, Schweden

Organic solar cells offer many potential advantages such as being light-weight, flexible and semi-transparent. Thus, new applications which were not possible with conventional silicon-based photovoltaics become feasible. Examples are solar windows, solar trees, clothes as well as an integration of organic photovoltaics into art and architecture. However, challenges such as the poor long-term stability of most organic solar cells has to be overcome and an up-scaling of the fabrication process has to be realized on the way to marketability.

Thus, we print active layers of organic solar cells using a meniscuis-guided slot-die coating technique. We study the degradation of the high-efficiency polymer donor PBDB-T-SF and the nonfullerene small molecule acceptor IT-4F under illumination. [1] PBDB-T-SF:IT-4F is printed out of chlorobenzene and 0.25 vol % 1,8-diiodooctane. The evolution of inner morphology is probed *in operando* with grazing incidence small-angle X-Ray scattering (GISAXS). (Figure 6.16) Simultaneously, Current-Voltage (JV) characteristics are probed to relate the degradation of device performance to morphological changes in the active layer. To rule out chemical degradation, the experiment is performed at stable temperature and under vacuum conditions. Thus, altering the chemical structure of the active material by reactions with oxygen or water is ruled out. In addition, the window of the vacuum chamber is non-transparent to UV-light and thus UV-light induced degradation of the active materials or the ZnO layer are prevented.

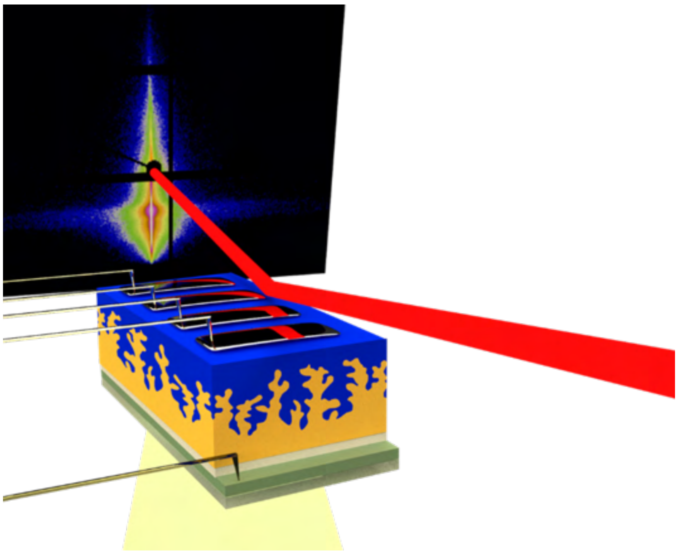

Figure 6.16:
Illustration of the *in operando* experiment to probe the evolution of inner morphology of the active layer with GISAXS under illumination of the organic solar cell. The X-Ray impinges the active layer. The scattering pattern provides information on the inner morphology. Simultaneously, Current-Voltage characteristics are probed.

In the *in operando* experiment, we found the degradation of the short-circuit current density (J_{SC}) to be the driving factor for the degradation of the device performance. [1] Furthermore, we developed a new model to predict the degradation of the normalized J_{SC} in an organic solar cell during operation. [1] In this model, the degradation of the normalized J_{SC} is related to a changing geometrical factor, the interface-to-volume ratio of the polymer cylinders in the active layer. The interface-to-volume ratio is given by the relative circumference C of the polymer cylinder (defined as the circumference of the cylinder normalized on the cross-sectional area).

The evolution of the J_{SC} under illumination is described by

$$J_{\mathrm{SC}}^{\mathrm{norm}}(t) = \frac{J_{\mathrm{SC}}(t)}{J_{\mathrm{SC}}(0)} = \frac{p \cdot e \cdot I \cdot C(t)}{p \cdot e \cdot I \cdot C(0)} = \frac{\frac{2\pi R(t)}{R(t)^2\pi}}{\frac{2\pi R(0)}{R(0)^2\pi}} = \frac{R(0)}{R(t)}. \tag{6.1}$$

In Equation 6.1, I refers to the light intensity, e is the elementary charge of an electron, and p is the probability that a photon which is absorbed in the donor polymer contributes to the photocurrent. The light intensity I is stable during the *in operando* experiment. As the chemical properties of the active layer do not change during the experiment, p is assumed to be constant. In this model approach, structure parameters R (medium cylinder radii) are determined from the GISAXS experiment.

In Figure 6.17, the evolution of the measured J_{SC} under illumination of a slot-die coated organic solar cell based on PBDB-T-SF:IT-4F is shown (black). The simulated J_{SC} (gray) is calculated based on the structure sizes obtained by the GISAXS experiment which was performed simultaneously. The error bars arise from the GISAXS modeling error.

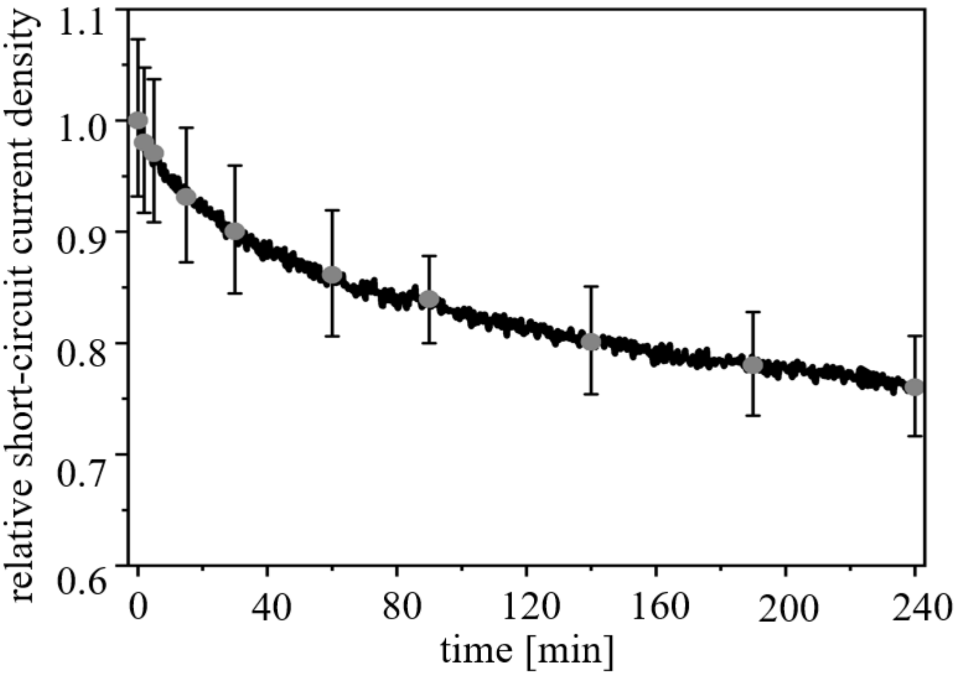

Figure 6.17:
Degradation of the normalized short-circuit current density under illumination of an organic solar cell. The measured J_{SC} (black) is in good agreement with the calculated J_{SC} (gray).

The calculated J_{SC} is in good agreement with the measured J_{SC}. Thus, the reduction of the interface-to-volume ratio of the polymer domains is found to be the driving factor for the degradation of PBDB-T-SF:IT-4F-based, printed organic solar cells. The present work provides insight into the physical degradation mechanism and evolution of inner morphology of organic photovoltaics under illumination. Thus, this work is an important step toward further optimization of device performance and long-term stability of printed organic solar cells.

[1] K. S. Wienhold, W. Chen, S. Yin, R. Guo, M. Schwartzkopf, S. V. Roth, P. Müller-Buschbaum, *Solar RRL* **4**, 2000251 (2020)

7 Instrumentation and new materials

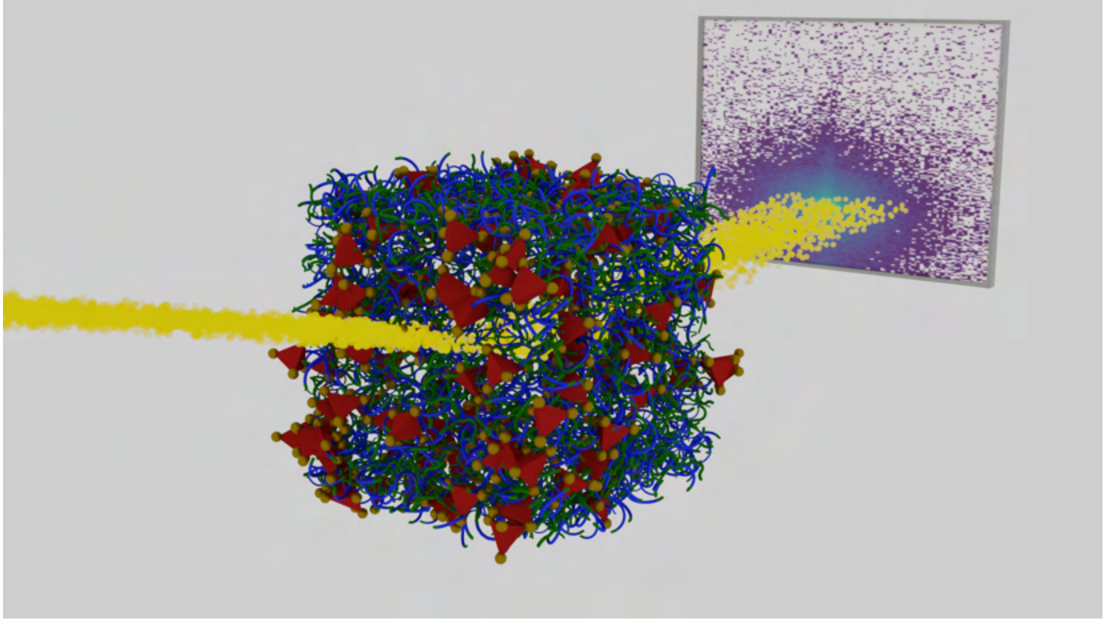

7.1 Non-destructive quanitification of lithium and electrolyte losses in cylinder-type Li-ion batteries

D. Petz, P. Müller-Buschbaum, A. Senyshyn[1]

[1] MLZ, Garching, Germany

Operation of lithium-ion batteries is supplemented by a mass transfer of lithium between two electrodes, where lithium diffusion proceeds through organic electrolyte. While the cell is being charged/discharged the lithium-ions get de-/intercalated from one electrode to the other and vice versa which also creates a decoupled electron transport. There is a selection of materials for battery applications: as cathode a range of lithium transition-metal oxides are typically used (e.g. $LiCoO_2$, $LiMn_2O_4$, $LiNi_{0.8}Co_{0.15}Al_{0.05}O_2$, $LiFePO_4$, etc.), as anode typically graphite or zero-strain lithium titanium oxide $Li_4Ti_5O_{12}$ are used. Electrolyte is often composed by a series of aprotic organic non-aqueous solvents and lithium salts ($LiPF_6$ etc.)

Intense cell operation is supplemented by a certain cell aging, where the amount of active lithium (movable lithium participating in the intercalation process) reduces due to different side reactions between electrolyte, electrode materials, current collectors and Li-ions. Among these, the formation of the so called solid-electrolyte-interface on the graphite anode is the dominant factor.

In the rolled over cell design the materials are not isotropically distributed (as sketched in Fig.7.1a). Furthermore heterogeneities in the distribution of current densities, temperature, pressure, reaction rate, etc. may occur and by this affect non-uniformities of lithium distribution inside the battery electrodes [1]. The increase of cell aging affects and facilitates lithium heterogeneities further [2]. As mentioned above, the primary reason for the loss of cell capacity is the side reaction between the negative electrode and the electrolyte, which connects the loss of active lithium to a loss electrolyte.

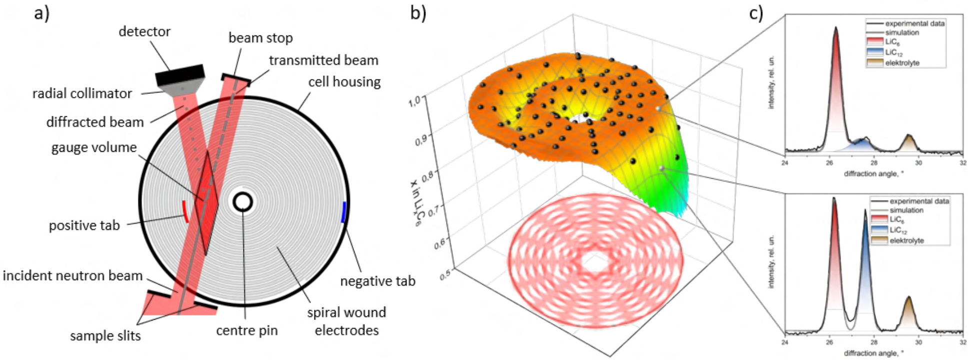

Figure 7.1:
a) Experimental scheme for spatially-resolved neutron powder diffraction experiment, b) Distibution of gauge volumes along with an exemplary reconstruction of the lithium distribution, c) Exemplary diffraction patterns showing the difference in peak intensities of the LiC_6, LiC_{12} and electrolyte reflection.

While the temperature of a battery is lowered down to about 250K the electrolyte freezes and therefore forms a long-range order visible for neutron diffraction[3]. Application of spatially-resolved neutron diffraction at a temperature of 150K was used for a combined quantification of the lithium and electrolyte distribution.

An experimental scheme is shown in Fig.7.1a). With translation and rotation, the small gauge volume ($2 \times 2mm^2$) can be used to map the whole cell (Fig.7.1b) bottom). The relation of the diffraction intensities of the LiC_6, LiC_{12} and the electrolyte refection (Fig.7.1c)) can then be used

for reconstruction of the local lithium concentration x in Li_xC_6 (Fig.7.1b) top).
Initially, an X-Ray computed tomography (Fig.7.2a)) has been performed in order to determine the cell layout with the position and dimension of the current tabs, center pin, electrode thickness, etc. As can be seen, the negative (blue) current tab in positioned close to the cell housing in the lower third of the cell. The positive (red) current tab is located in the middle of the electrode (rolled electrode stripe), whose length is nearly this of the complete height of the electrode stripe.
The lithium concentration x in Li_xC_6 in the graphite anode of the fully-charged cylinder-type cell (Fig.7.2b) left) exhibits a plateau-like lithium concentration with "valleys" of lower Li concentration corresponding to the positions of the positive/negative current tabs and the center pin (Fig.7.2a)). A directly related electrolyte distribution $n_{electrolyte}$ (Fig.7.2c) left) displays a radial-symmetric behaviour with a gradient having lower values in the cell middle and increasing towards higher electrolyte concentration at the cell housing. The gradient remains nearly the same throughout the height of the cell.

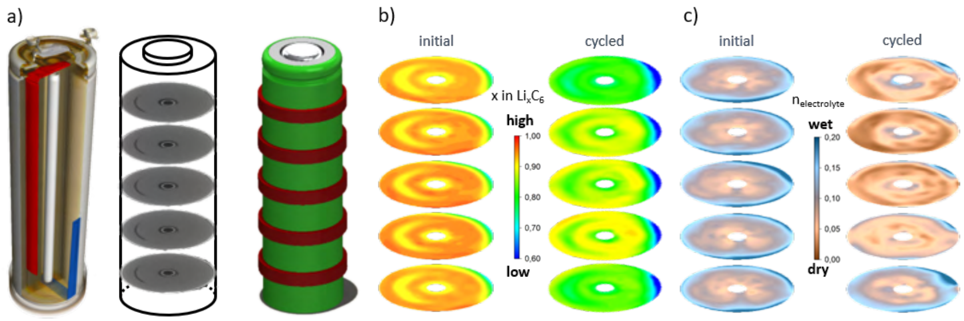

Figure 7.2:
a) Reconstructed cell layout (left) of the investigated commercial 18650-type Li-ion battery with the position of the positive (red) and negative (blue) current tabs obtained from X-Ray CT (gray), b) local lithium concentration x in Li_xC_6 and local electrolyte distribution $n_{electrolyte}$ at five different heights for an inital and cycled (600× at performance limits) cell.

In contrast to the initial state the lithium concentration in the cycled cell (Fig.7.2b) right) displays a generally lower lithium concentration and a remarkable height gradient with lower values towards the bottom and top of the cell.
The amount of electrolyte in the cycled cell (Fig.7.2c) right) displays lower values with remaining radial gradient. Besides this a remarkable height gradient is built up, whose character is different for lithium and electrolyte distributions, where lower lithium concentrations are observed at the top and bottom of the cylinder cell, whilst the electrolyte displays its maximum concentration at the bottom of the cell and the lowest content at the top. This height gradient can be associated with gravity effects as the cell was cycled and measured in the displayed orientation, where the liquid electrolyte accumulates at the bottom.
The above-mentioned findings suggest a non-uniform cell aging, which may lead to lower energy/power densities and shorter lifetimes due to internal heterogeneities and the development of local stresses. The obtained results can help the development of cell layouts resulting in a more homogeneous electrode aging, potentially increasing the cell performance without sophisticated material tuning.

[1] A. Senyshyn, M. J. Mühlbauer, O. Dolotko, M. Hofmann, H. Ehrenberg, *Sci. Rep* **5**, 18380 (2015)

[2] D. Petz, M. J. Mühlbauer, V. Baran, M. Frost, A. Schökel, C. Paulmann, Y. Chen, D. Garcés, A. Senyshyn, *J. Power Sources* **488**, 227446 (2020)

[3] A. Senyshyn, M. J. Mühlbauer, O. Dolotko, H. Ehrenberg, *J. Power Sources* **282**, 235-240 (2015)

7.2 Tack properties of pressure-sensitive adhesive-coated fibers

V. Körstgens, J. Corella Puertas, P. Müller-Buschbaum

Pressure sensitive adhesives (PSAs) constitute a class of adhesives that form a bond to a surface when slight pressure is applied on them. The stickiness of PSAs is based on its visco-elastic properties and no solidification by a cross-linking process or solvent evaporation is involved. There are a multitude of applications that range from industrial applications as in the assembling of mobile phones to scotch tape and sticky notes. Another application used in daily life is in hair styling products like hair gels. In order to quantify the adhesive properties and investigate the debonding mechanisms of PSAs the probe-tack test is a well-established methodology [1]. The probe-tack test uses a cylindrical probe approaching a flat PSA surface. For the investigation of adhesive layers on curved surfaces the method has to be adapted. We developed a new methodology for characterizing the adhesion of PSAs on fiber assemblies. This methodology is tested on assemblies of either human hair or nylon fibers coated with a polymer blend representing a PSA with tack properties depending on humidity conditions. A prerequisite for meaningful tack measurements on fibers is the reproducible preparation of homogeneous samples. We developed a method to densely align fibers in parallel on a substrate as a monolayer without harming the surface properties of the individual fibers [2]. In Fig. 7.3(a) the general concept of the tack measurement technique is demonstrated. Fig. 7.3(b) shows the top view of human hair fibers with (78±32) μm diameter attached to a glass slide. The optical microscopy image shows the close contact of the individual fibers. In a zoom-in Fig. 7.3(c) distinct surface features of the fibers like the cuticle structure of hair before coating and the surface after polymer coating, respectively.

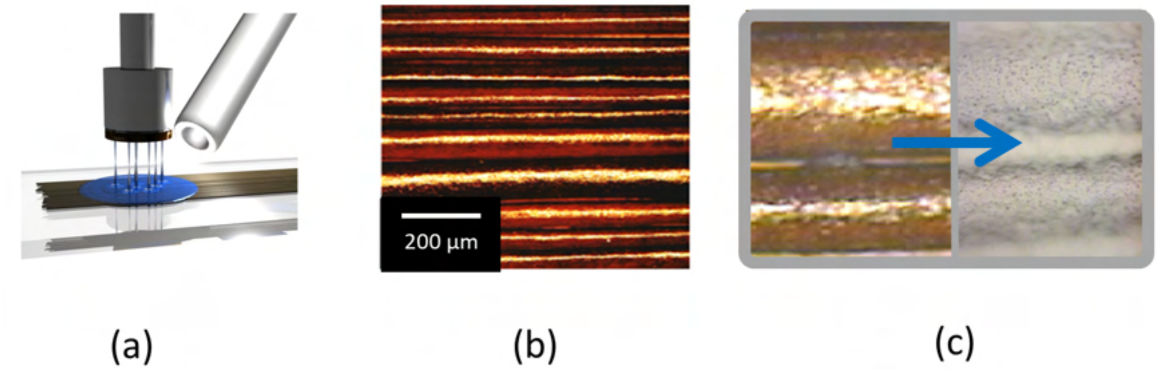

Figure 7.3:
(a) Illustration of a tack experiment of a polymer film on an array of parallel-aligned fibers attached to a glass substrate. (b) Top view of parallel-aligned human hair (c) Zoom-in on top view of hair sample before and after polymer coating.

As an example for the tack measurement on fibers we coated monolayers of human hair in a solution casting process with a blend of the copolymer polyvinylpyrrolidone-co-polyvinyl acetate (PVP-co-PVA, BASF VA64) and polyethlylene glycol 4000 (PEG) [2]. This polymer blend is investigated as a representative for a PSA with tack properties depending on humidity. The probe in a conventional probe tack test is a flat-ended incompressible cylinder of e.g. stainless steel. In our method we use a composite stamp which consists of natural leather at the top of the probe. Leather is chosen because of its similarity to skin. In this way the investigation of tack properties of polymer blends also used in commercial hair styling compositions mimics the experience of stickiness by touching hair with the fingers after hair styling product had been applied. The probe also contains a polyurethane foam core which allows the adaption of the leather to the probed curved adhesive surface.

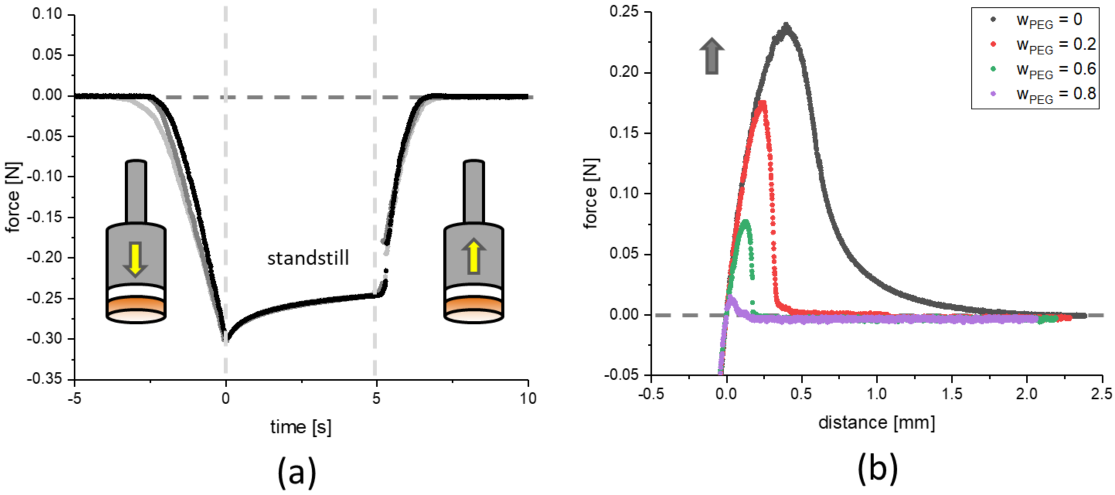

(a) (b)

Figure 7.4:
Tack measurements at 72% RH: (a) example of three individual measurements (light gray, gray, and black symbols) of human hair coated with PEG. Vertical dashed lines separate three phases of the experiment: approach, standstill and pull-off. (b) Force–distance curves for measurements of hair coated with PVP-co-PVA/PEG blend for different PEG content.

The film coated sample of fibers is fixed to the apparatus below the stamp. The stamp moves with a constant velocity of 50 μm/s towards the sample until it touches it with a force of -0.3 N. The stamp remains for 5 s motionless and then is retracted from the sample at a constant velocity of 100 μm/s. During this protocol the force and the distance are recorded. Fig. 7.4(a) shows a full measurement of polymer-coated fibers as measured force versus time. After the stamp stops moving as the maximum chosen force of -0.3 N is reached, relaxation of the measured force is observed. This is mainly due to the visco-elastic nature of the foam core and the leather of the stamp and has only a minor contribution by the thin adhesive layer. The stages of the experiment are given in in Fig. 7.4(a), comprising uniaxial compression (approach) and relaxation during standstill followed by the retraction part of the experiment. The tack measurement on PEG 4000 at 72% RH show the non-adhesive properties of the PEG layer. With increasing content of PVP-co-PVA in the PVP-co-PVA/PEG blend (Fig. 7.4(a)) distinct force maxima are observed in the force–distance curve during the debonding process at pull-off. Hydrogen bonding between PVP and PEG units does play a role in the observed adhesive behavior. However, the maximum adhesive force is measured for pure PVP-co-PVA, which indicates that the plasticizing effect of absorbed water is decisive for the different adhesive properties.This example for the application of the probe tack methodology for fibers shows that PVP-co-PVA is the component of the polymer blend responsible for the tack properties and how increasing the mass fraction of PEG in the polymer blend allows for the adjustment of tack properties at high humidity conditions. These reproducible measurements prove the concept of the customized tack experiment for such class of materials.

[1] P. Müller-Buschbaum, T. Ittner, E. Maurer, V. Körstgens, W. Petry, *Macromol. Mater. Engin.* **292**, 825-834 (2007)

[2] V. Körstgens, J. Corella Puertas, P. Müller-Buschbaum, *ACS Appl. Polym. Mater.* **2**, 3189-3195 (2020)

7.3 Solid electrolyte interface formation on silicon based anodes for lithium-ion batteries watched by neutron reflectometry

S. J. Schaper, H. Xie[1], M. Haese[2], G. Mangiapia[2], J. M. Buriak[1], P. Müller-Buschbaum

[1] University of Alberta, Edmonton, Canada
[2] GEMS at MLZ, Garching, Germany

Lithium-ion batteries (LIBs) still attract a lot of interest from industrial and academic research since there is still a large potential for improvements. For a well working, stable LIB the single components of the LIB, current collectors, anode, cathode, electrolyte, and separator have to match each other. So the interfaces and their development during use of the LIB are crucial for a reliable device. Especially, a electrochemically well engineered interface between the anode and the electrolyte is important. Already during the first charge of the LIB a solid electrolyte interface (SEI) is formed between the anode and the liquid electrolyte. This SEI is a passivating layer and prevents the electrolyte from corrosion. But a too thick SEI adds an additional internal resistance to the LIB and decreases its performance.

Silicon (Si) anodes for LIBs exhibit a high theoretical capacity of 3590 mA h g^{-1}, one magnitude higher than commonly used graphite, but they suffer a large volume expansion of around 300 % during cycling [1]. Changing the anode material requires re-optimization of the liquid electrolyte and the resulting SEI. Previous work showed that adhesion layers, alloying Si with titanium (Ti) and also 10 nm thin coatings have a large influence on the stability of the silicon based anode, hence also the cell [2]. Thereby, the role of the forming SEI is significant.

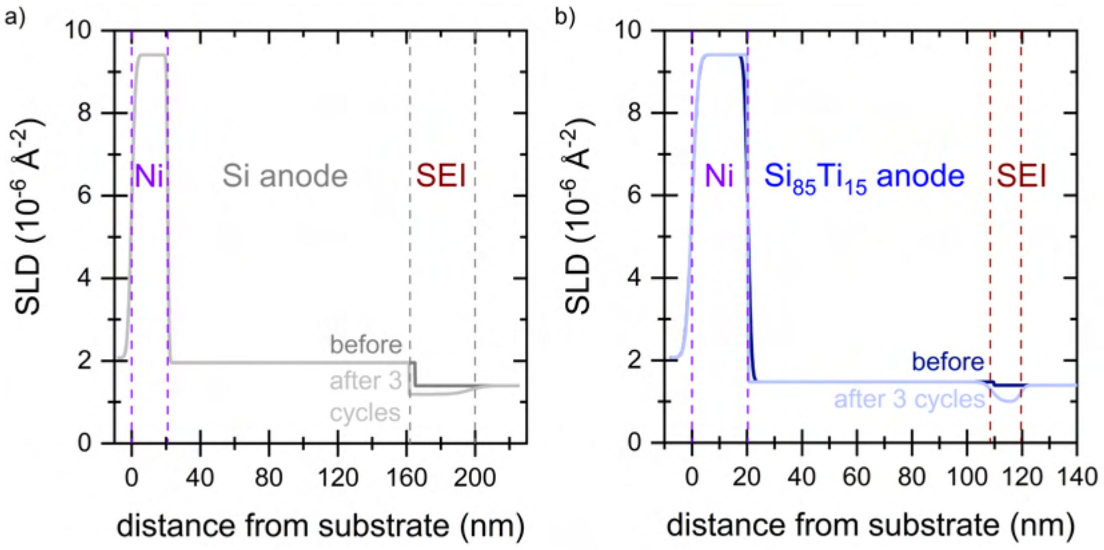

Figure 7.5:
Scattering length density (SLD) profiles from neutron reflectometry of a) Si anode and b) Si$_{85}$Ti$_{15}$ anode before and after three cycles at 0.4 C, respectively.

To reveal the influence of the initially forming SEI on Si-based anodes, *in situ* time-of-flight neutron reflectometry (TOF NR) measurements *dum operandum* are performed at the REFSANS beamline at the MLZ [3]. The anodes are prepared via sputter deposition on Si wafers. A 20 nm thick nickel (Ni) adhesion layer is also blocking lithium ions from migration into the substrate. Onto the Ni adhesion layer a 100 nm thick Si anode or Si$_{85}$Ti$_{15}$ alloy anode is deposited. A custom-built cell enables the TOF NR measurements at the beamline. Metallic lithium is used as counter electrode and copper current collectors serve as contacts. Both cells were cycled at 0.4 C. The TOF NR data is modeled and fitted using the MOTOFIT plugin for Igor [4].

In situ TOF NR measurements before and after the first three cycles show significant differences in the formed SEI (see Fig. 7.5). For the Si anode a SEI of 40 nm is formed, while the $Si_{85}Ti_{15}$ alloy anode's SEI is only 15 nm thick. The lower neutron scattering length density (SLD) of the SEI forming on the $Si_{85}Ti_{15}$ alloy compared to the SEI forming on Si suggests a higher content of low SLD compounds like lithium in the SEI.

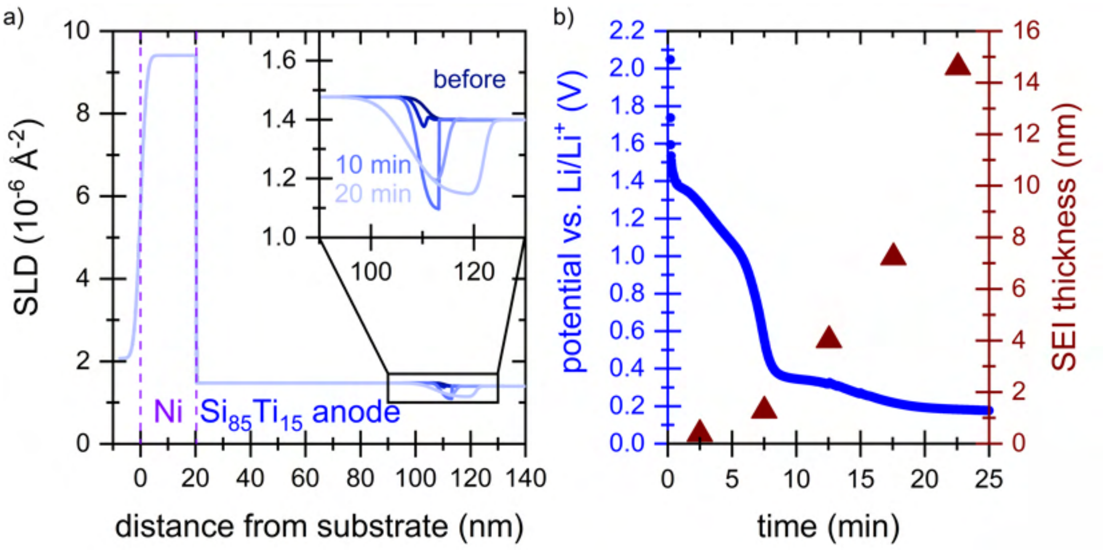

Figure 7.6:
Formation of the SEI on the $Si_{85}Ti_{15}$ anode during first lithiation at 0.4 C. a) Scattering length density (SLD) profiles from neutron reflectometry for the first 20 min, recorded in steps of 5 min. b) Potential vs. Li/Li$^+$ and SEI thickenss evolution with time.

The *in situ* TOF NR measurements during cycling enable a closer look into the formation process of the initial SEI on the $Si_{85}Ti_{15}$ alloy anode (see Fig. 7.6). After 5 min of lithiation there is only a little fluctuation of the SLD at the interface between the $Si_{85}Ti_{15}$ anode and the electrolyte visible. After 10 min a very thin SEI is formed with a SLD close to the final one, suggesting that the chemical composition and density of the SEI is already established. This SEI grows to its final thickness of 15 nm within the first 20 min of lithiation. During the growth in thickness the SLD of the SEI shows only little changes. Hence, the composition of the SEI is established before its final thickness.

Comparing these results to the stability of these two anodes over 200 cycles [2], the thinner SEI of the $Si_{85}Ti_{15}$ anode could be a reason for the higher capacity retention compared to the Si anode. However, the SEI formed on the $Si_{85}Ti_{15}$ anode has a lower SLD, which could explain the higher cumulative irreversible capacity loss.

The *in situ* TOF NR measurements *dum operandum* enable a fundamental understanding of the formation and growth of the SEI on these high-performance LIB anodes. This fundamental understanding is necessary to optimally design the SEI for silicon based anodes. Finding the best SEI composition and thickness is crucial for the long term stability, performance, and usability of the next generation LIBs.

[1] M. Ashuri, Q. He, L. L. Shaw, *Nanoscale* **8**, 74–103 (2016)

[2] H. Xie, S. Y. Sayed, W. P. Kalisvaart, S. J. Schaper, P. Müller-Buschbaum, E. J. Luber, B. C. Olsen, M. Haese, J. M. Buriak, *ACS Appl. Energy Mater.* **3**, 1609–1616 (2020)

[3] J.-F. Moulin, M. Haese, *JLSRF* **1**, A9 (2015)

[4] A. Nelson, *J. Appl. Cryst.* **39**, 273-276 (2006)

7.4 A flexible solar simulator measuring setup for inert atmospheres

L. V. Spanier, R. Funer, P. Müller-Buschbaum

The advent of novel solar cell materials such as organic and perovskite solar cells has sparked a rapid growth in research to increase their respective efficiencies and application use-cases, so far unprecedented in optoelectronic materials. Their high efficiency of up to 18.2% [1] and 25.5% [2] for organic and perovskite cells respectively, and their comparatively simple means to manufacture, as opposed to traditional thin-film materials, makes them ideal candidates for supplementing or even superseding commonly used silicon-based solar cells. This, however, comes at the cost of reduced chemical stability of these materials, which causes a notable decrease of device efficiency in the course of several days or sometimes even minutes.

In order to better understand these degradation processes [3], we developed a solar simulator setup for integration into a glovebox to conduct more accurate and reliable measurements on the energy conversion efficiency of the pristine solar cell materials. To minimize its space requirements, the setup was directly integrated into the floor of the glovebox, with the Class AAA solar simulator located underneath (see Fig. 7.7 for an explosion view). The combination of a xenon arc lamp light source and an all-fused-silica optical system create an excellent UV-transmissivity, enabling even the simulation of a space like solar spectrum for AM0 measurements.

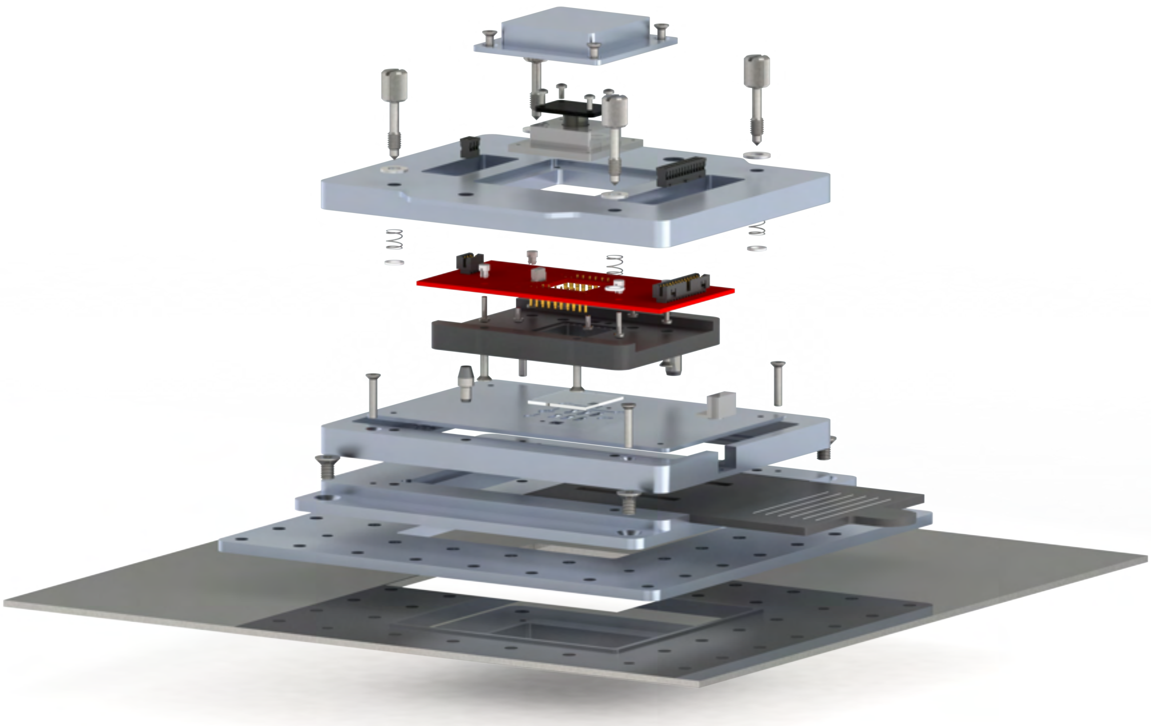

Figure 7.7:
Explosion view of the measuring setup of the solar simulator. The light source is positioned below the cutout in the bottom plate, illuminating the sample located in the bottom-half of the setup from the underside. The top-half of the setup houses the spring-loaded connectors to the solar cell as well as all additional instrumentation on light-intensity and temperature.

The solar cells are placed onto an exchangeable optical mask in the bottom-half, that defines the illuminated cell area, so that the setup can be easily adapted to a wide variety of cell geometries. All mechanical parts are designed for easy, save, and efficient operation inside the glovebox, i.e. for quick manual sample exchange without the need of external tools. The electrical contacts to the solar cells enable four-point measurements, established by a set of spring-loaded connectors located inside the top-half of the setup (see Fig. 7.8). Multiple guiding-pins and captive screws around the top-half aid in securely positioning and mounting the electrical contacts, preventing both scratching and uneven contact pressure especially for flexible solar cells.

Figure 7.8:
Detail view of a prototype system for contacting solar cells by means of spring-loaded connectors. The spring deflection of the connectors is limited by a flat stop surface onto which the solar cell is pressed, so that the solar cell's nano-layers are not damaged.

To both increase the precision of our efficiency measurements and to take maximum power point tracking measurements at varying light levels, a pair of light-intensity sensors is used for reference, enabling a real-time monitoring of the solar simulator's light source, while the solar cell's temperature can be assessed using two temperature sensors. This additional instrumentation suite is controlled through an I^2C-bus, making it easily expandable to allow future upgrades as for example to directly monitor the temperature of the solar cell by means of an integrated IR-camera. All sensors and spring-loaded connectors are positioned on a common printed circuit board to allow a quick and easy exchange for various solar cell geometries or in case of a sensor failure.

This setup enables us to take precise measurements on organic, perovskite, quantum-dot, and dye-sensitized solar cells in their pristine state, allowing for a better understanding of these novel materials.

[1] Q. Liu, Y. Jiang, K. Jin, J. Qin, J. Xu, W. Li, J. Xiong, J. Liu, Z. Xiao, K. Sun, S. Yang, X. Zhang, L. Ding, *Science Bulletin* **65.4**, 272-275 (2020)

[2] M. Green, E. Dunlop, J. Hohl-Ebinger, M. Yoshita, N. Kopidakis, X. Hao, *Prog. Photovolt. Res. Appl.* **29**, 3-15 (2021)

[3] F. C. Löhrer, C. Senfter, C. J. Schaffer, J. Schlipf, D. M. González, P. Zhang, S. V. Roth, P. Müller-Buschbaum, *Adv. Photonics Res.* **1**, 2000047 (2020)

7.5 3D-printed spherical environmental chamber for neutron experimentation

T. Widmann, P. Müller-Buschbaum

Responsive or 'smart' polymers undergo a strong change in one or multiple physical properties under the change of an external stimulus. Such stimuli can be for example changes in irradiation, pH-value, temperature, or humidity, which then lead to changes in conductivity, viscosity, or volume [1,2]. In order to choose and optimize such a material for a specific application, it is essential to have a good understanding of this responsive behavior. As such, suitable measurement techniques and sample environments are of utmost importance.

For the investigation of thin film soft matter samples via neutron reflectometry and grazing incidence small angle neutron scattering, we designed a spherical environmental chamber as shown in Figure 7.9a [3]. The spherical design is chosen to prevent condensation due to temperature gradients at edges and corners. Additionally, the chamber features liquid channels within its walls, better visible in Figure 7.9b, which help to optimize the homogeneity of the heat distribution within the chamber. The overall path length of the channels in the chamber is 2.4 m and assures a good heat transfer.

The chamber is produced via selective laser melting, a 3D metal printing procedure from a powder bed, using the metal alloy AlSi10Mg. The final print, shown in Figure 7.9c weighs 1.9 kg. There are four brass hose nipples for the fluid connection and two blue aluminum compression fittings that connect to an external gas-flow set-up, which is used to control the atmospheric composition within the chamber. A shrink-fitted flange, visible at the lower right, is used to connect electronics inside the chamber. The oval windows, which allow incident angles of up to 5° are covered by a 0.1 mm aluminum foil for minimal attenuation of the neutron beam.

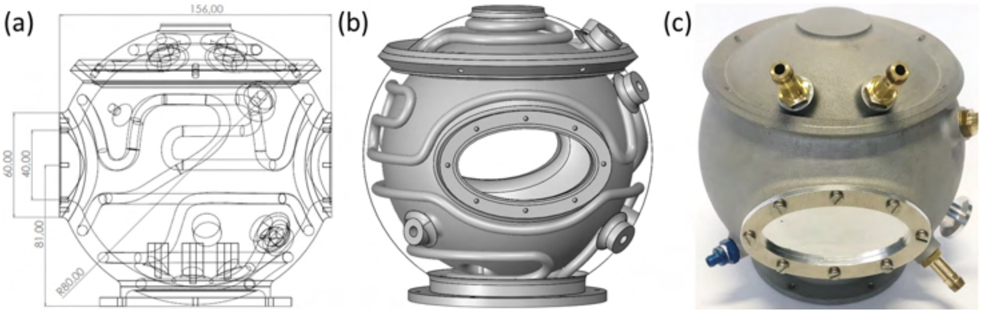

Figure 7.9:
Spherical environmental chamber as sample environment for neutron experiments. a) The wire frame model shows the dimensions of the design. b) A view through the outer surface of the chamber, revealing the liquid channels spanning around the whole chamber. c) The 3D metal printed chamber with connectors for electronics, gas, and liquid flow. The windows are covered with an aluminum foil clamped by aluminum rings.

In order to investigate the temperature stability and switching dynamics of the chamber, simulations using SolidWorks Flow Simulation were conducted and compared with real laboratory experiments using two thermal baths. We started with a 20 °C preheated chamber switching to a 50 °C preheated liquid flow and vice versa. In Figure 7.10a the temperature evolution of the central cross section is shown as a contour color plot with each color corresponding to a 1 °C temperature range. An elliptical profile around the center of the chamber is visible. The simulated and the measured temperature at the center of the chamber is plotted against the time in

Figure 7.10b and c for the heating and the cooling switch, respectively. We see a rapid change of the temperature within the chamber and a good agreement between simulation and experiment.

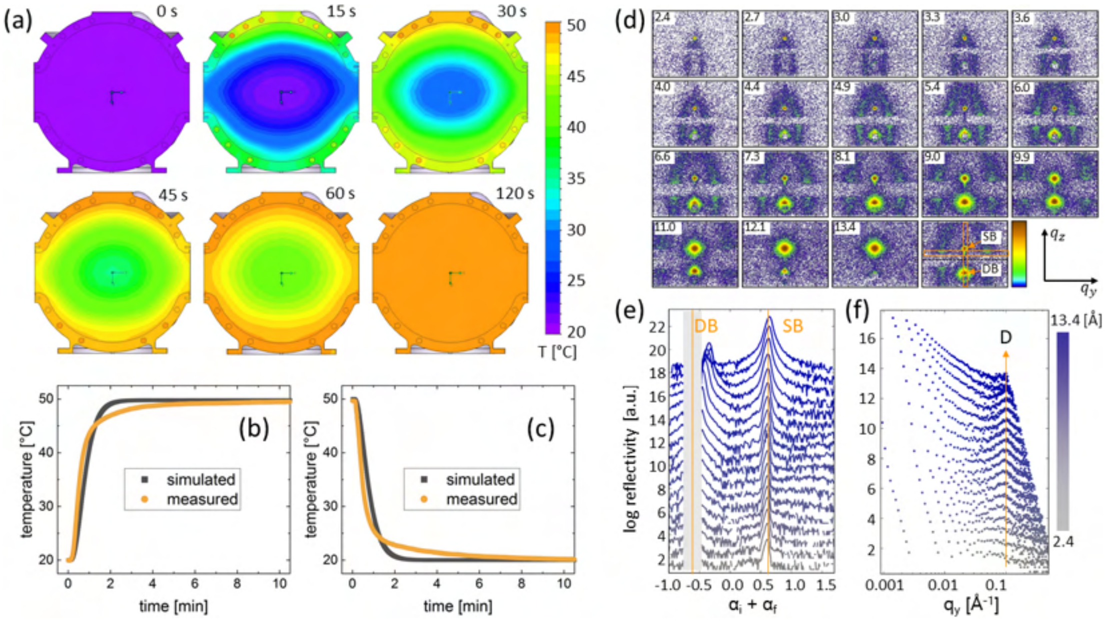

Figure 7.10:
a) Sectional views during a heating simulation, depicted as contour plots with 1 °C isothermals. Temperature at the center of the chamber during the simulation and the lab experiment for b) the heating from 20 to 50 °C and c) the cooling from 50 to 20 °C. d) 2D ToF-GISANS data of a PS-d8-b-PMMA thin film. Selected 10 % wavelength slices from 2.4 to 13.4 Å are depicted. The direct beam (DB) and specular beam (SB), as well as the integration boxes for the vertical and horizontal cuts are indicated in the last image. e) Vertical and f) horizontal line cuts. The Bragg feature is marked by the arrow as D.

Additionally, the performance of the chamber was tested in an actual neutron experiment. Therefore, we prepared a thin film sample of a deuterated diblock copolymer, namely PS-d8-b-PMMA, and measured GISANS in time of flight mode (ToF) on it. The experiments were performed under stable ambient conditions, set to 30 %RH and 20.4 °C. Figure 7.10d shows 18 selected wavelength slices from 2.4 to 13.4 Å, revealing a ring-shaped intensity, which indicates a defect-rich micro-phase separated structure. We find a similar signal to noise ratio compared to previous measurements indicating that secondary scattering from the chamber itself is not detected. The vertical and horizontal line cuts are plotted for all 18 wavelength slices in Figure 7.10e and f. In the horizontal line cuts we find the position of the Bragg peak arising from the micro phase separation and extract a structure size of 14 ± 1 nm with a structure distance of 58 ± 4 nm. They correspond to the PS domain size and the interdomain distance within the PMMA matrix, respectively. Overall the chamber provided a stable temperature and humidity while adding no additional background to the measurement and is a promising tool for future neutron experiments.

[1] T. Widmann, L. P. Kreuzer, N. Hohn, L. Bießmann, K. Wang, S. Rinner, J.-F. Moulin, A. J. Schmid, Y. Hannappel, O. Wrede, M. Kühnhammer, T. Hellweg, R. v. Klitzing, P. Müller-Buschbaum, *Langmuir* **35**, 16341-16352 (2019)

[2] L. P. Kreuzer, T. Widmann, L. Bießmann, N. Hohn, J. Pantle, R. Märkl, J.-F. Moulin, V. Hildebrand, A. Laschewsky, C. M. Papadakis, P. Müller-Buschbaum, *Macromolecules* **53**, 2841–2855 (2020)

[3] T. Widmann, L. P. Kreuzer, P. Müller-Buschbaum, *Rev. Sci. Instrum.* **91**,113903 (2020)

7.6 Antiferromagnetically coupled anti-phase domains under external field

U. Zweck[1], M. Leitner[1]

[1] MLZ, Garching, Germany

Ni_2MnZ based Heusler compounds have attracted a considerable amount of attention due to their various appealing properties such as the ferromagnetic shape-memory effect or the magnetocaloric effect. Since the magnetic properties are very sensitive to the degree of structural order in these systems [1], understanding the correlation of these two ordering parameters is crucial. The magnetic moments are mainly carried by the Mn atoms, which interact ferromagnetically in the $L2_1$-ordered state. However, it has been found that at structural antiphase domain boundaries (APBs) the magnetization tends to reverse, leading to atomically sharp ferromagnetic domain walls [2]. In a previous small-angle neutron scattering experiment at SANS-1 at the FRM II, Garching, under zero magnetic field we investigated the relation of structural and magnetic microstructure in powder samples of Ni_2MnAl and $Ni_2MnAl_{0.5}Ga_{0.5}$ in different annealing states and demonstrated that their characteristic length scales are of the same size.

To clarify the reason of this relation we studied further the influence of coupling across APBs by applying small-angle neutron scattering under external magnetic fields. Since the scattering signal is sensitive to the component of the magnetization perpendicular to $\vec{Q}$, we can distinguish between two possible scenarios of exchange coupling across APBs: In the first case there is no exchange coupling across APBs, leading to isolated ferromagnetic antiphase domains (APDs). The magnetic scattering signal of this scenario corresponds to that of ferromagnetic nanoparticles under a magnetic field. Under zero magnetic field the signal is isotropic, however applying an external magnetic field results in a redistribution of intensity in the SANS signal perpendicular to the magnetic field [3]. In the second scenario the APDs couple antiferromagnetically across APBs, displaying a behaviour similar to that of an elemental antiferromagnet. Here the spins align perpendicular to already small external magnetic fields, corresponding to a redistribution of intensity in the SANS signal along field direction.

The magnetic SANS experiment was carried out at the instrument D33 at the Institute Laue-Langevin (ILL), Grenoble, France. To study powder samples in different annealing states we used the same sample-to-detector distance for each sample and unpolarized incident neutrons with a mean wavelength of $\lambda = 5\,\text{Å}$. We measured the SANS signal in a temperature range of $50\,\text{K}$ to $500\,\text{K}$ and applied a magnetic field perpendicular to the incident beam in a range of $0\,\text{mT}$ to $640\,\text{mT}$. To distinguish between the two scenarios we compare the 2D detector images of measurements under zero magnetic field and with a small magnetic field present at temperatures well below the Curie temperature of the sample. The obtained 2D detector images of the sample Ni_2MnAl 10 d annealed, $T_C = 368\,\text{K}$, are shown in figure 7.11. Figure 7.11a) depicts the detector image of the measurement at 60 K under zero magnetic field. Here we observe an isotropic scattering picture from our powder sample, corresponding to an isotropic spin distribution in our sample. The 2D detector image of the measurement at 60 K with an applied magnetic field of 640 mT is illustrated in figure 7.11b). With a $B-$field present we see a distinct redistribution of intensity into the horizontal direction, corresponding to an elongation of the signal along the field direction. This redistribution indicates spins aligning perpendicular to the magnetic field.

In order to quantify the anisotropy of the scattering profiles we study the ratio of horizontal to vertical summed up intensities r. Figure 7.12 depicts the ratio of the system $Ni_2MnAl_{0.5}Ga_{0.5}$ in three annealing states 30 min, 3 h and 10 d in a temperature range of 50 K to 450 K with an applied magnetic field of 640 mT. Increasing the temperature from 50 K towards the transition temperature T_C the anisotropy decreases slowly. Approaching T_C the ratio declines from $r > 1$

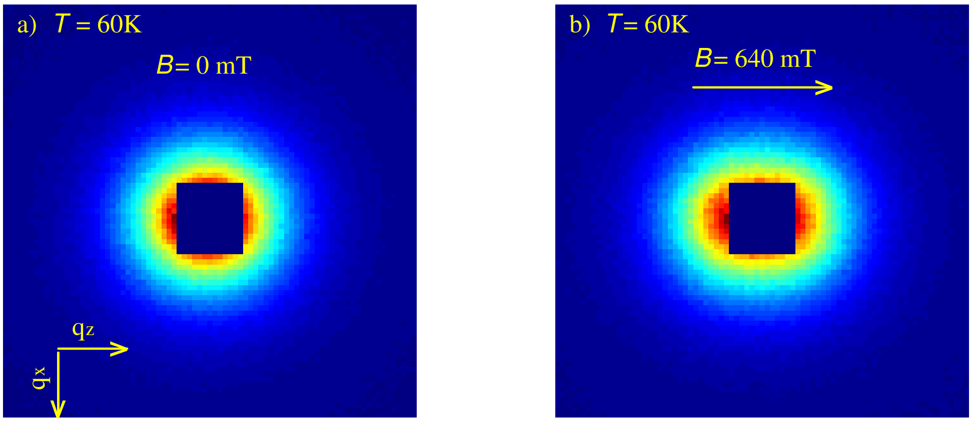

Figure 7.11:
2D SANS profiles of Ni_2MnAl 10 d annealed at 60 K a) under zero magnetic field and b) with a horizontally applied magnetic field of 640 mT.

to $r < 1$, indicating a change in the predominant spin orientation, turning them from perpendicular into parallel alignment to the $B -$ field. Increasing the temperature further the ratio increases again until it converges to 1, corresponding to the paramagnetic state.

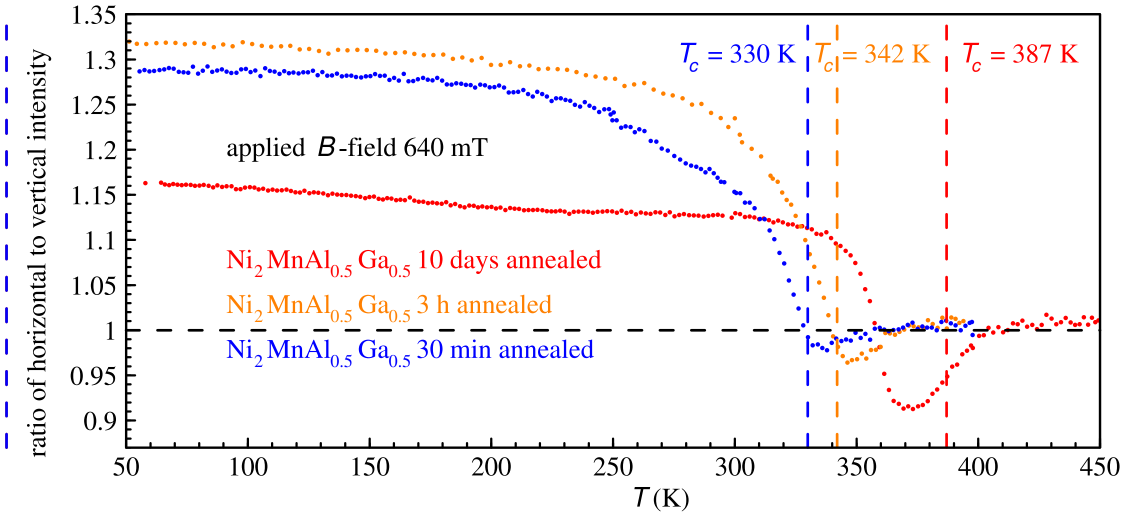

Figure 7.12:
Temperature dependent ratio of horizontal to vertical summed up intensities of the samples $Ni_2MnAl_{0.5}Ga_{0.5}$ 30 min, 3 h and 10d annealed with a B-field of 640 mT applied. The magnetic transition temperatures T_c of the samples were determined in differential scanning calorimetry measurements.

We observe this redistribution of intensity for samples of both alloy systems in all annealing states. From the presented results it can be clearly seen that we obtain signals from our powder samples similar to the temperature dependent response of an antiferromagnet in a magnetic field. This supports our model of antiferromagnetically coupled APDs.

[1] P. Neibecker, M. Leitner, G. Benka, W. Petry, *Appl. Phys. Lett.* **105**, 261904 (2014)

[2] H. Ishikawa, R. Y. Umetsu, K. Kobayashi, A. Fujita, R. Kainuma, K. Ishida, *Acta Mater.* **56**, 4789 (2008)

[3] W. Wagner, A. Wiedenmann, W. Petry, A. Geibel, H. Gleiter, *J. Mater. Res* **6**, 2305 (1991)

8 Teaching and outreach

8.1 Lectures, seminars and lab courses

Spring Term 2020

Prof. Dr. Peter Müller-Buschbaum, Dr. Volker Körstgens,
Angewandte Physik: Polymerphysik 2
Prof. Dr. Christine Papadakis, *Nanostructured Soft Materials 2*
Dr. Michael Leitner, *Materialphysik auf atomarer Skala 2*
Prof. Dr. Peter Müller-Buschbaum, Prof. Dr. Christian Große, *Mess- und Sensortechnologie*
Prof. Dr. Winfried Petry, *Physics with neutrons 2*
Prof. Dr. Christine Papadakis, *Höhere Physik 2*
Prof. Dr. Peter Müller-Buschbaum, *Seminar: Current problems in organic photovoltaics*
Prof. Dr. Peter Müller-Buschbaum, Prof. Dr. Christine M. Papadakis,
Bachelor-Seminar: Funktionelle weiche Materialien
Prof. Dr. Peter Böni, Dr. Alexandros Koutsioumpas, Dr. Christoph Morkel, Prof. Dr. Peter Müller-Buschbaum, Dr. Markos Skoulatos, *Seminar Neutronen in Forschung und Industrie*
Prof. Dr. Peter Müller-Buschbaum, Prof. Dr. Christine M. Papadakis,
Seminar: Structure und dynamics of condensed matter
Prof. Dr. Peter Müller-Buschbaum, Prof. Dr. Christine M. Papadakis, *Seminar: Polymers*

Autumn Term 2020/21

Prof. Dr. Peter Müller-Buschbaum, Dr. Volker Körstgens,
Angewandte Physik: Polymerphysik 1
Prof. Dr. Christine Papadakis, *Nanostructured Soft Materials 1*
Dr. Michael Leitner, *Materialphysik auf atomarer Skala 2*
Prof. Dr. Winfried Petry, *Physics with neutrons 1*
Prof. Dr. Peter Müller-Buschbaum, *Seminar: Current problems in organic photovoltaics*
Prof. Dr. Peter Böni, Dr. Christian Franz, Dr. Christian Lang, Dr. Christoph Morkel, Prof. Dr. Peter Müller-Buschbaum *Seminar Neutronen in Forschung und Industrie*
Prof. Dr. Peter Müller-Buschbaum, Prof. Dr. Christine M. Papadakis,
Seminar: Structure und dynamics of condensed matter
Prof. Dr. Peter Müller-Buschbaum, Prof. Dr. Christine M. Papadakis, *Seminar: Polymers*
Prof. Dr. Winfried Petry, Tobias Chemnitz, *Master course Radiation Biology: Neutrons for medicine*

Lab Courses 2020

Rasterkraftmikroskopie (Fortgeschrittenenpraktikum)
Neutron scattering at FRM II (Fortgeschrittenenpraktikum)
Darstellung von DNS im Rasterkraftmikroskop (Fortgeschrittenenpraktikum)
Charakterisierung von Polymeren mittels Dynamischer Differenzkalorimetrie (Fortgeschrittenenpraktikum)

8.2 Conferences and public outreach

Lund Institute of Advanced Neutron and X-Ray Science (LINXS) in collaboration with the
Heinz Maier-Leibnitz Zentrum Garching
NINXMACH, Workshop
02 – 04 March 2020, FRM II/MLZ Garching

NINXMACH 2020 took place from 2 to 4 March 2020 at the FRM II and was the 2nd GeoArchaeology Try-out workshop organized by the Lund Institute of Advanced Neutron and X-Ray Science (LINXS) in collaboration with the Heinz Maier-Leibnitz Zentrum (MLZ) inviting archaeologists and geologists to learn more about measurements with neutrons by means of computed tomography and prompt-gamma activation at the FRM II instruments ANTARES (imaging instrument for neutron radiography with cold neutrons), PGAA (prompt gamma activation analysis for trace elements) and NECTAR (Neutron radiography with thermal and high-energy fission neutrons), and the support of radiation protection for short-time irradiation gamma scans for rough composition/major elemental determination. The workshop consisted of lectures and hands-on exercises using own samples that were brought by the participants and testing different methods, types of radiation and instruments, before a full beam time proposal is written. This workshop also offered the opportunity to compare with experiments performed at synchroton facilities like ELETTRA/Triest (where the 1st workshop took place from 13 to 14 February 2020) and MAX-IV/Lund. The two-day workshop in Garching with 16 international participants also included a visit to the reactor (FRM II) and a joint restaurant visit.

Munich School of Engineering (MSE)
10th Energy Colloquium of the Munich School of Engineering: "10 years of MSE: Energy Research in Bavaria"
30 July 2020, Garching, virtual event

Munich School of Engineering
Technische Universität München

10th Energy Colloquium of the Munich School of Engineering
1st Virtual Edition

10 years of MSE: Energy Research in Bavaria

July 30, 2020 – 8:30 a.m. to 6:00 p.m.

Please register by July 23rd to get your login information: http://www.mse.tum.de

8:30 – 8:45 a.m.
Opening: Prof. Dr. Thomas Hamacher
Director, Munich School of Engineering, TUM

8:45 – 9:15 a.m.
Keynote: Hydrogen – Energy and Fuel of the Future or Great White Hope?
Dr. Tobias Brunner, Hynergy

9:15 – 11:00 a.m.
Energy Conversion and Storage at the Nanoscale
Session Chair: **Prof. Dr. Peter Müller-Buschbaum**

Phase Transitions in Ni-rich Cathode Materials for Lithium-Ion Batteries: Boon or Bane?
Felix Riewald, BASF SE/Chair of Technical Electrochemistry, TUM

Molecular Insight into the CO_2 and CH_4 Conversion: C-O and C-H Bond Activation and C-C Coupling
Nikita Levin, Chair of Physical Chemistry, TUM

In-Situ Identification of Active Electrocatalytic Sites on Metal-Based Catalysts for Oxygen Reduction and Evolution Reaction
Regina Kluge, Physics of Energy Conversion and Storage, TUM

In-Operando Stability Investigation of Biotemplated Photoactive Layers for Solar Cells
Julian Heger, Chair of Functional Materials, TUM

11:00 – 11:15 a.m.
Coffee Break

11:15 – 12:00 p.m.
Energy Storage from Cradle to Roll-Out
Session Chair: **Prof. Dr. Andreas Jossen**

Access Economy for Storage in Energy Communities
Niklas Vespermann, Chair of Renewable and Sustainable Energy Systems, TUM

Influence of Battery Energy Storage Systems on the Carbon Footprint of Energy Systems
Anupam Parlikar, Institute for Electrical Energy Storage Technology, TUM

12:00 – 12:30 p.m.
Lunch Break

12:30 – 2:00 p.m.
Poster Presentation and Q&A-Session

2:00 – 3:15 p.m.
From Energy Efficient to Smart Buildings
Session Chair: **Prof. Dr. Werner Lang**

Indoor Farming – Optimize Efficiency
Sabine Wittmann, Institute of Horticulture, HSWT

BIM-Based Embedded Energy and Greenhouse Gas Emissions Analysis – A Case Study
Patricia Schneider-Marin, Institute of Energy Efficient and Sustainable Design and Building, TUM

Fast Harmonic Estimation Using Real-Time Embedded Controllers in CoSES Smart Grid
Anurag Mohapatra, Center for Combined Smart Energy Systems, TUM

3:15 – 3:30 p.m.
Coffee Break

3:30 – 4:45 p.m.
Building Blocks of a Future Energy Supply
Session Chair: **Prof. Dr. Hartmut Spliethoff**

Power-to-Heat with Large Scale Thermochemical Energy Storage in Industrial Combined Heat and Power Plants
Gesa Backofen, Chair of Energy Systems, TUM

A Techno-Economic Optimization for Decentralized Waste-Heat Power Generation with a Steam-Rankine-Cycle
Florian Raab, Power and Storage Technologies, THN

100% Renewables for Bavaria - Structures, Costs and Benefits of Full Supply in All Sectors
Jakob Schweiger, ZAE Bayern - Energy Storage

4:45 – 5:15 p.m.
Keynote: Network TUM.PtX – Tackling the Energy Transition through Collaborative Research
Dr. Sebastian Fendt, Munich School of Engineering, TUM

5:15 – 5:30 p.m.
Summary and Closing

5:30 – 6:00 p.m.
Virtual Social Networking

Heinz Maier-Leibnitz-Zentrum (MLZ), Materials Growth and Measurement Laboratory (MGML) Prague, Eli Beamlines, Prague
Czech-Bavarian mini-school 2020 on large scale facilities and open data
18 – 22 October 2020, Garching, virtual event

19 October 2020, 9 am – 5 pm:
9 am – 12 pm: Lectures on neutron scattering techniques
2 pm – 5 pm: Tour of the FRM II reactor

Mini-school Schedule

Sunday
18 October 2020

Monday
19 October 2020

Tuesday
20 October 2020

Wednesday
21 October 2020

Thursday
22 October 2020

Lectures on neutron scattering techniques

The lectures will give a broad overview on the different neutron scattering techniques available at the MLZ:

- Neutron diffraction (Dr. Anatoliy Senyshyn) slides
- Small angle neutron scattering (Dr. Sebastian Mühlbauer) slides
- Inelastic neutron scattering (Dr. Astrid Schneidewind)
- Neutron spin echo techniques (Dr. Johanna K. Jochum) slides

09:00 - 12:00

MLZ, Garching, DE

Tour of the FRM II reactor

We will see the reactor pool and learn how neutrons are produced. The tour will continue in the neutron guidehall and experimental hall, where 26 state-of-the-art instruments are operated.

14:00 - 17:00

MLZ, Garching, DE

Heinz Maier-Leibnitz-Zentrum (MLZ)/Technical University of Munich (TUM)/Research Center Jülich
Inauguration festivities of the new MLZ buildings
22 October 2020, Garching, virtual event

In 2020, the Technical University Munich and the Research Center Jülich moved into the new MLZ buildings on the premises of the FRM II. Due to Covid 19-related restrictions, the inauguration festivities were held purely virtually on 22 October 2020, 2 pm- 4 pm, via streaming.
The ceremonial opening was addressed by the two MLZ Scientific Directors, Prof. Stephan Förster and Prof. Peter Müller-Buschbaum, followed by speeches of the Bavarian State Minister for Science and Art, Mr. Bernd Sibler, MdL, and the Parliamentary State Secretary at the Federal Ministry of Education and Research, Mr. Thomas Rachel MdB. Professor Dr. Thomas F. Hofmann, President of the Technical University of Munich, was also a speaker, as was Professor Dr.-Ing. Wolfgang Marquardt, Chairman of the Board of Directors of Forschungszentrum Jülich. In his speech, the architect Professor Dr.-Ing. Gunter Henn expressed his view on his architectural concept of the building design. Following the inauguration festivities – which also included the cutting of the inaugural ribbon as a symbolic act – featuring approximately 250 participants, a virtual tour of the buildings was provided.

Heinz Maier-Leibnitz-Zentrum (MLZ)
Serpent User Group Meeting
27 – 30 October 2020, Garching, virtual event

From 27 to 30 October 2020, 174 experts from 28 countries came together virtually at the 10th Serpent User Group Meeting to exchange about the neutronics code Serpent. Serpent is multi-purpose three-dimensional continuous-energy Monte Carlo particle transport developed at the VTT Technical Research Centre of Finland since 2004. The software is used by many scientists and institutions worldwide for traditional reactor physics applications, including spatial homogenization, criticality calculations, fuel cycle studies, research reactor modeling or validation of deterministic transport codes. It offers advanced interfaces for coupled calculations with thermal hydraulics, CFD and fuel performance codes and its Neutron and Photon transport simulation capabilities can be used for radiation dose rate calculations and medical applications. The Serpent User Group Meeting is held each year at different institutions. In 2020, the Heinz Maier-Leibnitz Center hosted the conference virtually due to the pandemic. The Serpent developers as well as its users participated in the conference sessions, which allowed for many productive exchanges and interactions. The speakers presented new functions and uses of the software, which were discussed in detail. The virtual format offered advantages over the previous years' conferences. It gave significantly more people the chance to participate. Instead of the usual 30-40 participants, 174 developers and users from 28 countries attended. Long journeys were spared, and so the organizers around Dr. Christian Reiter from FRM II were able to expand the range of presentations. In order to enable personal discussions despite the physical distance, there was also a social event for informal conversations.

Heinz Maier-Leibnitz-Zentrum (MLZ)
MLZ User Meeting
08 – 09 December 2020, Garching, virtual event

The MLZ User Meeting took place from 8 to 9 December 2020 as a purely virtual format and was linked to the German Neutron Scattering Conference DN2020 on 9 and 10 December 2020, which was hosted for the second time (since 2008) by FRM II/MLZ. A joint poster session was shared by both meetings; this provided the opportunity for exchange between the participants of both events. A total of 405 visitors attended the three days of the event (with workshops, plenary lectures), 96 lectures were given via ZOOM, 159 posters were shown in the poster session.

Heinz Maier-Leibnitz-Zentrum (MLZ) and the Technical University of Munich (TUM)
German Neutron Scattering Conference 2020
09 – 10 December 2020, Garching, virtual event

The German Neutron Scattering Conference 2020 took place virtually in Garching from December 9th to 10th, 2020. The meeting was organized by the Heinz Maier-Leibnitz-Zentrum (MLZ) and the Technical University of Munich (TUM) on behalf of the German Committee for Research with Neutrons (KFN) in conjunction with the User Meeting of the MLZ. In addition to scientists from all over Germany and from other European countries, scientists from Australia, Brazil, India, Japan, Morocco, Russia and the United States participated. Altogether, 400 participants discussed lively about developments in methods and instrumentation and insights ranging from fundamental mechanisms to technical applications and innovations that were only made possible by neutron experiments. The main topics, as presented in 35 special lectures, were materials science, instrumentation, magnetism soft matter, life science/biology and digitalization/machine learning. Six invited speakers additionally focused on novel neutron instrumentation, stimuli-responsive polymer microgels, the neutron beta decay, novel luminescence materials, disorder in triangular antiferromagnets and the structural dynamics of proteins. The joint poster session with the MLZ User Meeting was a great success with nearly 160 posters and vivid discussions, despite the online format. Moreover, the newest KFN strategy paper was handed over to the Federal Ministry of Education and Research. Last, but not least, the 12th board of the KFN was presented to the audience. A highlight of the conference was the bestowal of the Wolfram-Prandl-Prize 2020 to Dr. Sabrina Disch (University of Cologne) for her outstanding research on the structure, spin structure and dynamics of magnetic nanoparticles and the structures resulting from their self-organization.

Christine M. Papadakis, Technical University of Munich, Germany
Ina Lommatzsch, Heinz Maier-Leibnitz-Zentrum, Garching, Germany
Astrid Schneidewind, KFN chair, Heinz Maier-Leibnitz-Zentrum, Garching, Germany
Regine v. Klitzing, KFN, Technische Universität Darmstadt, Germany
Karin Griewatsch, KFN, Helmholtz-Zentrum Geesthacht, Germany

8.3 Service to the community

Prof. Dr. Peter Müller-Buschbaum:

- Since 4/2019 Vice Deputy of Association of Chemical Physics and Polymer Physics (CPP) at Deutsche Physikalische Gesellschaft (DPG)
- Since 7/2017 member of the Aptitude Committee of master course Materials Science and Engineering (MSandE) at TUM
- Since 9/2016 spokesman and board member of the Graduate School of "Munich School of Engineering" (MSE) at TUM
- Since 6/2016 member of the doctoral committee of "Munich School of Engineering" (MSE) at TUM
- Since 3/2015 member of "Advanced Light Source (ALS) Review Panel"
- Since 9/2014 member of "Heinz Maier-Leibnitz Zentrum (MLZ) Review Panel"
- Since 6/2014 member of Stanford Synchrotron Radiation Lightsource (SSRL) Review Panel
- Since 9/2012 Associate Editor of journal "ACS Applied Materials & Interfaces" of the American Chemical Society
- Since 3/2012 head of KeyLab "TUM.Solar" at TU Munich
- Since 1/2012 member of the Scientific Selection Panel of the Helmholtz-Zentrum Berlin für Materialien und Energie (HZB)
- Since 2011 member of European Spallation Source (ESS) Scientific Advisory Panel (Reflectivity)
- Since 2011 German representative at the European Polymer Federation (EPF) for polymer physics
- Since 2010 spokesman of the regenerative engergies section (NRG) at the Munich School of Engineering (MSE) of TU Munich
- Since 2010 member of TUM Energie at TU Munich
- Since 2010 German representative at the European Synchrotron User Organization (ESUO)
- Since 2008 chairman of "DESY Photon Science User Committee" at the synchrotron radiation laboratory DESY in Hamburg

Prof. Dr. Christine M. Papadakis:

- Since 4/2015 Editor-in-Chief for the journal "Colloid & Polymer Science", Springer-Verlag
- Vice women's representative of the Physics Department at TU München

Prof. Dr. Winfried Petry:

- Since 2018 TUM Emeritus of Excellence
- Since 2016 member of the Evaluation Panel for Neutron Research of the Swedish Research Council
- Since 2015 member of the Neutron Scientific Advisory Committee of the National Research Center Kurchatov Institute "Petersburg Nuclear Physics Institute" (PNPI, Gatchina)
- Since 2012 member of the Scientific Advisory Board of NaWi Graz
- Since 2007 member of the Steering Comittee of the Laue Langevin Institute and chairman of the instrumentation review panel of the CEA Leon Brillouin Laboratory
- Since 1999 liaison professor of Bayerische Eliteakademie (Bavarian Leadership Academy) and since May 2011 member of the Board of Trustees

9 Publications, talks, posters and funding

9.1 Publications

- F. Adams, T. M. Pehl, M. Kränklein, S. A. Kernbichl, J.-J. Kang, C. M. Papadakis, B. Rieger
  (Co)polymerization of (-)-Menthide and β-Butyrolactone with Yttrium-bis(phenolates): Tuning Material Properties of Sustainable Polyesters
  Polym. Chem. **11**, 4426-4437 (2020)

- K. H. Andersen, D. N. Argyriou, A. J. Jackson, J. Houston, P. F. Henry, W. Petry, et al.
  The instrument suite of the European Spallation Source
  Nuclear Instruments and Methods in Physics Research Section A: Accelerators, Spectrometers, Detectors and Associated Equipment **957**, 163402 (2020)

- E. Bergendal, R. A. Campbell, G. A. Pilkington, P. Müller-Buschbaum, M. W. Rutland
  3D texturing of the air–water interface by biomimetic self-assembly
  Nanoscale Horiz. **5**, 839-846 (2020)

- W. Cao, S. Xia, X. Jiang, M. Appold, M. Opel, M. Plank, R. Schaffrinna, L. P. Kreuzer, S. Yin, M. Gallei, M. Schwartzkopf, S. V. Roth, P. Müller-Buschbaum
  Self-Assembly of Large Magnetic Nanoparticles in Ultrahigh Molecular Weight Linear Diblock Copolymer Films
  ACS Appl. Mater. Interfaces **12**, 7557–7564 (2020)

- W. Chen, H. Tang, N. Li, M. A. Scheel, Y. Xie, D. Li, V. Körstgens, M. Schwartzkopf, S. V. Roth, K. Wang, X. W. Sun, P. Müller-Buschbaum
  Colloidal PbS quantum dot stacking kinetics during deposition via printing
  Nanoscale Horiz. **5**, 880-885 (2020)

- W. Chen, H. Tang, Y. Chen, J. E. Heger, N. Li, L. P. Kreuzer, Y. Xie, D. Li, C. Anthony, Z. Pikramenou, K. W. Ng, X. W. Sun, K. Wang, P. Müller-Buschbaum
  Spray-deposited PbS colloidal quantum dot solid for near-infrared photodetectors
  Nano Energy **78**, 105254 (2020)

- W. Chen, S. Liang, F. C. Löhrer, S. J. Schaper, N. Li, W. Cao, L. P. Kreuzer, H. Liu, H. Tang, V. Körstgens, M. Schwartzkopf, K. Wang, X. W. Sun, S. V. Roth, P. Müller-Buschbaum
  In situ Grazing-Incidence Small-Angle X-ray Scattering Observation of Gold Sputter Deposition on a PbS Quantum Dot Solid
  ACS Appl. Mater. Interfaces **12**, 46942-46952 (2020)

- J. Engström, C. J. Brett, V. Körstgens, P. Müller-Buschbaum, W. Ohm, E. Malmström, S. V. Roth
  Core-shell nanoparticle interface and wetting properties
  Adv. Funct. Mater. **30**, 1907720 (2020)

- F. Fang, M. Liu, W. Chen, H. Yang, Y. Liu, X. Li, J. Hao, B. Xu, D. Wu, K. Cao, W. Lei, P. Müller-Buschbaum, X. W. Sun, R. Chen, K. Wang
  Atomic layer deposition assisted encapsulation of quantum dot luminescent microspheres towards display applications
  Adv. Opto. Mater. **8**, 1902118 (2020)

- G. Färber, T. Hamacher, W. Petry
  Energie - Post-Corona
  Wissenschaft, Vernunft & Nachhaltigkeit, 102-105 (2020)
- P. Gu, B. Li, B. Wu, J. Wang, P. Müller-Buschbaum, Q. Zhong
  Controlled hydration, transition and drug release realized by adjusting layer thickness in alginate-Ca2+/poly(N-isopropylacrylamide) interpenetrating polymeric network hydrogels on cotton fabrics
  ACS Biomater. Sci. Eng. **6**, 5051-5069 (2020)
- P. Gu, J. Wang, P. Müller-Buschbaum, D. Qi, Q. Zhong
  Infrared thin film detectors based on thermoresponsive microgels with linear shrinkage behavior and gold nanorods
  ACS Appl. Mater. Interfaces **12**, 34180-34189 (2020)
- R. Guo, A. Buyruk, X. Jiang, W. Chen, L. K. Reb, M .A. Scheel, T. Ameri, P. Müller-Buschbaum
  Tailoring the orientation of perovskite crystals via adding two-dimensional polymorphs for perovskite solar cells
  J. Phys. Energy **2**, 034005 (2020)
- Q. Han, F. Tao, Y. Xu, H. Su, F. Yang, V. Körstgens, P. Müller-Buschbaum, P. Yang
  Tuning chain relaxation from an amorphous biopolymer film to crystals by removing air/water interface limitations
  Angew. Chem. Int. Ed. **59**, 20192-20200 (2020)
- N. Hohn, X. Wang, M. A. Giebel, S. Yin, D. Müller, A. E. Hetzenecker, L. Bießmann, L. P. Kreuzer, G. E. Möhl, H. Yu, J. G. C. Veinot, T. F. Fässler, Y. Cheng, P. Müller-Buschbaum
  Mesoporous GeOx/Ge/C as highly reversible anode material with high specific capacity for lithium-ion batteries
  ACS Appl. Mater. Interfaces **12**, 47002-47009 (2020)
- N. Hu, C. Chen, J. Tan, W. Wang, C. Wang, H. Fan, J. Wang, P. Müller-Buschbaum, Q. Zhong
  Enhanced adsorption of methylene blue triggered by the phase transition of thermoresponsive polymers in hybrid interpenetrating polymer network hydrogels
  ACS Appl. Poly. Mater. **2**, 3674-3684 (2020)
- N. Hu, L. Lin, J. Tan, W. Wang, L. Lei, H. Fan, J. Wang, P. Müller-Buschbaum, Q. Zhong
  Wearable bracelet monitoring the solar ultraviolet radiation for skin health based on hybrid IPN hydrogels
  ACS Appl. Mater. Interfaces **12**, 56480-56490 (2020)
- L. Janisova, A. Gruzinov, O. V. Zaborova, N. Velychkivska, O. Vaněk, P. Chytil, T. Etrych, O. Janoušková, X. Zhang, C. Blanchet, C. M. Papadakis, D. I. Svergun, S. K. Filippov
  Molecular Mechanisms of the Interactions of N-(2-Hydroxypropyl)methacrylamide Copolymers Designed for Cancer Therapy with Blood Plasma Proteins
  Pharmaceutics **12**, 105 (2020)

- X. Jiang, H. Kim, P. S. Deimel, W. Chen, W. Cao, D. Yang, S. Yin, R. Schaffrinna, F. Allegretti, J. V. Barth, M. Schwager, H. Tang, K. Wang, M. Schwartzkopf, S. V. Roth, P. Müller-Buschbaum
  Internal nanoscale architecture and charge carrier dynamics of wide bandgap non-fullerene bulk heterojunction active layers in organic solar cells
  J. Mater. Chem. A **8**, 23628–23636 (2020)

- F. A. Jung, A. V. Berezkin, T. H. Tejsner, D. Posselt, D.-M. Smilgies, C. M. Papadakis
  Solvent Vapor Annealing of a Diblock Copolymer Thin Film with a Nonselective and a Selective Solvent: Importance of Pathway for the Morphological Changes
  Macromol. Rapid Commun. **41**, 2000150 (2020)

- F. A. Jung, D. Posselt, D.-M. Smilgies, P. A. Panteli, C. Tsitsilianis, C. S. Patrickios, C. M. Papadakis
  Charge-Dependent Microphase Separation in Thin Films from a Multiresponsive Pentablock Quaterpolymer: A GISAXS Investigation
  Macromolecules **53**, 6255-6266 (2020)

- J.-J. Kang, F.A. Jung, C.-H. Ko, K. Shehu, L.C. Barnsley, F. Kohler, H. Dietz, J. Zhao, S. Pispas, C.M. Papadakis
  Thermoresponsive Molecular Brushes with Propylene Oxide/Ethylene Oxide Copolymer Side Chains in Aqueous Solution
  Macromolecules **53**, 4068 (2020)

- R. M. Kluge, N. Saxena, W. Chen, V. Körstgens, M. Schwartzkopf, Q. Zhong, S. V. Roth, P. Müller-Buschbaum
  Doping dependent in-plane and cross-plane thermoelectric performance of thin n-type polymer P(NDI2OD-T2) films
  Adv. Funct. Mater. **30**, 2003092 (2020)

- C.-H. Ko, K.- L. Claude, B.- J. Niebuur, F. A. Jung, J.- J. Kang, D. Schanzenbach, H. Frielinghaus, L. C. Barnsley, B. Wu, V. Pipich, A. Schulte, P. Müller-Buschbaum, A. Laschewsky, C. M. Papadakis
  Temperature-dependent phase behavior of the thermoresponsive polymer poly(N-isopropylmethacrylamide) in aqueous solution
  Macromolecules **53**, 6818-6827 (2020)

- V. Kochetov, M. J. Mühlbauer, A. Schökel, T. Fischer, T. Müller, et al.
  Powder diffraction computed tomography: a combined synchrotron and neutron study
  J. Phys.: Condens. Matter **33**, 105901 (2020)

- V. Körstgens, J. Corella Puertas, P. Müller-Buschbaum
  Tack Properties of Pressure-Sensitive Adhesive-Coated Fiber Assemblies
  ACS Appl. Polym. Mater. **2**, 3189-3195 (2020)

- L. P. Kreuzer, T. Widmann, L. Bießmann, N. Hohn, J. Pantle, R. Märkl, J. F, Moulin, V. Hildebrand, A. Laschewsky, C. M. Papadakis, P. Müller-Buschbaum
  Phase Transition Kinetics of Doubly Thermoresponsive Poly(sulfobetaine)-Based Diblock Copolymer Thin Films
  Macromolecules **53**, 2841-2855 (2020)

- L. P. Kreuzer, T. Widmann, N. Aldosari, L. Bießmann, G. Mangiapia, V. Hildebrand, A. Laschewsky, C. M. Papadakis, P. Müller-Buschbaum
  Cyclic Water Storage Behavior of Doubly Thermoresponsive Poly(sulfobetaine)-Based Diblock Copolymer Thin Films
  Macromolecules **53**, 9108-9121 (2020)

- A. Lak, T. Kahmann, S. J. Schaper, J. Obel, F. Ludwig, P. Müller-Buschbaum, J. Lipfert
  The dissociation rate of acetylacetonate ligands governs the size of ferrimagnetic zinc ferrite nanocubes
  ACS Appl. Mater. Interfaces **12**, 217-226 (2020)

- M. Landesberger, R. Koos, M. Hofmann, X. Li, T. Boll, W. Petry, W. Volk
  Phase Transition Kinetics in Austempered Ductile Iron (ADI) with Regard to Mo Content
  Materials 13, **22**, 5266 (2020)

- L. Lei, W. Wang, C. Wang, H. Fan, A. K. Yadav, N. Hu, Q. Zhong, P. Müller-Buschbaum
  Hydrogel-supported graphitic carbon nitride nanosheets loaded with Pt atoms as a novel self-water-storage photocatalyst for H2 evolution
  J. Mater Chem. A **8**, 23812-23819 (2020)

- B. Li, Y. Rui, J. Xu, Y. Wang, J. Yang, Q. Zhang, P. Müller-Buschbaum
  Solution-processed p-type nanocrystalline CoO films for inverted mixed perovskite solar cells
  J. Colloid. Interf. Sci. **573**, 78-86 (2020)

- N. Li, L. Song, N. Hohn, N. Saxena, W. Cao, X. Jiang, P. Müller-Buschbaum
  Nanoscale crystallization of a low band gap polymer in printed titania mesopores
  Nanoscale **12**, 4085-4093 (2020)

- N. Li, W. Chen, L. Song, R. Guo, M. A. Scheel, D. Yang, V. Körstgens, M. Schwartzkopf, S. V. Roth, P. Müller-Buschbaum
  In situ study of order formation in mesoporous titania thin films templated by a diblock copolymer during slot-die printing
  ACS Appl. Mater. Interfaces **12**, 57627-57637 (2020)

- S. Liang, Y. Cheng, J. Zhu, Y. Xia, P. Müller-Buschbaum
  A Chronicle Review of Nonsilicon (Sn, Sb, Ge)-Based Lithium/Sodium-Ion Battery Alloying Anodes
  Small Methods **4**, 2000218 (2020)

- S. Liang, Y. Xia, P. Müller-Buschbaum, Y. Cheng
  A Brief History of Conducting Polymers Applied in Lithium-ion Batteries
  Materials Research Foundations **80**, 28-62 (2020)

- S. Liang, Y. Xia, P. Müller-Buschbaum, Y. Cheng
  Conducting Polymers for Sodium-Ion Batteries
  Materials Research Foundations **76**, 251-271 (2020)

- B. Lin, X. Zhou, H.Zhao, J. Yuan, K. Zhou, K. Chen, H. Wu, R. Guo, M. A. Scheel, A. Chumakov, S. V. Roth, Y. Mao, L. Wang, Z. Tang, P. Müller-Buschbaum, W. Ma
  Balancing the pre-aggregation and crystallization kinetics enables high efficiency slot-die coated organic solar cells with reduced non-radiative recombination losses
  Energy & Environmental Science **13, 8**, 2467-2479 (2020)

- P. Liu, W. Chen, Y. Okazaki, Y. Battie, L. Brocard, M. Decossas, E. Pouget, P. Müller-Buschbaum, B. Kauffmann, S. Pathan, T. Sagawa and R. Oda
  Optically Active Perovskite CsPbBr3 Nanocrystals Helically Arranged on Inorganic Silica Nanohelices
  Nano Lett., **20**, 8453-8460 (2020)
- F .C. Löhrer, V. Körstgens, G. Semino, M. Schwartzkopf, A. Hinz, O. Polonskyi, T. Strunskus, F. Faupel, S. V. Roth, P. Müller-Buschbaum
  Following in situ the deposition of gold electrodes on low-bandgap polymer films
  ACS Appl. Mater. Interfaces **12**, 1132-1141 (2020)
- F. C. Löhrer, C. Senfter, C. J. Schaffer, J. Schlipf, D. Moseguí González, P. Zhang, S. V. Roth, P. Müller-Buschbaum
  Light-induced and oxygen-mediated degradation processes in photoactive layers based on PTB7-Th
  Adv. Photonics Res. **1**, 2000047 (2020)
- R. S. Märkl, N. Hohn, E. Hupf, L. Bießmann, V. Körstgens, L. P. Kreuzer, G. Mangiapia, M. Pomm, A. Kriele, E. Rivard, P. Müller-Buschbaum
  Comparing the backfilling of mesoporous titania thin films with hole conductors of different size sharing the same mass density
  IUCrJ **7**, 268-27 (2020)
- L. Mathes, Th. Gigl, M. Leitner, Ch. Hugenschmidt
  Breakdown of Arrhenius law of temperature-dependent vacancy concentration in fcc lanthanum
  Phys. Rev. B **101**, 134105 (2020)
- M. Molls, J. Eberspächer, H. Auernhammer, G. Färber, B. Herbst-Gaebel, et al.
  Wissenschaft, Vernunft und Nachhaltigkeit
  Zorneding 2020
- B.-J. Niebuur, C.-H. Ko, X. Zhang, K.-L. Claude, L. Chiappisi, A. Schulte, C. M. Papadakis
  Pressure Dependence of the Cononsolvency Effect in Aqueous Poly(N-isopropylacrylamide) Solutions: A SANS Study
  Macromolecules **53**, 3946-3955 (2020)
- N. Paul, J. F. Moulin, G. Mangiapia, A. Kriele, P. Müller Buschbaum, M. Opel, A. Paul
  Surface distortion of Fe dot-decorated TiO_2 *nanotubular templates using time-of-flight grazing incidence small angle scattering*
  Sci. Rep. **10**, 4038 (2020)
- V. Pipich, M. Dickmann, H. Frielinghaus, R. Kasher, C. Hugenschmidt, et al.
  Morphology of Thin Film Composite Membranes Explored by Small-Angle Neutron Scattering and Positron-Annihilation Lifetime Spectroscopy
  Membranes **10**, 3, 48 (2020)
- S. Pratap, J. Schlipf, L. Bießmann, P. Müller-Buschbaum
  Hierarchical Structures from Nanocrystalline Colloidal Precursors within Hybrid Perovskite Thin Films: Implications for Photovoltaics
  ACS Appl. Nano Mater. **3**, 11701-11708 (2020)

- S. Pröller, O. Filonik, S. Mansi, C. Zhu, E. Schaible, A. Hexemer, P. Müller-Buschbaum, E. M. Herzig
  Electrophoresis assisted printing: a method to tailor the morphology in organic solar cells
  ACS Appl. Mater. Interfaces **12**, 5219-5225 (2020)

- K. N. Raftopoulos, K. Kyriakos, M. Nuber, B.-J. Niebuur, O. Holderer, M. Ohl, O. Ivanova, S. Pasini, C. M. Papadakis
  Co-nonsolvency in Concentrated Aqueous Solutions of PNIPAM: Effect of Methanol on the Collective and the Chain Dynamics
  Soft Matter **16**, 8562-8372 (2020)

- L. K. Reb, M. Böhmer, B. Predeschly, S. Grott, C. L. Weindl, G. I. Ivandekic, R. Guo, C. Dreißigacker, R. Gernhäuser, A. Meyer, P. Müller-Buschbaum
  Perovskite and Organic Solar Cells on a Rocket Flight
  Joule **4**, 1880-1892 (2020)

- D. Schwaiger, W. Lohstroh, P. Müller-Buschbaum
  Investigation of Molecular Dynamics of a PTB7:PCBM Polymer Blend with Quasi-Elastic Neutron Scattering
  ACS Appl. Polym. Mater. **2**, 3797-3804 (2020)

- K. Shehu, C. Bojanowski, A. Bergeron, W. Petry, C. Reiter
  First steps to coupled hydraulic and mechanical calculations within a parameter study to define possible core designs for the conversion of FRM II
  American Nuclear Society (Hg.): Physor 2020. Physor. Cambridge, UK (2020)

- K. Shehu, J. Mercz, W. Petry, C. Reiter
  Mechanical Evaluations to Define Possible Fuel Element Designs for the Conversion of FRM II
  Société Francaise d´ Energie Nucléaire (Hg.): ATH 2020. Palaiseau, Frankreich

- J. Shi, C. Onofri, H. Palancher, X. Iltis, D. Drouan, H. Breitkreutz, W. Petry
  Microstructure evolution and phase transformation of heavy-ion irradiated U–Mo/Al fuels
  Journal of Nuclear Materials **541**, 152399 (2020)

- M. T. Sirtl, M. Armer, L. K. Reb, R. Hooijer, P. Dörflinger, M. A. Scheel, K. Tvingstedt, P. Rieder, N. Glück, P. Pandit, S. V. Roth, P. Müller-Buschbaum, V. Dyakonov, T. Bein
  Optoelectronic Properties of $Cs_2AgBiBr_6$ Thin Films: The Influence of Precursor Stoichiometry
  ACS Appl. Energy Mater. **3, 12**, 11597–11609 (2020)

- L. Song, M. A. Niedermeier, V. Körstgens, F. C. Löhrer, Y. Chen, S. V. Roth, P. Müller-Buschbaum
  In situ sputtering of gold nanometer-thick gold films onto 100 nanometer-thick spiro-OMeTAD films: Implications for perovskite solar cells
  ACS Appl. Nano Mater.**3**, 5987-5994 (2020)

- K. Sparnacci, R. Chiarcos, V. Gianotti, M. Laus, T. J. Giammaria, M. Perego, G. Munaò, G. Milano, A. De Nicola, M. Haese, L. P. Kreuzer, T. Widmann, P. Müller Buschbaum
  Effect of trapped solvent on the interphase between PS-b-PMMA thin films and P(S-r-MMA) brush layers
  ACS Appl. Mater. Interfaces **12**, 7777-7787 (2020)

- R. Stene, T. Chemnitz, W. Petry, F. Kraus
  Reductive photo-chemical separation of the hexafluorides of uranium and molybdenum
  Journal of Fluorine Chemistry **240**, 109655 (2020)

- R. Stene, B. Scheibe, A. J. Karttunen, W. Petry, F. Kraus
  Syntheses and Characterization of A [W2O2F9](A= Li–Cs)
  European Journal of Inorganic Chemistry **23**, 2260-2269 (2020)

- R. Stene, B. Scheibe, W. Petry, F. Kraus
  Synthesis and Characterization of the Hexafluoridomolybdates (V) A [MoF6](A= Li–Cs)
  European Journal of Inorganic Chemistry **19**, 1834-1843(2020)

- X. Tang, W. Chen, D. Wu, A. Gao, G. Li, J. Sun, K. Yi, Z. Wang, G. Pang, H. Yang, R. Guo, H. Liu, H. Zhong, M. Huang, R. Chen, P. Müller-Buschbaum, X. W. Sun and K. Wang
  In Situ Growth of All-Inorganic Perovskite Single Crystal Arrays on Electron Transport Layer
  Adv. Sci., **7**, 1902767 (2020)

- Ch. Tietz, T. M. Fritz, K. Holzweber, M. Legenstein, B. Sepiol, M. Leitner
  Diffusive dynamics in an amorphous superionic conductor
  Phys. Rev. Research **2**, 043141 (2020)

- M. J. Trimpl, A. D. Wright, K. Schutt, L. R. V. Buizza, Z. Wang, M. B. Johnston, H. J. Snaith, P. Müller-Buschbaum, L. M. Herz
  Charge-carrier trapping and radiative recombination in metal halide perovskite semiconductors
  Adv. Funct. Mater. **30**, 2004312 (2020)

- S. Valance, B. Baumeister, W. Petry, J. Höglund
  Innovative and safe supply of fuels for reactors
  EPJ N-Nuclear Sciences and Technologies **6**, 40 (2020)

- X. Wang, Y. Cheng, Q. Ji, S. Liang, L. Ma, Z. Xu, X. Zuo, J.-Q. Meng, J. Zhu, P. Müller-Buschbaum, Y. Xia
  In situ incorporation of super-small metallic high capacity nanoparticles and mesoporous structures for high-performance TiO2/SnO2/Sn/carbon nanohybrid lithium-ion battery anodes
  Energy Techol. **8**, 2000034 (2020)

- Y. Wang, L. Chao, T. Niu, D. Li, Q. Wei, H. Wu, J. Qiu, H. Lu, C. Ran, Q. Zhong, L. Song, G. Xing, Y. Xia, Y. Chen, P. Müller-Buschbaum, W. Huang
  Efficient and stable perovskite solar cells by fluorinated ionic liquid induced component interaction
  Solar RRL **5**, 2000582 (2020)

- T. Widmann, L. P. Kreuzer, G. Mangiapia, M. Haese, H. Frielinghaus, P. Müller-Buschbaum
  3D printed spherical environmental chamber for neutron reflectometry and grazing-incidence small-angle neutron scattering experiments
  Rev. Sci. Instrum. **91**, 113903 (2020)

- K. S. Wienhold, X. Jiang, P. Müller-Buschbaum
  Organic Solar Cells probed with Advanced Neutron Scattering Techniques
  Appl. Phys. Lett. **116**, 120504 (2020)

- K. S. Wienhold, V. Körstgens, S. Grott, X. Jiang, M. Schwartzkopf, S. V. Roth, P. Müller-Buschbaum
  In Situ Printing: Insights into the Morphology Formation and Optical Property Evolution of Slot-Die-Coated Active Layers Containing Low Bandgap Polymer Donor and Nonfullerene Small Molecule Acceptor
  Solar RRL **4**, 2000086 (2020)

- K. S. Wienhold, W. Chen, S. Yin, R. Guo, M. Schwartzkopf, S. V. Roth, P. Müller-Buschbaum
  Following in Operando the Structure Evolution-Induced Degradation in Printed Organic Solar Cells with Nonfullerene Small Molecule Acceptor
  Solar RRL **4**, 2000251 (2020)

- K. S. Wienhold, C. L. Weindl, S. Yin, T. Tian, A. Rothkirch, M. Schwartzkopf, S. V. Roth, P. Müller-Buschbaum
  Following In Situ the Evolution of Morphology and Optical Properties during Printing of Thin Films for Application in Non-Fullerene Acceptor Based Organic Solar Cells
  ACS Appl. Mater. Interfaces **12**, 40381–40392 (2020)

- M.-B. Wu, F. Yang, J. Yang, Q. Zhong, V. Körstgens, P. Yang, P. Müller-Buschbaum, Z.-K. Xu
  Lysozyme membranes promoted by hydrophobic substrates for ultrafast and precise organic solvent nanofiltration
  Nano Lett. **20**, 8760-8767 (2020)

- Y. Xia, W. Chen, P. Zhang, S. Liu, K. Wang, X. Yang, H. Tang, L. Lian, J. He, X. Liu, G. Liang, M. Tan, L. Gao, H. Liu, H. Song, D. Zhang, J. Gao, K. Wang, X. Lan, X. Zhang, P. Müller-Buschbaum, J. Tang and J. Zhang
  Facet Control for Trap-State Suppression in Colloidal Quantum Dot Solids
  Adv. Funct. Mater. **30**, 2000594 (2020)

- H. Xie, S. Y. Sayed, W. P. Kalisvaart, S. J. Schaper, P. Müller-Buschbaum, E. J. Luber, B. C. Olsen, M. Haese, J. M. Buriak
  Adhesion and surface layers on silicon anodes suppress formation of c-Li$_{3.75}$*Si and solid electrolyte interphase*
  ACS Appl. Energy Mater. **3**, 1609-1616 (2020)

- D. Yang, B. Cao, N. Saxena, N. Li, C. Bilko, S. Grott, W. Chen, X. Jiang, J. E. Heger, S. Bernstorff, P. Müller-Buschbaum
  Tailoring morphology compatibility and device stability by adding PBDTTPD-COOH as third component to fullerene-based polymer solar cells
  ACS Appl. Energy Mater. **3**, 2604-2613 (2020)

- D. Yang, S. Grott, X. Jiang, K. S. Wienhold, M. Schwartzkopf, S. V. Roth, P. Müller-Buschbaum
  In situ studies of solvent additive effects on the morphology development during printing of bulk heterojunction films for organic solar cells
  Small Methods **4**, 2000418 (2020)

- D. Yang, F.C. Löhrer, V. Körstgens, A. Schreiber, B. Cao, S. Bernstorff, P. Müller-Buschbaum
  In operando GISAXS and GIWAXS stability study of organic solar cells based on PffBT4T-2OD:PC71BM with and without solvent additive
  Adv. Sci. **7**, 2001117 (2020)

- S.-J. Yang, L.-Y. Zou, C. Liu, Q. Zhong, Z.-Y. Ma, J. Yang, J. Ji, P. Müller-Buschbaum, Z.-K. Xu
  Codeposition of levodopa and polyethyleneimine: Reaction mechanism and coating construction
  ACS Appl. Mater. Interfaces **12**, 54094-54103 (2020)

- B. Ye, Y. Miao, J. Shi, D. Salvato, K. Mo, et.al.
  Temperature Effects on Interdiffusion of Al and U-Mo under Irradiation
  Journal of Nuclear Materials **544**,152684 (2020)

- S. Yin, L. Song, S. Xia, Y. Cheng, N. Hohn, W. Chen, K. Wang, W. Cao, S. Hou, P. Müller-Buschbaum
  Key Factors for Template-Oriented Porous Titania Synthesis: Solvents and Catalysts
  Small Methods **4**, 1900689 (2020)

- S. Yin, T. Tian, K.S. Wienhold, C.L. Weindl, R. Guo, M. Schwartzkopf, S.V. Roth, P. Müller-Buschbaum
  Key factor study for amphiphilic block copolymer-templated mesoporous SnO_2 *thin film synthesis: Influence of solvent and catalyst*
  Adv. Mater. Interf. **7**, 2001002 (2020)

- H. Zhao, H. B. Naveed, B. Lin, X. Zhou, J. Yuan, K. Zhou, H. Wu, R. Guo, M. A. Scheel, A. Chumakov, S. V. Roth, Z. Tang, P. Müller-Buschbaum, W. Ma
  Hot Hydrocarbon-Solvent Slot-Die Coating Enables High-Efficiency Organic Solar Cells with Temperature-Dependent Aggregation Behavior
  Adv. Mater. **32**, 2002302 (2020)

- Q. Zhong, N. Hu, L. Mi, J.-P. Wang, E. Metwalli, L. Bießmann, C. Herold, J. Yang, G.-P. Wu, Z.-K. Xu, R. Cubitt, P. Müller-Buschbaum
  Impact of thermal history on the kinetic response of thermoresponsive poly(diethylene glycol monomethyl ether methacrylate)-block-poly(poly(ethylene glycol) methyl ether methacrylate) thin films investigated by in-situ neutron reflectivity
  Langmuir **36**, 6228-6237 (2020)

- Y. Zou, R. Guo, A. Buyruk, W. Chen, T. Xiao, S. Yin, X. Jiang, , L. P. Kreuzer, C. Mu, T. Ameri, M. Schwartzkopf, S. V. Roth, P. Müller-Buschbaum
  Sodium Dodecylbenzene Sulfonate Interface Modification of Methylammonium Lead Iodide for Surface Passivation of Perovskite Solar Cells
  ACS Appl. Mater. Interfaces **12**, 52643–52651 (2020)

9.2 Talks

- G. Budryte, C. Geiger, P. Müller-Buschbaum
  Soft Robotics Based on Thermo-responsive Polymer Films
  MaMaSELF status meeting, 08 – 11 July 2020

- W. Chen, P. Müller-Buschbaum
  Structure degradation in PbS quantum dots solar cell
  19th SAXS/WAXS/GISAXS satellite workshop of DESY usersmeeting, 30 January, 2020

- C. Geiger, L. P. Kreuzer, T. Widmann, P. Wang, R. Cubitt, C. Henschel, A. Laschewsky, C. M. Papadakis, P. Müller-Buschbaum
  Time-resolved analysis of the co-solvent fraction in thin films from contrasted ToF-NR experiments
  Project Meeting Co-nonsolvency TUM-AGL Laschewsky, 03 April 2020

- C. Geiger, J. Reitenbach, L. P. Kreuzer, T. Widmann, P. Wang, R. Cubitt, C. Henschel, A. Laschewsky, C. M. Papadakis, P. Müller-Buschbaum
  Co-nonsolvency-induced collapse transitions in thermo-responsive block copolymer films
  German Neutron Scattering Conference DN2020, 09 – 10 December 2020

- J. E. Heger, A.-L. Oechsle, S. Yin, S. Bernstorff, P. Müller-Buschbaum
  In operando stability investigation of biotemplated photoactive layers for solar cells
  10th Energy Colloquium of the Munich School of Engineering, 30 July 2020

- X. Jiang, S. J. Schaper, S. V. Roth, P. Müller-Buschbaum
  In-situ investigation of sputter deposition electrodes on different layers of non-fullerene organic solar cell
  MRS Spring and Fall Meeting 2020, 27 November – 04 December 2020

- C.-H. Ko, C. Henschel, G. P. Meledam, M. A. Schroer, A. Laschewsky, P. Müller-Buschbaum, C. M. Papadakis
  Self-Assembled Micelles from Thermoresponsive Poly(methyl methacrylate)-b-poly(N-isopropylacrylamide) Diblock Copolymers in Aqueous Solution
  EMBL Hamburg P12 Virtual User Meeting, 17 – 19 November 2020

- C.-H. Ko, K.-L. Claude, D. Schanzenbach, B.-J. Niebuur, F. A. Jung, J.-J. Kang, H. Frielinghaus, L. C. Barnsley, V. Pipich, B. Wu, A. Schulte, P. Müller-Buschbaum, A. Laschewsky, C. M. Papadakis
  Temperature-Dependent Phase Behavior of Thermoresponsive Polymer Poly(N-isopropylmethacrylamide) in Aqueous Solution
  MLZ User Meeting 2020, 08 – 09 December 2020

- V. Körstgens
  In situ morphology investigations of hybrid solar cells with grazing incidence x-ray scattering techniques
  Colloquium on Solid State Physics, TUM, Garching, 16 January 2020

- V. Körstgens, L. Diaz Piola, K. S. Wienhold, N. Li, W. Chen, M. Nuber, K. Stallhofer, M. Schwartzkopf, H. Iglev, S.V. Roth, R. Kienberger, P. Müller-Buschbaum
  Active layer printing of hybrid solar cells with in situ GISAXS and GIWAXS
  19th SAXS/WAXS/GISAXS satellite workshop of DESY usersmeeting, 30 January, 2020

- L. P. Kreuzer, C. Geiger, T. Widmann, P. Wang, R. Cubitt, V. Hildebrand, A. Laschewsky, C. M. Papadakis, P. Müller-Buschbaum
  Co-nonsolvency of poly(sulfobetaine)-based diblock copolymer thin films
  Projekttreffen Co-nonsolvency, 03 April 2020

- M. Leitner
  Oscillatory dynamics in simple systems at elevated temperatures — beyond a perturbational treatment of anharmonicity
  Institut für Materialwissenschaft, Universität Stuttgart, 06 July 2020

- P. Müller-Buschbaum
  Local structures at solid-liquid interfaces
  Kick-off „Schaumprojekt“ in Karlsruhe, 10 January 2020

- P. Müller-Buschbaum
  Polymer and hybrid nanostructures for applications in organic solar cells investigated with advanced scattering techniques
  Physikalisches Kolloquium in Chemnitz, 22 January 2020

- P. Müller-Buschbaum
  Studying organic solar cells in operando with GISAXS and GIWAXS
  19th SAXS/WAXS/GISAXS satellite workshop of DESY usersmeeting, 30 January, 2020

- P. Müller-Buschbaum
  Report of the Users Committee (DPS-UC) - report 2019
  DESY User Meeting, Hamburg, 31 January 2020

- P. Müller-Buschbaum
  Using neutrons in Archaeology, Geology and Cultural Heritage Studies
  NINXMACH, Garching, 02 March 2020

- P. Müller-Buschbaum
  MLZ Status
  Virtual International Facility Directors Meeting at ACNS, 16 July 2020

- P. Müller-Buschbaum
  Beispiele wissenschaftlicher Untersuchungen am FRM II
  Vortrag bei Besuch des Freisinger Landrats mit Delegation am FRMII, 03 September 2020

- P. Müller-Buschbaum
  Studying organic solar cells with GISANS
  GISANS workshop of ESS User Meeting, Lund, Sweden, 23 September 2020

- P. Müller-Buschbaum
  In-situ studies for the correlation of structure formation with functionality
  PETRA IV - Materials and Processes for Energy and Transport Technology, Hamburg, 16 October 2020

- P. Müller-Buschbaum
  Czech-Bavarian mini-school 2020 on large scale facilities and open data
  Mini-School 2020 Workshop, 19 October 2020

- P. Müller-Buschbaum
  The mission of MLZ and FRMII
  SERPENT User Group Meeting, Garching, 27 October 2020

- P. Müller-Buschbaum
  Examples of scientific research at FRM II
  AQWP Virtual Attaché Trip, Brussels, 28 October 2020

- P. Müller-Buschbaum
  Organic solar cells investigated with advanced scattering techniques
  e-conversion kick-off tandem projects, 09 November 2020

- P. Müller-Buschbaum
  In Situ and In Operando Scattering Studies on Polymer Based Organic Solar Cells
  MRS Virtual Spring/Fall Meeting, 12 November 2020

- P. Müller-Buschbaum
  Photovoltaic research at TU Munich
  ICL-TUM Sustainable Energy Futures Workshop - Photovoltaics, 17 November 2020

- P. Müller-Buschbaum
  Update on MLZ
  MLZ Virtual User Meeting 2020, Garching, 09 December 2020

- B. Niebuur, L. Chiappisi, F. Jung, Y. Zhang, A. Schulte, C. M. Papadakis
  Kinetics of Mesoglobule Disintegration in Aqueous Poly(N-isopropylacrylamide) Solutions Following Pressure Jumps
  German Neutron Scattering Conference, Garching, 09 – 10 Dec 2020

- W. Petry
  Welcome to the Neutron Research Source Heinz Maier-Leibnitz (FRM II) and the Heinz Maier Leibnitz Zentrum (MLZ)
  Visit of the ESA (European Supply Agency) Directorate, 13 February 2020

- W. Petry
  Neutronen – Wozu? und Kernenergie – vom Winde verweht
  MIHK Westerham, Techniktage Bayerische Eliteakademie, 15 September 2020

- W. Petry
  FRM II Conversion
  10th Serpent user group meeting, 27 – 30 October 2020, online-meeting

- S. J. Schaper, H. Xie, T. Widmann, L. P. Kreuzer, M. Haese, G. Mangiapia, J. M. Buriak, P. Müller-Buschbaum
  In-operando neutron reflectometry reveals the solid electrolyte interface formation on surface coated silicon based anodes for lithium-ion batteries
  MLZ User Meeting 2020, 08 – 09 December 2020

- S. Szabò F. Yang, D. Holland-Moritz, T. Voigtmann, A. Meyer, W. Petry
  Structure-dynamics relation in Zr-Ti melts
  MLZ User Meeting 2020, 08 – 09 December 2020

- C.L. Weindl, C. Fajman, M. A. Giebel, T. F. Fässler, P. Müller-Buschbaum
  Germanium-based nanostructure synthesis guided by amphiphilic diblock copolymer templating
  ATUMS: Annual Meeting, 09 November 2020

- K. S. Wienhold, V. Körstgens, S. Grott, X. Jiang, S. Yin, C. L. Weindl, T. Tian, M. Schwartzkopf, A. Rothkirch, S. V. Roth, P. Müller Buschbaum
  In Situ Printing: Insights into the Evolution of Morphology and Optical Properties of Slot-Die Coated Active Layers for Application in Organic Solar Cells
  9th SolTech Conference, 05 – 06 October 2020

9.3 Posters

- W. Cao, S. Yin, M. Plank, M. Plank, M. Opel, M. Gallei, A. Chemezov, C. J. Brett, M. Schwartzkopf, S. V. Roth, P. Müller-Buschbaum
  Spray deposited anisotropic magnetic hybrid thin films containing PS-b-PMMA and strontium hexaferrite magnetic nanoplates
  MLZ User Meeting 2020, 08 – 09 December 2020

- W. Chen, P. Müller-Buschbaum
  Structure degradation in PbS quantum dots solar cell
  DESY Photon Science Users' Meeting 2020, 29 – 31 January 2020

- W. Chen, P. Müller-Buschbaum
  Structure degradation in PbS quantum dots solar cell
  10th Energy Colloquium of the Munich School of Engineering, 30 July 2020

- C. Geiger, J. Reitenbach, L. P. Kreuzer, T. Widmann, P. Wang, R. Cubitt, C. Henschel, A. Laschewsky, C. M. Papadakis, P. Müller-Buschbaum
  Co-nonsolvency induced collapse transitions in thermo-responsive block copolymer films
  MLZ User Meeting 2020, 08 – 09 December 2020

- M. Gensch, M. Schwartzkopf, C. J. Brett, S. J. Schaper, L. P. Kreuzer, A.-L. Oechsle, W. Chen, S. Liang, N. Li, J. Drewes, O. Polonskyi, T. Strunskus, F. Faupel, P. Müller-Buschbaum, S. V. Roth
  Sputter deposition of Ag on nanostructured PMMA-b-P3HT copolymer thin films
  Desy Photon Science Users Meeting 2020, 27 – 28 January 2020

- M. Gensch, M. Schwartzkopf, C. J. Brett, S. J. Schaper, L. P. Kreuzer, A.-L. Oechsle, W. Chen, S. Liang, N. Li, J. Drewes, O. Polonskyi, T. Strunskus, F. Faupel, P. Müller-Buschbaum, S. V. Roth
  Sputter deposition of Ag on nanostructured PMMA-b-P3HT copolymer thin films
  10th Energy Colloquium of the Munich School of Engineering, 30 July 2020

- M. Gensch, M. Schwartzkopf, C. J. Brett, S. J. Schaper, L. P. Kreuzer, A.-L. Oechsle, W. Chen, S. Liang, N. Li, J. Drewes, O. Polonskyi, T. Strunskus, F. Faupel, P. Müller-Buschbaum, S. V. Roth
  Sputter deposition of Ag on nanostructured PMMA-b-P3HT copolymer thin films
  MLZ User Meeting 2020, 08 – 09 December 2020

- S. Grott, L. Bießmann, N. Saxena, W. Cao, S. Bernstorff, P. Müller-Buschbaum
  Investigations on the morphology of fullerene-free bulk heterojunction blends for photovoltaic applications
  MLZ User Meeting 2020, 08 – 09 December 2020

- T. Guan, W. Chen, S. Liang, N. Li, C. L. Weindl, S. V. Roth, L. Jiang, P. Müller-Buschbaum
  Fabrication on Plasmonic Nanostructures in Photovoltaics
  10th Energy Colloquium of the Munich School of Engineering, 30 July 2020

- T. Guan, W. Chen, H. Tang, S. Liang, N. Li, C. L. Weindl, S. V. Roth, L. Jiang, P. Müller-Buschbaum
  Fabrication on Plasmonic Nanostructures in Photoelectronic Devices
  MLZ User Meeting 2020, 08 – 09 December 2020

- R. Guo, D. Han, W. Chen, L. Dai, K. J, Q. X, S. Li, L. K. Reb, M .A .Scheel, S. Pratap, N. Li, S. Yin, A. L. Oechsle, X. Tian, S .Liang, C. L, Weindl, H. Ebert, N. Greenham, S. Stranks, R. Friend, P. Gao, M. Yuan, M. Schwartzkopf, S. V. Roth, P. Müller-Buschbaum
  Atmosphere Affecting Lattice and Degradation Mechanisms of High-Efficiency Perovskite Solar Cells
  10th Energy Colloquium of the Munich School of Engineering, 30 July 2020

- R. Guo, D. Han, W. Chen, L. Dai, K. J, Q. X, S. Li, L. K. Reb, M .A .Scheel, S. Pratap, N. Li, S. Yin, A. L. Oechsle, X. Tian, S .Liang, C. L, Weindl, H. Ebert, N. Greenham, S. Stranks, R. Friend, P. Gao, M. Yuan, M. Schwartzkopf, S. V. Roth, P. Müller-Buschbaum
  Atmosphere Affecting Lattice and Degradation Mechanisms of High-Efficiency Perovskite Solar Cells
  The nineth international SolTech conference, 05 October – 08 October 2020

- R. Guo, D. Han, W. Chen, L. Dai, K. J, Q. X, S. Li, L. K. Reb, M .A .Scheel, S. Pratap, N. Li, S. Yin, A. L. Oechsle, X. Tian, S .Liang, C. L, Weindl, H. Ebert, N. Greenham, S. Stranks, R. Friend, P. Gao, M. Yuan, M. Schwartzkopf, S. V. Roth, P. Müller-Buschbaum
  Atmosphere Affecting Lattice and Degradation Mechanisms of High-Efficiency Perovskite Solar Cells
  2020 virtual MRS spring/fall meeting, 23 November – 04 December 2020

- R. Guo, D. Han, W. Chen, L. Dai, K. J, Q. X, S. Li, L. K. Reb, M .A .Scheel, S. Pratap, N. Li, S. Yin, A. L. Oechsle, X. Tian, S .Liang, C. L, Weindl, H. Ebert, N. Greenham, S. Stranks, R. Friend, P. Gao, M. Yuan, M. Schwartzkopf, S. V. Roth, P. Müller-Buschbaum
  Atmosphere Affecting Lattice and Degradation Mechanisms of High-Efficiency Perovskite Solar Cells
  MLZ User Meeting 2020, 08 – 09 December 2020

- J. E. Heger, C. Geiger, T. Widmann, L. P. Kreuzer, S. Yin, A. Koutsioumpas, P. Müller-Buschbaum
  A GISANS study of bio-hybrid films: Influence of pH on spraycoated ß-lactoglobulin:TiO_2 *film morphology for biotemplated titania nanostructures*
  MLZ User Meeting 2020, 08 – 09 December 2020

- X. Jiang, S. J. Schaper, S. V. Roth, P. Müller-Buschbaum
  In-situ Investigation of Sputter Deposition Electrodes of Non-Fullerene Organic Solar Cells
  10th Energy Colloquium of the Munich School of Engineering, 30 July 2020

- X. Jiang, S. J. Schaper, S. V. Roth, P. Müller-Buschbaum
  In-situ sputter deposition of Al electrodes on active layers of non-fullerene organic solar cells
  MLZ User Meeting 2020, 08 – 09 December 2020

- F. A. Jung, P. A. Panteli, C.-H. Ko, J.-J. Kang, L. C. Barnsley, C. Tsitsilianis, C. S. Patrickios, C. M. Papadakis
  Structural Properties of Micelles formed by Telechelic Pentablock Quaterpolymers with pH-responsive Midblocks and Thermoresponsive End Blocks in Aqueous Solution
  MLZ User Meeting 2020, 08 – 09 December 2020

- J.-J. Kang, C. Sachse, C.-H. Ko, M.A. Schroer, S. Da Vela, J. Kohlbrecher, R. Jordan, C.M. Papadakis
  Concentration-conformation relation of a poly(2-oxazoline)-based bottlebrush polymer in good solvent
  EMBL Hamburg P12 Virtual User Meeting, 17 – 18 November 2020

- J.-J. Kang, F.A. Jung, C.-H. Ko, K. Shehu, L.C. Barnsley, F. Kohler, H. Dietz, J. Zhao, S. Pispas, C. M. Papadakis
  Dehydration of thermoresponsive molecular brushes with block or random copolymer side chains
  MLZ User Meeting 2020, 08 – 09 December 2020

- C.-H. Ko, K.-L. Claude, D. Schanzenbach, B.-J. Niebuur, F. A. Jung, J.-J. Kang, H. Frielinghaus, L. C. Barnsley, V. Pipich, B. Wu, A. Schulte, P. Müller-Buschbaum, A. Laschewsky, C. M. Papadakis
  Temperature-Dependent Phase Behavior of Thermoresponsive Polymer Poly(N-isopropylmethacrylamide) in Aqueous Solution
  MLZ User Meeting 2020, 08 – 09 December 2020

- V. Körstgens, L. Diaz Piola, K. S. Wienhold, N. Li, W. Chen, M. Scheel, C. Geiger, L. Kreuzer, T. Widmann, M. Nuber, K. Stallhofer, M. Schwartzkopf, G. Mangiapia, H. Iglev, S.V. Roth, R. Kienberger, P. Müller-Buschbaum
  Morphology investigation of printed active layers of hybrid solar cells with grazing incidence neutron and x-ray scattering techniques
  MLZ User Meeting 2020, 08 – 09 December 2020

- V. Körstgens, L. Diaz Piola, K. S. Wienhold, N. Li, W. Chen, M. Nuber, K. Stallhofer, M. Schwartzkopf, H. Iglev, S.V. Roth, R. Kienberger, P. Müller-Buschbaum
  Active layer printing of hybrid solar cells with in situ GISAXS and GIWAXS
  DESY Photon Science Users' Meeting 2020 , 29 – 31 January 2020

- L. P. Kreuzer, T. Widmann, L. Bießmann, N. Aldosari, G. Mangiapia, V. Hildebrand, A. Laschewsky, C. M. Papadakis, P. Müller-Buschbaum
  Switchable thermo-responsive polymer coatings as self-cooling approach for buildings
  10th Energy Colloquium of the Munich School of Engineering, 30 July 2020

- L. P. Kreuzer, T. Widmann, L. Bießmann, N. Hohn, J. Pantle, R. Märkl, J. F, Moulin, V. Hildebrand, A. Laschewsky, C. M. Papadakis, P. Müller-Buschbaum
  Phase transition kinetics in a doubly thermo-responsive poly(sulfobetaine)-based block copolymer thin film
  MLZ User Meeting 2020, 08 – 09 December 2020

- M. Leitner
  Oscillatory dynamics in simple systems at elevated temperatures — beyond a perturbational treatment of anharmonicity
  German Neutron Scattering Conference DN2020, 09 – 10 December 2020

- N. Li, L. Song, N. Hohn, N. Saxena, W. Cao, X. Jiang, P. Müller-Buschbaum
  Nano-confinement on chain alighment and crystallization of conjugated polymers P3HT and PffBT4T-2OD by printed mesoporous TiO_2 photoanodes
  10th Energy Colloquium of the Munich School of Engineering, 30 July 2020

- N. Li, R. Guo, W. Chen, V. Körstgens, J. E. Heger, S. Liang, C. J. Brett, M. A. Hossain, J. Zheng, P. S. Deimel, A. Buyruk, F. Allegretti, M. Schwartzkopf, J. G. C. Veinot, G. Schmitz, J. V. Barth, T. Ameri, S. V. Roth, P. Müller-Buschbaum
  Highly ordered titania films with incorporated germanium nanoparticles for photoanodes
  MLZ User Meeting 2020, 08 – 09 December 2020

- Y. Li, J.-J. Kang, A. Skandalis, V. Chrysostomou, A. Radulescu, S. Pispas, C. M. Papadakis
  Stimuli-Responsive Micelles from Amphiphilic Diblock Copolymers
  MLZ User Meeting 2020, 08 – 10 December 2020

- S. Liang, W. Chen, S. Yin, M. Schwartzkopf, S. V. Roth, P. Müller-Buschbaum
  In-situ GISAXS Observation of Sputter-Deposition Gold Plasmonic Nanostructures on TiO_2 *Templates*
  10th Energy Colloquium of the Munich School of Engineering, 30 July 2020

- S. Liang, W. Chen, S. Yin, M. Schwartzkopf, S. V. Roth, P. Müller-Buschbaum
  Tailoring Optical Properties of Sputter-Deposited Au Nanostructures on TiO_2 *Templates with in situ GISAXS Determined Growth Laws*
  MLZ User Meeting 2020, München, 8-9 Dec 2020

- A. L. Oechsle, J. E. Heger, N. Li, S. Yin, S. Bernstorff, P. Müller-Buschbaum
  Conductivity stability of EMIM-DCA post-treated semi-conducting PEDOT:PSS polymer thin films under elevated temperatures
  MLZ User Meeting 2020, 08 – 09 December 2020

- D. Petz, M. J. Mühlbauer, V. Baran, A. Schökel, M. Hofmann, P. Müller-Buschbaum, A. Senyshyn
  Non-destructive quantification of lithium and electrolyte losses in Li-ion batteries using neutron powder diffraction
  MLZ User Meeting 2020, 08 – 09 December 2020

- I. Pivarnikova, N. Paul, J. B. Habedank, L. Kraft, V. Baran, A. Jossen, M. F. Zaeh, P. Müller-Buschbaum, R. Gilles
  Structured graphite anodes for Li-ion batteries
  MLZ User Meeting 2020, 08 – 09 December 2020

- S. Pratap, J. Schlipf, L. Bießmann, P. Müller-Buschbaum
  Hierarchical Structures in Hybrid Perovskite Thin Films: Implications for Photovoltaics
  MLZ User Meeting 2020, 08 – 09 December 2020

- L. K. Reb, M. Böhmer, B. Predeschly, S. Grott, C. L. Weindl, G. I. Ivandekic, R. Guo, C. Dreißigacker, R. Gernhäuser, A. Meyer, P. Müller-Buschbaum
  Perovskite and Organic Solar Cells on a Rocket Flight
  9th SolTech Conference, 05 – 06 October 2020

- L. K. Reb, M. Böhmer, B. Predeschly, S. Grott, C. L. Weindl, G. I. Ivandekic, R. Guo, C. Dreißigacker, R. Gernhäuser, A. Meyer, P. Müller-Buschbaum
  Perovskite and Organic Solar Cells on a Rocket Flight
  ATUMS: Annual Meeting, 09 November 2020

- L. K. Reb, W. Chen, S. J. Schaper, X. Jiang, M. Schwartzkopf, P. Pandit, M. Gensch, J. Drewes, O. Polonskyi, T. Strunskus, F. Faupel, S. V. Roth, P. Müller-Buschbaum
  Following the Interface Formation During Sputter Deposition on Perovskite Films
  MLZ User Meeting 2020, 08 – 09 December 2020

- J. Reitenbach, C. Geiger, T. Widmann, L. P. Kreuzer, G. Mangiapia, C. Henschel, A. Laschewsky, C. M. Papadakis, P. Müller-Buschbaum
  Cononsolvency-Induced Collapse Transition in Thin PMMA-b-PNIPMAM Films
  MLZ User Meeting 2020, 08 – 09 December 2020

- S. J. Schaper, F. C. Löhrer, S. Xia, M. Schwartzkopf, P. Pandit, A. Hinz, O. Polonskyi, T. Strunskus, F. Faupel, S. V. Roth, P. Müller-Buschbaum
  Investigating the growth of copper as contacts for polymer thin film lithium-ion batteries
  10th Energy Colloquium of the Munich School of Engineering, 30 July 2020

- M. A. Scheel, L. K. Reb, R. Guo, M. Schwartzkopf, S. V. Roth, P. Müller-Buschbaum
  In situ GIWAXS studies on 2-step printed MAPI films
  MSE Winter School: Energy and Food 2020, 16 – 20 February 2020

- M. A. Scheel, L. K. Reb, R. Guo, S. Grott, M. Schwartzkopf, S. V. Roth, P. Müller-Buschbaum
  In-situ Annealing GIWAXS Studies of 2-Step Printed MAPI for Large Area PSCs
  MLZ User Meeting 2020, 08 – 09 December 2020

- D. M. Schwaiger, W. Lohstroh, P. Müller-Buschbaum
  Investigation of molecular dynamics of PTB7:PCBM polymer blends with quasielastic neutron scattering
  MLZ User Meeting 2020, 08 – 09 December 2020

- T. Tian, S. Yin, M. Schwartzkopf, S. V. Roth, P. Müller-Buschbaum
  Mesoporous ZnO Templated by Diblock Copolymer for Hybrid Solar Cells
  10th Energy Colloquium of the Munich School of Engineering 2020, 30 July 2020

- T. Tian, S. Yin, M. Schwartzkopf, S. V. Roth, P. Müller-Buschbaum
  In situ investigation of printed mesoporous ZnO films templated by diblock copolymer
  MLZ User Meeting 2020, 08 – 09 December 2020

- S. Tu, T. Tian, O. Anna-Lena, P. Müller-Buschbaum
  Increase the thermoelectric properties of PEDOT: PSS films via a facile one-step post-treatment
  10th Energy Colloquium of the Munich School of Engineering, 30 July 2020

- S. Tu, T. Tian, O. Anna-Lena, P. Müller-Buschbaum
  Feasible tuning of microstacking structure and oxidation level in PEDOT: PSS films via sequential post-treatment
  MLZ User Meeting 2020, München, 08 – 09 December 2020

- A. Vagias, S. J. Schaper, W. Chen, S. Liang, C. Geiger, N. Li, L. P. Kreuzer, M. Gensch, P. Pandit, M. Schwartzkopf, S. V. Roth, J. Drewes, N. Carstens, T. Strunskus, F. Faupel, A. Laschewsky, P. Müller-Buschbaum
  Monitoring gold cluster growth/formation on zwitterionic block copolymer coatings as functional interlayers
  10th Energy Colloquium of the Munich School of Engineering, 30 July 2020

- A. Vagias, A. Papagiannopoulos, L. P. Kreuzer, D. Giaouzi, S. Busch, S. Pispas, P. Müller-Buschbaum
  Polymer block length and temperature effects on the nanoscale morphology of thermoresponsive double hydrophilic block copolymers
  German Neutron Scattering Conference DN2020, 09 – 10 December 2020

- P. Wang, L. P. Kreuzer, C. Geiger, T. Widmann, S. Liang, A. Laschewsky, C. M. Papadakis, R. Cubitt, P. Müller-Buschbaum
  Co-Nonsolvency Transition of PNIPMAM-based Diblock Copolymer Thin Films in a Series of Binary Mixtures
  MLZ User Meeting 2020, 08 – 09 December 2020

- C.L. Weindl, C. Fajman, M. A. Giebel, T. F. Fässler, P. Müller-Buschbaum
  Germanium-based nanostructure synthesis guided by amphiphilic diblock copolymer templating
  MSE Energy and Food 2020, 16 – 20 February 2020

- C.L. Weindl, C. Fajman, M. A. Giebel, T. F. Fässler, P. Müller-Buschbaum
  Germanium-based nanostructure synthesis guided by amphiphilic diblock copolymer templating
  10th Energy Colloquium of the Munich School of Engineering, 30 July 2020

- C.L. Weindl, C. Fajman, M. A. Giebel, T. F. Fässler, P. Müller-Buschbaum
  Germanium-based nanostructure synthesis guided by amphiphilic diblock copolymer templating
  MLZ User Meeting 2020, 08 – 09 December 2020

- T. Widmann, L. P. Kreuzer, P. Müller-Buschbaum
  3D-printed humidity chamber for neutron scattering on thin films
  MLZ User Meeting 2020, 08 – 09 December 2020

- K. S. Wienhold, V. Körstgens, S. Grott, X. Jiang, M. Schwartzkopf, S. V. Roth, P. Müller-Buschbaum
  In Situ Study of Printed Active Layers of Conjugated Polymers and Small Acceptor Molecules for Application in High-Efficiency Organic Solar Cells
  10th Energy Colloquium of the Munich School of Engineering, 30 July 2020

- K. S. Wienhold, V. Körstgens, S. Grott, X. Jiang, M. Schwartzkopf, S. V. Roth, P. Müller-Buschbaum
  In Situ Printing: Insights into the Morphology Formation and Optical Property Evolution of Slot-Die-Coated Active Layers Containing Low Bandgap Polymer Donor and Nonfullerene Small Molecule Acceptor
  MLZ User Meeting 2020, 08 – 09 December 2020

- T. Xiao, W. Chen, W. Cao, S. Wöhnert, S. V. Roth, P. Müller-Buschbaum
  Hybrid Energy Harvester based on Triboelectric Nanogenerator and Solar Cell
  10th Energy Colloquium of the Munich School of Engineering, 30 July 2020

- T. Xiao, W. Chen, W. Cao, S. Wöhnert, S. V. Roth, P. Müller-Buschbaum
  Hybrid Energy Harvester based on Triboelectric Nanogenerator and Solar Cell
  MLZ User Meeting 2020, München, 08 – 09 December 2020

- D. Yang, F. C. Löhrer, V. Körstgens, A. Schreiber, S. Bernstorff, J. M. Buriak, Peter Müller-Buschbaum
  Investigating the effects of solvent additives on the stability of organic solar cells
  10th Energy Colloquium of the Munich School of Engineering, 30 July 2020

- B. Yazdanshenas, B.-J. Niebuur, D. Schanzenbach, A. Laschewsky, M. Zamponi, D. Noferini, A. Schulte, C. M. Papadakis
  Water dynamics in a concentrated aqueous solution of perdeuterated poly(N-isopropylacryamide) across the cloud point
  MLZ User Meeting 2020, 08 – 09 December 2020

- S. Yin, W. Cao, M. Schwartzkopf, S. V. Roth, P. Müller-Buschbaum
  Morphology control of PS-b-P_4VP templated monolayer mesoporous Fe_2O_3 thin films
  MLZ User Meeting 2020, 08 – 09 December 2020

- S. Yin, P. Müller-Buschbaum
  Key Factors Study in Amphiphilic Block Copolymer-Oriented Porous SnO_2 Synthesis Process
  Materials Research Society Fall Meeting, 28 November - 4 December, 2020

- Y. Zou, R. Guo, M. Scheel, B. Ali, S. Yin, X. Jiang, L. P. Kreuzer, C. Mu, T. Ameri, M. Schwartzkopf, S. V. Roth, P. Müller-Buschbaum
  Sodium dodecylbenzene sulfonate interface modification of methylammonium lead iodide as surface passivation of perovskite solar cells
  10th Energy Colloquium of the Munich School of Engineering, 30 July 2020

- Y. Zou, M. Scheel, T. Xiao, S. Pratap, B. Ali, S. Yin, C. Mu, T. Ameri, M. Schwartzkopf, S. V. Roth, P. Müller-Buschbaum
  Compositional engineering for high performance perovskite solar cells via Cs doping
  MLZ User Meeting 2020, 08 – 09 December 2020

- U. Zweck, M. Leitner
  Antiferromagnetically coupled anti-phase domains under external magnetic fields
  Joint European Magnetic Symposia 2020, 07 – 11 December 2020

9.4 Invited talks

- Borislav Polovnikov, LMU München
  Fluctuations and Criticality in Reaction-Diffusion Systems
  FluFabrication of BiSCCO Nanowires for Single-Photon Detection
  23 Jan 2020

- Prof. Dr. Felix H. Schacher, Friedrich-Schiller Universität Jena
  Polyampholytes as Versatile Materials in Catch & Release Applications
  12 Feb 2020

- Prof. Dr. Prof. Seema Agarwal, University of Bayreuth
  Non-ionic polymers and networks with UCST-type transitions in water
  19 Feb 2020

- Prof. Dr. Aristeidis Papagiannopoulos, National Hellenic Research Foundation, Athens, Greece
  Design and physicochemical studies of polysaccharide-based soft biomaterials
  26 Feb 2020

- Lukas Spanier
  Formation of Perovskite Thin Films on Silicon Substrates for Tandem Solar Cells
  21 Jul 2020

- Fabian Apfelbeck
  Growth, Characterization and Transfer of Highly-Ordered Semiconductor Thin Films
  30 Oct 2020

- Prof. Letizia Tavagnacco, Physics Department, University of Rome La Sapienza, Italy
  Using molecular modeling to explore Poly(N-isoproylacrylamide) coil-to-globule transition induced by pressure
  11 Nov 2020

- Dr. Daniel F. Sunday, Polymer Processing Group, National Institute of Standards and Technology (NIST), Gaithersburg, MD, U.S.A.
  Characterizing Bottlebrush Structure in Solution and Thin Films
  25 Nov 2020

9.5 Funding

Deutsche Forschungsgemeinschaft:

- *In-situ Untersuchungen zu Kondensation, Nukleation und Wachstum von Metallfilmen und Nanostrukturen auf organischen Oberflächen während Sputterbeschichtung*
  Grant Number: MU 1487/18-2
  Project Leader: Prof. Dr. Peter Müller-Buschbaum

- *Transport und Morphologie, Einfluss auf nichtgeminale Rekombination in Organischen Solarzellen*
  Grant Number: MU 1487/22-1
  Project Leader: Prof. Dr. Peter Müller-Buschbaum

- *Rheologie und Grenzflächenstrukturen von Protein- und Partikelstabilisierten Schäumen – ein Multiskalenansatz*
  Grant Number: MU 1487/32-1
  Project Leader: Prof. Dr. Peter Müller-Buschbaum

- *Investigation of polymer templated Silicon-Germanium gas photovoltaic and battery applications*
  Internationales Graduiertenkolleg: GRK 2022/2
  Alberta Universität/Technische Universität München Internationale Graduiertenschule für Funktionelle Hybridmaterialen (ATUMS)
  Project Leader: Prof. Dr. Peter Müller-Buschbaum

- *High efficiency perovskite solar cells*
  Internationales Graduiertenkolleg: GRK 2022/2
  Alberta Universität/Technische Universität München Internationale Graduiertenschule für Funktionelle Hybridmaterialen (ATUMS)
  Project Leader: Prof. Dr. Peter Müller-Buschbaum

- *In-situ Neutron and x-ray scattering on printed perovskite thin films for photovoltaic application*
  Im Rahmen des Exzellenzclusters e-conversion
  Project Leader: Prof. Dr. Peter Müller-Buschbaum

- *Impact of morphology on the polaron dynamics in polymer: non-fullerene blends for photovoltaic applications*
  Im Rahmen des Exzellenzclusters e-conversion (Seedfunding)
  Project Leader: Prof. Dr. Peter Müller-Buschbaum/ Prof. Dr. Reinhard Kienberger

- *Cononsolvency-induzierte Selbstorganisation thermoresponsiver Blockcopolymere in Lösung und im dünnen Film*
  Grant Number: MU 1487/29-1, Project Leader: Prof. Dr. Peter Müller-Buschbaum
  Grant Number: PA 771/20-1, Project Leader: Prof. Dr. Christine Papadakis

- *Kinetik der Aggregation in thermoresponsiven Polymerlösungen bei Drucksprüngen*
  Grant Number: PA 771/22-1
  Project Leader: Prof. Dr. Christine Papadakis

- *Dünne Filme aus pH und thermoresponsiven Triblockcopolymeren: von der Netzwerkdynamik zum defektfreien Film*
  Grant Number: PA 771/19-1
  Project Leader: Prof. Dr. Christine Papadakis

Bundesministerium für Bildung und Forschung:

- *FlexiProb: Flexible Probenumgebungen für die Untersuchung weicher Materie zur Implementierung an der ESS*
  Teilprojekt: 3
  Project Leader: Prof. Dr. Peter Müller-Buschbaum

Bayerisches Staatsministerium für Wissenschaft und Kunst:

- *Solar Technologies Go Hybrid (SolTech) - Forschungsnetzwerk TUM.solar*
  Im Rahmen der Munich School of Engineering (MSE)
  Project Leader: Prof. Dr. Peter Müller-Buschbaum
- *Aufbau eines interdisziplinären Netzwerks aus Lehrstühlen der Technischen Universität München und anderen Forschungseinrichtungen zur Förderung der Forschungsaktivitäten im Bereich der regenerativen Energien*
  Im Rahmen der Munich School of Engineering (MSE): Netzwerk Regenerative Energien
  Project Leader: Prof. Dr. Peter Müller-Buschbaum

Others:

- *Understanding the simultaneous evolution of structure-function properties of hybrid metal halide perovskites toward high performance, stable, and sustainable photovoltaics*
  Im Rahmen des Bayerisch-Kalifornischen Hochschulzentrums (BaCaTeC):
  Förderprojekt Nr. 9
  Principal Investigator: Prof. Dr. Peter Müller-Buschbaum
- *Protein/polysaccharide nanoparticles by biocompatible protocols for the encapsulation of natural pharmaceutical compounds (BioEncaps)*
  Im Rahmen des Deutschen Akademischen Austauschdienstes (DAAD)
  Programm Projektbezogener Personenaustausch Griechenland 2020 - 2022
  Project Leader: Prof. Dr. Christine Papadakis

10 The chair

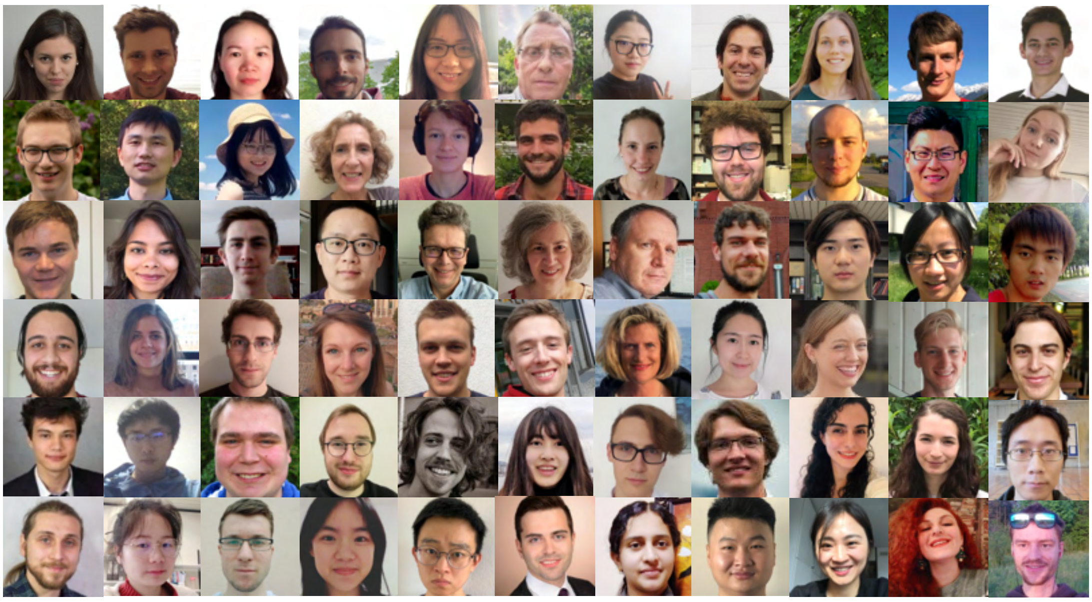

10.1 Staff

Chair:

Prof. Dr. Peter Müller-Buschbaum

Professor:

Prof. Dr. Christine Papadakis

Emerited Professor:

Prof. Dr. Winfried Petry

Fellows:

Dr. Wei Chen
Dr. Florian Jung
Dr. Volker Körstgens
Dr. Michael Leitner
Dr. Wiebke Lohstroh
Dr. Geethu Pathirassery Meledam
Dr. Jürgen Neuhaus
Dr. Neelima Paul
Dr. Apostolos Vagias

PhD Students:

Neslihan Aslan
Bruno Baumeister
Wei Cao
Tobias Chemnitz
Wei Chen
Stefan Döge
Christopher Reck Everett
Christina Geiger
Marc Gensch
Sebastian Grott
Tianfu Guan
Renjun Guo
Constantin Harder
Julian Eliah Heger
Alexander Ewin Heldmann
Tanja Huber
Xinyu Jiang
Florian Jung
Jia-Jhen Kang
Chia-Hsin Ko
Lucas Philipp Kreuzer
Nian Li
Xiaohu Li
Yanan Li
Suzhe Liang
Franziska Carina Löhrer
Anna-Lena Oechsle
Dominik Petz
Thien An Pham
Ivana Pivarnikova
Shambhavi Pratap
Lennart Reb
Julija Reitenbach
Roy Schaffrinna
Simon Jakob Schaper
Manuel Andree Scheel
Dominik Schwaiger
Christian Schwarz
Jingyi Shi
Lukas Spanier
Riane Elizabeth Stene
Sandro Szabò
Ting Tian
Suo Tu
Peixi Wang
Christian Ludwig Weindl
Tobias Widmann
Kerstin Sabrina Wienhold
Tianxiao Xiao
Dan Yang
Shanshan Yin
Yuqin Zou
Ulrike Zweck

Master Students:

Amina Aliç
Johannes Allwang
Gintare Budryte
Debamitra Chakraborty
Pauline Chotard
Lautaro Diaz Piola
Georg Glänzer
Naifei Guo
Linus Huber
Goran Ivkovic Ivandekiç
Kexun Luo
Aikaterina Panagiotou
Dominik Petz
Julija Reitenbach
Ronja Schönecker
Oleg Shindelov
Magdalini Spyranti
Daniel Steger
Cristian Telescu
Rika Unkelbach
Bahar Yazdanshenas
Rui Wang

Bachelor Students:

Sebastian Coen
Lewin Deville
Mateo Gabriel Flohr Reija
Luka Gaetani
Michael Kopp
Ahmed Krifa
Christoph Lindenmeir
Andreas Lukas
Florian Karl Peter Maly
Sabine Matuschik
Andreas Meyer
Michael Mühlbacher
Lorenz Plank
Andreas Steinhart
Franziska Wilfinger
Andreas Wirler

Students Assistants:

Johannes Allwang
Pia Sapelza

Technical/Administrative Staff:

Reinhold Funer
Josef Huber
Josef Kaplonski
Carola Kappauf
Dieter Müller
Marion Waletzki

10.2 Graduations

- **Accomplished PhD Theses**

  Tobias Chemnitz
  Development of a dry-chemical extraction process for 99Mo and plasma-aided synthesis of transition metal hexafluoride

  Wei Chen
  Quantum Dots Based Novel Device Architectures

  Florian Jung
  Self-Assembly of Multi-Responsive Multiblock Copolymers

  Riane Elizabeth Stene
  Development of Dry and Non-Aqueous Techniques for the Separation of Molybdenum from Uranium and Investigations of Group Six Metal Fluoride and Oxyfluoride Chemistry

  Sandro Szabò
  Influence of the short-range order on the atomic dynamics in metallic melts

  Dan Yang
  Investigating the effects of solvent additives on the stability of organic solar cells

- **Accomplished Master Theses**

  Gintare Budryte
  Soft Robotics Based on Thermo-responsive Polymeric Thin Films

  Pauline Chotard
  Printed organic solar cells

  Lautaro Diaz Piola
  Morphology study of water-processed active layers for hybrid photovoltaic applications

  Georg Glänzer
  Interfaces between polymer electrolyte, electrodes and metal current collectors of thin film Lithium-Ion batteries

  Naifei Guo
  Fabrication of non fullerene organic solar cells with slot die coating technique

  Linus Huber
  Effect of temperature on the morphology and device performance of printed nonfullerene acceptor based organic solar cells

  Dominik Petz
  Fading of lithium-ion batteries: combined investigation by neutron diffraction and electrochemistry

  Julija Reitenbach
  Cononsolvency-induced collapse transition in thin thermoresponsive films

  Ronja Schönecker
  Development, Verification and Discussion of a PLTEMP Model for Research Reactors with a Compact Core

  Magdalini Spyranti
  Sponge-like mesoporous TiO_2*: Impact of template concentration and comparison with various polymers for photovoltaic applications*

  Daniel Steger
  Influence of solvents on the active layer based on non-fullerene acceptors

Cristian Telescu
Polymers for lithium ion batteries investigating composite electrodes

Rika Unkelbach
Investigation of long-term reliability of adhesive joints under high-cyclic loading in MEMS devices

Bahar Yazdanshenas
Water dynamics in an aqueous solution of perdeuterated poly(N-isopropylacrylamide) across the demixing transition

- **Accomplished Bachelor Theses**

Sebastian Coen
High efficiency organic solar cells

Lewin Deville
Influence of humidity on EMIM-DCA treated PEDOT:PSS layers for use in thermoelectric devices

Luka Gaetani
Co-nonsolvency Effect in Novel Thermoresponsive Homo- and Block Copolymers

Michael Kopp
Printing of active layers and electron transporting layers for application in organic solar cells

Ahmed Krifa
Printing of thin films for upscalable manufacture of organic solar cells

Christoph Lindenmeir
Dünne Funktionshydrogelfilme und deren potentielle Anwendung in weicher Robotik

Sabine Matuschik
Production and Heavy-Ion Irradiation of Tungsten Coatings as Diffusion Barrier in the U-Mo/Al Fuel System

Dominik Mayer
A Light Scattering Study of a Polystyrene-b-poly(N-isopropylacrylamide) Diblock Copolymer under High Pressure

Andreas Meyer
Structure and morphology analysis on slot-die coated PbI_2 *and* $MAPbI_3$ *thin films for photovoltaic application*

Michael Mühlbacher
Single-ion polymer electrolytes for lithium-ion batteries

Lorenz Plank
Single-ion polymer lithium-ion batteries

Wise Soo-Penning
Photochromic paper – Experimental investigation of the photochromic effect on cellulose based colloid films

Franziska Wilfinger
Modeling TOF-spectra

10.3 Guests

- Prof. Felix Schacher, Friedrich-Schiller Universität Jena, Jena Center for Soft Matter (JCSM)
  11 – 13 Feb 2020

- Prof. Seema Agarwal, Universität Bayreuth
  19 Feb 2020